Pyrite oxidation in river basins of India: Spatio-temporal study of sulfur and oxygen isotopes of dissolved sulfates

विद्या वाचस्पति की
उपाधि की अपेक्षाओं की आंशिक पूर्ति में प्रस्तुत शोध प्रबंध

A thesis submitted in partial fulfillment of the requirements of the degree of Doctor of Philosophy

द्वारा / By
राकेश कुमार राउत
Rakesh Kumar Rout

पंजीकरण सं. / Registration No.: 20193683

शोध प्रबंध पर्यवेक्षक /
Thesis Supervisor: **Dr. Gyana Ranjan Tripathy**

भारतीय विज्ञान शिक्षा एवं अनुसंधान संस्थान पुणे
INDIAN INSTITUTE OF SCIENCE EDUCATION AND RESEARCH PUNE
2025

This page has been intentionally left blank.

Dedicated to

My Parents

This page has been intentionally left blank.

भारतीय विज्ञान शिक्षा एवं अनुसंधान संस्थान पुणे
INDIAN INSTITUTE OF SCIENCE EDUCATION AND RESEARCH PUNE
डॉ. होमी भाभा मार्ग, पुणे 411008, महाराष्ट्र, भारत | Dr. Homi Bhabha Road, Pune 411008, Maharashtra, India
T +91 20 2590 8001 W www.iiserpune.ac.in
IISER PUNE

CERTIFICATE

Certified that the work incorporated in the thesis entitled **"Pyrite oxidation in river basins of India: Spatio-temporal study of sulfur and oxygen isotopes of dissolved sulfates"** submitted by **Mr. Rakesh Kumar Rout** was carried out by the candidate, under my supervision. The work presented here or any part of it has not been included in any other thesis submitted previously for the award of any degree or diploma from any other University or Institution.

Date: 15/Jan/25
Place: Pune

Dr. Gyana Ranjan Tripathy
(Supervisor)

This page has been intentionally left blank.

भारतीय विज्ञान शिक्षा एवं अनुसंधान संस्थान पुणे
INDIAN INSTITUTE OF SCIENCE EDUCATION AND RESEARCH PUNE
डॉ. होमी भाभा मार्ग, पुणे 411008, महाराष्ट्र, भारत | Dr. Homi Bhabha Road, Pune 411008, Maharashtra, India
T +91 20 2590 8001 W www.iiserpune.ac.in
IISER PUNE

Declaration by student

Name of Student: **Rakesh Kumar Rout**

Reg. No.: **20193683**

Thesis Supervisor(s): **Dr. Gyana Ranjan Tripathy**

Department: **Earth and Climate Science**

Date of joining program: **1st August 2019**

Date of Pre-Synopsis Seminar: **14th November 2024**

Title of Thesis: **Pyrite oxidation in river basins of India: Spatio-temporal study of sulfur and oxygen isotopes of dissolved sulfates**

I declare that this written submission represents my idea in my own words and where others' ideas have been included; I have adequately cited and referenced the original sources. I declare that I have acknowledged collaborative work and discussions wherever such work has been included. I also declare that I have adhered to all principles of academic honesty and integrity and have not misrepresented or fabricated or falsified any idea/data/fact/source in my submission. I understand that violation of the above will be cause for disciplinary action by the Institute and can also evoke penal action from the sources which have thus not been properly cited or from whom proper permission has not been taken when needed.

The work reported in this thesis is the original work done by me under the guidance of Dr./Prof. Gyana Ranjan Tripathy.

Date: 15th January 2025

Rakesh Kumar Rout.

Signature of the student

This page has been intentionally left blank.

Acknowledgments

This thesis is the result of the guidance, motivation, perseverance, and inspiration of many individuals. I want to express my sincere gratitude to all of them, without whom it wouldn't have been possible to complete this work successfully.

Firstly, I would like to thank my thesis supervisor Dr. Gyana Ranjan Tripathy for his endless guidance, encouragement and support throughout my Ph.D. journey. Since my coursework days, he has shaped me in all aspects for my scientific growth. A few of his words like “everything is possible, keep patience”, “keep struggling”, “it has to be perfect”, “the exact number”, “can we quantify?”, will always be with me. He has motivated me to follow the art of perfection in science and to keep all the details of specific scientific numbers. He has introduced me to the domain of isotope geochemistry, mass spectrometry and mathematical modeling. He has guided me in developing scientific communication skills, the art of presentation, and critical thinking. I will always miss the tea-time discussions with him on various aspects of mass spectrometry and several scientific concepts. He has given me an ample amount of time to establish the analytical protocol of sulfur and oxygen isotopes in the IRMS facility of IISER Pune, which is a significant part of my thesis work. During my PhD journey, I have been able to collaborate with both national and international scientific teams through him, which has accelerated my scientific growth. His faith in me during all the ups and downs of my doctoral degree will remain a gift to me. He always kept me motivated and guided me throughout this important chapter of my life, and it probably is difficult for me to present everything in these few words. I sincerely thank you for all the immense efforts you put into me.

I would also like to thank my Research Advisory Committee (RAC) members, Dr. Santosh Kumar Rai and Dr. Anirban Das for their guidance and scientific input. Additionally, I would like to take this opportunity to extend my sincere thanks to Prof. Santosh K. Rai for his help and support during spatial sampling and strontium isotopic analysis.

I want to express my gratitude to Dr. Shreyas Managave, who has thoroughly guided me during the establishment of the analytical protocol of sulfur and oxygen isotopes. His input and suggestions have helped me immensely in shaping my doctoral thesis. The help and support of Satyabrata Das during my field campaigns in the Himalayan terrain is greatly acknowledged. I express my sincere gratitude to him for providing the strontium and carbon isotope data. I cherish all the discussions with him regarding various topics on geochemistry and climatology. I would like to thank Dr. Malik Zubair Ahmad for his help and support for Indus time-series sampling. I would like to thank Prof. Abhayanand Singh Maurya and Nitish Kumar for their help in the oxygen, deuterium and carbon isotopic analyses. The help and support of Dr. Ravi Bhushan, Dr. Ankur J. Dabhi and Dr. Sanjit K. Jena are thankfully acknowledged. Shahbaz Hyder Ganie and Tarique Ahmad are thanked for their help during the sampling of the Indus time-series. Soumya Prakash Dhal and Omar Jan Paul are thanked for their help and support during this thesis work. The help and support of Dr. Vineet Goswami, Dr. Naveen Gandhi and Dr. Rakesh Chandra are thankfully acknowledged. A special thanks to Dr. Alok Kumar Saini

and Dr. Amiya Kumar Samal for sparking my interest in the field of Geochemistry during my Masters program and for encouraging me to pursue research under the supervision of Dr. Tripathy at IISER Pune. I am also deeply thankful to my other Professors, Siben Mitra, L. K. Kar and Suvendu Ray for their guidance, support and encouragement which has always inspired me to achieve many goals in my life. I would like to thank other ECS faculty members (Dr. Argha Banerjee, Dr. Shyam S. Rai, Dr. Sudipta Sarkar, Dr. Devapriya Chttopadhaya and others) for their suggestions and guidance.

The instruments are a crucial part of the Ph.D. journey, as most of the time we rely on them for quality data generation. My journey became smooth at IISER through a number of distinguished engineers. I want to thank Shrikant Gedla, Gaurav Khondale, Priyesh Patil, Ravikant Joshi, Mahesh Jawahire, Sunil Kumar Pathak, Ebin Varghese, Arvinth, Parveen Nasa, Piyush Deokar and other service engineers for their valuable supports and unconditional help.

I think, no Ph.D. is possible without the help of supportive lab seniors, colleagues, and juniors. I will take this opportunity to thank all of them individually. First, I would like to thank my colleague and friend (Achyuth Venugopal) for his kind help, support and suggestions during my doctoral work. His help during the Monte-Carlo simulation is greatly acknowledged. A special thanks to my junior, Kruttika Mohapatra for her care, help, and support. Her input and suggestions during the inverse modeling and Matlab coding, were very beneficial for me. I would like to thank Shuvashree Maity for her care, help and support. I acknowledge the help and support of present and past GRASP Lab members (Yogesh, Amir, Sourojit, Vaishnavi, Priyasha, Ayrton, Samarpan, Sanket, Rani, Anagha, Ashna, Neha, Debashis, Kankan, Akashi and Vaishali).

Seniors are another vital part of my doctoral thesis journey. I started my Ph.D. journey with a geological field trip at Eastern Ghats, Odisha with one of my beloved lab seniors Mohd Danish (Danish Bhaiya). Since that day, he has never left my hand, from making me aware of all the details of Ph.D. journey to building my personal and professional scientific outlook. I will never forget your crucial contribution to teaching me Rhenium column chemistry. His strong boost during my Ph.D. journey has helped me a lot to stay motivated always. I want to thank Anupam Samanta from whom I have learned in-depth instrumentation and many scientific skills. He is the senior with whom I have spent most of my early Ph.D. time. The motivation, guidance and scientific discussion with Anirban Mondal were always constructive. I have learned the Sr-Nd isotope chromatography from Dr. Damodar Kari Rao. Thank you, Bhaiya, for your guidance, help and support. I would like to thank my elder brother, Tapash Kumar Rout for his help in the time-series sampling from the Mahanadi River. Thank you for your care, love, support and affection. The help and suggestions of Mrs. Sharada Das in one of the graphical abstract preparations is thankfully acknowledged. I would like to thank my other IISER seniors, friends and juniors (Amrita, Maheshwori, Rashi, Venu, Avinash, Sagar, Umashish, Milan, Shasank, Sindoora, Rauf, Ashish, Gopi, Chandan, Subhashish, and Susant) for their help, company and support during this journey.

I thank Vikrant Bartakke and Vibhas Shevde for their logistic help and support and Rubi Soni for her administrative help. The help and support of other IISER Pune members, Ranjan

Kishore Sahu, Prabhas Patnakar, Swapnil Bhuktar are thankfully acknowledged. I thank the electric, IT and other Departments of IISER Pune for their constant support and help.

I would like to thank IISER Pune for the financial support and research fellowship. The travel grant from DST SERB, Infosys and EGU are thankfully acknowledged.

I thank, all the other non-teaching staffs of IISER Pune for their help in keeping the lab environment clean.

I would like to thank the India-Water Resource Information System (WRIS), India Meteorological Department (IMD) and NASA Prediction of Worldwide Energy Resources (POWER) for providing the climatological datasets. The Bhukosh GSI (https://bhukosh.gsi.gov.in) is thanked for providing the lithological map. I would like to thank GRDC (http://www.grdc.sr.unh.edu) for providing the discharge data and the USGS Earth Explorer portal (https://earthexplorer.usgs.gov) for providing the digital elevation model data.

Last but not least, I would like to thank my parents and other family members for their blessings, motivation, guidance and invaluable support. Lastly, I would like to thank all who have helped me during my Ph.D. journey.

This page has been intentionally left blank.

Abstract

Oxidation of pyrites, despite being a trace lithology, plays dominant role in key continental (acid-alkalinity balance), oceanic (Fe, S and trace elemental supply) and atmospheric (oxygen and CO_2 cycling) processes. This thesis work has aimed to investigate the spatial and temporal variations in the sulfide oxidation pattern of Indian river basins by using water chemistry and dissolved sulfur ($\delta^{34}S$) and oxygen ($\delta^{18}O$) isotopes of sulfate fractions. The analysed samples for this work include (i) weekly collection of water from the upper Indus (at Leh) and Mahanadi (at Kusunpura) rivers for one-year duration, and (ii) spatial collection of water from Indus headwater basin. Forward and inverse modeling of these datasets were used to apportion the cationic and sulfate sources, which helped to assess their effect on carbon cycle.

Time-series chemical and isotopic data for the Mahanadi river from the Peninsular India (from core-monsoon zone) were employed to constrain the seaonality in weathering processes in a transport-limited basin. Concentrations for most of the elements and also, $\delta^{34}S_{SO4}$ values show significant seasonal changes, with relatively higher values being observed for the lean-flow stages. The $\delta^{34}S_{SO4}$ varies between 8.8 ‰ and 17 ‰, with a discharge-weighted average of 12 ± 4 ‰ (global riverine value ~ 4.4 ± 4.5 ‰). Calculations involving $\delta^{34}S_{SO4}$ values and its possible sources compute the relative supply of sulfates from atmospheric deposition (38 %), gypsum (46 %), and sulfides (16 % (a lower limit)) to the river. The minimal contribution via sulfide oxidation confirms low CO_2 release (0.1 ± 0.1 tC/km^2/yr) in this basin through sulfuric-acid mediated carbonate weathering. Mass balance calculations involving Ca, Mg and Si values confirm that these seasonal changes are mainly due to increase (by 18 ± 9 %) of groundwater supply to the stream during non-monsoon seasons. The silicate-derived cations (Cat_s) for the Mahanadi show minimal changes during monsoon (36 ± 5 %) and non-monsoon (33 ± 8 %) seasons. These data correspond to a CO_2 consumption rate of 2.4 ± 1.6 tC/km^2/yr, which is about two times higher than that reported for global rivers. Low sulfide oxidation in this supply-limited regime is possibly linked to limited exposure of fresher minerals, whereas high silicate erosion in the basin is consistent with its silicate-dominated lithology and tropical climate.

Further, efforts were also made to establish seasonal changes in pyrite oxidation and related controlling factors using time-series (weekly to biweekly) data of water chemistry and $\delta^{34}S_{SO4}$ - $\delta^{18}O_{SO4}$ values for the Indus headwater at Leh, India. Data on $\delta^{34}S_{SO4}$ (-2.6 to 2.9 ‰) and $\delta^{18}O_{SO4}$ (-5.9 to 2.6 ‰) exhibit significant variations, with relatively depleted values for

the lean-flow samples. Apportionment of the cationic and sulfate sources using an inverse model also confirms seasonal changes. Fluctuations in Ca/Na* ratio and Cat_s indicate relatively higher silicate weathering during the early phase of summer than other seasons. This trend is different than earlier-reported enhanced carbonate weathering during the whole summer season for other Himalayan basins, and is linked to strong control of temperature on rock dissolution in early summer for the Indus basin. Further, the fraction of sulfide-derived sulfates is systematically higher during lean-flow than high-flow stages, attributable to diffusion of atmospheric oxygen to deeper weathering fronts with pyrite availability. This diffusion is promoted via microfractures, possibly produced by tectonic stresses along the shear zone of the basin, and limited by interflow of groundwater in this highly-elevated catchment. Outcomes of this study predict increase in subsurface pyrite oxidation and hence, river acidity in response to any future change (fall) in groundwater table.

We also present new dataset on dissolved major ions, and $\delta^{34}S_{SO4}$ and $\delta^{18}O_{SO4}$ for the Indus headwater basin. This dataset and its modeling were used to evaluate the net effect of Himalaya weatheirng on the global Cenozoic cooling event. The $\delta^{34}S_{SO4}$ of these samples vary between - 11 ‰ and 5 ‰, with depleted $\delta^{34}S_{SO4}$ values being observed for the mainstream samples (- 4 ± 2 ‰; n = 12) than that reported earlier for the Indus outflow (0.8 ‰). The $\delta^{18}O$ of water samples (- 10 ± 3 ‰) and their sulfate fractions (- 1 ± 5 ‰) exhibit strong linear correlation, with their regression slope being a function of f_{py} (fraction of sulfide-derived sulfate). Inversion and Monte-Carlo simulation of the chemical and isotopic datasets were used to estimate the fraction of silicate-derived cations (0.2 ± 0.1 %; n = 61), and f_{py} (0.6 ± 0.2; n = 50) values. The low silicate weathering rate ((2.0 ± 0.1) $\times 10^5$ mol/km^2/yr) for this high-elevated and low relief terrain (at Batalik) is attributable to strong temperature control, whereas the high sulfide oxidation ((3.7 ± 0.4) $\times 10^5$ mol/km^2/yr) for this basin is consistent with the basin lithology dominated by Palaeozoic carbonates and organic-rich shales, and high glacial coverage. These rates confirm net release of CO_2 from the upper Indus basin, whereas modeling of literature data point to net CO_2 consumption at the Indus outflow. The net supply of CO_2 from the mountainous regions is in clear contrast to previous suggestion of significant CO_2 removal during Himalaya weathering and hence, challenges the role of land surface processes in the NW Himalaya in regulating the Cenozoic cooling event.

Table of contents

List of Tables

List of Figures

This page has been intentionally left blank.

Chapter 1
Introduction

This page has been intentionally left blank.

1. Introduction

The habitability of our planet is mainly regulated by the atmospheric CO_2 level, which maintains an optimal surface temperature for the occurrence of water in liquid form. Long-term atmospheric CO_2 level is regulated by both its natural sources (volcanic input, oxidative weathering of organic matter (OM) and sulfide minerals, and metamorphic decarbonation) and sinks (silicate weathering and organic carbon burial) (Berner et al., 1983; Sarin et al., 1989; Derry and France-Lanord, 1997; France-Lanord and Derry, 1997; Lerman et al., 2007; Gaillardet and Galy, 2008; Torres et al., 2014; Horan et al., 2019; Hilton and West, 2020; Fig. 1.1.). Any fluctuations in the source/sink contribution have led to severe climatic and chemical perturbations, and also mass extinction events in the past (Penman et al., 2020).

1.1. Long-term carbon cycle

Among the major CO_2 sources and sinks (Fig. 1.1.), the negative feedback of silicate weathering on climate has received considerable attention (Walker et al., 1981; Gaillardet et al., 1999). The CO_2 consumption during carbonic acid-mediated weathering of silicate minerals and subsequent removal of alkalinity and cations as oceanic carbonates have been well studied (Box 1; Gaillardet et al., 1999; Galy and France-Lanord, 1999; Krishnaswami et al., 1999; Dalai et al., 2002a; Bickle et al., 2005, 2018; Tipper et al., 2006; Tripathy and Singh, 2010; Jacobson et al., 2015; Samanta et al., 2019). These studies in tropical regions have mainly been motivated by the suggested uplift-weathering trigger for the global Cenozoic cooling event (Raymo et al., 1988). A large number of studies have computed the CO_2 uptake rate via silicate weathering using source apportionment modeling of river chemistry datasets; these estimates reveal that the silicate weathering rate (SWR ~ 47 - 72 MtC/yr; Gaillardet et al., 1999) at a global scale is lower than the organic carbon burial rate (~ 170 MtC/yr; Hilton and West, 2020). The SWR for different river basins exhibits large spatial variability with disproportionally higher rates being observed for mountainous and tropical regions (Larsen et al., 2014), specifically in the South Asian River basins (Hilley and Porder, 2008). These basins are mostly weathering-limited regimes where the weathering processes are incomplete and the weathered products are removed faster than their generation in the catchment (Stallard and Edmond, 1983). High SWR in these regimes, therefore, is linked to continuous exposure of fresh minerals with faster dissolution kinetics, and also, coupled with conducive climate (high runoff, and temperature; West et al., 2005). In contrast, the weathering processes are nearly complete in transport-limited basins, due to the slower removal process which allows the accumulation

of thick soil cover. Although supply-limited basins are largely characterized by low SWR, the weathering rates in these basins may also be influenced by other factors (glacial cover, and soil thickness; West et al., 2005).

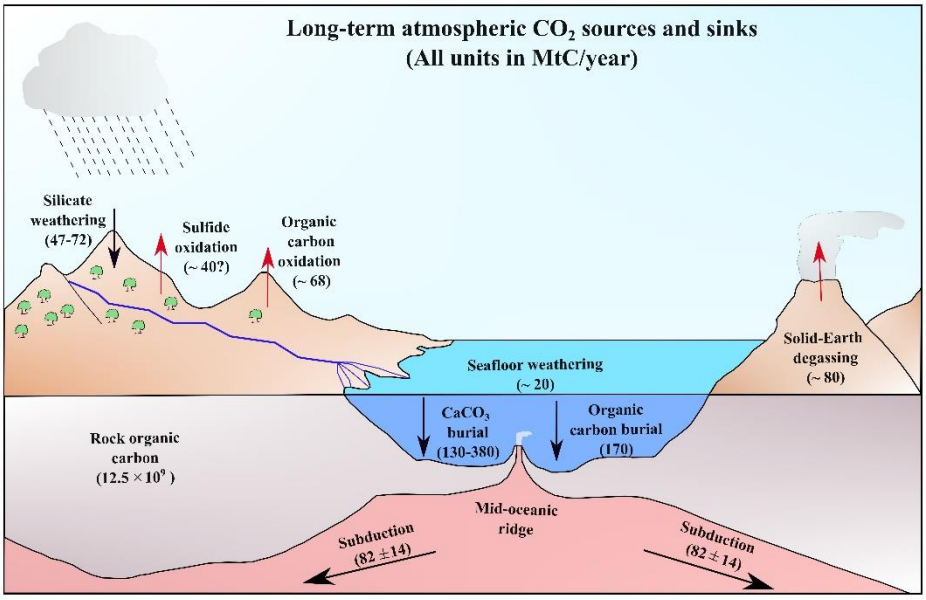

Figure 1.1. *Long-term atmospheric CO_2 sources and sinks. Data for carbon fluxes are from Hilton and West, 2020 and Zondervan et al., 2023.*

The burial of biogenic components of the organic matter also consumes the atmospheric CO_2. However, the burial of petrogenic (rock-derived) OM is only relevant for the spatial transfer of these materials and does not contribute to the long-term CO_2 cycle (France-Lanord and Derry, 1997; Galy et al., 2015). The CO_2 uptake via organic carbon burial is also found high in the weathering-limited, and climatically-favorable (for high landslides and floods) basins by increasing burial efficiency through mineral-organic matter association, low transit time, and high sedimentation rate (West et al., 2005; Hilton and West, 2020). These rates are more controlled by sediment transport through physical erosion and less sensitive to terrestrial productivity (Galy et al., 2015).

These CO_2 sinks are often counter-balanced by its release during oxidation of organic matter (Dalai et al., 2002b; Horan et al., 2017, 2019) and sulfides (e.g. pyrites (FeS_2); Spence and Telmer, 2005; Calmels et al., 2007; Lerman et al., 2007; Das et al., 2012; Torres et al., 2014; Kemeny et al., 2021a; Hemingway et al., 2020) present in bedrocks, in addition to volcanic supplies. The oxidation of petrogenic organic matter supplies substantial amount of CO_2 to the atmosphere (~ 68^{+18}_{-6} MtC/yr; Zondervan et al., 2023). These rate estimations for river basins are largely computed using concentrations of rhenium (Re), which is a reliable proxy for the weathering of petrogenic-OM (Dalai et al., 2002b; Jaffe et al., 2002). The

BOX 1: Chemical reactions involved with major weathering pathways

The natural acids that serve as major proton donors for chemical weathering of continental rocks are carbonic, sulfuric, and organic acids. Here, we restrict our discussion on influence of only carbonic and sulfuric acids-mediated weathering on carbon cycle (Spence and Telmer, 2005 ; Kemeny et al., 2021a).

(i) Carbonic acid-mediated weathering:

The carbonic acid is formed *via* dissolution of CO_2 in soil (where partial pressure is higher (by one to two orders of magnitude) than the atmosphere due to organic decay) with water.

$$CO_2 + H_2O \rightarrow H_2CO_3 \quad (1.1)$$

As organic matter fixes atmospheric CO_2, the soil CO_2 may reflect atmospheric CO_2 level for long-term carbon cycle.

H_2CO_3-mediated carbonate weathering:

On Land: $$H_2CO_3 + CaCO_3 \rightarrow 2HCO_3^- + Ca^{+2} \quad (1.2)$$

In Oceans: $$2HCO_3^- + Ca^{+2} \rightarrow CaCO_3 + CO_2 + H_2O \quad (1.3)$$

Above two reactions reflect relocation of $CaCO_3$ from land to ocean and hence, do not influence the atmospheric CO_2 for timescales greater than residence time of HCO_3^- (0.083 Ma) in seawater.

H_2CO_3-mediated silicate weathering:

On Land: $$H_2CO_3 + CaSiO_3 + H_2O \rightarrow 2HCO_3^- + Ca^{+2} + H_4SiO_4 \quad (1.4)$$

In Oceans: $$2HCO_3^- + Ca^{+2} \rightarrow CaCO_3 + CO_2 + H_2O \quad (1.5)$$

Net: $$CaSiO_3 + H_2O + CO_2 \rightarrow CaCO_3 + H_4SiO_4 \quad (1.6)$$

Above reaction confirms that CO_2-mediated silicate weathering serves as a sink for atmospheric CO_2 for timescale between residence time of seawater HCO_3^- (0.083 Ma) and sedimentary $CaCO_3$ (356 Ma).

(ii) Sulfuric acid-mediated weathering:

Oxidation of sulfide minerals involving reduction of O_2 or, Fe^{+3} can produce sulfuric acid, which may promote weathering of silicate and carbonate minerals.

$$4FeS_2 + 15O_2 + 8H_2O \rightarrow 16H^+ + 8SO_4^{2-} + 2Fe_2O_3 \quad (1.7)$$

$$FeS_2 + 15Fe^{+3} + 9.5H_2O \rightarrow 19H^+ + 2SO_4^{2-} + 0.5Fe_2O_3 + 15Fe^{+2} \quad (1.8)$$

H_2SO_4-mediated carbonate weathering:

$$8H_2SO_4 + 16CaCO_3 \rightarrow 16HCO_3^- + 8SO_4^{2-} + 16Ca^{+2} \quad (1.9)$$

Above reaction confirms consumption of alkalinity and oxygen during H_2SO_4-mediated carbonate weathering. Effect of this weathering pathway on CO_2 cycle is effective in a timescale of residence of SO_4^{2-} in seawater (~8.7 Ma).

H_2SO_4-mediated silicate weathering:

$$8H_2SO_4 + 8CaSiO_3 + 8H_2O \rightarrow 8H_4SiO_4 + 8SO_4^{2-} + 8Ca^{+2} \quad (1.10)$$

The H_2SO_4-mediated silicate weathering, therefore, has no effect on the atmospheric pCO_2.

In addition to these reactions, oxidation of petrogenic organic carbon and burial of organic matter also serve as source and sink for long-term pCO_2 level, respectively.

intensity of the organic oxidation in a basin is controlled by several factors, which include total OM in bedrocks, abundance of resistant organic phases, availability of oxygen, type of glacial and periglacial processes, physical erosion and orographic precipitation (Horan et al., 2019). Typically, these rates are found to be higher in weathering-limited regimes (Horan et al., 2017). The proportion of exhumed OC that go through weathering varies significantly for mountain watersheds (10 - 40 %), mountain soils (~ 70 %) and floodplains (> 90 %; Hilton and West, 2020) in tropical river basins (Hilton and West, 2020).

This thesis work largely focuses on the rate and controlling factors for sulfide oxidation in river basins, which is another source of atmospheric CO_2. Oxidative weathering of sulfide minerals and related sulfate supply play a dominant role in several oceanic (e.g. iron, sulfur, and other redox-sensitive elements) and atmospheric (CO_2, O_2) cycles. This chemical reaction, either by aerobic oxidation of FeS_2 or, reduction of Fe^{+3}, can produce stronger acid (H_2SO_4), which when reacts with carbonates consume alkalinity, and hence, influence the riverine acid-alkalinity budget and global climate as a transient long-term source of CO_2 (~ 10 Ma; Spence and Telmer., 2005; Relph et al., 2021).

Available studies reveal that the oxidation of pyrite is a complex process with several intermediate pathways (Druschel and Borda, 2006; Ódri et al., 2020), which makes it difficult to quantify the rate of these processes for river basins. The $\delta^{34}S$ value of sulfates, owing to its distinct isotopic signatures for the major sources (viz. gypsum (~ 17 ‰), pyrites (~ -12 ‰)), serves as a robust proxy for apportioning sulfide-derived sulfates and related CO_2 release rates for river basins (Burke et al., 2018). The $\delta^{34}S_{SO4}$ values of rivers vary significantly between -6.3 (Kaoping) and 19.3 ‰ (Lena), indicating large spatial variation in pyrite oxidation in river basins (Burke et al., 2018). Mass balance modeling involving $\delta^{34}S_{SO4}$ of the global river and major sulfate sources has estimated that about half of the riverine sulfate fluxes to the global ocean are derived from sulfide oxidation. Earlier studies also show that the amount of CO_2 released through this pathway is ~ 40 MtC/yr. (Burke et al., 2018) which is comparable in magnitude to the CO_2 consumption via silicate weathering (~ 70 MtC/yr) and CO_2 release (~ 68 MtC/yr) during organic oxidation (Zondervan et al., 2023; Hilton and West, 2020).

Calmels et al., (2007) have considered available estimates for sulfide oxidation rates as a lower limit, mainly due to limited data, heterogeneity in rates in different basins, and the complexity to apportion the sulfide-derived sulfate in rivers. It also shows large variation at an inter-basinal scale; for instance, only three rivers (covering only 2 % of the global drainage area) have been observed to account for about one-third of its global flux (Das et al., 2012). These spatial variations are often linked to areal exposure of sulfides, seasonal changes in the shallow-to-deeper flow path, and/or intensity of physical erosion in the basin, which facilitates continuous exposure of fresher pyrite minerals for efficient weathering (Tipper et al., 2006; Calmels et al., 2007; Torres et al., 2014; Kemeny et al., 2021a). At a basin-wide scale, the oxidation rates are found higher in mountainous (weathering-limited) than in the floodplain (transport-limited) regions, attributable to the constant supply of fresher pyrite minerals via physical erosion (Hilton and West, 2020). These observations, however, are limited by (i)

snapshot sampling, and (ii) large variability of $\delta^{34}S$ of pyrites. The wider ranges for pyrites are largely linked to variable isotopic fractionation, depending on the inventory of sulfate and reactive iron, basin restriction, and biological uptake rates during the pyrite formation process (Venugopal et al., 2023). A part of this isotopic limitation has been resolved in recent studies by using both $\delta^{34}S$ and $\delta^{18}O$ of sulfates.

The seasonality in $\delta^{34}S_{SO4}$ and $\delta^{18}O_{SO4}$ values for rivers may reflect the sensitivity of pyrite oxidation with flow stages. Available limited studies show that the $\delta^{34}S_{SO4}$ of rivers exhibit both large (5 - 7 ‰) and minimal (< 2 ‰) variations over a hydrological cycle (Killingsworth et al., 2018; Burke et al., 2018; Rout and Tripathy, 2024). These differences in isotopic spreads are independent of the catchment area, and possibly linked to erosion rate, channel incision, flow paths of tributaries (Shaughnessy et al., 2023), and anthropogenic supplies (Otero et al., 2008; Killingsworth et al., 2018). Despite these inter-basinal differences, these time-series studies show systematically lower $\delta^{34}S_{SO4}$ values during baseflow (than high flow) stages, indicating higher intensity of pyrite oxidation (Winnick et al., 2017; Gu et al., 2020a; Kemeny et al., 2021a). This higher rate during low flow periods has been linked to the supply of oxidants (O_2, Fe (III) and NO_3) to deeper pyrite front in the weathering profile, which is controlled by subsurface diffusion of gases, fracture density, and erosion rates (Gu et al., 2020b). In particular, intense carbonate dissolution during high flow stages may produce more fractures, which may promote more oxidation during baseflow seasons (Liao et al., 2022). Recently, Kemeny et al., (2021a) have also linked the deeper flow paths of reactive fluids in supplying a higher amount of sulfide-derived sulfates to the Ganga River during baseflow than during high flow stages. A similar role of fluid paths has earlier been proposed to explain a relatively higher solute supply from carbonates (than silicates) during monsoon season (Krishnaswami et al., 1999; Tipper et al., 2006). This increase in carbonate dissolution has been linked to fast dissolution kinetics, water-rock interaction and shallower groundwater input (Bickle et al., 2005; Samanta et al., 2019). These observations indicate that a combined study of silicate and carbonate weathering, and pyrite oxidation rates over a hydrological cycle can constrain the impact of subsurface weathering processes on the carbon cycle.

1.2. Research gap and objectives

Chemical weathering of exhumed rocks during mountain building processes is one of the major components of the global carbon cycle (Chamberlin, 1899; Edmond and Huh, 1997; Hilton and West, 2020). These steep and highly eroding terrains produce about 3 - 4 times

higher amounts of solutes (~ 40 %) and silicate-driven cations (~ 60 %) compared to their areal extent (~ 15 % of Earth's land surface; Larsen et al., 2014) and hence, impart large negative feedback on global climate (Walker et al., 1981). Consistent with this tectonic-weathering-climate linkage, Raymo et al., (1988) have proposed intense silicate weathering over young orogenic belts, such as the Himalayan-Tibetan plateau (HTP) regions, as one of the prime controllers of the global Cenozoic cooling event. Whilst this proposition draws support from the steady rise in the oceanic Sr, Os and Li isotopic trends (Krishnaswami et al., 1992; Ravizza and Zachos, 2003; Mishra and Froelich, 2012), it has also been argued against by (i) weathering of metamorphosed carbonate and vein calcites (Bickle et al., 2001; Jacobson et al., 2000), (ii) high burial efficiency of terrestrial organic carbon from basins with high erosion rates (France-Lanord and Derry, 1997; Galy et al., 2015), (iii) lithological exposure and preferential reactivity of minerals (Li et al., 2008; Li and Elderfield, 2013), and (iv) clay authigenesis (Mackenzie and Kump, 1995; Mishra and Froelich, 2012; Tipper et al., 2021). In addition, emerging studies have also emphasized the importance of release of CO_2 during the oxidation of petrogenic carbon (Dalai et al., 2002b; Hilton et al., 2021) and sulfide minerals (Lerman et al., 2007; Spence and Telmer, 2005; Kemeny et al., 2021a and b) in counterbalancing the CO_2 consumed by silicate weathering in basins (Rout and Tripathy, 2024). These oxidative weathering rates exhibit a linear relationship with erosion rates (Calmels et al., 2007; Das et al., 2012) attributable to continuous exposure of fresh materials with fast dissolution kinetics and/or glacial oxidation of disseminated pyrites (Torres et al., 2014). Consistently, Torres et al., (2014), based on discrepancies between $^{87}Sr/^{86}Sr$ and $^{187}Os/^{188}Os$ trends, have also invoked the importance of sulfide oxidation in regulating the Cenozoic pCO_2 level, although the rate and pattern of sulfide oxidation in the HTP River basins remain understudied (Das et al., 2021; Kemeny et al., 2021a; Relph et al., 2021; Xu et al., 2024). Further, there exist very limited studies on sulfide oxidation rates for the Peninsular Indian Rivers, despite their disproportionally higher importance in global climatic and chemical cycles (Das et al., 2011; Samanta et al., 2021; Rout and Tripathy, 2024). These river basins mainly flow through silicate-dominated (mostly, Archean granites; cf. Chapter 2) terrains, and also, strongly influenced by south-west rainfall. These geohydrological factors are expected to be conducive for intense silicate weathering in these tropical basins and hence, can play dominant role in global carbon cycle.

The main objectives of this thesis work are:

I. To constrain the intensity of sulfide oxidation and other weathering processes in the Peninsular Indian River basins using temporal water chemistry and $\delta^{34}S$ data for sulfates.

II. To investigate the sensitivity of pyrite oxidation with respect to seasonal changes in flow stages of the Indus headwater using time-series investigation of water chemistry and $\delta^{34}S$-$\delta^{18}O$ for sulfates.

III. To quantify the intensity of sulfide oxidation in the northwestern Himalayan region (Indus headwater) and associated CO_2 release rate using sulfur and oxygen isotopes of sulfate fractions.

1.3. Thesis structure

This thesis consists of six chapters; the broad outlines of these chapters are highlighted below.

Chapter 1: This chapter introduces the research topic and reviews the previous literatures. Details on the existing research gap and objectives of this study are also part of this chapter.

Chapter 2: This chapter provides details on sample collection and geohydrology of the study area. Further, a detailed description of the analytical methodology adopted during this work is also included.

Chapter 3: This chapter highlights the intensity of sulfide oxidation and other weathering processes and their net effect on the carbon cycle in one of the Peninsular Indian River basins (Mahanadi River, India).

Chapter 4: This chapter emphasizes the sensitivity of pyrite oxidation with flow stage variation of the Indus mainstream at Leh, India. Here, time-series data (at weekly intervals for one-year duration) on water chemistry and $\delta^{34}S_{SO4}$-$\delta^{18}O_{SO4}$ were used to establish the seasonal variation in pyrite oxidation intensity and its regulating factors.

Chapter 5: This chapter focuses on the spatial distribution of pyrite oxidation in the Indus headwater basin. The pyrite oxidation and other weathering rates for this basin from the northwestern Himalayan region were estimated using dissolved major ions, silica concentrations and sulfur-oxygen isotopic ratios of sulfate fraction. These outcomes were used to evaluate whether these terrains serve as a net CO_2 source or sink.

Chapter 6: This chapter summarizes the conclusions from this study and also, highlights the future scope of research on this topic.

This page has been intentionally left blank.

Chapter 2

Materials and methods

This page has been intentionally left blank.

The primary goals of this thesis, as mentioned earlier, are i) to quantify the pyrite oxidation and related CO_2 release rates for the Indus headwater basin, ii) to establish the effect of water stage fluctuation on pyrite oxidation in the upper Indus, and iii) to constrain the intensity of sulfide oxidation and other weathering processes in a Peninsular Indian (Mahanadi) river basin. To fill these research gaps, detailed time-series sampling of water samples from two river basins (Indus and Mahanadi), and high-resolution spatial sampling in the upper Indus basin were strategically planned. These samples were carefully analysed for their chemical and isotopic ($\delta^{34}S_{SO4}$-$\delta^{18}O_{SO4}$) compositions. This chapter provides all details related to the geohydrology of these river basins, sample collection, and analytical methodologies followed during this work.

2.1. The Indus River

The Indus River originates from the Kailash Mount (elevation ~ 5,486 m) in Tibet on northern side of the Himalayas (Ahmad et al., 1998; Karim and Veizer, 2000). It initially flows westward parallel to the geological strike of Indus Shyok Suture Zone for ~ 1,125 km, and subsequently turns south near the Nanga Parbat and travels about 1,750 km before draining into the Arabian Sea (Fig. 2.1.). The northern sector of this basin is bordered by the Karakorum and the Harmosh ranges, whereas the eastern part is covered by the Himalaya. The western part of it is surrounded by the Sulaiman and the Kirthar ranges, while the southern part is bounded by the Arabian Sea. It has a total drainage area of 912,000 km^2, out of which ~ 24 % (219,830 km^2) forms the high-elevated (average elevation ~ 4600 km) upper Indus basin (UIB; Ali and De Boer, 2010). The UIB is generally considered the part of the basin that is upstream to the Guddu Barrage (Fig. 2.1.). The present study focuses on the UIB lying in India only. In this region, the river covers one-third (~ 422 km; Tiwari et al., 2021) length of the upper Indus.

2.1.1. Major tributaries of the upper Indus River

The UIB meets with several tributaries (Shyok, Shigar, Hunza, Gilgit, Kabul, Swat, Kurram, Zanskar, and Astore) along its course (Fig. 2.1.). Additionally, the Jhelum, Chenab, Ravi and Sutlej sub-basins also contribute to the upper basin, although they ultimately join the mainstream in its lower reach (Fig. 2.1.). Table 2.1. lists drainage and annual water discharge for selected tributaries for the UIB.

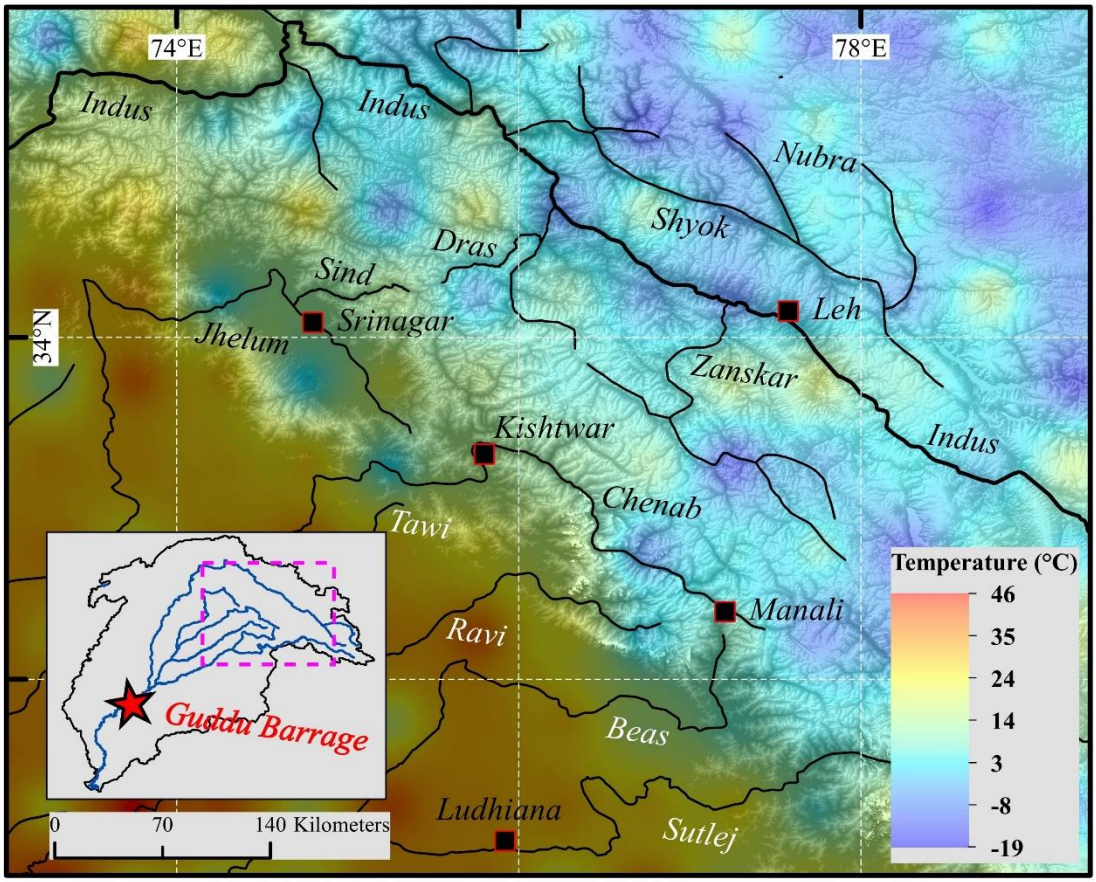

Figure 2.1. *Drainage map of a part of the upper Indus basin, where this study is conducted. The background colour contour reflects the average annual temperature during 2021-22 (https://power.larc.nasa.gov/data-access-viewer). The red star marked in the inset figure shows the location of the Guddu Barrage. The dotted box depicts the study area.*

Table 2.1. *Drainage area and annual water discharge for the upper Indus and its selected tributaries.*

River	Discharge ($\times 10^{12}$ L/yr)	Area (km^2)	*Reference*
Indus R.	43	44358	*[1]*
Zanskar R.	9	13962	*[1]*
Shyok R.	18	40981	*[1]*
Nubra R.	10	3170	*[1]*
Suru R.	12	3186	*[1]*
Dras R.	8	3978	*[1]*
Jhelum R.	7	12494	*[2]*
Chenab R.	25	22681	*[2]*
Ravi R.	8	5703	*[2]*
Beas R.	16	18274	*[2]*
Sutlej R.	16	20303	*[3]*

[1] Bhat et al., 2023; [2] GRDC portal; [3] Central Pollution Control Board, 2019.

2.1.1.1. The Zanskar River

The Zanskar tributary originates from the Zanskar range of the Himalayas (Fig. 2.1.). It flows for about 150 km, before meeting with the mainstream Indus at Nimoo, Ladakh (Fig. 2.1.). It covers an area of 14,939 km^2 and is fed by five major streams (Stod, Tsarap, Oma, Markha and Khurna River). About 8 % of the Zanskar drainage area is covered by glaciers (Taylor and Mitchell, 2000; Owen, 2011). There are also report of terminal and recessional moraines in the river valley. The precipitation in this basin is controlled by both the Indian summer monsoon during summer and westerlies during the winter season (Benn and Owen, 1998). The basin lithology includes the Higher Himalaya, Indus suture zone, and sedimentary sequences of the Tethyan Himalaya. The major rock types from this terrain are sandstones, carbonates, dolostones, shales, leucogranites and ophiolitic mélange (Jonell et al., 2017).

2.1.1.2. The Dras River

The Dras River originates from the Machoi glacier near Zojila pass in the Kargil district of Ladakh, and drains a total length of about 85 km in the Dras valley (Fig. 2.1.). The river mainly drains through the Higher Himalayan crystalline, Indus suture zone and the Ladakh batholith.During its course of flow towards the northeast direction, it is fed by numerous glacial streams. The major tributaries for this river are Shingo, and Suru. The Suru stream has a total length of 185 km and covers an area of ~ 3187 km^2. It originates from the Drang Dung glacier in the Zanskar region and mainly flows through the Great Himalayan Mountain (Wani et al., 2020).

2.1.1.3. The Shyok and Nubra River

The Shyok River is one of the major tributaries of the Indus River, which emerges from the Rimo group of glaciers (Fig. 2.1.). It flows along a longitudinal valley for about 500 km parallel to the Indus in the northwest direction before meeting Indus at the Keris village, Ladakh. Snow and glaciers predominantly fed this river (Juyal, 2014). One of the major tributaries for this stream is the Nubra River, which originates from the Siachin glacier (Fig. 2.1.). The climatology of this “cold desert” catchment is semi-arid to arid with limited precipitation (Juyal, 2014). The catchment is situated between the central Karakorum and Ladakh range which is intersected by the Karakorum fault (Dunlap et al., 1998; Chevalier et al., 2005). Sand dunes and bars are also found in this catchment.

2.1.1.4. The Jhelum River

The river Jhelum is a major tributary of the Indus River, and is a perennial river. The source of Jhelum is a deep spring situated in the south-eastern part of the Kashmir valley at Verinag, Anantnag (Fig. 2.1.). The river takes a U-turn, meets the Wular lake and after passing through a deep gorge at Uri, Baramulla, it subsequently enters to the lower part of the basin. This catchment is mainly covered by mountains, forests, alpine meadows and low-lying alluvial plains. A permanent thick snow covers from the mountainous (with greater than ~ 3500 m asl) region supply water to this river. The climatology of this basin is mainly sub-humid temperate type. This catchment receives major rainfall during March-May, and heavy snowfall during November - February (Rather et al., 2016). The basin lithology is comprised of Panjal Traps, Silurian shale, Syringothris limestone, quartzite, Fenestella shale, Muth quartzite, and Agglomeratic slate (Middlemiss, 1910). Several snow and glacier fed tributaries also join this river on both the right and left flanks of the stream. Among these, the Sind is a major tributary which originates from Machoi glacier near Zojila Pass. It mainly drains through Higher Himalayan Crystalline and Quaternary alluvium, and joins the Jhelum near the Srinagar city.

2.1.1.5. The Chenab River

The Chenab River is another tributary of the Indus River that originates from the confluence of two rivers, the Chandra and the Bhaga at Tandi, Himachal Pradesh (Fig. 2.1.). Large snowfields situated near the southeastern sides of Baralacha Pass are the major water source for the Chandra River, while the northwestern side is the dominant source for the Bhaga River. After their confluence, Chenab flows ~ 300 km in Himachal Pradesh and Jammu and Kashmir, India. It forms an elongated shaped basin that covers 22,200 km^2 area (till Akhnoor) with a varying elevation gradient of 305 m to 7,500 m. The Zanskar and the Pirpanjal range form the upper part of the basin, whereas the lower part is bounded by Dhauladhar and other outer Himalayan ranges (Singh et al., 1997).

The river Tawi is a major tributary of the Chenab River which emerges from the Kailash Kund glacier (Fig. 2.1.). It flows ~ 140 km with an aerial extent of 2168 km^2 (Singh et al., 2023). The elongated shaped upper part of the basin is covered by rugged mountainous terrain, whereas the broad circular lower part is covered by low hills and aggradational plains. The upper part of the catchment is made up of metamorphic terrain and granite intrusions, and the lower part is covered by sedimentary rocks. The physiographic regions of the basin is divided

into three parts based on the thrust planes present in the catchment. These are i) the part of the basin present in the north of the Panjal thrust ii) the middle part laying between the Panjal thrust and Udhampur thrust and iii) the lower part present between the Udhampur and Jammu region. The major water source for the basin are snow and the westerlies, whereas the summer monsoon contributes moisture for the lower reaches. The basin records varying annual rainfall, ranging from ~ 90 to ~ 190 cm (Verma et al., 2012).

2.1.1.6. The Ravi River

The Ravi River is a tributary of the main Indus which originates near the Rohtang Pass, Himachal Pradesh (Fig. 2.1.). It has a total length of ~ 720 km with a catchment area of ~ 14,442 km^2. The basin is surrounded by the Pirpanjal and Dhauladhar ranges. The Ujh and Baira Nalla streams serve as major tributaries for the Ravi River (Jain et al., 2007).

2.1.1.7. The Sutlej River

The Sutlej River, another tributary of the Indus River, rises from the southern slopes of the Mount Kailash (Fig. 2.1.). It is one of the major tributaries of the Indus River having a total length of 1550 km and area of 205,000 km^2. The river flows through the Tethyan sedimentary series then traverses over the Higher Himalayan Crystalline, Lesser Himalaya, Siwaliks sedimentary facies and the Quaternary plain, before joining the Indus mainstream. The source region of the basin is covered by permanent snow and ice. One of the major tributaries for this river is the Beas River, which starts from a glacial lake in Beas Kund near the Rohtang pass. It has a length of 470 km and an area of 20,303 km^2. It also drains through the similar litho-units as that of the Sutlej River.

2.1.2. Climate

The Indus basin mainly drains through arid to semi-arid regions as it falls in the rain-shadow zone of the Indian summer monsoon (Fig. 2.1.). It is covered by ~ 13 % of perennial snow and glaciers, whereas about three-fourth of the area gets covered by snow in winter seasons. The precipitation and temperature show significant variations throughout the catchments of the Indus (Fig. 2.2.). A substantial spatial precipitation variability is observed with more rainfall in the upper part of the basin than in the lower part (Fig. 2.1.). This variability is largely linked to the occurrence of the mountain ranges within the upper part of the basin. Average annual rainfall for the UIB is about 115 mm (Lone et al., 2019). About two-third of

this precipitation occurs as snow during the winter due to moisture supply via westerlies, whereas the remaining rainfall occurs during the summer via southwest monsoon. The UIB water flux is mainly contributed by glacier and snow (~ 61 %) melts, and rainfall (~ 38 %). About 14 % of evapotranspiration and negligible (~ 4 %) groundwater contribution has also been reported for the UIB (Gupta et al., 2021). Annually about 132 rainy days are observed in the upper Indus, whereas for the lower Indus it is about 84 days. The Indian summer monsoon is the dominant source of precipitation for the whole basin and provides about 55 % of total annual basin precipitation. In contrast, winter precipitation contributes ~ 17 % of the annual precipitation in the entire basin, and up to 30 % in the upper basin (Shrestha et al., 2015).

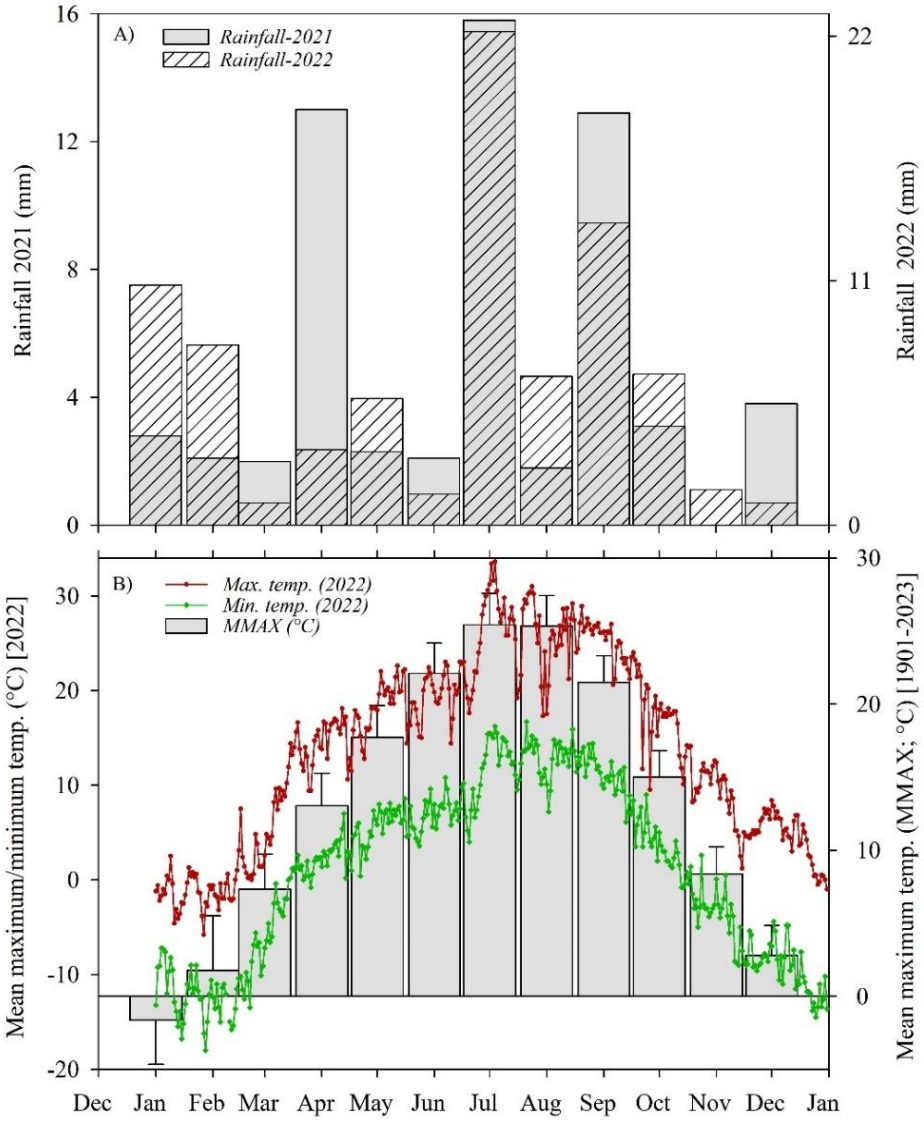

***Figure 2.2**. Monthly average A) rainfall and B) mean maximum air temperature from 1901 to 2023 at Leh, India. Additionally, the maximum and minimum temperature for the sampling period is also shown. Data source: IMD portal (https://mausam.imd.gov.in).*

The average basinal maximum temperature is approximately 30 °C in summer and 13 °C in winter, while the average minimum temperatures range from 18 °C in summer to - 0.3 °C in winter (Fig. 2.2.). January is the coldest month, and June is considered the warmest (Shrestha et al., 2015). A cold-arid climate has been observed in the upper part of the basin near Karakorum and Ladakh region, whereas dry and humid climate prevailed in the lower catchment near the Punjab region (Fig. 2.1.). At Srinagar, the average monthly temperatures fluctuate from 1.2 °C to 24.7 °C, with the highest recorded temperature reaching 37 °C and the lowest falling to -14 °C. In contrast, Leh experiences a broader range of mean monthly temperatures, spanning from - 8.4 °C to 17.5 °C, with extremes of 35 °C and - 25 °C. The rainfall for the year 2021-2022 and monthly (1901 - 2023) average temperature at Leh are presented in Figure 2.2. The region of Ladakh is characterized by exceptionally high pan evaporation rates, peaking at 521 mm during the summer months (May to September; Rai et al., 2016).

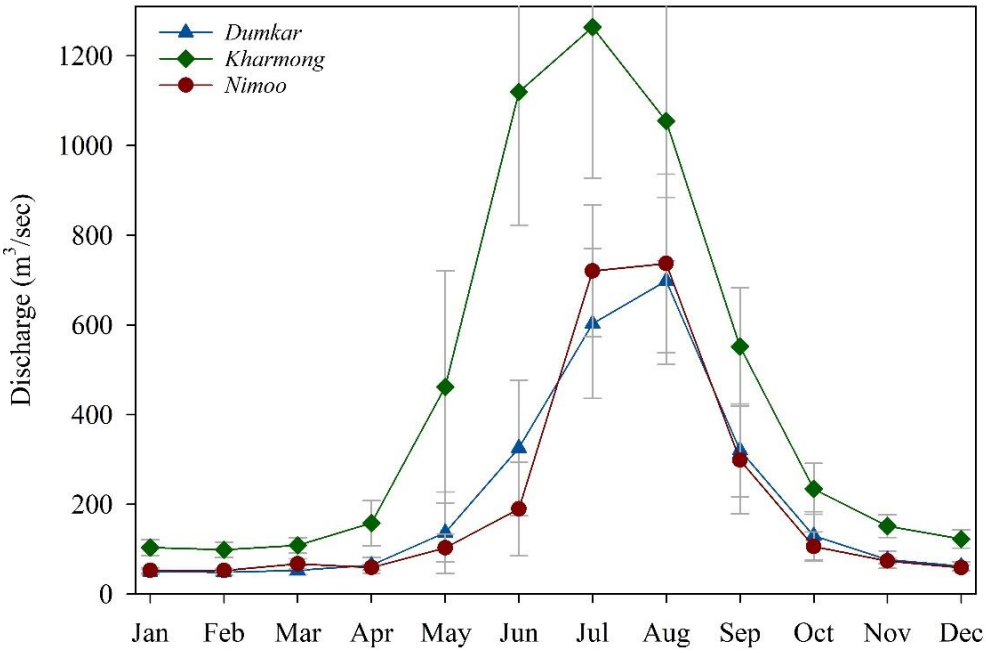

Figure 2.3. *Average monthly discharge of the main Indus at three different sites (Kharmong, Dumkar and Nimoo). Data for the Kharmong and Dumkar stations are taken from literature (Mukhopadhyay and Khan, 2015) whereas, that for Nimoo is taken from Nimoo Bazgo power station.*

The upper half of the mountainous catchment of the basin is characterized by a severe winter with massive snowfall, however, the lower reaches of the basin prevail a mild winter and hot summer. The glacier (18,195 km^2) and snow cover (2, 74, 686 km^2) area are highest for the Indus basin among the Himalayan River basins (Qazi et al., 2020). Earlier model estimations have suggested the highest meltwater index for the Indus compared to the Ganga and Brahmaputra River (Qazi et al., 2020; Immerzeel et al., 2010). These observations point to the dominant role of glacial weathering in the Indus River basin. The discharge of the Indus mainstream is significantly higher during June to September, than that of during other months (Fig. 2.3.).

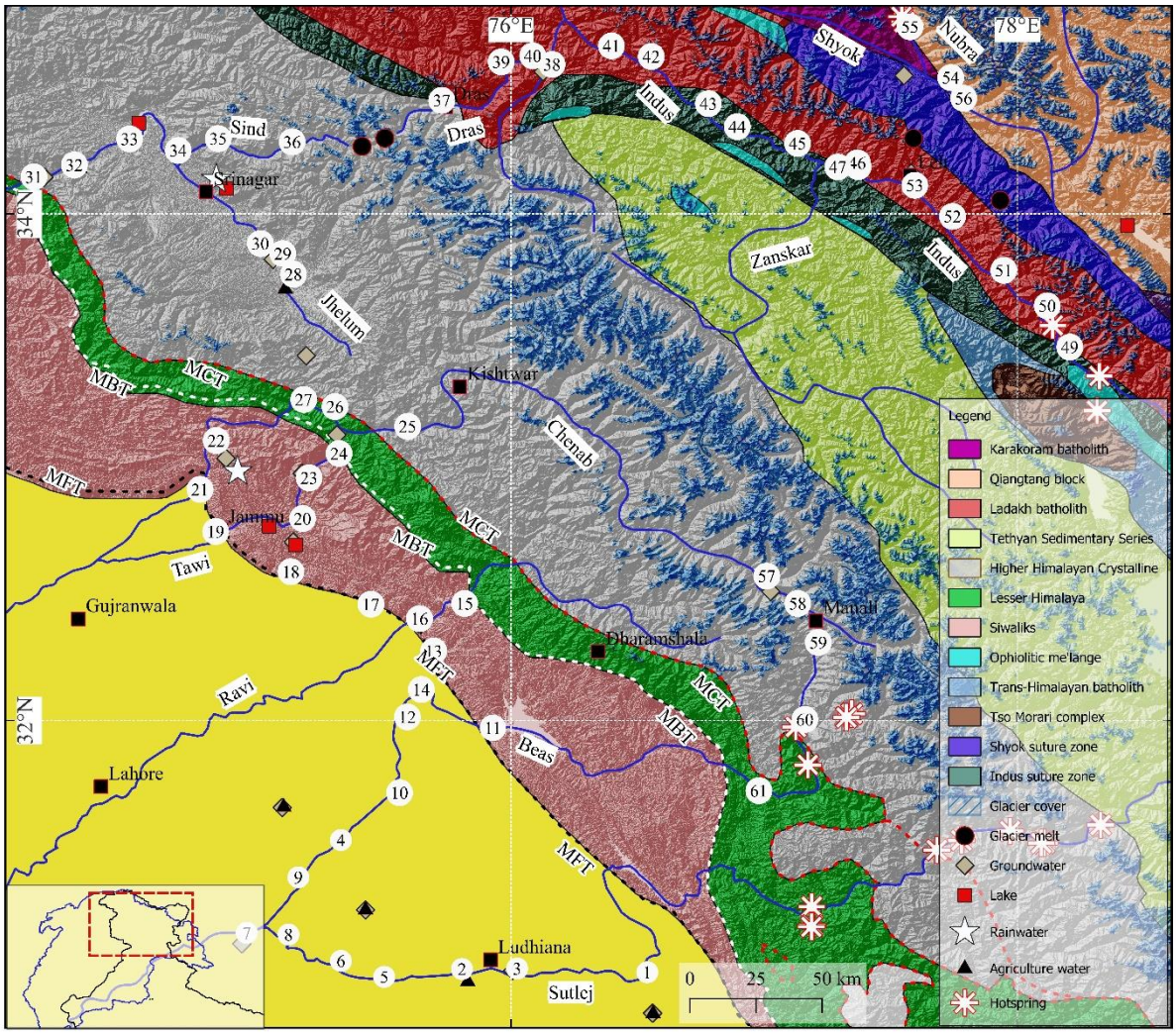

Figure 2.4. *Lithological map showing the sampling sites of the Indus headwater. The basin lithology is modified after Parsons et al., 2020.*

2.1.3. Geology of the study area

The geology of the Indus basin is comprehensively discussed in earlier studies (Karim and Veizer 2000; Garzanti et al., 2005; Pande et al., 1994; Bhat et al., 2023), and is briefly

presented here (Fig. 2.4.). The upper Indus basin drains over the following litho-units; i) Karakorum-Lhasa block (granites, andesitic volcanics and meta-sedimentary sequences), ii) Indo-suture zone (Ladakh batholith with peridotites, granites and trench sediments), iii) Tethyan sedimentary series (carbonates, sandstones, black shales and gypsum/evaporites), iv) Higher and Lesser Himalaya [crystallines; (schist, gneiss, granites and calc-silicates), metapelites; (marbles and quartzites) and sedimentary rocks (shales, sandstones and carbonates)], and v) Siwaliks (sandstones, shales and conglomerates). Besides, a number of hot springs (sulfurous; Gupta et al., 1975; Tiwari et al., 2016) and saline/freshwater lakes are also reported in the UIB. The sediment discharge of the UIB is 250 Mt/yr, which is about 85 % of total sediment flux (~ 290 Mt/yr; Qazi et al., 2020) for the Indus outflow. The corresponding erosion rate of the UIB (3.2 mm/yr) has been estimated to be about eight times higher than that reported as global average for rivers (~ 0.38 mm/yr; Ali and De Boer, 2010). The sediments produced from these terrains are mainly composed of quartz, feldspar and meta-basite grains, and are largely supplied from the Karakorum (~ 60 %), Trans-Himalayan arc (~ 21 %) and Himalayan (~ 19 %) regions (Garzanti et al., 2005).

The northwestern Himalayan zone contains granitic rocks from the Higher Himalaya (Grazanti et al., 2005), Tethyan sedimentary (shale and carbonates of Cambrian-Eocene age) sequences (Karim and Veizer, 2000), and metamorphosed granitoids and sedimentary (fossiliferous carbonate and shale) rocks from the Zanskar Supergroup (Ahmad et al., 1998). The Indus-Shyok suture zone houses ophiolite sequences, Ladakah plutonic complexes, and Dras island arcs (Ahmad et al., 1998). In contrast, the Karakorum zone is mainly comprised of granitoids and sedimentary (shale and carbonates) rocks from Permian-Cretaceous ages. Further, existing studies have documented the occurrence of sulfide minerals in the different rock types from the studied basins. In the Mahanadi basin, occurrence of pyrite and galena are reported in black shale, limestone and pyritiferous feldspathic and quartz arenite from the Chhattisgarh Group (Sarkar et al., 2010; Sinha et al., 2001). Additionally, chalcopyrite and sphalerites are also reported in the Singhbhum and Bastar craton of the basin (Dora et al., 2020; Rai and Changkakoti, 1996). Likely, fresh sulfide minerals (pyrite, chalcopyrite, pyrrohotite, marcasite, sphalerite and massive sulfides) were also observed in the Western Himalaya, Kumaun Himalaya and Kohistan-Ladakh Arc rock types in the upper Indus basin (Farhan et al., 2023; Govil et al., 2021; Stebbins et al., 2019; Sharma et al., 2010). All these sulfide minerals are expected to serve as sulfate sources for the Indus headwaters.

2.2. The Mahanadi River

The Mahanadi River, a large tropical river system from peninsular India, originates at an elevation of 442 m in the central part of India and travels about 850 km before falling into the Bay of Bengal (Fig. 2.5.). The drainage area of the basin is 141,589 km^2 (Jain et al., 2007). The river meets with several major tributaries from the right (e.g. Seonath, Hasdeo, Mand, Ib) and left (e.g. Jonk, Ong and Tel) sides of the stream. In addition to the major tributaries, it also constitutes of several distributaries (Kushabhadra, Biluakhai, Devi, Kandala, Luna, Kuakhai, Daya, Bhargavi, Kathajodi, Birupa, Chitrotpala, Karandia, Paika and Badagenguti), which ultimately falls into the Bay of Bengal or, the Chilika lagoon. The present time-series study is conducted in one of the distributaries, the Paika River. It originates from the Tarapur town of Cuttack district, and travels for about 50 km before draining to the Bay of Bengal (Fig. 2.5.).

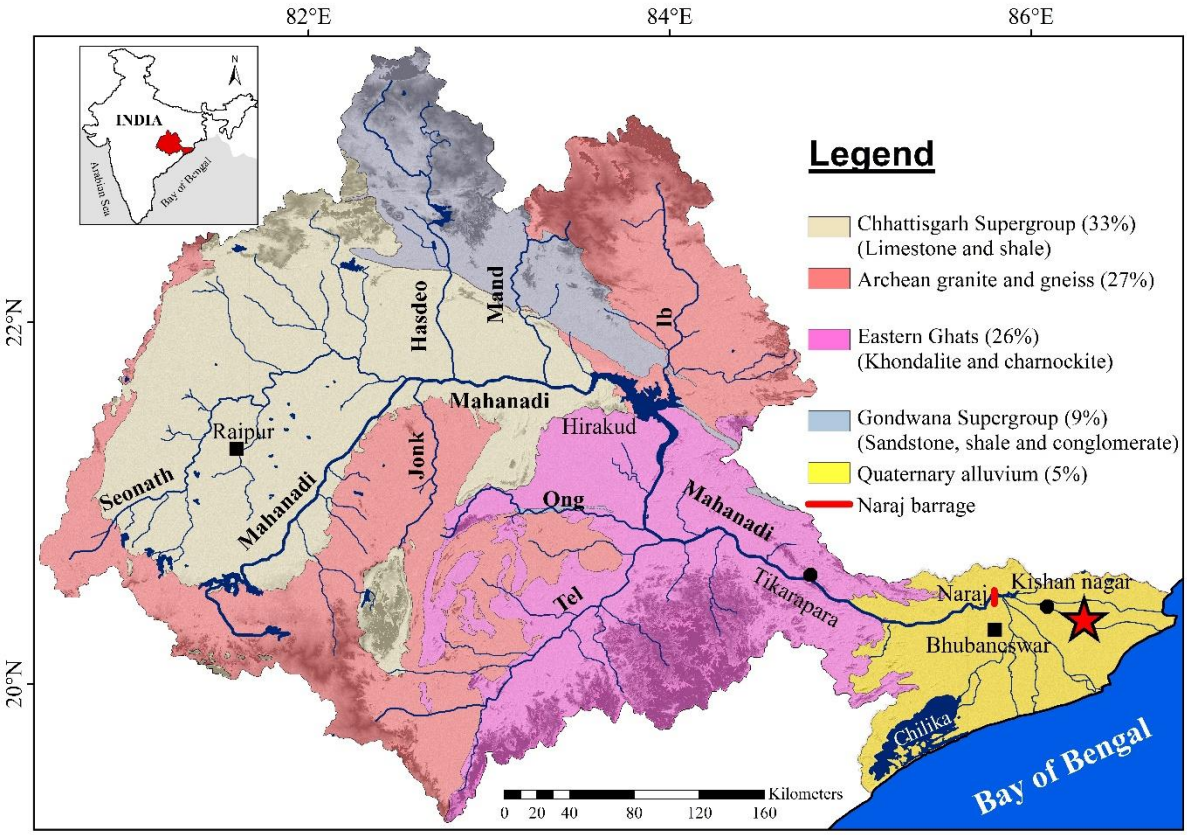

Figure 2.5. *Lithological map of the Mahanadi River basin (https://bhukosh.gsi.gov.in/Bhukosh/Public). The star mark shows the time-series sampling station.*

Figure 2.6. shows the monthly variations in the temperature and humidity for the year 2019-2020 (present study period) near the study site (Bhubaneswar, Odisha). In the absence of real-time discharge data, the monthly average discharge from 1965 to 1970 from a nearby site (Kaimundi, Odisha) was taken from the GRDC portal (Fig. 2.6.) In this region, the temperature

is maximum for May and minimum for January, whereas the humidity is maximum for August and minimum for the month of February (Fig. 2.6.). The river basin receives an average annual rainfall of 141.7 cm, with about 80 % of the precipitation occurring during the southwest monsoon season, from June to September. The annual evaporation rate in the basin, measured at Cuttack, is 53.8 cm (Jain et al., 2007). On average, it supplies approximately 57×10^{12} L/yr of water (Jain et al., 2007) and 12×10^{6} tons/yr of sediments (Bastia and Equeenuddin, 2016) annually to the Bay of Bengal. The discharge is highest for July-August and lowest for the months of December - January, hints to typical Indian summer monsoon signature over the basin.

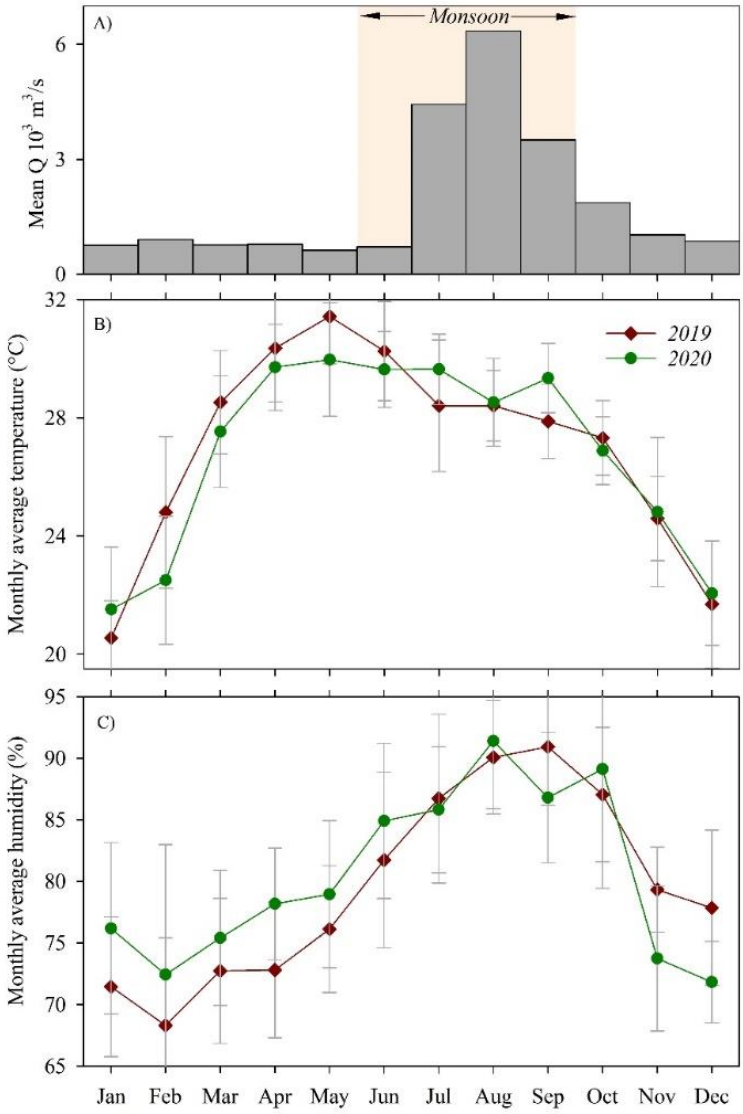

Figure 2.6. *Monthly average A) discharge near the sampling site (http://www.grdc.sr.unh.edu), B) temperature, and C) humidity for the years 2019-2020 near the sampling location (Bhubaneswar, Odisha). Data source: https://www.wunderground.com.*

The lithology of the Mahanadi basin is diverse, and comprises of various litho-units. For instance, the Chhattisgarh Supergroup constitutes ~ 33 % of the basin area and consists mainly of Precambrian limestone and shales. Archean granite and gneiss account for around 27 % of the basin, while the Eastern Ghats, composed of khondalite and charnockite rocks, covers about 26 % of the basin. The Gondwana Supergroup, containing sandstone, shale, and conglomerate, occupies ~ 9 % of the basin area. Additionally, recent alluvial deposits contribute around 5 % of the geology of basin (Fig. 2.5.). Apart from its geological significance, the Mahanadi basin also hosts several mineral belts, such as iron ore, coal, bauxite, lead, and copper. The river basin thus plays a multifaceted role in the ecological, hydrological, and economic landscape of central and eastern part of India.

2.3. Sampling

2.3.1. Spatial sampling

Sixty-one water samples from the Indus headwater and its tributaries have been collected during southwest monsoon (July-August, 2021). These samples cover streams draining through most of the major lithologies present in the upper Indus basin (Fig. 2.4.). Additionally, few glacier and snow melt, rain, agricultural waste, lake and ground water were also collected for source characterization. The river samples were collected in a 2 L pre-cleaned High Density Polyethylene (HDPE) bottles after rinsing it at least three times with the ambient water. Samples were collected from the middle of the stream either by using local boat or, from overbridges. Selected samples were also collected from the river bank. The pH and temperature of the samples were measured on site using a portable sensor (Hanna HI98128). All these samples were filtered using 0.2 μm size nylon filter papers within 24 hours of their collection. Some of these filter papers were also stored, and subsequently dried to quantify the suspended load. The filtered water samples were spilt into two aliquots, out of which, one aliquot was acidified by adding distilled HNO_3 acid to bring the water pH < 2. The acidified aliquots were stored and used for isotopic, trace elements and cations analyses, whereas the non-acidified aliquots were used for the anion analysis. For water oxygen isotopic measurement, an additional aliquot was also collected on-site in an amber bottle, which was completely filled with no bubbles. These bottles were tightened and sealed properly to avoid any evaporation and atmospheric exchange.

2.3.2. Temporal sampling

We have also carried out detailed investigation of time-series chemical and isotopic studies of the Indus mainstream and Mahanadi outflow to assess seasonality in the pyrite oxidation in both weathering- and transport-limited regimes, respectively. For the Indus, water samples at Leh, India (elevation ~ 3,500 m) have been collected at weekly to biweekly intervals for a duration of one-year (September, 2021 to September 2022; Fig. 2.7.). This site is located about five-hundred km downstream to the river source in Tibet (7,502 m), and about thirty km upstream to the Indus-Zanskar confluence at Nimmo (Fig. 2.7.). In case of the Mahanadi, surface water samples from one of the distributaries (Paika River at Kusunpura, Odisha (20.364° N, 86.293°E)) of the Mahanadi River were collected at a weekly time-interval for a duration of 15 months (August 2019 to October 2020). This site location is downstream of the Naraj barrage (with design flood discharge of ~ 29,500 m^3/s; India WRIS data; Fig. 2.5.) and hence, can provide a precise estimation of modern-day delivery of chemical and isotopic constituents from the Mahanadi basin to the Bay of Bengal.

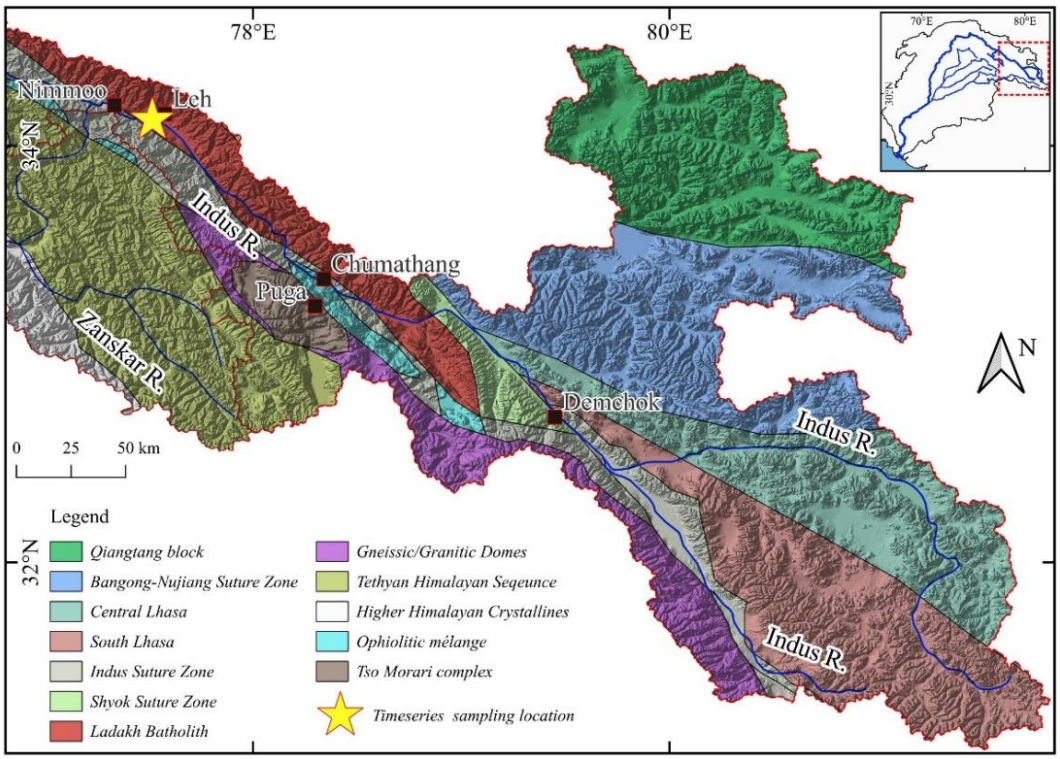

Figure 2.7. *Sampling map of the Indus headwater basin. The time-series sampling is conducted at Leh, India (shown as a star symbol) between September, 2021 and September, 2022. The lithological details are from Parsons et al., (2020).*

Additionally, few groundwater (n = 9) and rainwater (n = 8) samples were also collected from the nearby locations for source characterization. These time-series samples from both these locations were collected and stored in HDPE bottles, after rinsing it few times with the

ambient water. After completion of sample collection, these samples were brought to IISER Pune for their isotopic and geochemical analyses. We have also collected few suspended sediments from about 20 L water volume, after keeping it undisturbed for 24 hours. These samples were centrifuged, dried after decanting the supernatant, and stored for further analyses.

2.4. Analytical methods

A comprehensive chemical analyses of the collected water and sediment samples, and isotopic measurement of water samples were conducted during this thesis work. Figure 2.8. depicts the workflow of these measurements.

2.4.1. Elemental analyses

2.4.1.1. Major ions, alkalinity and silica analyses

The alkalinity, major ions, and silica concentrations were measured following our established analytical methodology (Samanta et al., 2019 and Tripathy et al., 2019). The alkalinity of the spatial samples was measured both in the field within 24 hours of their collection, and in the laboratory (auto-titrator: Metrohm Titrino plus 877) using standard calibration method. The coefficient of variation (CV) for these two datasets are computed using the following equation and is found to be ~ 4 % (n = 96).

$$\text{CV (in \%)} = \left(\frac{\sigma}{\mu}\right) \times 100 \tag{2.1}$$

where, σ is the standard deviation and μ is the mean of the data sets.

The major ions concentrations were analysed using an Ion chromatograph instrument (Metrohm compact IC plus 882). The anions (Cl, NO_3 and SO_4) were measured using a positive polarity mode column, whereas the cations (Na, K, Ca and Mg) were analysed in a negative polarity mode column. The standards of known concentrations were analysed to form the calibration curve, which is used to estimate the unknown sample concentrations. The accuracy of these analyses was constrained using reference materials (ICP multi-element standard IV, IC multi-element standard V and VI). Comparisons of the measured and recommended values (Table 2.2. and 2.3.) establish the accuracy (~ 3 %) of these measurements. The precision of the analysis was 3 %, which was estimated by running samples in replicates.

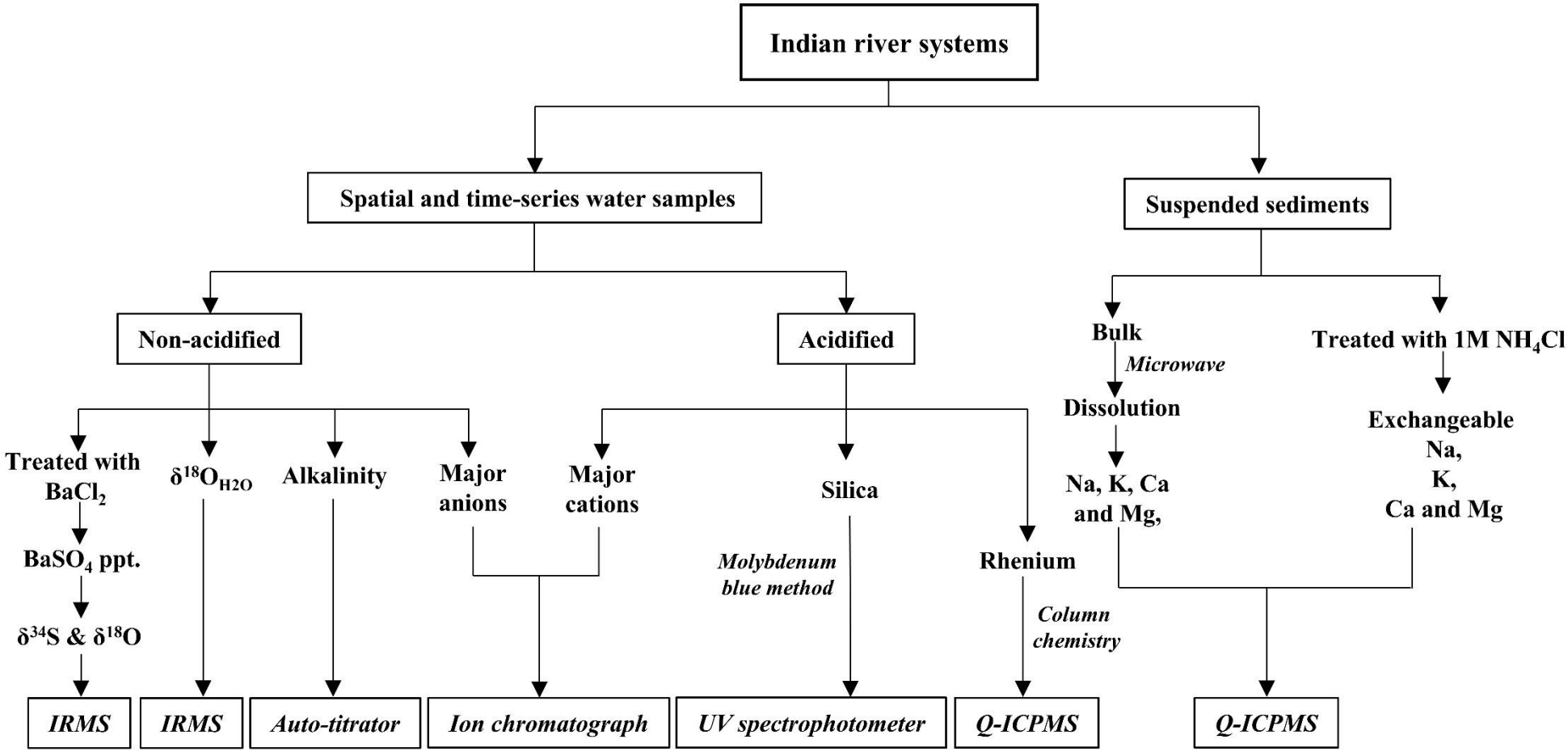

Figure 2.8. *Flow chart of the analytical methodologies on chemical and isotopic analyses adopted during this thesis work.*

The normalized inorganic charge balance (NICB = 100 × [(TZ^+ − TZ^-) / ((TZ^+ + TZ^-)/2)], where TZ^+ and TZ^- stand for total cations and anions in equivalent units) for most of the samples are found to be less than ± 10 %, which ensures good data quality and/or insignificant presence of other organic complexes. The silica concentrations of the samples were measured using a spectrophotometer (Evolution 300, Thermo Scientific and MDT International). These concentrations were measured by quantifying absorbance of their molybdenum blue complexes. A standard calibration approach was followed to estimate the concentration of the silica in the water sample. Table 2.4. compares the measured silica concentrations for replicate samples. The average accuracy and precision of the analysis were ~ ± 4 %.

Table 2.2. *Measured and recommended concentrations of major cations of reference materials used in this study are provided.*

Cations	**IC multi-element standard VI**		**ICP multi-element standard IV**	
	Measured (mg/L)	***Recommended (mg/L)***	***Measured (mg/L)***	***Recommended (mg/L)***
Na	98 ± 2; n = 38	100	989 ± 12; n = 16	1000
K	50 ± 2; n = 36	50	1006 ± 14; n = 16	1000
Ca	97 ± 3; n = 40	100	999 ± 13; n = 15	1000
Mg	98 ± 6; n = 42	100	1011 ± 13; n = 14	1000

Table 2.3. *Measured and recommended values of major anions for the reference materials.*

Anions	**IC multi-element standard V**	
	Measured (mg/L)	***Recommended (mg/L)***
Cl	98 ± 2; n = 53	100
NO_3	50 ± 8; n = 42	50
SO_4	200 ± 8; n = 46	200

Table 2.4. *Replicate analyses of silica concentrations to check the measurement reproducibility.*

Sample ID	**SiO_2(µM)**	
	Replicate-1	***Replicate-2***
INDW-21/40	60	59
GW-21/1	368	367
INDL-21/1	40	39
IND-18/2	39	39
INDW-21/26	43	44
GLW-21/1	52	52
INDW-21/2	80	80

In this thesis, the measured cations and anions concentration for the river water are symbolized only as elements instead of ionic forms, so as to use the superscript/subscript place for correction/source related annotations. For example, the concentration of Ca^{2+} is written as concentration of Ca for river water.

2.4.1.2. Major ions analyses in the sediments

The suspended sediments of time-series site for the Mahanadi River were dissolved using Microwave digestion (Anton Paar) unit (Samanta et al., 2022, Venugopal et al., 2023). Briefly, ~ 0.1 g of sediment samples were treated with HF-HNO_3-HCl acid in the Microwave for dissolution. After complete sample dissolution, the representative solution was stored in 0.32 N HNO_3 for further analyses. The bulk Na, K, Ca and Mg concentrations were measured using a Q-ICPMS (Thermo Scientific; Model: iCAP Qc) facility at IISER Pune. The exchangeable fraction of sediments is isolated after treating ~ 50 mg of sample with 1M NH_4Cl and ultrasonicating it. Concentrations of these solutions were measured using a standard calibration approach. Samples of standard reference material (BHVO-2 and BCR-2) were also dissolved and analysed to check the accuracy (Table 2.5.), whereas few samples were also processed in replicates to constrain the precision. Average accuracy and precision of these analyses were ± 3 %.

Table 2.5. *Measured and recommended values for major elements in the standard reference material (BHVO-2).*

Elements	***Measured (wt%)***	***Recommended (wt%)***	***Counts***
Na	1.62 ± 0.004	1.64 ± 0.06	2
K	0.40 ± 0.003	0.43 ± 0.01	2
Ca	8.31 ± 0.39	8.17 ± 0.12	2
Mg	4.38 ± 0.04	4.36 ± 0.07	2

The cation exchange capacity (CEC in meq/100g units) for these samples were computed by adding these exchangeable cation concentrations. The maximum amount of exchangeable Na and K in the sediments are computed as (Tipper et al., 2021):

$$Na_{exchange} = CEC \times SPM \times \beta_{Na} \quad (2.2)$$

$$K_{exchange} = CEC \times SPM \times \beta_{K} \quad (2.3)$$

Here, SPM stands for the suspended particulate load for the river. The β_{Na} (and β_K) reflects the fraction of exchangeable Na (and K) present in the exchangeable cationic pool.

2.4.1.3. Rhenium analysis

The analysis of dissolved rhenium concentrations for this study is carried out via isotope dilution technique using a Quadruple-Inductively Coupled Plasma Mass Spectrometer (Q-ICPMS, Thermo Scientific; Model: iCAP Qc; Danish et al., 2021). A schematic diagram of this approach is shown in Figure 2.9. Briefly, about 50 to 100 gm of water samples were spiked with a known amount of ^{185}Re (abundance: ^{185}Re = 96.74 %, ^{187}Re = 3.26 % and concentration: 4.96 ± 0.04 ng/g) spike solution. The sample and spike solutions are allowed to equilibrate for 24 hours. This equilibrated mixture was completely dried at 100 ºC and refluxed with 0.8 N HNO_3. Pure rhenium cut from this solution was extracted using an anion exchange (1 ml of AG1x8, Bio-Rad, 100 - 200 mesh, Cl^- form) column. The isotopic signals of these pure rhenium cut were analysed in the Q-ICPMS. The instrumental mass fractionation and internal precision of the analysis were continuously monitored by measuring a rhenium standard (Sigma Aldrich). The measured ^{185}Re/^{187}Re ratio (R_m) was corrected for mass fractionation (by comparing ratios of bracketed standards) and the corrected ratios were used to compute the Re concentrations using the following isotope dilution equation (Faure and Mensing, 2009):

$$N_W = \frac{S_W \times W_N}{W_S}\left[\frac{Ab_S^A - R_m Ab_S^B}{R_m Ab_N^B - Ab_N^A}\right] \quad (2.4)$$

where,

N_w = Weight of the Re in the mixture

S_w = Weight of the spike in the mixture

W_N = Atomic weight of Re

Ws = Atomic weight of Re in the spike

Ab_S^A = Abundance of ^{185}Re in the spike

Ab_S^B = Abundance of ^{187}Re in the spike

Ab_N^A = Natural abundance of ^{185}Re

Ab_N^B = Natural abundance of ^{187}Re

The analytical reproducibility of the rhenium measurement was obtained by processing and measuring samples in replicates (Table 2.6.). Few procedural blank samples were processed and these blank levels were always 2 to 3 orders of magnitude lower than the sample load, and hence, no blank correction was applied.

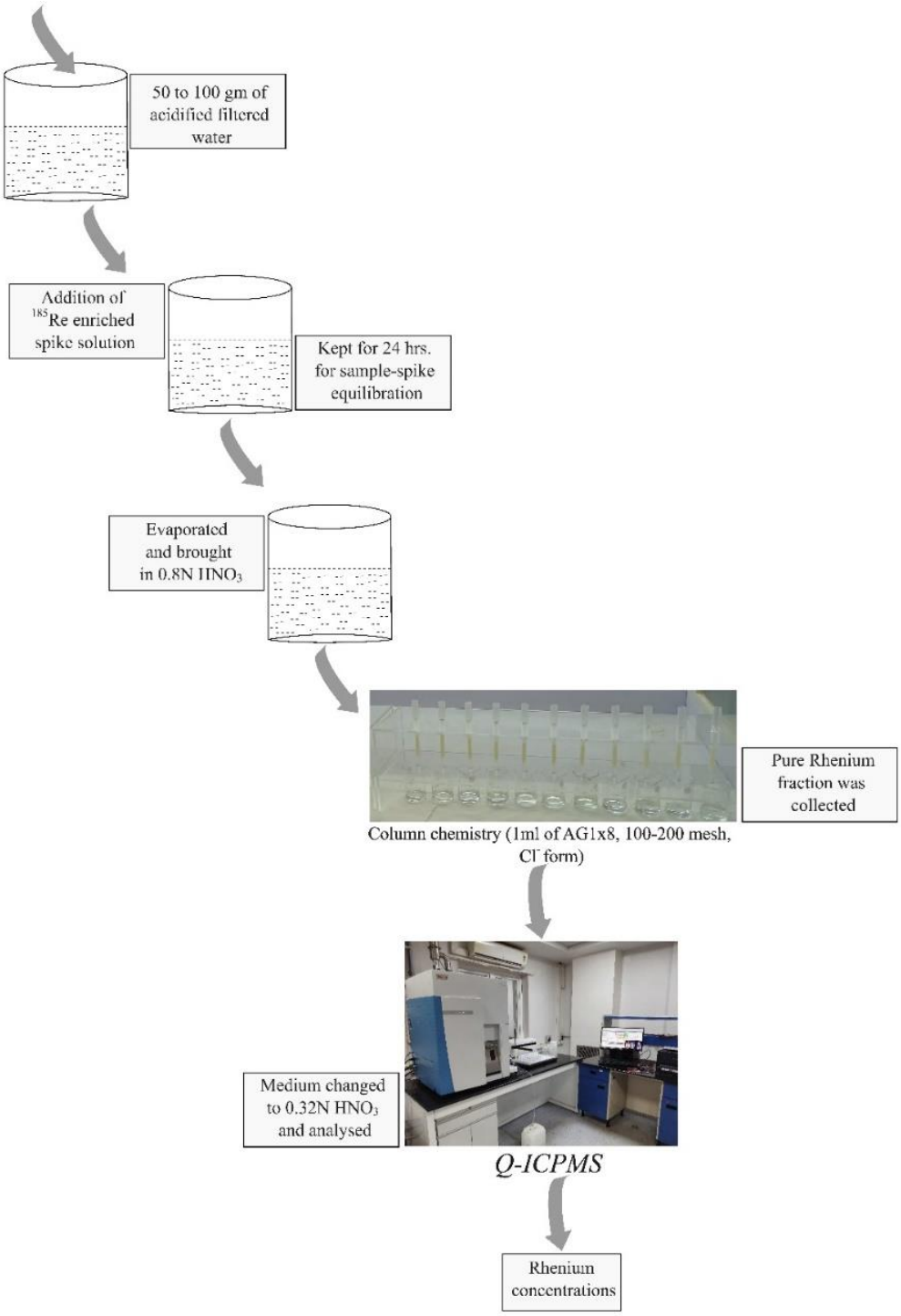

Figure 2.9. *Analytical protocols followed for Re analysis using an isotope dilution approach.*

Table 2.6. *Replicate analyses of dissolved Re concentrations for the samples constrain the external precision.*

Sample ID	Re (pmol/kg)	
	Replicate-1	***Replicate-2***
PKW19/15	3.5	3.4
PKW19/20	1.7	1.9
INDW-21/12	21.4	21.5
INDW-21/41	18.4	18.9
INDW-21/52	15.4	15.7
IND22/25	25.2	24.6
IND22/34	19.9	20.6

Table 2.7. *Measured and recommended values of Re concentrations for international reference materials to establish the accuracy of the analyses.*

Sample ID	Re (ppb)	
	Measured (2σ)	***Recommended (2σ)***
BHVO-2	1.05 ± 0.12	~ 0.54
BCR-2	11.55 ± 0.21	~ 12.6

Seven surface Bay of Bengal and Southern Ocean samples were also processed to check the accuracy of the analysis. The measured Re concentration (39 ± 2 pmol/kg; n = 7) for these samples match well with that reported for the Bay of Bengal waters (Colodner et al., 1993; Singh et al., 2011). We have also analysed two international standards (BHVO-2 and BCR-2) to check the accuracy of the analysis. The measured (1.05 ± 0.12; 2σ, n = 3) and recommended (0.54 ± 5.3; 2σ, n = 6; Jochum et al., 2016) values for BHVO-2 are found overlapping. Similarly, the measured (11.55 ± 0.21; 2σ, n = 3) and recommended (12.6 ± 15.9; 2σ, n = 4; Jochum et al., 2016) Re concentrations for BCR-2 are in good agreement. These observations confirm good data quality. The details of these values are provided in the Table 2.7.

2.4.2. Isotopic analyses

2.4.2.1. Sulfur and oxygen isotopic analyses of sulfates

The sulfur isotopic composition of the sulfate fraction of the samples were measured following our established analytical protocol (Rout and Tripathy, 2024). The flow chart of the analytical methods is also shown in Figure 2.10. About 300 - 400 ml of unacidifed samples were treated with few drops of 1 M HCl and left for about 5-10 minutes to allow complete degassing of the carbonates as CO_2. Then sufficient amount of saturated $BaCl_2.2H_2O$ (20 wt%)

solution was added to supersaturate the solution with respect to barite. The precipitated $BaSO_4$ particulates was filtered, dried, and stored in a micro centrifuge tube for further isotopic analysis. Towards this, about 0.2 mg of the $BaSO_4$ powder was packed in a tin boat which was combusted at 1120 °C in an Elemental analyser combined with an isotope ratio mass spectrometer (IRMS; Elementar- isoprime precisION) instrument. The SO_2 released was measured for their isotopic ratios using the IRMS facility at IISER Pune.

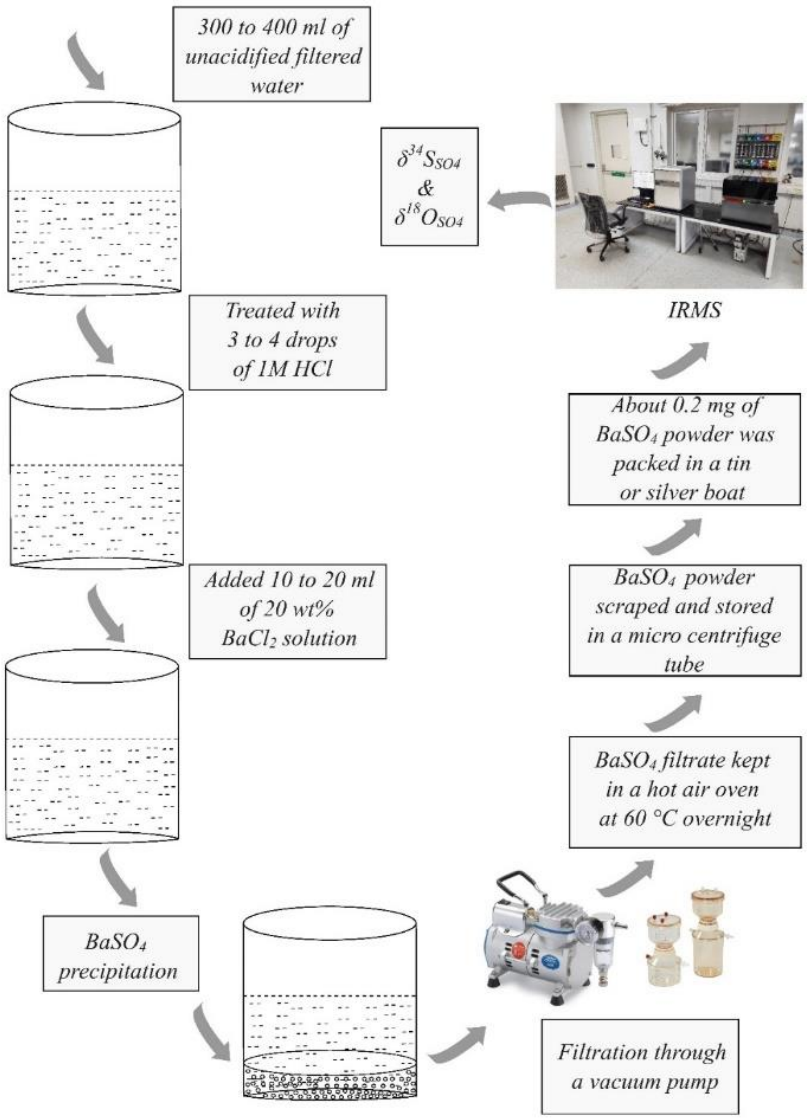

Figure 2.10. *Schematic diagram showing the sulfur and oxygen isotopic measurement in sulfate fractions of water samples.*

Accuracy of $\delta^{34}S_{SO4}$ analyses were established through regular measurement of our in-house laboratory standards (sulfanilamide (-5.66 ± 0.4 ‰; n = 51), and $BaSO_4$ powders (9.76 ± 0.5 ‰; n = 34)). The internal precision for the sulfur isotopic analysis was always better than ± 0.3 ‰ (n = 24; Table 2.8.).

Table 2.8. *The table provides the $\delta^{34}S_{SO4}$ of replicate analysis of water samples for the estimation of internal precision of the analyses.*

Sample ID	$\delta^{34}S_{SO4}$ (‰)	*STDEV (1σ)*
PKW-20/37	17.03	0.10
PKW-20/37 (Rpt.)	17.17	
INDW-21/41	-6.41	0.04
INDW-21/41 (Rpt.)	-6.35	
INDW-21/43	-6.30	0.10
INDW-21/43 (Rpt.)	-6.44	
INDL-21/06	9.51	0.16
INDL-21/06 (Rpt.)	9.29	
INDW-21/48	-4.58	0.82
INDW-21/48 (Rpt.)	-3.42	
IND-22/01	-0.70	0.05
IND-22/01 (Rpt.)	-0.77	
IND-22/02	-0.61	0.37
IND-22/02 (Rpt.)	-0.08	
IND-22/07	0.37	0.13
IND-22/07 (Rpt.)	0.19	
IND-22/19	0.34	0.16
IND-22/19 (Rpt.)	0.11	
IND-22/24	2.41	0.04
IND-22/24 (Rpt.)	2.48	
CHS-1	6.61	0.33
CHS-1 (Rpt.)	6.14	
BSD-16/09	5.07	0.04
BSD-16/09 (Rpt.)	5.01	

Note: here Rpt. refers to the replicate samples

Further, we have also analysed surface water samples (n = 4) from the Bay of Bengal and compared with available literature data. Average $\delta^{34}S_{SO4}$ value (21 ± 0.5 ‰) for these samples compares well with the reported isotopic ranges for modern-day seawater (21 ± 0.1 ‰; Kampschulte and Strauss, 2004; Tostevin et al., 2014). Two samples from a local river (Mula River, Pune, India) and a groundwater sample from the Deccan traps were also measured in replicates to check the analytical reproducibility of the $\delta^{34}S_{SO4}$ measurements. The average $\delta^{34}S_{SO4}$ values of the river (13.4 ± 0.3 ‰; n = 2) and groundwater (9.4 ± 0.2 ‰; n = 3) samples constrains the external reproducibility of these analyses.

For $\delta^{18}O_{SO4}$ measurement, the $BaSO_4$ powder was pyrolyzed at 1420 °C and the isotopic signal of the released CO (Eq. 2.5; Kornexl et al., 1999; Bao et al., 2006) was measured in the IRMS instrument facility at IISER Pune.

$$BaSO_4 + 4C \xrightarrow{Pyrolysis\ at\ 1420\ °C} BaS + 4CO \quad (2.5)$$

The accuracy and precision of these analyses were regularly monitored by measuring several internal laboratory standards (Benzoic acid (23.3 ± 0.3 ‰; n = 8), Barium sulfate (13.2 ± 0.4 ‰; n = 6), Cellulose (28 ± 0.2 ‰; n = 4) and Sucrose (32.4 ± 0.7 ‰; n = 4)) and few primary standards (IAEA SO6 (-11.35 ‰), IAEA-600 (- 3.48 ‰), IAEA-601 (23.14 ‰) and USGS-32(25.4 ‰)). The internal precision of $\delta^{18}O_{SO4}$ analysis was always better than ± 0.5 ‰. We have also analysed $\delta^{18}O_{SO4}$ values for few samples by treating with or, without Diethylenetriaminepentaacetic acid (DTPA); both these processes yielded overlapping $\delta^{18}O_{SO4}$ values within analytical uncertainty (Table 2.9.; Bao et al., 2006; Relph et al., 2021). Additionally, the $\delta^{18}O_{SO4}$ values for few surface waters of Bay of Bengal were measured; their average value (9.2 ± 0.5 ‰; n = 3) matches well with that reported for the modern-day seawater (~ 9.3 ‰; Relph et al., 2021 and reference therein).

Table 2.9. *The DTPA treatment method (before and after) results of few Bay of Bengal samples are provided.*

Sample ID	$\delta^{18}O_{SO4}$ (non-treated; ‰)	$\delta^{18}O_{SO4}$ (DTPA treated; ‰)
BB-21/43	9.53	8.42
BB-21/17	9.40	9.26
BB-21/08	8.65	8.52

2.4.2.2. The water oxygen isotopic ($\delta^{18}O$) analysis

The water samples collected in amber bottles were equilibrated with known volumes of CO_2, and their isotopic abundances are obtained using an isotope ratio mass spectrometer (Thermo Scientific, MAT 253 Plus) in a continuous flow mode at IIT Roorkee. Additionally, few samples were also measured in replicates and these results are provided in Table 2.10. Accuracy of these analyses was continuously monitored by measuring an in-house reference material. The measured $\delta^{18}O_{H2O}$ (-8.39 ± 0.05 ‰; n = 20) values of this material match well with its reported (-8.41 ± 0.1 ‰) values.

The measured $\delta^{18}O$ values for sulfate and water samples were used to compute the $\Delta^{18}O$ (Relph et al., 2021), as follows:

$$\Delta^{18}O = \delta^{18}O_{SO_4} - \delta^{18}O_{H_2O} \quad (2.6)$$

Table 2.10. *Replicate measurement of water $\delta^{18}O$ values for the spatial samples of the Indus headwater.*

Sample ID	***$\delta^{18}O_{H2O}$ (‰)***	
	Replicate-1	***Replicate-2***
INDW-21/7	-6.51	-6.53
INDW-21/60	-7.91	-7.89
GWSN21/7	-7.84	-7.82
GWSN21/16	-12.24	-12.25
AGRW-21/5	-6.15	-6.16

Chapter 3

Time-series study of water $\delta^{34}S_{SO4}$ of a large tropical river (Mahanadi, India) system

This page has been intentionally left blank.

3.1. Introduction

Continental weathering of rocks, involving interaction between geosphere, atmosphere and biosphere, serve as dominant pathway to supply nutrients and suspended sediments to global ocean (Berner and Berner, 1996). Any past fluctuation in the rate of these surficial processes has led to major climatic and chemical excursions (Raymo et al., 1988). Intensity of chemical weathering is mainly controlled by lithology (Bluth and Kump, 1994; Gaillardet et al., 1999), climate (runoff and temperature; Dalai et al., 2002a), and vegetation pattern (Stallard and Edmond, 1983). Specifically, chemical weathering in tropical regions has been found to supply disproportionally higher chemical fluxes due to conducive climate and lithology (Krishnaswami and Tripathy, 2012). Earlier studies on the Indian river basins have documented significant seasonal changes in the weathering rates (Tipper et al., 2006; Samanta et al., 2019), and have linked it to preferential dissolution of carbonates (over silicates) during monsoon seasons. In addition to monsoon, researches from the silicate-dominated terrains of the peninsular region of India have confirmed comparable to higher rates of silicate weathering in these weathering-limited regions than those from the Himalayan River basins (Gurumurthy et al., 2012; Jha et al., 2009; Das et al., 2005; Samanta et al., 2021). These basins are characterized with high rainfall (via Indian summer monsoon) and also, comprised of Archean granites and gneisses (Chakrapani and Subramanian, 1993). A recent study using cosmogenic radionuclides has also emphasized on the importance of basin slope in regulating weathering intensity in the Peninsular Indian rivers (Mandal et al., 2015). Unlike silicate and carbonate weathering rates, there have been limited efforts to estimate the sulphide and organic oxidation rates for the Peninsular Indian rivers to assess the net effect of these basins on carbon cycle, and factors regulating their intensities in these basins.

This chapter focuses on the temporal variations in water chemistry and sulfur isotopic compositions of one of the large river systems (Mahanadi River) from the Peninsular India. This river basin falls in the core monsoon zone and hence, may be used to evaluate the climatic sensitivity of tropical erosion. We have used these chemical and isotopic datasets to quantify the silicate weathering and sulfide oxidation rates for this river system and also, established their temporal changes in response to runoff changes. Further, we have also used available literature data for rhenium and organic carbon concentrations and isotopic values for this basin to compute the organic oxidation and burial rates, respectively. These four weathering rates for this basin is combined to establish the net effect of chemical weathering in this basin on carbon

cycle. Details on the seasonal variations in datasets, and their souce-apportionment calculations are presented in this chapter to establish significance of weathering in tropical regions.

3.2. Results

Time-series data of major ions, and silica concentrations, and sulfur isotopic ($\delta^{34}S_{SO4}$) values for the Paika River (a distributary of the Mahanadi), its possible source waters (rain and groundwater) are presented in Table 3.1.-3.2., and concentrations data for the exchangeable cations in the suspended sediments are provided in Table 3.5.

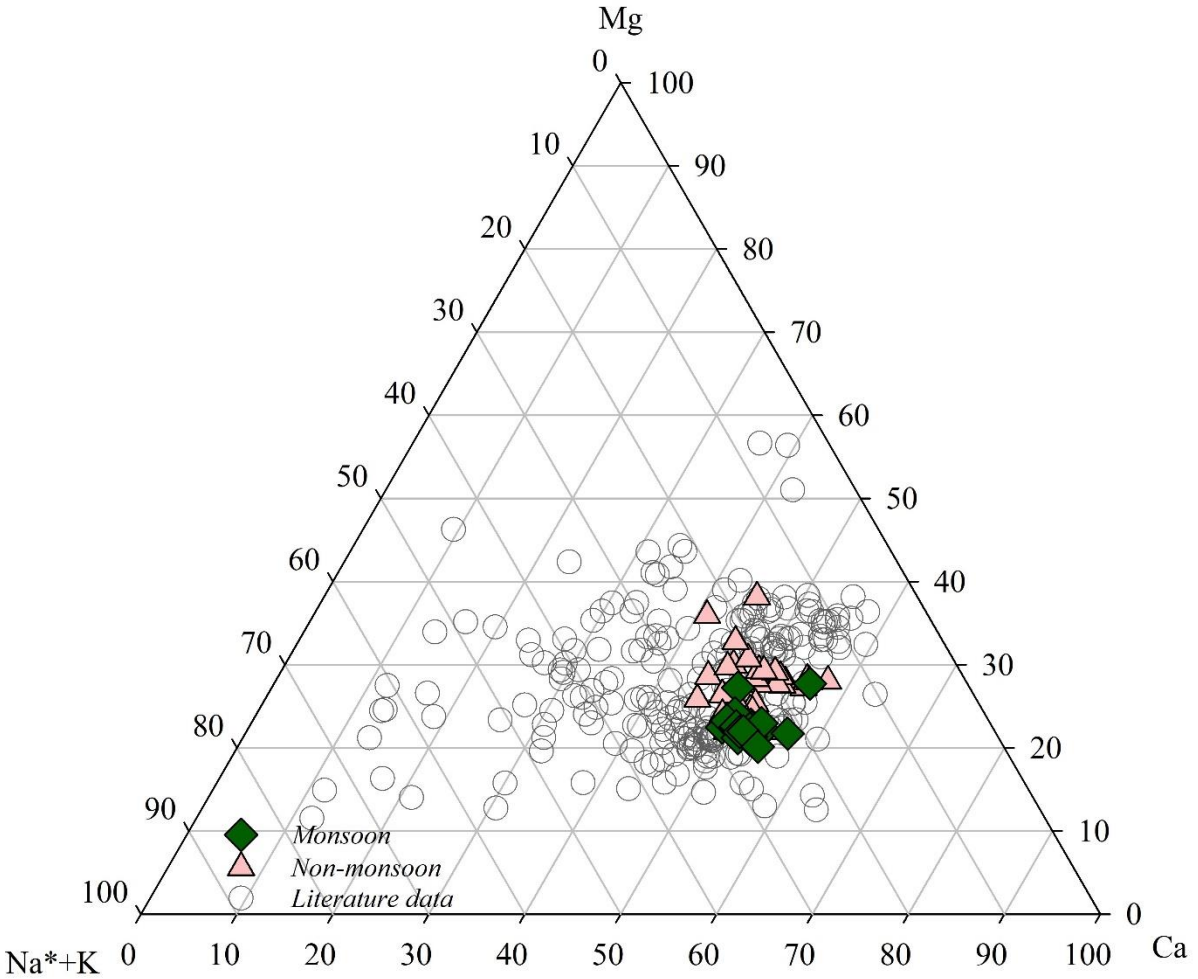

Figure 3.1. *Ternary diagram for Na*+K, Ca and Mg concentrations of the Mahanadi River water during monsoon (diamond symbol) and non-monsoon (triangle symbol) periods. The literature data (Jha et al., 2009; Pattnaik et al., 2013; Dessert et al., 2001; Bastia and Equeenuddin, 2019; Acharya et al., 2022; Das et al., 2005) for other peninsular rivers are also shown in open grey circles for reference.*

The total dissolved solids (TDS) in the Mahanadi River range between 90 and 305 mg/L, with an average value of 183 ± 64 mg/L. Major ion chemistry of the river is of Ca-Mg-

HCO_3 type, indicating dominant solute supply via carbonate weathering (Fig. 3.1.). The Ca and Mg concentrations (in Eq. units) together account ~ 70 % of the TZ^+ load. The (Ca+Mg) values (in Eq. units) are linearly correlated with HCO_3 (r^2 = 0.97; n = 65), with a slope of ~ 1 (Fig. 3.2.). On average, the HCO_3 concentration (average: 1638 ± 467 µM; n = 65) accounts for 73 % of the total anionic (TZ^-) load, whereas the chlorides contribute to 18 % of TZ^- content. The dissolved silica in these samples varies widely from 143 to 505 µM (Table 3.1.). Average silica concentration of these samples (264 ± 118 µM; n = 65) is about two times higher than the reported global average Si value for rivers (~ 127 µM; Gaillardet et al., 1999).

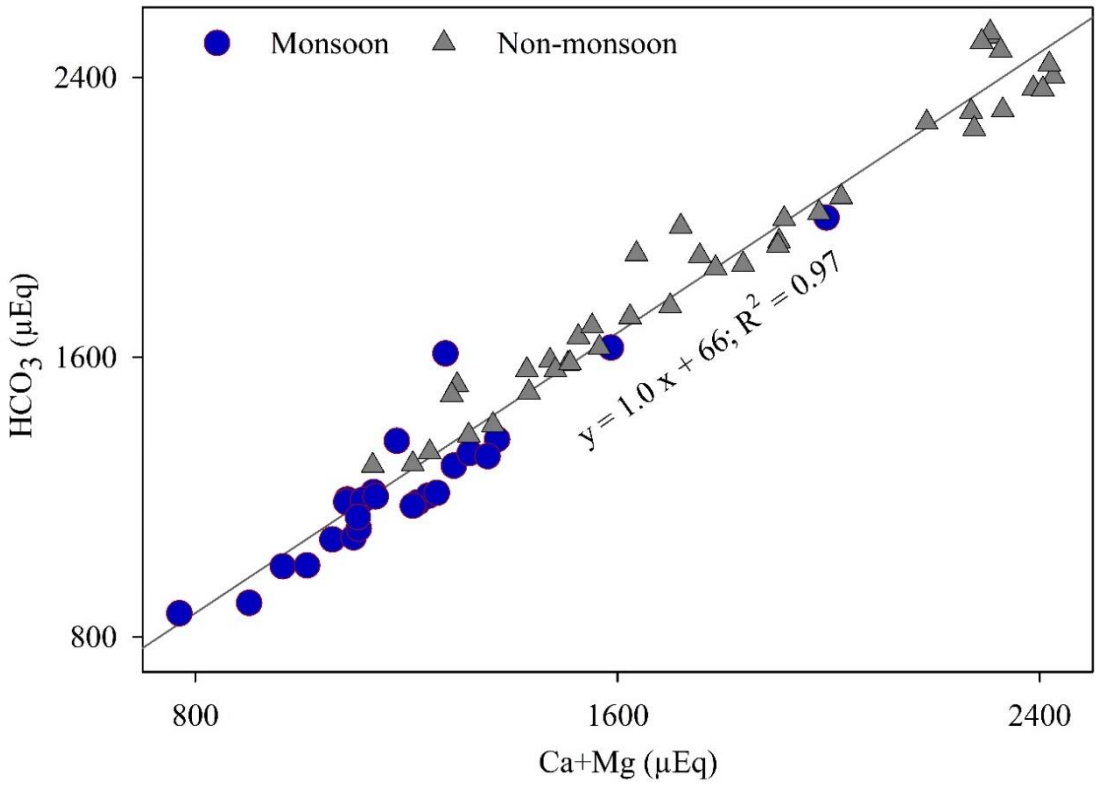

Figure 3.2. *Correlation between Ca+Mg and HCO_3 concentrations. The unit slope of the linear regression line indicates dominancy of the carbonic acid-mediated weathering in the basin.*

The Na concentrations of these samples vary by an order of magnitude (180 - 1514 µM) with an average value of 568 ± 382 µM. About 40 % of the average Na concentration is associated with the chloride phases (Na* = Na - Cl). The average Na* concentration (171 ± 43 µM) is lower than that reported as global average for rivers (244 µM; Tripathy and Das, 2014). In contrast to Na, the K (67 ± 14 µM) and NO_3 (26 ± 13 µM) concentrations show minimal changes. The sulfate concentrations of the samples vary between 36 and 132 µM; the average

SO_4 concentration (93 ± 24 µM) is higher than that observed for the rainwater samples (~ 35 µM; Table 3.2.). Water chemistry of the Mahanadi River shows significant temporal variation. Figure 3.2. depicts that the concentrations of most of the elements are lower during the monsoon compared to the non-monsoon season. For instance, the average Ca concentration of the non-monsoon samples (587 µM) is about 1.4 times higher than that of the monsoon samples (416 µM). The non-monsoon-to-monsoon concentration ratios are although found different for Na* (1.3), K (1.2), Mg (1.7), SO_4 (1.1), HCO_3 (1.5) and SiO_2 (1.7), all these constituents are found to have lower concentrations during high flow stages. Similar seasonal trends have earlier been reported for several river systems from this sub-continent (Galy and France-Lanord, 1999; Bickle et al., 2005; Singh et al., 2005; Tipper et al., 2006; Chapman et al., 2015; Samanta et al., 2019). In contrast to elements, the non-monsoon-to-monsoon ratios for Ca/Na* (1.1) and Ca/Si (1.1) ratios are found closer to unity. In addition to these general trends, the Mahanadi water chemistry also shows significant fluctuations during non-monsoon season (Fig. 3.3.). These changes in low flow stages are often synchronous to the water level at this site. The studied location is located downstream of a large dam, which influences the river hydrology of this location. In particular, a significant decline in concentrations is observed during pre-monsoon season (Feb-Mar, 2020). The water level during February and March months have also increased significantly (Fig. 3.3. A), which may dilute the elemental abundances. This high water level is possibly linked to water release from an upstream dam, as it does not commensurate with high rainfall.

Table 3.1. *Dissolved major ions, and silica concentrations, and sulfur isotopic values for the Mahanadi outflow (Paika; a distributary of Mahanadi).*

Sample ID	Date	Na	K	Ca	Mg	Cl	NO_3	SO_4	HCO_3	SiO_2	$\delta^{34}S_{SO4}$	TDS	TZ^+	TZ^-	TZ^+/TZ^-	NICB
		(µM)									(‰)	(mg/L)	(µEq)			(%)
PKW19/01	11-08-2019	180	53	261	124	95	30	36	867	153	--	90	1003	1065	0.9	-6
PKW19/02	18-08-2019	253	69	385	159	133	11	86	1192	186	10.2	125	1409	1508	0.9	-7
PKW19/03	25-08-2019	257	62	382	161	133	8	84	1185	178	8.8	124	1403	1494	0.9	-6
PKW19/04	01-09-2019	235	64	369	161	122	10	93	1078	173	--	117	1358	1397	1.0	-3
PKW19/05	08-09-2019	206	57	338	145	101	49	77	1001	154	--	108	1229	1306	0.9	-6
PKW19/06	15-09-2019	227	55	403	166	102	37	68	1213	189	--	125	1421	1488	1.0	-5
PKW19/07	22-09-2019	261	55	421	170	111	11	57	1360	223	11.3	135	1498	1595	0.9	-6
PKW19/08	29-09-2019	279	57	443	194	110	9	50	1610	228	--	160	1609	1829	0.9	-13
PKW19/09	06-10-2019	251	55	431	175	116	30	80	1294	168	--	132	1517	1601	0.9	-5
PKW19/10	13-10-2019	259	55	432	190	114	8	75	1328	179	12.0	133	1558	1600	1.0	-3
PKW19/11	20-10-2019	303	53	445	203	128	13	61	1520	201	11.5	148	1652	1783	0.9	-8
PKW19/12	27-10-2019	255	57	389	179	128	23	65	1290	179	--	130	1448	1572	0.9	-8
PKW19/13	03-11-2019	301	57	440	203	130	9	66	1492	193	--	146	1645	1764	0.9	-7
PKW19/14	10-11-2019	405	62	558	260	204	11	69	1895	235	12.5	178	2104	2248	0.9	-7

PKW19/15	17-11-2019	427	55	525	335	171	0	65	1974	231	12.7	187	2202	2275	1.0	-3
PKW19/16	24-11-2019	793	78	717	376	617	9	98	2271	365	--	251	3058	3092	1.0	-1
PKW19/17	01-12-2019	922	75	777	378	803	36	107	2517	458	14.6	286	3307	3571	0.9	-8
PKW19/18	08-12-2019	999	80	773	380	838	21	110	2528	466	--	289	3385	3606	0.9	-6
PKW19/19	15-12-2019	1015	82	758	387	872	20	112	2501	462	15.1	289	3387	3617	0.9	-7
PKW19/20	22-12-2019	1064	78	774	389	915	18	113	2477	468	14.5	291	3470	3638	1.0	-5
PKW19/21	29-12-2019	1120	78	799	414	906	29	114	2402	468	--	290	3623	3564	1.0	2
PKW20/22	05-01-2020	1021	73	734	401	827	33	105	2302	430	14.9	273	3364	3372	1.0	0
PKW20/23	12-01-2020	1169	82	782	412	955	24	117	2368	454	15.5	289	3639	3580	1.0	2
PKW20/24	19-01-2020	1241	84	778	425	990	19	117	2366	454	15.6	292	3731	3610	1.0	3
PKW20/25	26-01-2020	1268	87	743	422	1031	20	118	2306	464	--	290	3685	3594	1.0	3
PKW20/26	02-02-2020	1296	89	716	422	1084	24	124	2253	456	--	288	3662	3608	1.0	1
PKW20/27	09-02-2020	1338	89	773	436	1137	19	128	2437	465	16.3	305	3846	3847	1.0	0
PKW20/28	16-02-2020	611	78	546	304	387	17	119	1746	211	12.7	191	2388	2388	1.0	0
PKW20/29	23-02-2020	1078	87	604	387	865	29	126	2013	365	--	251	3148	3159	1.0	0
PKW20/30	01-03-2020	421	71	504	249	208	22	100	1580	150	12.1	162	1998	2010	1.0	-1
PKW20/31	08-03-2020	861	84	640	372	685	24	108	2058	320	--	238	2969	2982	1.0	0

PKW20/32	15-03-2020	564	80	485	278	331	37	95	1658	202	13.5	178	2169	2217	1.0	-2
PKW20/33	22-03-2020	1021	84	584	374	845	23	106	1995	390	14.6	245	3022	3074	1.0	-2
PKW20/34	29-03-2020	873	87	544	349	678	23	103	1855	329	--	222	2745	2762	1.0	-1
PKW20/35	05-04-2020	1209	94	554	399	1040	25	113	1931	449	--	257	3209	3222	1.0	0
PKW20/36	12-04-2020	1385	94	490	429	1204	24	118	1865	476	16.7	263	3316	3329	1.0	0
PKW20/37	19-04-2020	1514	90	516	436	1413	37	128	1919	505	17.0	281	3507	3624	1.0	-3
PKW20/38	26-04-2020	478	58	525	258	298	22	88	1627	212	--	173	2102	2124	1.0	-1
PKW20/39	03-05-2020	332	77	456	203	188	24	84	1376	158	--	143	1728	1756	1.0	-2
PKW20/40	10-05-2020	382	60	510	226	198	16	93	1590	173	12.2	161	1915	1989	1.0	-4
PKW20/41	17-05-2020	396	60	501	240	219	29	92	1563	185	13.4	162	1938	1993	1.0	-3
PKW20/42	24-05-2020	380	54	486	230	207	14	93	1499	194	--	156	1865	1905	1.0	-2
PKW20/43	31-05-2020	380	60	459	223	210	20	100	1406	195	--	150	1803	1837	1.0	-2
PKW20/44	07-06-2020	613	70	509	285	430	19	100	1627	282	--	186	2271	2276	1.0	0
PKW20/45	14-06-2020	749	74	667	331	627	19	105	1998	328	--	229	2821	2854	1.0	-1
PKW20/46	21-06-2020	366	60	462	224	185	16	104	1364	183	--	146	1797	1773	1.0	1
PKW20/47	29-06-2020	350	72	420	191	182	45	130	1184	198	--	138	1645	1671	1.0	-2
PKW20/48	05-07-2020	368	70	422	199	205	32	130	1203	173	--	138	1679	1700	1.0	-1

PKW20/49	12-07-2020	354	72	420	186	204	37	132	1174	178	--	137	1639	1678	1.0	-2
PKW20/50	19-07-2020	360	70	458	187	201	45	109	1289	176	--	143	1719	1752	1.0	-2
PKW20/51	26-07-2020	352	67	468	192	172	40	108	1325	191	--	145	1740	1753	1.0	-1
PKW20/52	02-08-2020	346	67	485	192	175	43	116	1316	179	11.9	146	1768	1766	1.0	0
PKW20/53	09-08-2020	253	58	350	156	127	48	72	1004	155	--	111	1322	1323	1.0	0
PKW20/54	16-08-2020	311	56	441	188	153	57	93	1211	173	11.9	134	1625	1608	1.0	1
PKW20/55	23-08-2020	248	56	389	161	117	54	78	1084	155	11.7	118	1405	1410	1.0	0
PKW20/56	30-08-2020	186	49	315	136	94	54	66	897	143	--	98	1138	1178	1.0	-3
PKW20/57	06-09-2020	202	54	401	154	102	43	67	1109	151	--	116	1365	1387	1.0	-2
PKW20/58	13-09-2020	252	47	392	167	96	29	54	1191	196	10.5	122	1415	1423	1.0	-1
PKW20/59	20-09-2020	253	47	401	170	97	29	58	1201	192	10.4	123	1442	1444	1.0	0
PKW20/60	27-09-2020	242	54	404	150	105	29	79	1142	162	--	120	1403	1434	1.0	-2
PKW20/61	04-10-2020	338	47	496	218	108	29	55	1563	222	--	154	1814	1810	1.0	0
PKW20/62	11-10-2020	360	49	530	225	132	25	80	1582	199	13.3	159	1918	1900	1.0	1
PKW20/63	20-10-2020	374	51	537	239	135	27	69	1688	228	13.6	167	1977	1988	1.0	-1
PKW20/64	27-10-2020	394	51	562	250	144	14	79	1715	223	--	171	2068	2032	1.0	2
PKW20/65	30-10-2020	433	49	604	274	186	22	73	1889	257	--	188	2239	2243	1.0	0

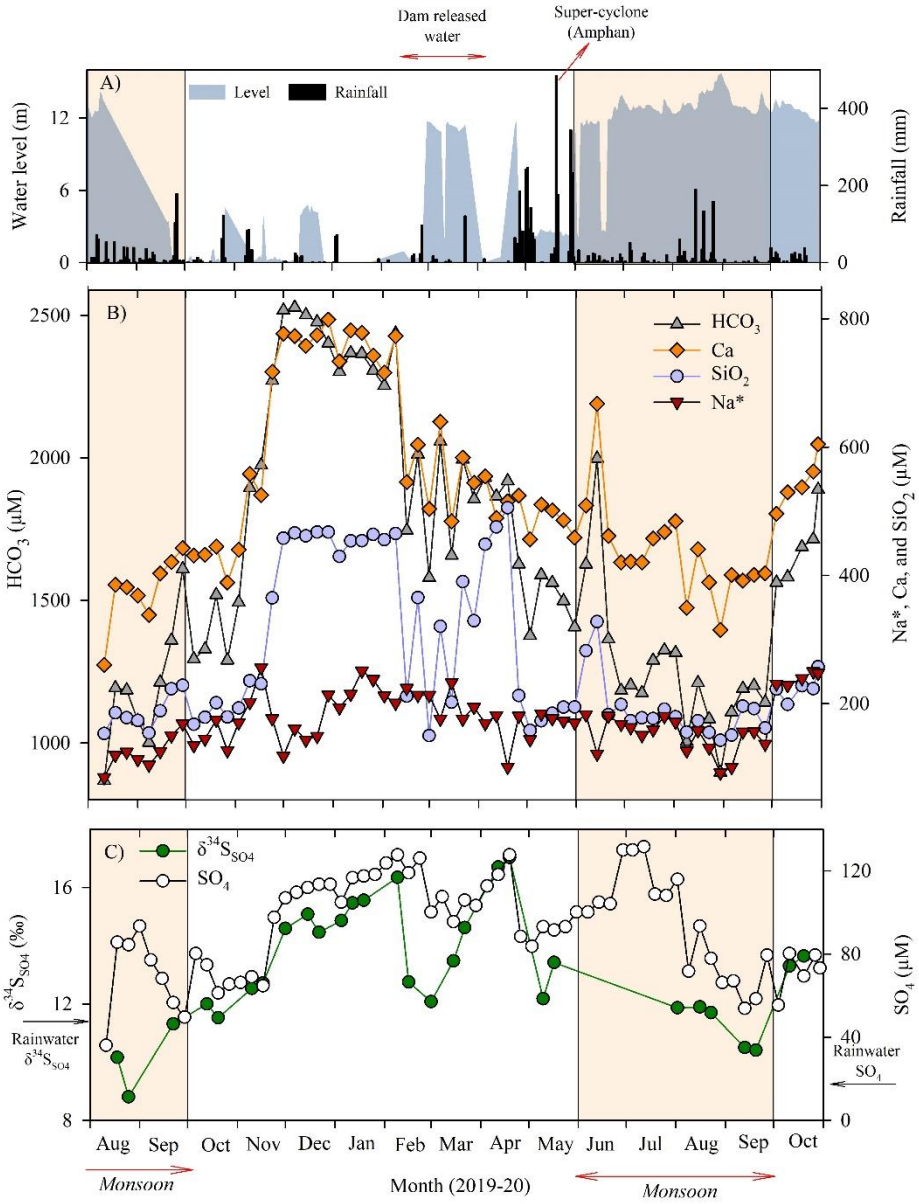

Figure 3.3. *Time-series variation of (A) hydrological water level and rainfall (https://indiawris.gov.in/wris), (B) concentrations of Na*, silica, Ca and HCO_3, and (C) sulfate concentrations and $\delta^{34}S_{SO4}$ values are shown. The arrow marks in (C) stand for the typical rainwater composition (see, Table 3.2. and 3.3. for data source). These trends depict relatively higher concentrations and enriched $\delta^{34}S_{SO4}$ values during low flow stages.*

The $\delta^{34}S_{SO4}$ values of the Mahanadi River vary between 8.8 ‰ and 17 ‰, with an average value of 13 ± 2 ‰ (n = 29). These isotopic values are higher compared to the global average $\delta^{34}S_{SO4}$ value reported for rivers (4.4 ± 4.5 ‰; Burke et al., 2018). Figure 3.4. compares the $\delta^{34}S_{SO4}$ of the Mahanadi with earlier reported data for peninsular Indian (Das et al., 2012; Burke et al., 2018) and Himalayan (Karim and Veizer, 2000; Chakrapani and Veizer, 2006; Kemeny et al., 2021a; Burke et al., 2018) rivers.

Table 3.2. *Chemical data for rain and groundwater samples from the lower reaches of the Mahanadi basin.*

Sample ID	Date	Lat (°N)	Lon (°E)	Na	K	Ca	Mg	Cl	NO_3	SO_4	HCO_3	SiO_2	Re	TDS	TZ^+	TZ^-	TZ^+/TZ^-
				(µM)									(pmol/kg)	(mg/L)	(µEq)		
Rainwater																	
RW20/1	24-04-2020	20.3711	86.2947	9	14	11	8	15	35	9	--	2	0.5	5	61	70	0.87
RW20/2	01-05-2020	20.3711	86.2947	12	15	19	13	18	57	19	--	4	0.4	8	91	114	0.8
RW20/3	12-06-2020	20.3711	86.2947	2	13	9	3	12	8	2	--	bdl	0.2	2	38	24	1.58
RW20/4	27-07-2020	20.3711	86.2947	60	17	24	23	41	24	51	--	7	0.9	12	172	167	1.03
RW20/5	13-08-2020	20.3711	86.2947	15	12	23	11	26	53	21	--	3	0.5	8	97	121	0.8
RW20/6	18-08-2020	20.3711	86.2947	68	59	28	14	117	72	16	--	9	0.5	16	210	222	0.95
RW20/7	25-08-2020	20.3711	86.2947	12	14	17	7	21	25	17	--	1	0.1	6	73	80	0.92
RW20/8	01-10-2020	20.3711	86.2947	2	8	10	4	9	1	2	--	bdl	0.3	1	36	15	2.46
Groundwater																	
GW20/1	11-08-2020	20.3713	86.2955	745	242	438	471	73	0	27	2032	657	1.4	224	2806	2159	1.3
GW20/2	11-08-2020	20.3711	86.2998	545	72	459	441	842	223	292	1202	742	1.9	234	2418	2851	0.85
GW20/3	11-08-2020	20.3687	86.301	252	83	254	167	231	35	62	779	91	2.6	93	1177	1168	1.01
GW20/4	11-08-2020	20.3685	86.3019	536	31	601	313	167	16	17	2250	631	0.7	229	2393	2466	0.97
GW20/5	11-08-2020	20.3594	86.2987	4207	60	3264	1924	10946	19	470	3267	459	8.5	938	14644	15173	0.97
GW20/6	11-08-2020	20.3643	86.294	904	37	1238	485	210	12	28	4155	530	1.8	380	4388	4433	0.99
GW20/7	11-08-2020	20.3711	86.2947	875	240	553	472	578	20	45	2488	692	0.9	283	3165	3177	1.0
GW20/8	11-08-2020	20.3699	86.2943	12015	302	191	107	6344	77	44	7635	246	0.8	1013	12913	14144	0.91
GW20/9	11-08-2020	20.37	86.2936	699	58	472	587	327	20	35	2433	637	0.6	254	2874	2850	1.01

bdl: below detection limit

These datasets show that the peninsular Indian rivers are systematically higher in $\delta^{34}S_{SO4}$ than the Himalayan Rivers and global average values. The sulfur isotopic values of the Mahanadi River also exhibit seasonal changes (Fig. 3.3. C). The average $\delta^{34}S_{SO4}$ for the monsoon samples (11 ± 1 ‰; n = 8) are found lower than the non-monsoon samples (14 ± 2 ‰; n = 21). This seasonal $\delta^{34}S_{SO4}$ trend is consistent with those reported for Fraser River (Burke et al., 2018). Further, the seasonal $\delta^{34}S_{SO4}$ variation is also similar to that observed for the sulfate concentrations, which are also characterized with lower concentrations during high flow (than low flow) stages (Fig. 3.3. C).

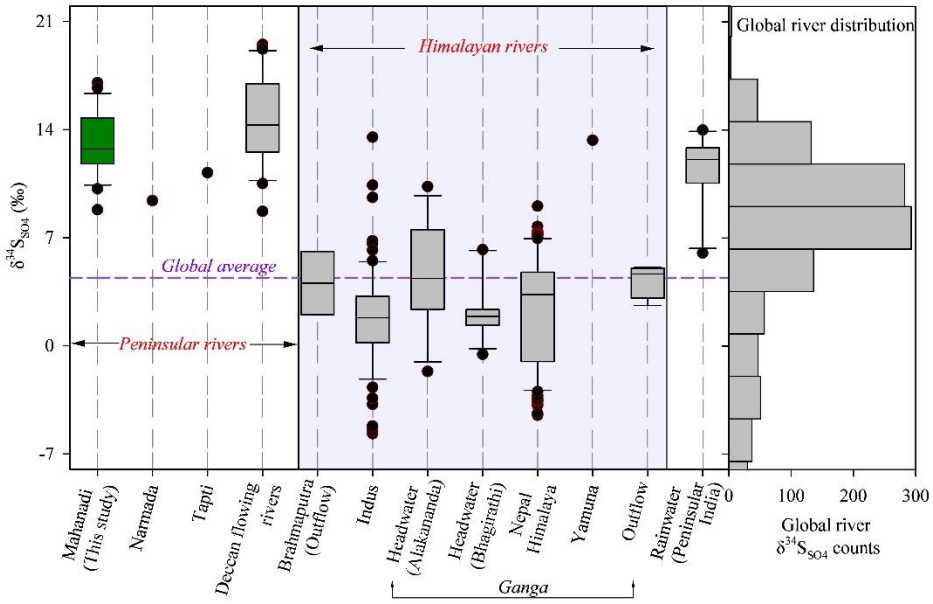

Figure 3.4. *Box plot showing the $\delta^{34}S_{SO4}$ distribution for the Mahanadi River. For comparison, literature-available $\delta^{34}S_{SO4}$ data distributions for Himalayan [Indus (Karim and Veizer, 2000), Ganga (Chakrapani and Veizer, 2006), Nepal Rivers (Kemeny et al., 2021a), Brahmaputra, Yamuna and Ganga outflow (Burke et al., 2018)] and Peninsular Indian [Narmada and Tapti (Burke et al., 2018) and Deccan flowing Rivers (Das et al., 2011)] rivers, rainwater (Jacks et al., 1994), and global rivers (Hemingway et al., 2020) are also presented.*

3.3. Discussion

3.3.1. Seasonal variations

Seasonality in the water chemistry is largely regulated by intensity of chemical weathering in basins, impact of fluid flow path and residence time, water-mineral interaction, and groundwater contribution to river system (Tipper et al., 2006; Godsey et al., 2009; Maher, 2011; Ibarra et al., 2016; Hilton et al., 2021). Available studies, based on lower fractional change in solute concentrations than the discharge variations, have suggested intensification of

chemical weathering (than dilution) during high flow stages (Bickle et al., 2005; Samanta et al., 2019). Additionally, time-series concentrations data have also indicated relatively higher silicate (than carbonate) weathering (Galy and France-Lanord, 1999; Krishnaswami et al., 1999; Tripathy et al., 2010) and/or groundwater input (Tipper et al., 2006) to rivers during low flow stages. Further, the concentration-discharge (C-Q) relationship has also shown that high fluid residence time may cause minimal seasonal change in water chemistry by attaining chemical equilibrium within basins (Maher, 2011).

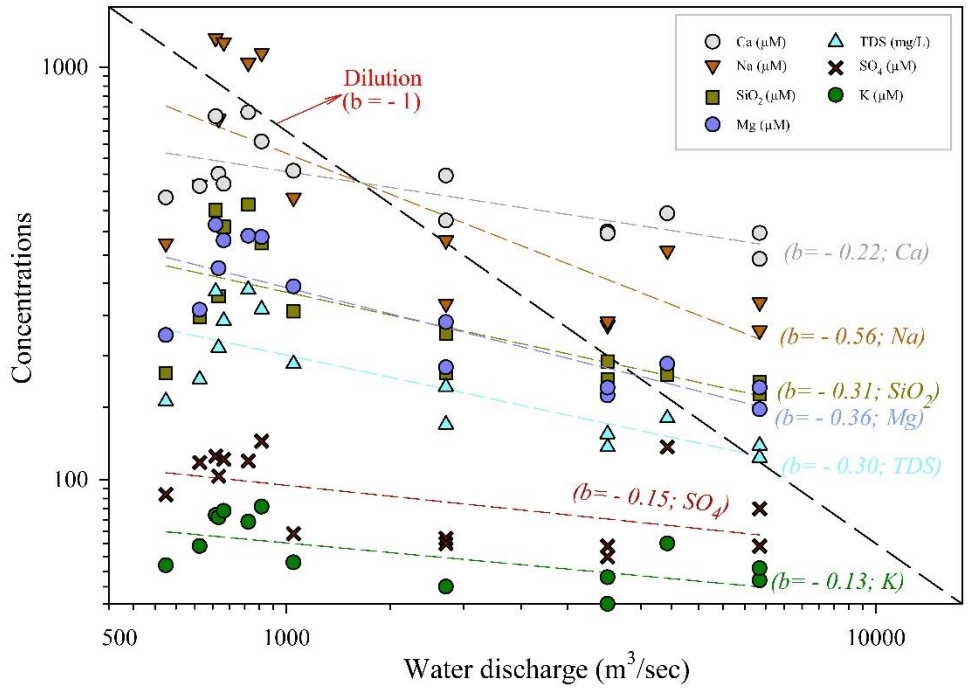

Figure 3.5. *Concentration-discharge relationship for selected chemical constituents (Na, Ca, Mg, K, SiO_2, SO_4 and TDS) of the Mahanadi River.*

The C-Q relationships for dissolved constituents are mostly in the form of $C = Q^b$; here, the constant b value (ranging between 0 and - 1) varies depending on chemostatic (b = 0) and dilution (b = - 1) effect on water chemistry (Godsey et al., 2009). Figure 3.5. depicts the monthly-averaged C-Q relationship for the Mahanadi basin. The b-values for all elements are different than unity, confirming that our time-series data cannot be explained by the dilution effect alone, and hence, points to change in weathering process during this period. Further, these values are observed to be different for these elements. The b-values exhibit high fluctuation for Na (b ~ - 0.56), and minor changes for K (b ~ - 0.13), SO_4 (b ~ - 0.15) and Ca (b ~ - 0.22; Fig. 3.5.). Concentrations of Si, Mg and TDS show intermediate variability (b ~ -

0.36 to - 0.30) during the studied period. One possible factor that can cause the observed chemical changes (Fig. 3.5.) is seasonal changes in relative contributions from solute sources. These source changes are possible due to different weatherability of minerals, fluid composition, flow path and residence time. Earlier studies have documented that river system may attain chemical equilibrium with high residence time during low flow stages, which allows sufficient time to dissolve resistant (silicate) minerals (Maher, 2011). In contrast, higher dissolution of silicates (than carbonates) during low flow stages have also been reported for several river basins (Tipper et al., 2006).

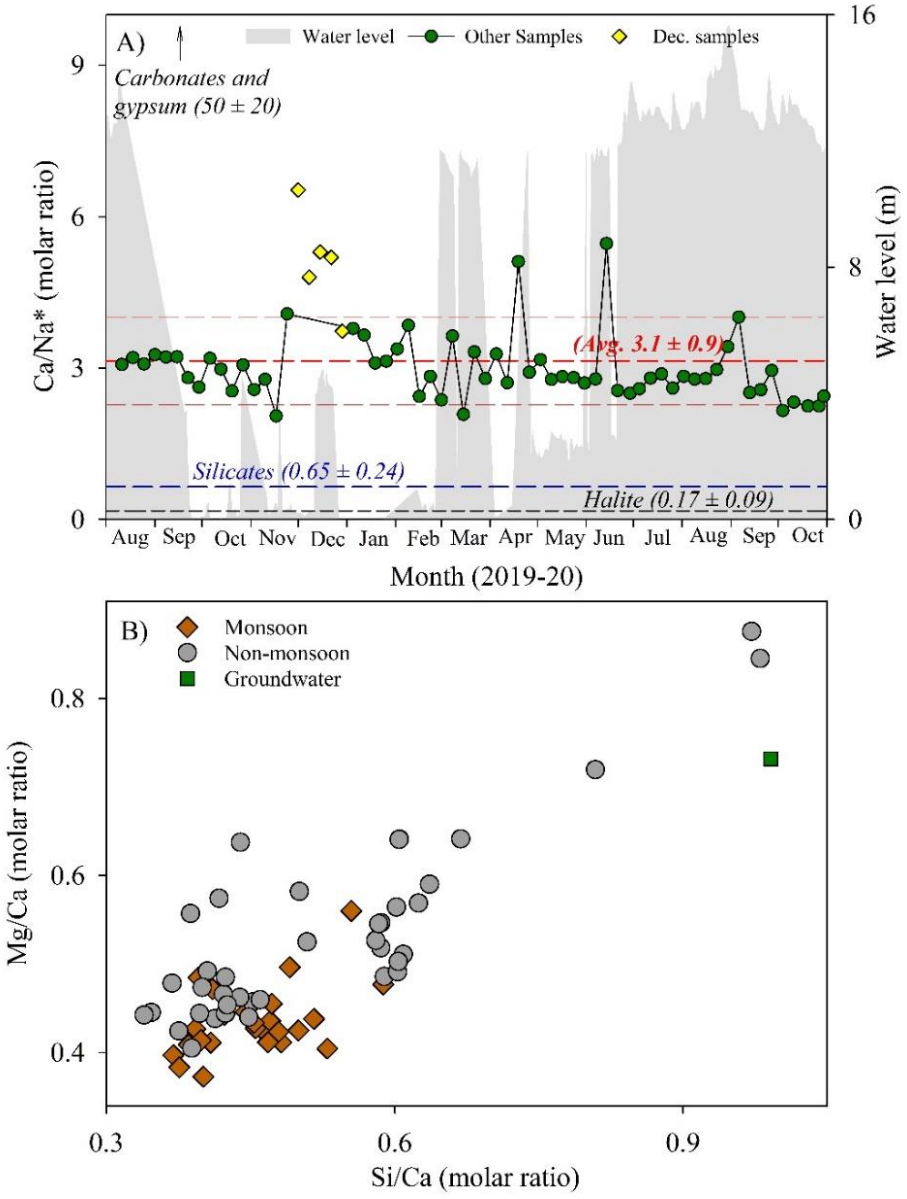

Figure 3.6. *(A) Monthly variations in Ca/Na* (an index for relative silicate-to-carbonate erosion) show no major change with water level. For reference, typical compositions for silicate, carbonate (Gailardet et al., 1999) and halites (Moon et al., 2007) are also shown. (B) Co-variation plot between Si/Ca and Mg/Ca ratio points to impact of groundwater on water chemistry during low flow stages.*

To evaluate this possibility, we have investigated the temporal change in Ca/Na* ratio of the river (Fig. 3.6. A). The Ca/Na ratios for silicates (0.65 ± 0.24: cf. section 3.2.2.1.1.) and carbonates (50 ± 20; Gaillardet et al., 1999) are distinctly different and hence, any seasonal change in solute supply from these sources can be traced using the riverine Ca/Na* ratios. Additionally, dissolution of evaporites, such as halites and gypsum, may also supply solutes to the rivers.The Ca/Na* for halites (0.17 ± 0.09; Moon et al., 2007) are expected to be lower than that of gypsum and carbonates (Fig. 3.6. A). Average Ca/Na* ratio for the Mahanadi samples (3.1 ± 0.9) is intermediate to that of these rock types. This ratio for the monsoon (3.0 ± 0.6) and non-monsoon (3.2 ± 1.0) samples show no distinct seasonal change (Fig. 3.6.). It is further noticed that the Ca/Na* ratio for the December-2019 samples increased significantly. This excursion is synchronous to a water-level rise, which is likely linked to water release from an upstream dam. If we exclude samples from this event (December-2019), the Ca/Na* ratios for monsoon (3.0 ± 0.6; n = 25), non-monsoon (3.0 ± 0.6; n = 35) and all (3.0 ± 0.6; n = 60) samples are found to be indistinguishably same (Fig. 3.6.), confirming minimal change in relative solute contribution from silicates in response to flow stage. Additional to December, there have been several episodes of water level rise possibly due to dam release and/or super-cyclonic disturbances. However, water chemistry of all these episodes do not show a similar rise in Ca/Na* ratio. This indicates a dynamic response of water chemistry to hydrological changes and most of these events seem to have a constant Ca/Na* ratio (Fig. 3.6.). The observed near-constancy in Ca/Na* ratio is in contrast to earlier observation of higher silicate (than carbonate) weathering during low flow stages in the Himalayas (Tripathy et al., 2010), which has been linked to efficient dissolution of resistant minerals due to high water-rock interaction time. This difference may be attributed to high fluid residence time for this supply-limited watershed (Maher, 2011), which may promote chemical equilibrium in terms of relative mineral dissolution and may not cause any preferential mineral weathering.

Tipper et al. (2006), based on seasonal changes in water chemistry of the Marsyandi River, have suggested influence of subsurface flow to the river. Further, a recent study on Sr isotopes of the Chilika lagoon (connected to the Mahanadi outflow) has also showed appreciable groundwater discharge during low flow stages compared to the monsoon period (Danish et al., 2020). A similar subsurface supply may also contribute to the observed chemical variability of the Mahanadi (Fig. 3.6.). The chemical composition of the groundwater samples analysed during this study exhibit large variability. For instance, the concentrations of Na, Ca, Mg, Re and TDS vary by a factor of ~ 4, whereas, the silica and sulfate concentrations vary by a factor of 8 and 17, respectively (Table 3.2.).

Table 3.3. *Compiled sulfur isotopic data for possible sulfate sources for the Mahanadi River basin.*

Sources	Location/Rock-types	$\delta^{34}S$ (‰)					Ref.
		Min	*Max*	*Average*	*Std. dev.*	*count*	
Atmospheric supply	Peninsular India (southern part)	6.0	14	11.4	2	10	[1]
Groundwater	Mahanadi delta region (Odisha, India)	--	--	15.9	--	1	This study
Groundwater	Peninsular India (southern part)	6.4	12.3	9.1	1.6	16	[1]
Groundwater	Gangetic plain region*	4.9	21.6	11.9	5.0	15	[2,3]
Groundwater	All (Peninsular and Gangetic plain)	4.9	21.6	10.4	3.9	31	[1-3]
Pollution	Deccan Traps and Southern India	0.54	11.5	4.6	3.7	9	[1,4]
Saline-alkaline Soil	Deccan Traps	11.2	13.6	12.8	0.9	7	[4]
Silicates (Gneiss/charnockite)	Peninsular India (southern part)	0.1	1	0.6	0.6	2	[1]
Gondwana coal (pyrites)	China	-6.6	10.5	2.1	5.9	9	[5]
Sulfates (Gypsum/barite)	Peninsular India	10	17.6	12.4	3	9	[1,6]
Sulfides (Sedimentary)	Chhattisgarh Supergroup	18.8	40.7	26.9	5.3	22	[7,8]
Sulfides (Magmatic)	Bastar and Singhbhum Cratons	-4.8	11.1	-0.2	3.2	41	[6,7,9]

**Excluding one outlier; [1]: Jacks et al., 1994; [2]: Mukherjee and Fryar, 2008; [3]: Stüben et al., 2003; [4]: Das et al., 2011; [5]: Chmielewski et al., 2002; [6]: Dora et al., 2020; [7]: Sinha et al., 2001; [8]: Sarkar et al., 2010; [9]: Rai and Changkakoti, 1996.*

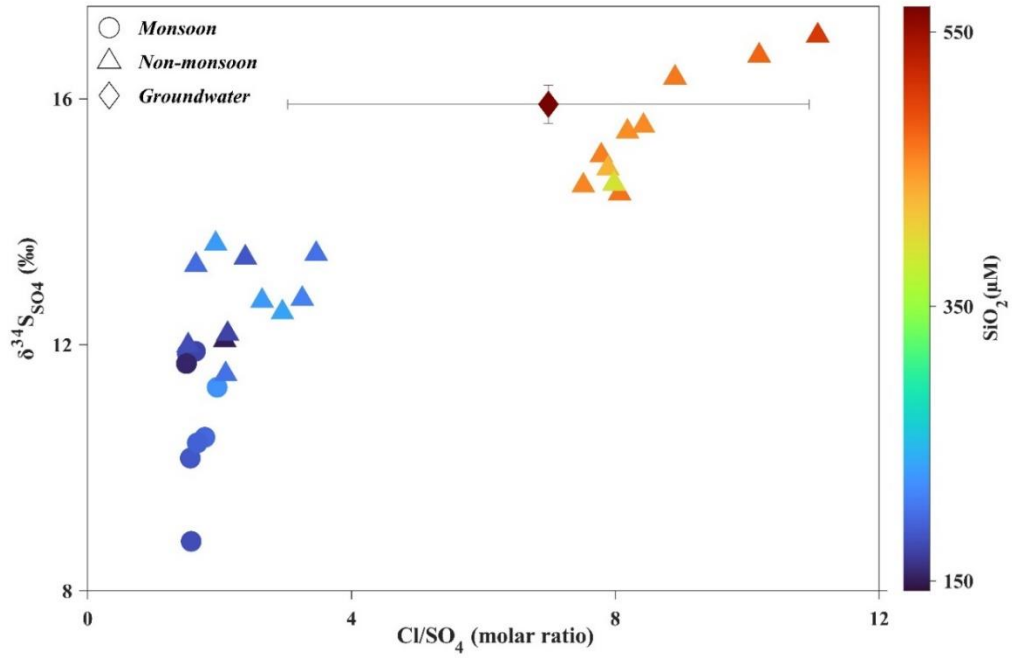

Figure 3.7. *Linear relationship between $\delta^{34}S_{SO4}$ and Cl/SO_4 concentrations of the Mahanadi samples. The silica concentrations for these samples and average groundwater compositions for the basin are also included.*

Two samples yield negative Na* values with high Cl concentrations, which are not included in the subsequent discussion. Despite of these large variabilities, average Ca/Na* ratio for the groundwater (~ 2.8) samples from this basin overlaps to that of the river (3.0 ± 0.6; excluding outlier December samples (cf. above discussion)) samples, indicating same relative contribution from silicates and carbonates to both surface and groundwater samples. We have assessed the Mg/Ca and Si/Ca covariation of these samples to constrain the groundwater supply (Fig. 3.6. B). These two major constituents were strategically used as proxies for subsurface flow mainly due to distinctly higher concentrations of Mg (~ 420 µM) and Si (~ 569 µM; Table 3.2.) concentrations for the groundwater than the high flow surface waters (Mg ~ 182; Si ~ 188 µM; Table 3.1.). Figure 3.6. B clearly shows that the Si/Ca and Mg/Ca ratios of non-monsoon samples are found systematically higher than that of the monsoon samples. Further, the non-monsoon compositions, when compared with the average groundwater ratios, can be explained as a mixture of groundwater and monsoon river water (Fig. 3.6. B). However, a closer inspection of the Si/Ca-Mg/Ca plot indicates that the non-monsoon data fall systematically towards the left of expected mixing line for average groundwater and monsoon data. Although this trend can be explained by groundwater composition variability, this deviation may also arise due to removal of Ca from the system via calcite precipitation during low flow phases (Acharya et al., 2022). This possibility, however, is less likely as the Ca/Na* of the Mahanadi samples do not show any seasonal variation (Fig. 3.6. A), confirming insignificant loss of Ca from the system. These elemental ratios, therefore, indicate an increase in groundwater contribution during low flow stages (Fig. 3.6. B). The proposed increase in groundwater flow to the system is consistent with the decline in surface water table during low flow stages, allowing base flow to enter the river system (Tipper et al., 2006). Consistent with this trend, the observed enriched $\delta^{34}S_{SO4}$ ratios for non-monsoon (14 ± 2 ‰; n = 21) samples than the monsoon (11 ± 1 ‰; n = 8) (Fig. 3.3.) also support influx of groundwater during this period. The $\delta^{34}S_{SO4}$-Cl/SO_4 plot (Fig. 3.7.) also depicts that the $\delta^{34}S_{SO4}$ non-monsoon samples are characterized with isotopic values which are closer to the groundwater $\delta^{34}S_{SO4}$ value (15.9 ‰; Table 3.3.). Further, high silica concentrations and enriched $\delta^{34}S_{SO4}$ ratios of these low flow samples hint at significant groundwater contribution during this season.

Efforts were also made to quantify the groundwater supply to the Mahanadi basin during low flow stages. For this, we have used the following mass balance equation for Si/Ca and Mg/Ca ratios:

$$\left(\frac{Si}{Ca}\right)_{riv} = \left(\left(\frac{Si}{Ca}\right)_{mon} \times (1-g)\right) + \left(\left(\frac{Si}{Ca}\right)_{GW} \times g\right) \quad (3.1)$$

$$\left(\frac{Mg}{Ca}\right)_{riv} = \left(\left(\frac{Mg}{Ca}\right)_{mon} \times (1-g)\right) + \left(\left(\frac{Mg}{Ca}\right)_{GW} \times g\right) \quad (3.2)$$

where, the subscripts, *riv*, *mon* and *GW* stand for riverine, average monsoon composition, and groundwater, respectively, whereas g stands for the fractional supply of Ca from the groundwater. The above equations (3.1-3.2) assume no groundwater supply to the river during the monsoon season. Also, it has been assumed that the riverine Si/Ca and Mg/Ca ratios during low flow stages is a mixture of groundwater and surface water compositions only, and these ratios have not been influenced by any relative change in weathering pattern. For this computation, average Si/Ca and Mg/Ca ratios for the groundwater (1.3 ± 0.9; 0.9 ± 0.4 (excluding two outliers with higher concentrations); Table 3.2.) samples and the riverine samples during monsoon (0.45 ± 0.06; 1.0 ± 0.1; Table 3.1.) were used. Calculations using equation (4-5) estimate that the average Ca fraction supplied through groundwater inflow is 24 ± 12 %. Considering average Ca concentrations for monsoon (416 µM) and groundwater (574 µM) samples (Table 3.1.-3.2.), this fractional Ca value accounts for a water supply of 18 ± 9 % via groundwater to the Mahanadi River during low flow stage. This estimate may only be considered as a first-order approximation of groundwater supply to this basin, as several assumption involving seasonality in weathering, minimal groundwater flow during high flow stage, and water chemistry needs to be ascertained further.

3.3.2. Source apportionment and erosional rate estimations

River water chemistry is controlled by solute supply from atmospheric deposition, anthropogenic supplies, and bed rock dissolution. The dissolved cations and anions in rivers, therefore, must be corrected for atmospheric and anthropogenic sources to investigate the weathering processes. We have adopted the approach of Das et al., (2005) to correct for the atmospheric contributions. This approach uses Cl concentrations and its elemental ratios for rainwater correction, as the two major rock-types (silicate and carbonates) are void of chlorides. The average Cl concentration for the rainwater samples (Table 3.2.), excluding one outlier with high Cl concentration (117 µM), is 20 ± 11 µM. Considering an evapotranspiration factor of ~ 0.5, the maximum Cl supply from rain ($Cl_{critical}$) to the river system is 40 µM. The remaining amount of riverine chloride may be derived from halites, saline soils and anthropogenic sources, if any. These additional sources are also assumed to be of NaCl type (Negrel et al., 1993). The rain contribution to the concentration of element (X) is computed (Negrel et al., 1993) using the following equation:

$$X^* = X_{riv} - Cl_{critical} \times \left[\frac{X}{Cl}\right]_{rain} \quad (3.3)$$

The subscripts, *riv* and *rain*, stand for riverine and rain compositions respectively. The rain-corrected $\delta^{34}S_{SO4}$ value is computed as:

$$(\delta^{34}S_{SO4})^{*} = \frac{(\delta^{34}S_{SO4})_{riv} - (\delta^{34}S_{SO4})_{rain} \times f}{(1-f)} \quad (3.4)$$

where, *f* represents the fraction of sulfate supplied by rain. The $\delta^{34}S_{rain}$ stands for the average rainwater $\delta^{34}S_{SO4}$ value (11 ± 2 ‰), which was constrained using the earlier reported values for peninsular India (Table 3.3.; Jacks et al., 1994).

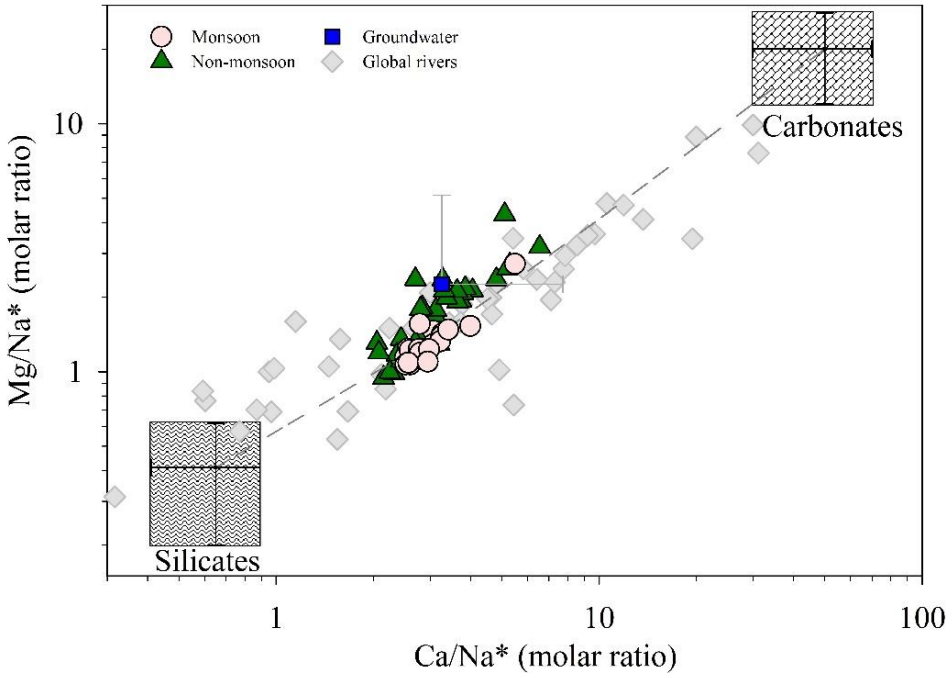

Figure 3.8. *Mixing plot between Ca/Na* and Mg/Na* ratios indicates dominant solute supplies through silicate and carbonate erosion to the basin. For reference, compositions of the global river waters are also shown (Gaillardet et al., 1999). The end-members for the silicate (see, Table 3.4.) and carbonates (Gaillardet et al., 1999) are from literature. Error shown for the groundwater reflects for the data spread.*

The rain corrected nitrates in rivers are largely supplied through fertilizers, and domestic and industrial effluents. Therefore, we have assumed that all the riverine nitrates, after rain-correction, is expected to be supplied through anthropogenic sources. Computations involving Eq. (3.3) show that the rain alone can supply nitrate up to 58 µM, which is higher than the average NO_3 for the samples (26 ± 13 µM; Table 3.1.) and hence, no additional NO_3 source is required. This observation clearly demonstrates that the anthropogenic input to this large tropical river system is not significant. We, therefore, have used the rain-corrected

chemical and isotopic data to compute the CO_2 uptake (via silicate weathering and organic burial), and release (via oxidation of sulfides and organic matter) rates.

3.3.2.1. Estimation of CO_2 uptake rates

3.3.2.1.1. Silicate weathering

Carbonic acid-mediated weathering of silicate minerals is an important sink for atmospheric CO_2. This consumption rate for river basins can be quantified using their water chemistry, after correcting for atmospheric deposition. The Mahanadi basin is comprised of both silicate and carbonate rock-types (Fig. 2.5.). The silicate rocks present in the basin, as mentioned in an earlier section (cf. section 2.2.1.), include (i) Archean granite and gneisses, (ii) Charnockite and Khondalites from the Eastern Ghats, and (iii) clastic sedimentary rocks in the Chhattisgarh and Gondwana basins. The limestone and dolostones from the Chhattisgarh and Gondwana basins are the major carbonate lithologies from the basin.

Table 3.4. *Average chemical compositions for silicate end-members for the basin.*

Endmembers	**Ca/Na**			**Mg/Na**			**Counts**	**Reference**
	Min	*Max*	*Average*	*Min*	*Max*	*Average*		
Singhbhum Granites	0.2	0.4	0.30 ± 0.1	0.08	0.16	0.12 ± 0.04	3	[1]
Granite (Eastern Ghats)	0.4	1.2	0.7 ± 0.3	0.3	1.0	0.6 ± 0.2	9	[2-4]
Charnockite (Eastern Ghats)	0.3	1.2	0.8 ± 0.3	0.1	1.0	0.5 ± 0.3	13	[2-4]
Bed sediments (Mahanadi)	0.2	5.9	0.8 ± 1	0.1	2.0	0.4 ± 0.5	18	[5]
Average	0.65 ± 0.24			0.41 ± 0.21			4	This study

[1]: Saha, 1994; [2]: Narayana et al., 1999; [3]: Paul et al., 1990; [4]: Rao and Rao 1988; [5]: Bastia et al., 2020

A recent study (Acharya et al., 2022), based on spatial data of dissolved major ions and $^{87}Sr/^{86}Sr$ ratios of the Mahanadi River, has documented dominancy of carbonate weathering in supplying cations to the basin (Chakrapani and Subramanian, 1990; Bastia and Equeenuddin, 2019). Consistently, our data also fall closer to the HCO_3 apex in a ternary plot for anions, which indicates dominant role of carbonic acid-mediated weathering of silicates and carbonates. Further, the slope (~ 1.0; n = 65; r^2 = 0.97) of the linear regression trend between Ca+Mg and HCO_3 (Fig. 3.2.) concentrations (in Eq. units) is also closer to the expected (1:1) line for CO_2-mediated silicate and carbonate weathering. We have also investigated the binary mixing plot between Ca/Na* and Mg/Na* ratios for a qualitative source apportionment (Fig. 3.8.). In this plot, the elemental ratios of the river water are compared with that of their major

sources. The representative Ca/Na (50 ± 20) and Mg/Na (20 ± 8) ratios for the carbonate rocks have been reported earlier (Gaillardet et al., 1999) and are used in this study. These elemental ratios for silicate rocks from the Mahanadi River basins, however, show wide variation (Table 3.4.). For instance, average Ca/Na and Mg/Na (molar) ratios for the Singhbhum granites (0.30 ± 0.1, 0.12 ± 0.04; Saha, 1994), Charnockites from Eastern Ghats (0.8 ± 0.3, 0.5 ± 0.3; Narayana et al., 1999, Paul et al., 1990, Rao and Rao 1988), Gondwana shales (8 ± 10, 20 ± 12; Ray and Paul, 2021) and Mahanadi bed sediments (0.8 ± 1, 0.4 ± 0.5; Bastia et al., 2020) vary significantly. In this study, mean of these Ca/Na (0.65 ± 0.24) and Mg/Na (0.41 ± 0.21) ratios (cf. Table 3.4.) have been used as end-member composition for the silicate sources.

A forward method approach (Krishnaswami et al., 1999; Galy and France-Lanord, 1999) has been adopted to quantify the solute contribution from weathering of silicates and carbonates to the Mahanadi River. We have assumed that the rain-corrected K concentrations are supplied by both cation exchange processes (Tipper et al., 2021) and silicate dissolution. Further, a part of riverine Na* may also be supplied by saline soils and/or halites with NaCl-type composition (Rai et al., 2010). Appreciable solute supply from these sources is evident from low contribution (21 ± 13 %) of rain to the Cl concentrations, which requires an additional source for the remaining (~ 79 %) amount of riverine Cl. Recognizing this, we have computed the silicate-derived Na ($Na_{silicate}$) as follows:

$$Na_{silicate} = (Na_{riv} - Cl_{riv}) - Na_{exchange} \quad (3.5)$$

$$K_{silicate} = K^{*} - K_{exchange} \quad (3.6)$$

Table 3.5. *Concentrations data for exchangeable cations of suspended sediments.*

Sample ID	Date of sampling	Na	K	Ca	Mg	Cation Exchange Capacity (CEC)	β_{Na}	β_{K}	β_{Ca}	β_{Mg}
		(wt %)				(mEq/100g)	(mEq/100g)			
PKSS-20/01	26-07-2020	0.16	0.11	0.60	0.10	48	0.14	0.06	0.62	0.17
PKSS-20/05	28-08-2020	0.17	0.12	0.62	0.10	50	0.15	0.06	0.62	0.16
PKSS-20/06	30-08-2020	0.16	0.11	0.58	0.09	46	0.15	0.06	0.62	0.17
PKSS-20/07	06-09-2020	0.15	0.11	0.65	0.10	50	0.13	0.06	0.64	0.17
PKSS-20/10	27-09-2020	0.16	0.10	0.52	0.09	43	0.16	0.06	0.61	0.17
PKSS-20/11	04-10-2020	0.15	0.10	0.56	0.10	46	0.14	0.06	0.62	0.19

Marine sedimentary rocks are often characterized with high fraction of exchangeable amount of Na (β_{Na} ~ 0.6) than river sediments (with low β_{Na} ~ 0.017 and high β_{Ca} ~ 0.81) in their exchangeable pool, and hence, release Na and K to river water during ion-exchange processes (Tipper et al., 2021). Our data show that the average CEC (47 ± 3 meq/100g; cf.

Table 3.5.), and β_{Na} (0.15 ± 0.01) and β_K (0.06 ± 0.003) values for the Mahanadi suspended sediments match well with that reported for global rivers (Tipper et al., 2021). Considering earlier reported SPM (110 ± 34 mg/L; Bastia and Equeenuddin, 2016) load, the $Na_{exchage}$ (7.5 ± 0.4 μM) and $K_{exchange}$ (3.1 ± 0.2 μM) values for the Mahanadi River are computed using Eq. (3.5-3.6). The $Na_{exchange}$ accounts for only 4 % of the average Na* value, which is comparable to that reported for the Ganga (9 %) and Brahmaputra (8 %) River basins, but lower than that reported as an average for global rivers (12-28 %; Tipper et al., 2021). The riverine Ca and Mg can be supplied by both silicate and carbonate weathering. The silicate-derived Ca ($Ca_{silicate}$) and Mg ($Mg_{silicate}$) abundances are computed assuming congruent dissolution of silicate rocks.

$$Ca_{silicate} = Na_{silicate} \times \left[\frac{Ca}{Na}\right]_{silicate} \quad (3.7)$$

$$Mg_{silicate} = Na_{silicate} \times \left[\frac{Mg}{Na}\right]_{silicate} \quad (3.8)$$

The remaining amount of Ca and Mg in these samples are considered to be supplied through carbonate dissolution. The carbonate-derived Ca (Ca_{carb}) and Mg (Mg_{carb}), therefore, are estimated as:

$$Ca_{carb} = Ca^* - Ca_{silicate} \quad (3.9)$$

$$Mg_{carb} = Mg^* - Mg_{silicate} \quad (3.10)$$

This computation yields relative cationic contributions from silicate ($Cat_{silicate}$), which varies between 265 and 814 μE, with an average contribution of 34 ± 7 %. The average $Cat_{silicate}$ (in %) for monsoon (36 ± 5 %) and non-monsoon (33 ± 8 %) samples are observed to be similar, indicating minimal seasonal change in the silicate dissolution. The $Cat_{silicate}$ values are lower than the carbonate-derived cations (Cat_{carb}), which range from 487 to 1955 μE, with a discharge-weighted Cat_{carb} value of 908 ± 753 μE. High cation supply from carbonates is consistent with its faster dissolution kinetics than the silicate minerals. The discharge-weighted $Cat_{silicate}$ value of these samples (503 ± 319 μE) corresponds to a CO_2 consumption rate of (2 ± 1) × 10^5 mol/km^2/yr, or 2.4 ± 1.6 tC/km^2/yr. These rate estimates are comparable to those reported for some of the peninsular Indian Rivers, such as Krishna (3.6 × 10^5 mol/km^2/yr; Das et al., 2005), Godavari (5.8 × 10^5 mol/km^2/yr; Jha et al., 2009), Nethravati (2.9 × 10^5 mol/km^2/yr; Gurumurthy et al., 2012), and Kaveri (3.83 × 10^5 mol/km^2/yr; Pattanaik et al., 2013). The CO_2 uptake rate for the Mahanadi basin, however, is about two times higher than the global average value (0.9 × 10^5 mol/km^2/yr; Gaillardet et al., 1999). High silicate weathering and related CO_2 uptake in this basin is consistent with its silicate-dominated lithology (Fig. 2.5.) and tropical climate with high temperature and runoff.

3.3.2.1.2. Burial of organic carbon

The organic matter (OM) transported by rivers and their ultimate burial in sedimentary basins serve as another sink for atmospheric CO_2 over longer timescales (France-Lanord and Derry, 1997). The OM in river sediments can either be supplied from sedimentary rocks present in the basin and/or biogenic components of living/dead organisms (Galy et al., 2015). The burial of rock-derived organic carbon (OC_{petro}) mostly reflects relocation of material from the continents to sea, and does not influence the carbon cycle. In contrast, the burial of biogenic organic carbon (OC_{Bio}) has a negative effect on the atmospheric CO_2 budget. In this study, we have used available literature data to compute the carbon burial rate for the Mahanadi basin. This rate estimation was carried out using the following equation (after Hilton et al., 2008):

$$J_{Burial} = \left(\left(\frac{SPM \times Q}{A}\right) \times TOC \times f_{Bio} \times f_{Burial}\right) \quad (3.11)$$

where, SPM and TOC stand for concentrations of suspended sediments and organic carbon, respectively. The terms, Q and A reflect the water discharge and drainage area of the basin. The f_{Bio} and f_{Burial} stand for fraction of biogenic component in the TOC, and efficiency of organic burial in the sedimentary basin respectively. Bastia and Equeenuddin (2016), based on 20-years (2000-2020) sediment load data, have estimated the sediment load ($(12 \pm 5) \times 10^6$ tons/yr) and flux (95 ± 39 tons/km^2/yr) for the Mahanadi outflow, which has been used in the present calculation. Gupta et al. (2008) have reported the TOC (1.40 - 1.97 wt%) for four Mahanadi distributaries during the monsoon season. We have used the average TOC (1.7 ± 0.3 wt%) value of these samples for the burial rate estimation.

The fraction of biogenic component (f_{Bio}) is calculated using a stable carbon isotopic balance approach (Hilton et al., 2008), as radiocarbon data for this river sediment are not available. The Mahanadi distributaries supply sediments to the northern sectors of the Chilika lagoon (Fig. 2.5.). Mukherjee et al. (2019) have reported an average $\delta^{13}C$ value of (-26.1 ± 2.7 ‰) for organic fractions of suspended sediments for this sector, which can be used as a representative value for the Mahanadi sediments ($\delta^{13}C_{riv}$) at its outflow. The $\delta^{13}C$ for the vegetation is constrained using $\delta^{13}C$ values reported for surface (soil) litter from the Chhattisgarh basin (-28.7 ± 0.3 ‰; Laskar et al., 2016). These regions are mostly dominated by medium to large sized C3 plants. There exists limited organic carbon isotopic data for the sedimentary rocks of the Mahanadi basin. The $\delta^{13}C$ data for eight (shale/limestone) rock

samples from the Chhattisgarh Supergroup constrain the average TOC (1.1 ± 1.3 wt%) and $\delta^{13}C$ (-25.6 ± 3.2 ‰) value for the rock-derived organic material for the basin (Banerjee et al., 1992). Assuming that the $\delta^{13}C$ of rivers (~ - 26.1 ‰) is controlled by OM supplied by rocks (~ - 25.6 ‰) and biogenic components (~ - 28.7 ‰), the f_{Bio} for this basin is calculated to be 0.16. This estimated f_{Bio} value, however, is associated with large uncertainty mainly due to $\delta^{13}C$ variability in rock and riverine sediments. We have also compared the TOC values for the bedrock (~ 1.1 wt%; Banerjee et al., 1992) and suspended sediments (~ 1.7 %); the difference between these two (0.6 wt%) values should reflect the TOC enrichment in sediments, which may be attributed as the biogenic component present in basin (Hilton et al., 2008). This estimation, although yields a f_{Bio} value of ~ 0.35, can only serve as a first-order approximation as no corrections for size sorting, sediment dilution from different sub-basins and variability in TOC values have been considered. We have used an average value of the two f_{Bio} values (0.26 ± 0.13) computed using isotopic (~ 0.16) and TOC mass balance (~ 0.35) approaches for the Mahanadi basin. This approximate f_{Bio} estimate although fall within the earlier reported range (0.21 to 0.98; Hilton and West, 2020 and references therein) for global rivers, the average f_{Bio} value for the Mahanadi River (~ 0.35) is lower by two times than the global average (0.71 ± 0.19; Hilton and West, 2020). In absence of proper f_{Bio} estimation, we have estimated the oxidation rate for both f_{Bio} for Mahanadi (~ 0.35) and global river (~ 0.71) data.

The burial efficiency of terrestrial organic matter has been reported to be higher in basins with high physical erosion rates (Galy et al., 2015). The f_{Burial} values show significant spatial variation depending on sedimentation rate and type of organic matter supplied by the rivers (Emerson and Hedges, 1988; Canfield, 1994). In absence of similar data for the Mahanadi basin, we have used f_{Burial} values (30 - 100 %), similar to that used in earlier studies (Galy et al., 2015; Hilton et al., 2015). Using these data in equation (3.11) and f_{Bio} value of 0.35, the amount of biogenic carbon from the Mahanadi basin that gets buried is estimated to vary between 0.13 ± 0.07 (for f_{Burial} ~ 30 %) and 0.42 ± 0.22 (for f_{Burial} ~ 100 %) tC/km^2/yr. These estimates correspond to an average burial rate of 0.27 ± 0.12 tons/km^2/yr (for f_{Bio} ~ 0.35) and 0.55 ± 0.24 tons/km^2/yr (for f_{Bio} ~ 0.71) for the Mahanadi. This rate is systematically lower than the biospheric carbon flux reported for the Ganga-Brahmaputra (1.45-5.90 tC/km^2/yr), Godavari (1.47 tC/km^2/yr) and global-average (1.46 tC/km^2/yr) for river basins (Galy et al., 2015 and references therein). Further, this CO_2 consumption rate via organic burial is about ~ 10 times lower compared to that estimated for silicate weathering (2.4 ± 1.6 tons/km^2/yr) for the basin. Our observed organic burial rate, however, is consistent with that reported for river basins (0.06-1.16; 0.42 ± 0.34 (n = 19) tC/km^2/yr (excluding one outlier)) with low suspended

yield (<100 ton/km^2/yr; Galy et al., 2015), underscoring importance of physical erosion in regulating the carbon burial in the basin.

3.3.2.2. Estimates of CO_2 release rates

3.3.2.2.1. Sulfide oxidation

Oxidation of sulfide minerals and subsequent dissolution of carbonates through sulfuric acid releases CO_2 to the atmosphere. This source influences the long-term CO_2 cycle on a timescale (<10 Myrs) within which the seawater sulfate removed as sedimentary sulfide or gypsum. Quantifying this oxidation pathway requires source apportionment of riverine sulfate, which may be sourced from multiple sources (rain, pollution and weathering of gypsum/pyrite). The rain-derived sulfate for the Mahanadi samples have been computed using Eq. (3.3). These results show that the fraction of SO_4 derived from rain varies between 0.26 and 0.97, with an average fractional value of 0.41 ± 0.13. Rain-corrected $\delta^{34}S_{SO4}$ values are computed using Eq. (3.4) and earlier reported rain $\delta^{34}S_{SO4}$ values for locations from the peninsular India (11 ± 2 ‰; Table 3.3.). The $\delta^{34}S_{SO4}$* values vary from 7.0 to 19.1 ‰, and its average value (14 ± 3 ‰) shows no significant change from the measured $\delta^{34}S_{SO4}$ (13 ± 2 ‰) values.

The rock-derived component of sulfate concentrations varies between 19 and 93 µM with an average value of 58 ± 23 µM. This SO_4 component, on average, accounts for 63 % of total riverine sulfate of the Mahanadi River. The $\delta^{34}S_{SO4}$ value reflects the relative sulfur contributions from the major sulfate sources, viz. gypsum, and pyrites. Typically, the $\delta^{34}S$ value of the gypsum minerals are closer (or depleted by ~ 1.6 ‰) to the seawater isotopic value during the mineral formation, whereas the $\delta^{34}S$ of pyrites is heavily (~ 30 ‰) lower due to isotopic fractionation during microbial reduction process. This distinct $\delta^{34}S_{SO4}$ value for gypsum and pyrites allow reliable source apportionment for riverine sulfate (Burke et al., 2018). Table 3.1. compiles the expected $\delta^{34}S_{SO4}$ values for various sources for the Mahanadi basin. The average $\delta^{34}S$ values for the magmatic pyrites (- 0.2 ± 3.2 ‰) and the coal deposits (2 ± 6 ‰) are found depleted with respect to the $\delta^{34}S$ of the gypsum minerals (12 ± 3 ‰) from the peninsular Indian regions (Table 3.3.). However, the $\delta^{34}S$ of the sedimentary pyrites for the basin is found comparable or, enriched than the gypsum $\delta^{34}S$ values, making it difficult to use $\delta^{34}S_{SO4}$ for sulfate source apportionment for this basin. These unexpectedly heavy $\delta^{34}S$ values for the Precambrian sedimentary pyrites have been linked to high pyrite burial in low-sulfate reducing oceanic basins (Sarkar et al., 2010). In absence of distinct source composition, we have assumed two sulfate sources: (i) sulfides including the magmatic pyrites and Gondwana

coal with an average $\delta^{34}S$ value of 0.9 ± 2 ‰, (ii) combined source of heavy $\delta^{34}S$ values (20 ± 10 ‰), including both gypsum and sedimentary pyrites. The former source has only been used further for sulfide oxidation rate estimation, although we recognize that sedimentary pyrite is also a major sulfide source for the basin. Hence, our calculation based on sulfur isotopes computes minimum amount of SO_4 derived from sulfide oxidation. With this assumption, we have computed the fraction of sulfates derived via sulfide oxidation using the following isotopic balance equation:

$$(\delta^{34}S)_{Riv} = (\delta^{34}S)_{Pyrite} \times f + (\delta^{34}S)_{Gypsum} \times (1 - f) \quad (3.12)$$

where, f stands for the fraction of sulfide-derived sulfates in the sample. This computation estimates that the sulfide-derived sulfates in the Mahanadi samples vary between 3 and 33 µM with an average of 15 ± 8 µM. Average of these values for monsoon (21 ± 10 µM) and non-monsoon (13 ± 6 µM) samples are found overlapping. The discharge-weighted sulfide-derived sulfate concentrations is found to be 19 ± 19 µM which is about an order of magnitude lower than the global average for riverine sulfates (~ 100 µM). The CO_2 release rate through sulfuric-acid-mediated carbonate weathering (Hilton and West, 2020) is computed using the following equation:

$$J_{sulfide} = SO4_{sulfide} \times \left(\frac{Cat_{carb}}{(Cat_{silicate}+Cat_{carb})}\right) \times Q/A \quad (3.13)$$

The estimated CO_2 release rate for the Mahanadi (0.1 ± 0.1 tC/km^2/yr) is found few times lower than that reported for other basins (Ganga-Brahmaputra (0.66 tC/km^2/yr; Galy and France-Lanord, 1999), and Mackenzie (0.71 tC/km^2/yr; Calmels et al., 2007) and Kaoping (Taiwan) (28.8 tC/km^2/yr; Das et al., 2012)). Low sulfide oxidation in this supply-limited basin is mainly due to lower fraction of sulfate (~ 16 %) supplied by pyrite oxidation than other river basins, such as the Mackenzie (~ 85 %; Calmels et al., 2007) and the Kaoping (~ 85 %; Das et al., 2012). The sulfide oxidation and corresponding CO_2 release associated with carbonate dissolution from the Mahanadi (0.02 MtC/yr) is about 0.04 % of the corresponding global flux (40 MtC/yr; Hilton and West, 2020), which is lower by 3-4 times than its fractional area (0.13 %) and water discharge (0.15 %) of global riverine data. In contrast, the sulfide-SO_4 flux from the Mackenzie River supplies about 20-27 % of global riverine flux from an area of 2 % of global area. The disproportionally higher sulfide oxidation rate for the Mackenzie basin has been linked to continuous exposure of reactive phases via physical erosion in the basin (Calmels et al., 2007). The physical erosion in the Mahanadi basin is low, as evident from low amount of total suspended sediment (110 ± 34 mg/L; 20-year average data (Bastia and Equeenuddin, 2016)). This sediment data corresponds to annual flux of (12 ± 5) × 10^6 tons/yr,

which is only ~ 0.1 % of the global riverine sediment flux (18×10^9 tons/yr) from an area of 0.13 % of total global drainage area (Milliman and Syvitski, 1992). Low physical erosion rate in the basin, therefore, may explain the observed lower sulfide oxidation rate. Further, the basin lithology for this river (and other from the peninsular Indian regions) mainly drain through Precambrian silicates (granitic and gneissic rocks), which may also not contribute to sulfide oxidation. This is evident from higher Si/SO_4 (2.87; Table 3.1.) and lower SO_4/HCO_3 (0.06; Table 3.1.) ratios for the Mahanadi River compared to that for global rivers (2.83 and 0.18, respectively; Gaillardet et al., 1999). These ratios mostly indicate that the river chemistry is mainly dominated by silicate dissolution with minimal sulfide oxidation, which is consistent with its basin lithology.

3.3.2.2.2. Organic oxidation

Oxidation of petrogenic carbon is another long-term source of atmospheric CO_2. This release rate for a river basin can be estimated using both direct (Soulet et al., 2018; Roylands et al., 2022) and indirect (Dalai et al., 2002b) approaches. In the direct approach, the amount of CO_2 released from a rock chamber is measured in-situ to assess the oxidation rate at a local-to-regional scale. For a basin-wide estimation, riverine rhenium concentrations have served as a reliable proxy for organic oxidation (Dalai et al., 2002b; Hilton et al., 2014). The Re concentrations of organic-rich sedimentary rocks are often found to be high due to its strong affinity to form organo-metallic complexes during its removal from water columns. During oxidative weathering processes, this trace element gets mobilized to dissolved phases by forming perrhenate (ReO_4^-) ions. The rate of the petrogenic OM, therefore, can directly be linked to Re abundance in river waters (Dalai et al., 2002b) to compute the CO_2 release rates. We have used our earlier reported rhenium data for these samples (Danish et al., 2021) to estimate the organic oxidation and corresponding CO_2 release rate for the Mahanadi basin. Re concentrations at this location vary from 1.7 to 12 pmol/kg, with an average value of 5 ± 3 pmol/kg (n = 30). The discharge-weighted Re concentration is 5.1 pmol/kg. The lowest Re concentration is observed for a low flow sample (December), whereas the highest Re concentration is observed for a monsoon sample (July). In general, higher rhenium concentrations are observed for samples with higher water level (Fig. 3.3.). This seasonal trend is in clear contrast to that observed for Alpine (Hilton et al., 2021) and Himalayan (Rahaman et al., 2012) catchments, where a negative correlation between Re and runoff has been observed. These earlier reported negative Re-runoff relationships have been attributed to higher release of rhenium during longer water-rock interaction time during low flow stages (Hilton et

al., 2021). Although the exact cause for the difference in seasonal Re trend is not known, groundwater supply with lower Re (1.4 ± 0.7 pmol/kg (excluding two outliers with high Cl- value > 6000 μM; Table 3.2.) concentration than the riverine Re data (~ 5.1 pmol/kg) may contribute to the observed trend for the Mahanadi. These lower concentrations in groundwater can be linked to subsurface rhenium removal in the prevailing redox (sulfidic and methanogenic) zones in the aquifers (Mukherjee and Fryer, 2008). These samples with lower rhenium concentrations are also characterized with high silica and Mg concentrations, further ascertaining the groundwater influx during the low flow stages. Our concentration-discharge relationship for major ions with higher concentration during low flow stages also indicates larger solute supply via groundwater during non-monsoon periods (Fig. 3.6. B). A similar process with larger groundwater influx during non-monsoon season with lower rhenium concentration may partly explain the broad seasonal Re trend. Water rhenium concentration is mainly regulated by weathering of bedrocks.

Table 3.6. *Average compositions of possible major sources (silicates (granites), sulfides (pyrite) and organic-rich shales (OC)) for dissolved rhenium.*

End members	Re (pg/g)	Na (wt%)	S (ppm)	Re/Na (pmol/μmol)	Re/S (pmol/μmol)	Ref.
Silicates	148 ± 16	0.7 ± 0.3	621	0.003 ± 0.001	0.041 ± 0.004	[1,2,3]
Pyrite	4,800 ± 1,431	0.17 ± 0.1	532,000 ± 7,000	0.35 ± 0.23	0.002 ± 0.0005	[4,5]
OC	76,751 ± 106,315	0.21 ± 0.05	21,667 ± 16,609	4 ± 6	0.61 ± 0.97	[6,7]

[1]: Danish et al., 2021; [2]: Bastia et al., 2020; [3]: Rudnick et al., 2003; [4]: Tripathy and Singh, 2015; [5]: Lin et al., 2022; [6]: Sheen et al., 2018; [7]: Pandalai et al., 1991.

As mentioned earlier, the lithology of the Mahanadi basin is comprised of silicate (Charnockite and granite and gneisses) rocks, black shales and coal deposits (cf. section 2.2.1.); all these rock-types are expected to supply rhenium to the river water. We have employed a forward approach to apportion the rhenium contribution for these end-members. We have constrained the end-member compositions by compiling Na/Re and S/Re data for major sources (Table 3.4.). For silicates, the reported Re (Danish et al., 2021) and Na (Bastia et al., 2020) concentrations for Mahanadi sediments, and S concentrations for the upper continental crust (Rudnick et al., 2003) have been used. For sulfide end-member, the Re and Na concentrations for the pyrites (Tripathy and Singh, 2015) from the Vindhyan Supergroup and typical S concentrations for pyrites (Lin et al., 2022) have been used. For OM sources, the average Na and S concentrations for the Vindhyan shales (Pandalai et al., 1991; Tripathy and Singh, 2015) and typical rhenium concentrations for ancient organic-rich shales (Sheen et al., 2018) have been used. Figure 3.9. B compares the Na*/Re and S*/Re ratios of these samples with their

possible major sources. This clearly depicts that rhenium concentrations in these samples are regulated by solute supply from all these sources. We have computed the rhenium contributions from all these sources using the following mass balance equation:

$$\begin{pmatrix} Na/Re \\ S/Re \\ 1 \end{pmatrix}_{riv} = \begin{pmatrix} Na/Re_{sil} & Na/Re_{py} & Na/Re_{oc} \\ S/Re_{sil} & S/Re_{py} & S/Re_{oc} \\ 1 & 1 & 1 \end{pmatrix} \begin{pmatrix} f_{sil} \\ f_{py} \\ f_{oc} \end{pmatrix} \quad (3.14)$$

where, the subscripts *sil*, *py* and *oc* stand for the silicate, pyrite sources, and organic oxidation respectively. This computation indicates that 58 - 96 % (average: 85 ± 10 %) of rhenium in these samples are supplied through organic oxidation in the basin. The average supply of rhenium from other sources, such as silicates (13 ± 8 %) and sulfides (2 ± 2 %), are found to be very minimal. The discharge weighted organic oxidation-derived Re concentrations (5.1 pmol/kg) and water discharge (57×10^{12} L/yr) at the Mahanadi outflow indicates that 291 mol/yr of rhenium, is being supplied to the Bay of Bengal. We have used this flux to compute the corresponding CO_2 release rate (J_{OC}) using the following equation (modified after Hilton et al., 2014):

$$J_{OC} = \left[Re_{OC} \times \left(\frac{OC}{Re}\right)_{BS} \times f_{petro} \times f_c \times (1 - f_{graphite})\right] \times \frac{Q}{A} \quad (3.15)$$

Here, the $(OC/Re)_{BS}$ stands for the organic-rich shale composition, whereas f_{petro} and $f_{graphite}$ stand for fraction of rock-derived OC and graphitic OC respectively. The f_c reflects the ratio of OC loss to rhenium loss during weathering of organic-rich rocks. Precise data for these parameters are expected to vary widely and hence, are not well constrained, which in turn can introduce large uncertainties in the rate estimates. The $(Re/OC)_{BS}$ ratio (~ 3.5×10^{-7}) is constrained from Tripathy and Singh (2015). This ratio is comparable to that reported for other river basins (Horan et al., 2019 (0.4-6.03 $\times 10^{-7}$); Dalai et al., 2002b (5×10^{-8})). There exists no data for the amount of graphite present in these sediments. In absence of this information, we have measured the weight loss of river sediment (Danish et al., 2021) due to combustion between 375 and 950 °C to get a qualitative assessment of resistant organic phases. In this approach, we assume that the resistant OM get combusted only in 375-950 °C, which may provide a first-order approximation of graphite present in the sediments. These data yield a $f_{graphite}$ value of 6 ± 3 %, and have been used in this study. We have used an average f_c value (64 ± 39 %) based on carbon to rhenium loss observed for a weathering profile developed on an organic-rich shale (Peucker-Ehrenbrink and Hannigan, 2000) for our calculation. These values yield a CO_2 release rate of 0.50 ± 0.57 tC/km^2/yr via organic oxidation in the Mahanadi basin. This oxidation rate is although well within reported rates for other river basins (Hilton and West, 2020), it is lower by a few times than that reported for Ganga and Yamuna (~ 4

tC/km^2/yr) Rivers (Dalai et al., 2002b).The estimated CO_2 flux through OC oxidation in the Mahanadi basin, which accounts for ~ 0.13 % of global area, is 0.7 × 10^5 tons/yr. The corresponding global flux varies between 40 and 100 MtC/yr. The flux of Mahanadi, therefore, accounts for 0.07 - 0.18 % of the global flux, which is similar in rate when normalized to its basin area. This basin is comprised of several coal mines.

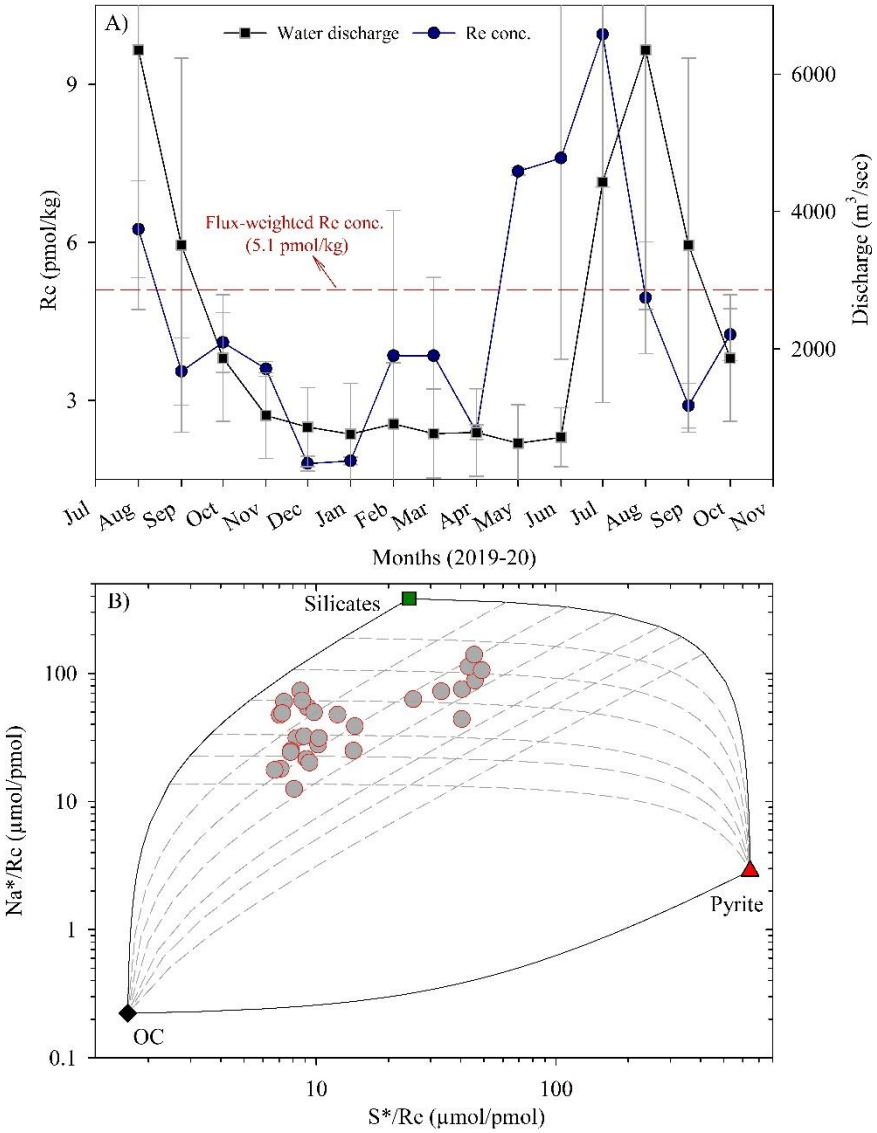

Figure 3.9. *(A) Monthly variation of the rhenium concentrations (Danish et al., 2021) and average water discharge (http://www.grdc.sr.unh.edu) for the Mahanadi River. (B) Source mixing plot for S*/Re and Na*/Re ratios. See text for details on the data for the three possible sources.*

These Gondwana coals are rich in carbon (70 - 76%) with low sulfur (~ 1 %) contents (Mishra et al., 2019), and hence, are likely to contribute to the organic oxidation in the basin. Further, tropical climate with high temperature may also contribute to these rates. The estimated CO_2

release in this basin, although associated with large error, warrants more regional basin studies for precise estimation of global oxidation rate.

3.3.3. Net CO_2 budget for the Mahanadi basin

The dissolved inorganic carbon budget of a river system is controlled by its continental weathering (silicate and carbonate weathering, sulfide and organic oxidation) and ocean-atmosphere output (organic carbon burial, reverse weathering and carbonate deposition) fluxes.

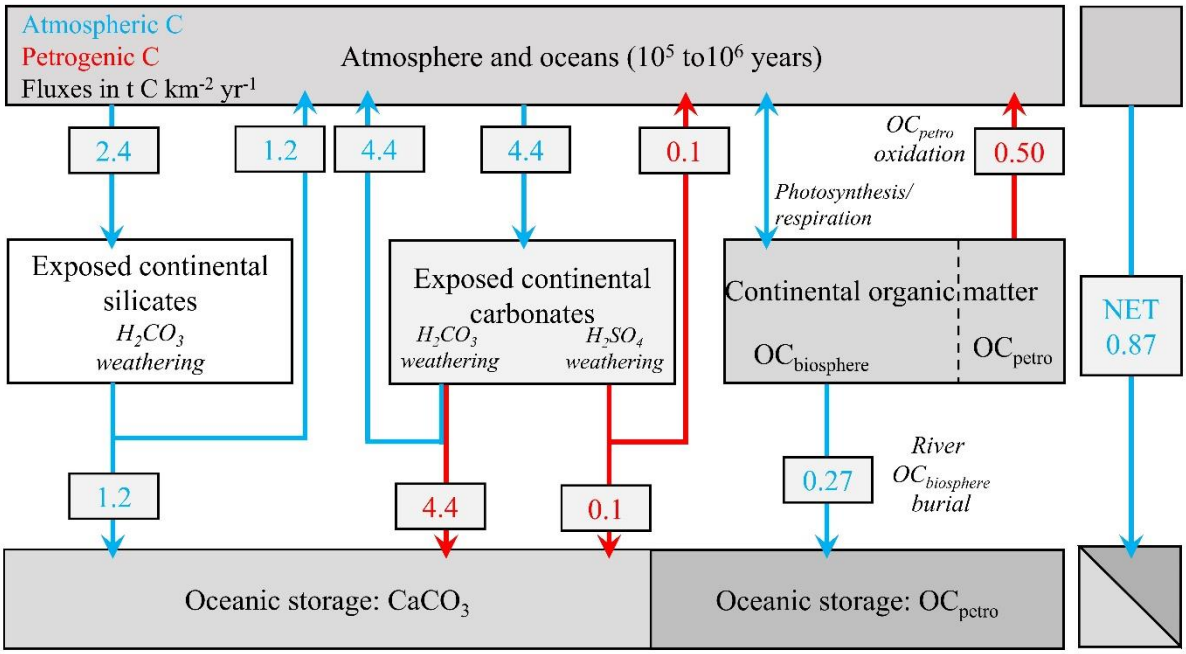

Figure 3.10. *Estimated CO_2 release/uptake rates for silicate and carbonate weathering, organic carbon burial, organic oxidation and sulfide oxidation for the Mahanadi River basin. The figure is adopted from Horan et al., (2019).*

Among these, reverse weathering scavenges riverine solutes (e.g. Na, K and Si) to form authigenic clays in ocean and reduces efficiency of silicate weathering by consuming alkalinity (Isson and Planavsky, 2008). At a global scale, this process removes ~ 20 - 25 % of riverine silica supplied to ocean (Holland, 2005; Treguer and De La Rocha, 2013). Although we recognize importance of this ion-exchange process, our data are not suitable to quantify this ocean alkalinity sink. Further, the H_2CO_3 acid-mediated carbonate weathering also supplies dissolved inorganic carbon to the ocean-atmosphere system. The transient CO_2 consumption through this process, however, is only relevant in shorter period and does not contribute to the global carbon cycle on longer timescales. The average CO_2 consumption rate via carbonate weathering for the Mahanadi is 4.4 ± 3.7 tC/km^2/yr (Fig. 3.9.) with highest (12 ± 2 tC/km^2/yr)

for August and lowest (0.44 ± 0.01 tC/km^2/yr) for the month of December. This observed consumption rate for the carbonate is expectedly higher than the silicate weathering rate due to faster dissolution kinetics of carbonate minerals. Figure 3.10. compares the CO_2 consumption rate via silicate weathering (2.4 ± 1.6 tC/km^2/yr) and organic burial (0.27 ± 0.12 tC/km^2/yr), and CO_2 release rate via organic (0.50 ± 0.57 tC/km^2/yr) and sulfide (0.1 ± 0.1 tC/km^2/yr) oxidation for the Mahanadi basin. These estimates clearly establish dominant role of two processes (silicate weathering and organic oxidation) on the carbon cycle for the basin. Available limited data on four weathering rates for river basins (Hilton and West, 2020) have shown that basins with high sulfide and organic oxidation serve as a net source of CO_2. The Mahanadi River acts as a net CO_2 sink mainly due to dominancy of silicate erosion and low sulfide oxidation (Fig. 3.10.). As discussed earlier, low sulfide oxidation in this supply-limited basin is possibly linked to low physical erosion. Earlier studies have documented that the oxidation rates are higher in basins with high physical erosion which promotes continuous exposure of minerals with faster dissolution kinetics (Calmels et al., 2007; Das et al., 2012). In contrast to sulfide oxidation, appreciable amount of CO_2 release via organic oxidation is observed for the basin. The petrogenic-C oxidation is mainly facilitated by lithological occurrences of coal deposits from the Gondwana Supergroups. The silicate weathering rate of the basin is about two times higher than that reported as global average for rivers (Gaillardet et al., 1999). High silicate weathering in the basin is possibly linked to its silicate-dominant lithology (Fig. 2.5.), and tropical climate (high temperature and runoff).

This page has been intentionally left blank.

Chapter 4

Seasonality in pyrite oxidation with flow stage variation of the Indus headwater basin

This page has been intentionally left blank.

This chapter focuses on seasonal variation in the pyrite oxidation pattern of the Indus headwater basin. There exist limited studies that focus on sensitivity of flow stage fluctuations on oxidation rates and related controlling factors. In this study, we collected water samples from the Indus mainstream at Leh, India at weekly interval for a duration of one-year period (cf. chapter 2 for details). These samples were measured for their major ions and $\delta^{34}S_{SO4}$-$\delta^{18}O_{SO4}$ isotopic values. Distribution of major ions was used to constrain the solute sources and their seasonal changes, whereas the isotopic values and their inverse modeling enabled us to quantify the sulfate source(s) contributions. These results were used to assess the role of climatic and geological parameters in regulating the seasonality of weathering intensity of different minerals in this river basin. Outcomes of this study reveal crucial effect of temperature on silicate weathering and subsurface reactive front on pyrite weathering intensity during flow stage variations. Details on elemental co-variations, source apportionment modeling and seasonal changes in weathering type have been discussed here.

4.1. Results

Chemical and $\delta^{34}S_{SO4}$-$\delta^{18}O_{SO4}$ isotopic data for the Indus headwater at Leh are listed in Table 4.1. The dominant cation and anion for these samples are Ca and HCO_3, respectively. On average, the Ca concentrations account for 46 ± 9 % of TZ^+, whereas the HCO_3 corresponds to 68 ± 5 % of TZ^- (Eq. units). The discharge-weighted Ca (557 ± 71 µM) and HCO_3 (1876 ± 240 µM) concentrations are a few times higher than that reported as global average for rivers (297 and 798 µM respectively; Meybeck, 2003). The Na (924 ± 192 µM) and Mg (392 ± 62 µM) concentrations correspond to about one-fourth of the cationic load (28 % and 24 % of TZ^+ respectively). The chloride (Cl) concentrations of these samples vary between 252 µM and 579 µM. The average Cl concentrations (384 ± 80 µM) of these samples are higher by about an order of magnitude than that of rain (26 ± 13 µM; n = 62; Tiwari et al., 2012) and glacier melt (8 ± 5 µM; n = 5, Bhat et al., 2023) waters reported from the nearby regions. Dissolved sulfate concentrations at Leh vary between 181 µM and 554 µM, with an average discharge-weighted value of 293 ± 38 µM. This average value is significantly higher than the global average of SO_4 for rivers (~ 88 µM; Meybeck, 2003). The dissolved load (TDS) of the Indus samples (162 - 371 mg/L) is about two times higher than that of global rivers (92 mg/L; Meybeck, 2003). The TDS values co-vary linearly with the silica concentrations of these samples ($r^2 = 0.62$; $p < 0.01$; n = 33).

Table 4.1. *Time-series chemical and isotopic ($\delta^{34}S_{SO4}$ and $\delta^{18}O_{SO4}$) data for the Indus headwater (at Leh, India) at weekly intervals for a duration of one-year (Sept. 2021 to Sept. 2022).*

Sample ID	Sampling Date	Na	K	Ca	Mg	Cl	NO_3	SO_4	HCO_3	SiO_2	$\delta^{34}S_{SO4}$	$\delta^{18}O_{SO4}$	$\Delta_{SO4-H2O}$*	TDS	TZ^+	TZ^-	NICB
		(µM)									(‰)			(mg/L)	(µEq.)		(%)
IND-22/01	25-09-2021	817	53	859	352	308	20	308	2198	119	-0.70	-5.32	7.3	243	3292	3142	5
IND-22/02	01-10-2021	779	49	815	343	310	20	286	2255	119	-0.61	-3.59	9.1	241	3145	3157	0
IND-22/03	11-10-2021	828	51	885	360	333	24	284	2360	126	-1.11	-4.59	8.1	253	3370	3285	3
IND-22/04	18-10-2021	817	49	867	357	337	24	285	2393	130	-1.87	-4.50	8.2	255	3312	3324	0
IND-22/05	23-10-2021	846	58	848	362	349	25	286	2409	123	0.12	-3.88	8.8	256	3325	3355	-1
IND-22/06	30-10-2021	919	56	932	387	369	25	292	2492	131	0.30	-3.71	8.9	269	3614	3471	4
IND-22/07	13-11-2021	868	56	885	378	352	30	297	2449	137	0.37	-2.01	10.6	263	3449	3424	1
IND-22/08	21-11-2021	894	49	919	382	354	50	305	2462	144	0.84	-1.95	10.7	268	3544	3476	2
IND-22/09	30-11-2021	917	51	917	377	370	40	319	2526	149	-0.30	-2.69	10.0	266	3557	3575	-1
IND-22/10	07-12-2021	904	53	887	372	358	24	299	2469	143	1.25	-1.85	10.8	265	3474	3449	1
IND-22/11	17-12-2021	1016	58	1004	405	391	38	306	2669	165	0.48	-2.46	10.2	289	3891	3711	5
IND-22/12	26-12-2021	1014	60	978	405	408	38	322	2626	164	0.69	-3.55	9.1	287	3841	3716	3
IND-22/13	06-01-2022	951	56	957	371	399	137	318	2584	169	1.06	-2.04	10.6	287	3663	3755	-2
IND-22/14	26-01-2022	884	53	806	337	363	40	288	2222	148	0.83	-4.98	7.7	246	3222	3201	1
IND-22/15	06-02-2022	890	51	812	342	370	40	292	2308	153	0.60	-1.49	11.2	252	3250	3302	-2
IND-22/16	28-02-2022	917	49	828	354	378	56	301	2350	152	-0.12	-2.42	10.2	258	3332	3385	-2
IND-22/17	11-03-2022	848	49	782	328	360	37	283	2126	147	0.58	-2.61	10.0	237	3117	3088	1
IND-22/18	22-03-2022	781	49	742	339	325	34	273	2040	136	0.13	-4.42	8.2	226	2992	2943	2

IND-22/19	01-04-2022	947	53	848	390	408	42	319	2359	148	0.34	-4.05	8.6	263	3476	3447	1
IND-22/20	13-04-2022	949	62	897	383	394	29	317	2425	127	-0.03	-1.78	10.9	267	3572	3483	3
IND-22/21	26-04-2022	1234	135	1284	538	579	24	554	3168	148	-0.19	0.13	12.8	371	5012	4878	3
IND-22/22	15-05-2022	1358	85	854	555	571	17	458	2729	148	1.77	-0.05	12.6	318	4261	4233	1
IND-22/23	25-05-2022	1313	58	509	533	547	19	433	2019	125	2.58	-0.27	12.4	255	3456	3451	0
IND-22/24	11-06-2022	1339	42	363	484	526	27	413	1735	70	2.41	-0.78	11.9	227	3075	3113	-1
IND-22/25	17-06-2022	1333	35	432	482	540	22	434	1855	59	2.92	2.61	15.3	238	3196	3284	-3
IND-22/26	26-06-2022	917	56	880	375	370	20	328	2513	125	0.40	-2.26	10.4	270	3484	3559	-2
IND-22/28	21-07-2022	913	26	299	364	352	27	238	1494	6	1.15	-0.04	12.6	171	2267	2349	-4
IND-22/29	01-08-2022	775	38	379	367	308	27	181	1583	18	0.68	-1.75	10.9	170	2304	2280	1
IND-22/30	11-08-2022	645	60	398	345	296	17	204	1470	5	1.54	-0.72	11.9	162	2190	2191	0
IND-22/31	22-08-2022	730	74	642	413	351	17	339	1904	76	-0.28	-1.74	10.9	220	2913	2950	-1
IND-22/32	02-09-2022	745	65	658	441	366	16	336	2002	20	0.99	-2.54	10.1	226	3009	3055	-2
IND-22/33	10-09-2022	791	72	432	406	384	71	319	1482	4	2.47	-1.51	11.1	187	2539	2575	-1
IND-22/34	18-09-2022	605	42	726	297	252	19	302	1844	104	-2.57	-5.88	6.8	206	2694	2719	-1

**Computed assuming the $\delta^{18}O_{H2O}$ of reactive water to be same as the annual (amount-weighted) average $\delta^{18}O_{H2O}$ value for rain at Leh (Lone et al., 2019). Here, NICB stands for Normalized Inorganic Charge Balance.*

The silica concentrations vary widely between 4 and 169 µM, and the corresponding discharge-weighted average value (63 ± 8 µM) overlaps with the average Si concentration for global rivers (145 µM; Meybeck, 2003).

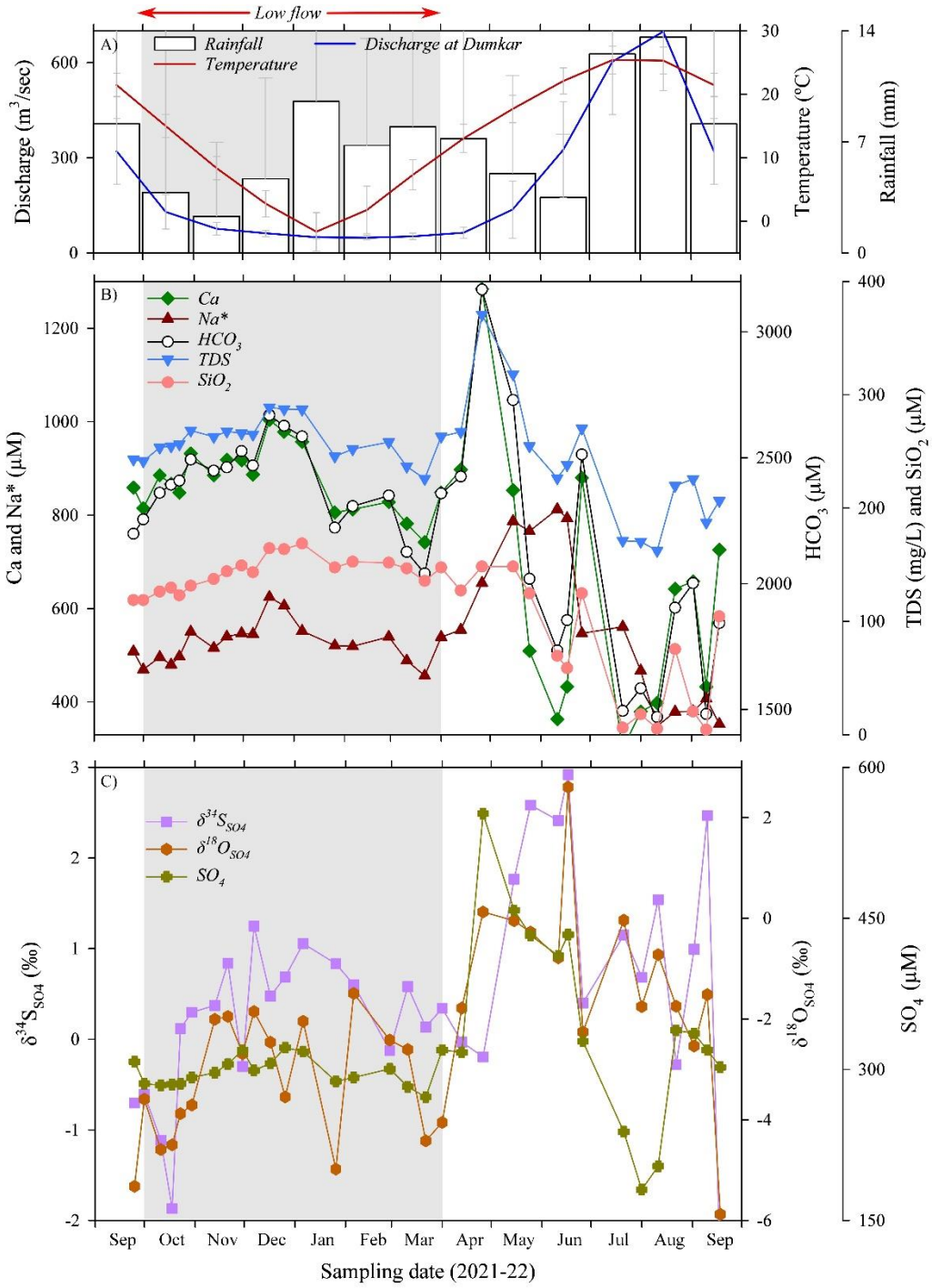

Figure 4.1. *Seasonal variation of (A) hydro-climatological (rainfall, temperature, and water discharge) parameters (data source: India Meteorological Department, India; https://mausam.imd.gov.in), (B) major ions concentrations, and (C) sulfate concentrations, and $\delta^{34}S_{SO4}$ and $\delta^{18}O_{SO4}$ of riverine sulfates for the Indus River at Leh. The monthly-average water discharge data shown here depict 26-years (1977-2003) of average measured data for a nearby location (at Dumkar; Mukhopadhyay and Khan, 2015).*

The observed variations in concentrations also exhibit several inter-elemental correlations. The Na concentrations co-vary with Mg, Cl and SO_4, whereas Ca concentrations show significant correlations with HCO_3 and Si. Strong correlations are also observed between K and SO_4, Cl and SO_4, and Mg and Cl. Principal component analyses of cations (Na, K, Ca, Mg, Si) and anions (HCO_3, SO_4, Cl and NO_3) identify three independent factors, with an eigen value greater than unity. These three components explain 89 % of the observed variation. The first component, with a weightage of 49 %, is characterized by high (positive) loading for most of the constituents. The second component is characterized with high loading of Ca, Mg and HCO_3, and accounts for 29 % of the total variance. High positive loadings of K, Ca, SO_4 and HCO_3, and negative Na and NO_3 loadings constitute the third component.

The elemental concentrations (C) of river waters mostly follow a power relation ($c = a \times Q^{-b}$; where, a and b are constant values) with water discharge (Q). The b-value depicts the impact of dilution (b = 1) and chemostatic weathering (b = 0) behavior of elements in a basin (Godsey et al., 2009). The b-values for Na (0.03), Mg (- 0.02), Cl (0) and SO_4 (0.053) point to their near-chemostatic nature, whereas those for K (0.12), Ca (0.3), HCO_3 (0.15), Si (0.8) and NO_3 (0.27) vary between dilution and chemostatic behavior. Except for Si, the b-values for most of the constituents are found relatively lower than that observed for other Himalayan Rivers (Samanta et al., 2019). Figure 4.1. depicts significant seasonal fluctuation in the elemental concentrations of the Indus headwater. Broadly, most of the constituents show higher concentrations during low flow stages, which is consistent with earlier reported trends for other river systems from the Himalayas. The relative standard deviation for Na (21 %), Ca (29 %), Mg (16 %), HCO_3 (18 %), Cl (21 %), Si (45 %) and TDS (17 %) datasets show wide variations. The degree of seasonal changes in elemental concentrations is significantly lower than the discharge variations (~ 300 %; Mukhopadhyay and Khan, 2015), indicating dilution effect is not sufficient to explain these concentration changes. In addition to the broad seasonal trend, the silica concentrations decline to very low (81 ± 56 µM; n = 16) concentrations during high flow stages (April-September). The $\delta^{34}S_{SO4}$ of the Indus River varies from - 2.9 ‰ (June) to 2.6 ‰ (September), with an average value of 0.5 ‰. This value is comparable to that reported for the Indus outflow (0.8 ‰), and about 4 ‰ depleted than that of global rivers (~ 4.4 ‰). Our measured $\delta^{34}S_{SO4}$ values fall intermediate to that of the gypsum (15 ± 2 ‰; Xu et al., 2024), pyrite (- 6 ± 10 ‰; Stebbins et al., 2019) and hot springs (9 ± 5 ‰; Turchyn et al., 2013) sources (Table 4.2.). Although the $\delta^{34}S_{SO4}$ shows limited seasonal variation (1 σ ~ 1.2 ‰), the

$\delta^{34}S_{SO4}$ value broadly follows the seasonal trends of SO_4 concentrations with enriched values being observed for high flow stages.

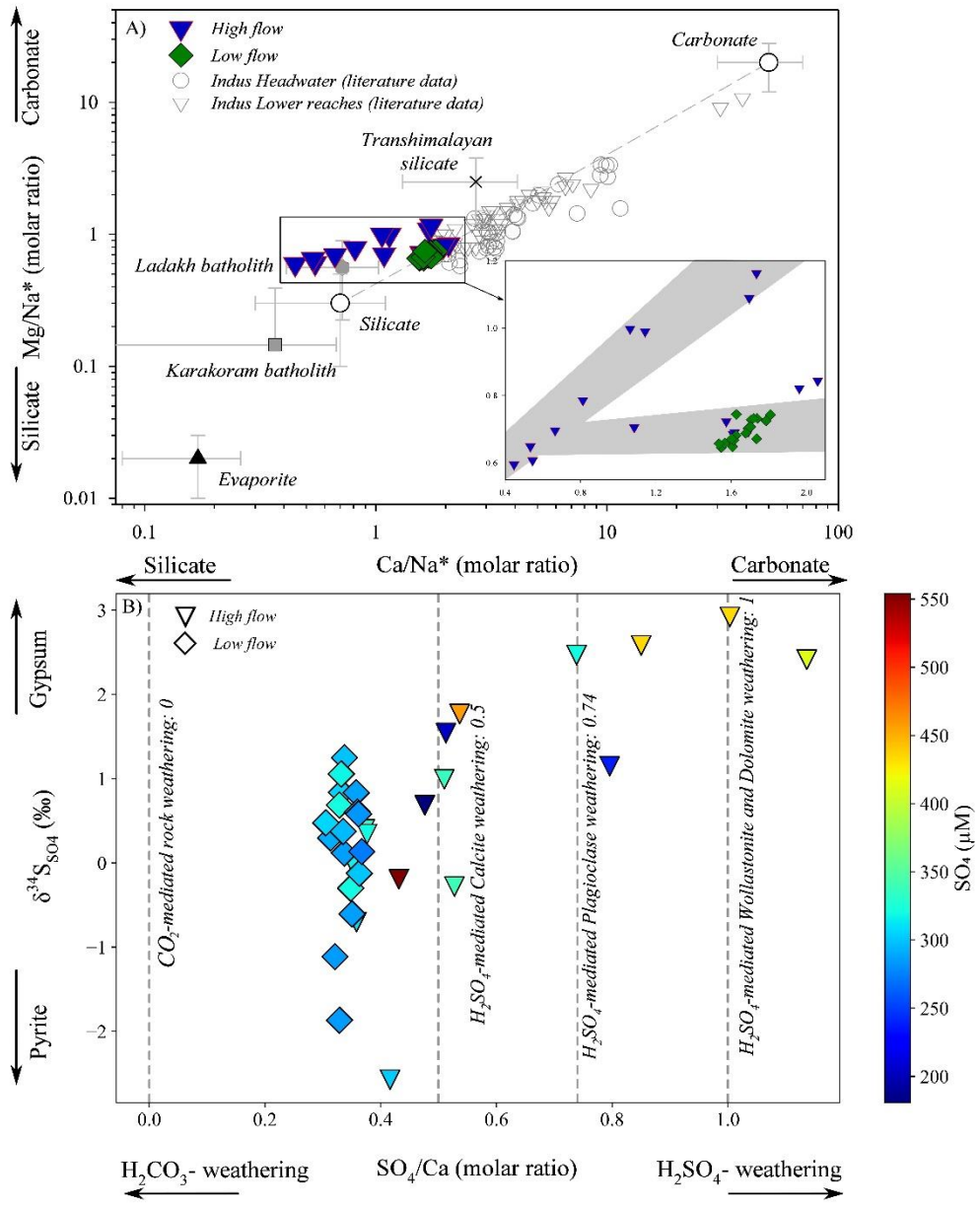

Figure 4.2. *Mixing plot between (A) Ca/Na* and Mg/Na*, and (B) SO_4/Ca and $\delta^{34}S_{SO4}$ values for the Indus River. The colorbar represents the SO_4 concentrations for the corresponding samples. The typical compositions for the end-members (Millot et al., 2003; Singh et al., 2005; Reichardt et al., 2010; Heri et al., 2015) and stoichiometric reactions (Drever, 1997) are from the literature. For reference, earlier-reported Indus water chemistry for the upper (Pande et al., 1994; Ahmad et al., 1998; Bhat et al., 2023) and lower (Karim and Veizer, 2000) reaches are also shown.*

This seasonal $\delta^{34}S_{SO4}$ trend is consistent with that reported earlier for Marsyandi (Turchyn et al., 2013), Mahanadi (Rout and Tripathy, 2024) and Ganga (Kemeny et al., 2021a) Rivers. Likely, the $\delta^{18}O_{SO4}$ values, which fluctuate between - 6 and 3 ‰, also exhibit enriched isotopic values for the high flow stage. The average $\delta^{18}O_{SO4}$ values at Leh for high flow stages (-1.6 ‰) are depleted by ~ 5 ‰ than that reported for the Indus outflow (4.2 ‰; Karim and Veizer, 2000). Considering an amount-weighted $\delta^{18}O_{H2O}$ value (-12.65 ‰; Lone et al., 2019) for rainwater at Leh, this average $\delta^{18}O_{SO4}$ in sulfates corresponds to an average $\Delta^{18}O$ (= $\delta^{18}O_{SO4}$ - $\delta^{18}O_{H2O}$) value of 10 ± 2 ‰. The $\Delta^{18}O$ for the Indus overlaps with the ranges reported for global rivers (12 ± 7 ‰ (n = 273); Relph et al., 2021), and the typical $\Delta^{18}O$ values reported for evaporites (19 ‰ to 27 ‰), and aerobic (~ 6.2 ‰) and anaerobic (~ 2.9 ‰) oxidation of pyrites (Relph et al., 2021).

4.2. Discussion

The major solute sources for the Indus River are atmospheric deposition, hot springs, weathering of bedrocks (silicates, carbonates and evaporites), and oxidation of sulfide minerals (Pande et al., 1994; Bhat et al., 2023). This river flows through a barren and high-elevation terrain, and hence, is expected to receive insignificant anthropogenic input. The binary mixing plot between Ca/Na* and Mg/Na* ratios ascertain the dominant cation supply from the weathering of silicates and carbonates (Fig. 4.2. A). The average Ca/Na* ratios for the Indus samples (1.5 ± 0.4) is closer to the silicate (~ 0.7; Krishnaswami et al., 1999) than the carbonate (~ 50; Gaillardet et al., 1999) end-member values, pointing to dominant sodium supply from the silicates. Likely, the average Mg/Na* ratios (0.7 ± 0.1) also fall closer to the silicate (~ 0.3; Krishnaswami et al., 1999) end-member than that of the carbonates (~ 20; Gaillardet et al., 1999). This plot also reveals that the samples mostly follow two broad trends with different slopes. The samples with relatively higher slopes (Ca/Mg ~ 1.6) mainly belong to the summer season (high flow stage: Apr.-Sept.), whereas the lower slopes (~ 2.4) belong to the winter samples (low flow stage: Oct.-Mar.). Further, samples with lower Ca/Mg ratios also found to have lower Ca/Na* (~ 1.3) and enriched $\delta^{34}S_{SO4}$ (0.84 ‰) values than the other set (1.7; 0.19 ‰ respectively). This observation hints at appreciable seasonal changes in solute sources, which are quantified in the subsequent sections.

In addition to these major lithologies, the SO_4/Ca - $\delta^{34}S_{SO4}$ plot establishes the dominant sulfate sources and their seasonal contributions (Fig. 4.2. B). The SO_4/Ca ratio mostly hovers around 0.3 during low flow stages, whereas it varies significantly between 0.35 and 1.14 during high flow stages (Fig. 4.2. B). The average SO_4/Ca during low (0.34 ± 0.02; n = 17) and high (0.59 ± 0.24; n = 16) flow stages, however, falls intermediate to the expected stoichiometric ratio for the H_2CO_3 and H_2SO_4-mediated rock dissolution (Drever, 1997; Fig. 4.2. B). Similar to SO_4/Ca, the $\delta^{34}S_{SO4}$ for the high (0.8 ± 1.4 ‰) and low (0.19 ± 0.80 ‰; Table 4.1.) flow stages indicates significant seasonal change with dominant sulfate contribution via pyrite oxidation than gypsum dissolution.

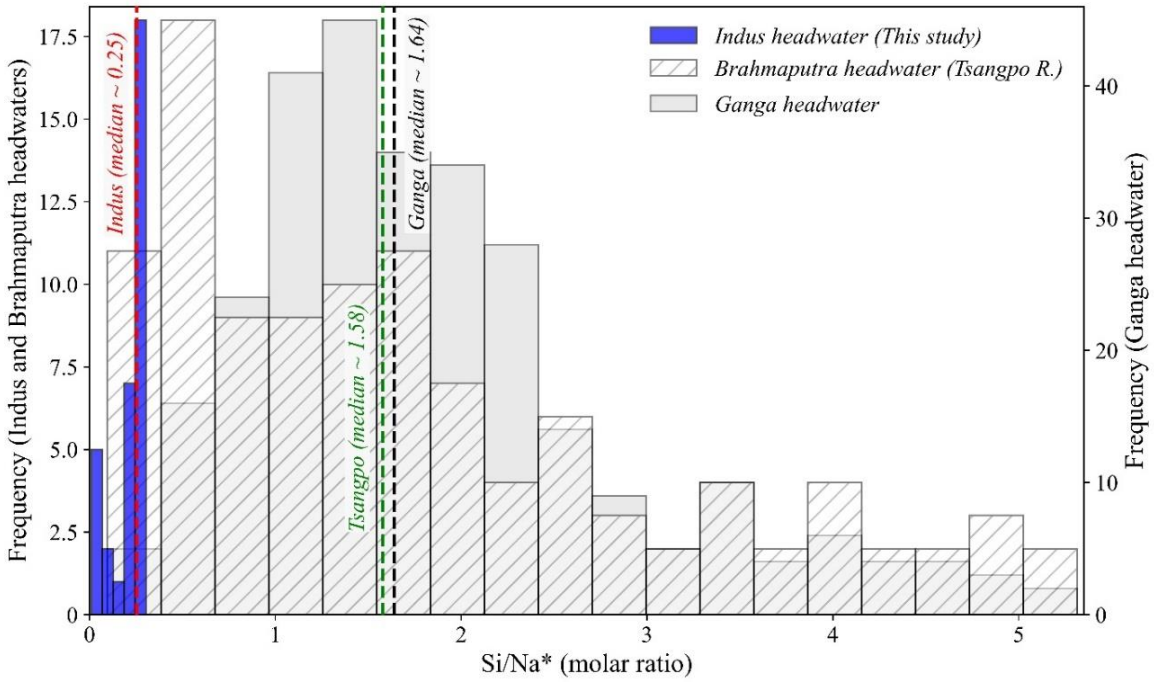

Figure 4.3. *Frequency distribution of the Si/Na* values for the Indus headwater at Leh is compared with that of the Ganga and Brahmaputra (Tsango) headwaters. These data for the Ganga (Sarin et al., 1992; Dalai et al., 2002a; Oliver et al., 2003; Quade et al., 2003; Tipper et al., 2006) and Tsangpo (Hren et al., 2007) Rivers are from earlier publications.*

Further, the frequency distribution for Si/Na* of the Indus River provides an indirect evidence for additional sources of sodium and sulfate for this basin (Fig. 4.3.). The average Si/Na* ratio of these samples (0.2 ± 0.1; Table 4.1.) is about an order of magnitude lower than that reported for the Ganga headwaters (~ 2.0; Sarin et al., 1992; Dalai et al., 2002a; Oliver et al., 2003; Quade et al., 2003; Tipper et al., 2006). The average Si/Na* value for the Ganga (~ 2.0) is consistent with that expected for weathering of plagioclase to kaolinites (Singh et al., 2005). These lower values can be attributed to either Si loss or, sodium gain from the system. Any loss of silica may happen through its adsorption onto clay and Mn-hydroxides, and

biological uptake (Fontorbe et al., 2013). Here, the Si adsorption onto particulates may also influence sodium and hence, may not explain the lower Si/Na* values for the Indus. Earlier studies have shown the removal of Si from water columns via various biological pathways involving diatoms, sponges and phytoliths (Fontorbe et al., 2013). The removal of biogenic silica is evident for selected samples from the summer monsoon period with near-zero silica concentrations (Fig. 4.1. B). Although the summer season are expected to have conducive temperature for biological growth in these cold-arid regions, the average Si concentration for the low flow season samples (~ 140 μM) are comparable or, marginally higher than that observed for the Ganga headwaters (~ 130 μM). This comparison indicates that biological uptake may not influence the dissolved silica concentrations of the low flow seasons with a cold climatology. The observed lower Si/Na* values, therefore, have to be driven by an additional supply of sodium to the Indus headwater, in addition to rain, halite and silicates. These additional sources for the Indus could be hot springs and/or Na_2SO_4-type evaporites (e.g. mirabilite and thernadite; Dutta et al., 2023; Xu et al., 2024). Earlier reported chemical data for the hot springs from this basin provide a median Si/Na* value of ~ 0.7 (Tiwari et al., 2016), which matches with that reported for the Nepal Himalaya (~ 0.5; Evans et al., 2004). Whilst these values are lower than the plagioclase-driven Si/Na* value (~ 2), these values are systematically higher than the Si/Na* value for the Indus headwater (Fig. 4.3.). We, therefore, hypothesize significant supply of sodium from the dissolution of mirabilites to this cold and arid basin. Occurrence of mirabilites or, its dehydrated minerals have been reported from the Tibetan regions with high evaporation, and can be an important solute source (Xu et al., 2024).

We have assessed the seasonal variation in Ca/Na* to evaluate the relative strength of silicate and carbonate weathering during different flow stages. Figure 4.4. compares the time-series fluctuations in Ca/Na* for the Indus mainstream at Leh with that reported earlier for other Himalayan River systems. The average Ca/Na* for the Indus is 1.5 ± 0.4 (n = 33), which is distinctly lower compared to that for upper (~ 8 at Rishikesh (Tripathy et al., 2010); ~ 11 for Marsynadi (Tipper et al., 2006)) and lower (2.5 ± 0.9; n = 77 at Farakka, Bickle et al., 2018) Ganga, and Brahmaputra (5.9 ± 1.5; n = 40 at Guwahati, Samanta et al., 2019) Rivers. The lower Ca/Na* for the Indus points to the dominancy of silicate weathering in this headwater compared to other river basins and/or, additional supply of Na from other sources (e.g. non-chloride containing evaporites). In addition to the average value, the temporal trends for Ca/Na* for the Indus also exhibit a contrasting trend than that for the Ganga and Brahmaputra

Rivers. The Ca/Na* shows a declining trend between April (~ 1.7) and July (~ 0.5), which subsequently increases to reach a plateau around September (~ 1.6; Fig. 4.4.).

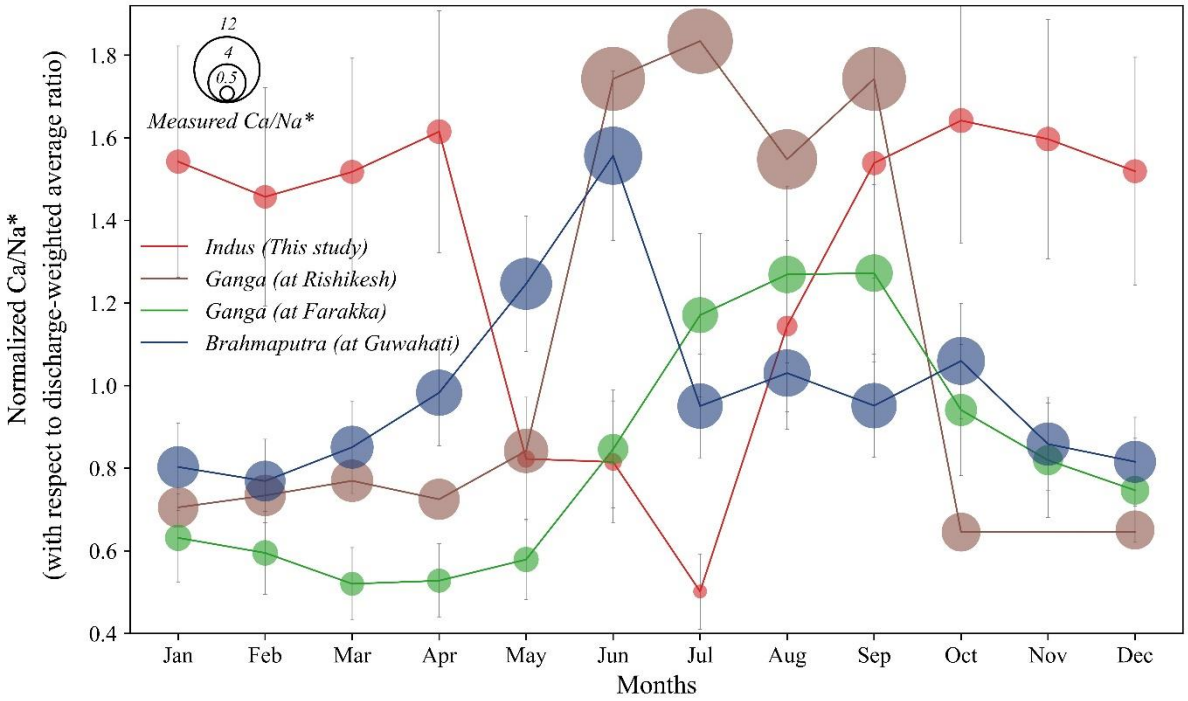

Figure 4.4. *Monthly variations of the normalized Ca/Na* ratio for the Indus and other Himalayan (upper (Tripathy et al., 2010) and lower (Bickle et al., 2018) Ganga, and Brahmaputra (Samanta et al., 2019)) Rivers. The normalized ratios were computed by dividing monthly-averaged Ca/Na* data with the annual discharge-weighted ratio for the river. The data symbols reflect the measured Ca/Na* ratio. The seasonal trends for the Indus are different than other rivers and depict enhanced silicate weathering during the early part of the summer, which later shifts to relatively higher carbonate input.*

This trend is different than other rivers which show an elevated Ca/Na* ratio during high flow stages, which is linked to relatively higher dissolution of carbonates than that during low flow stages (Tipper et al., 2006; Samanta et al., 2019). To better understand the controlling factors, we have quantified the monthly changes in source contribution for cations for the Indus using an inverse model (see section 4.3. for computational details). In the model calculation, we have considered Na_2SO_4-type evaporites and hot springs as one end-member due to their chemical similarity.

4.3. Source-apportionment

4.3.1. Cationic sources

We have adopted the inverse model approach of Tripathy and Singh (2010) to estimate the solute contributions from different sources for cations. This model relies on the following mass balance equations which relate the observed data (Table 4.1.) and end-member (Table 4.2.) values.

$$\left(\frac{X}{Na}\right)_{riv} = \sum_{i=1}^{4}\left(\frac{X}{Na}\right)_i \times f_i \quad (4.1)$$

$$1 = \sum_{i=1}^{4} f_i \quad (4.2)$$

where, the subscripts, *riv* stands for composition of river samples. The X/Na reflects the Na-normalized ratios for element, X (Ca, Mg, Cl, and HCO_3), whereas f_i is the relative contribution of Na from the source, *i* (rain/halite, silicate, carbonate and hot springs).The model uses a Quasi-Newton non-linear optimization algorithm, which iterates from a set of *a-priori* compositions for end-members to find the best-fit for all the model parameters which can explain the above equations with the least residual (Tripathy and Singh, 2010). The result, therefore, provides *a-posteriori* data (and associated uncertainties) for end-member values and the relative contribution of Na from the major sources. The model estimates that the cations at Leh, on average, are supplied by carbonates (692 μM; 32 ± 6 %), silicates (756 μM; 35 ± 9 %), rain (227 μM; 11 ± 4 %) and hot springs (459 μM; 21 ± 8 %; Fig. 4.5. A). Similar to Ca/Na*, the cationic contribution from silicates and carbonates are also showing significant seasonal changes (Fig. 4.5. A). The Cat_s shows an increasing trend between April to July, which increases subsequently to reach a plateau value in September (Fig. 4.5. B). The initial Cat_s rise during early summer season is linked to temperature-sensitive dissolution of silicate rocks, which is discussed below.

The chemical weathering pattern of river systems is largely controlled by lithology, relief, runoff and temperature (Drever, 1997). As lithology and relief are not likely to vary at seasonal scale, runoff and temperature may explain the Ca/Na* variations for the Indus. The water discharge (Q) at this location starts to increase in April and reaches its maximum value in July (Fig. 4.1. A). The rise in Q is expected to favor dissolution of carbonates (with fast dissolution kinetics) than resistant silicates due to limited water-rock interaction time. The Ca/Na* and Cat_s trends for the Indus, however, indicate a relative increase in silicate

weathering from April to July. The Cat_s values, however, show a declining trend between July (maximum Q) and September, which clearly shows a runoff-dependent enhancement of carbonate dissolution in the later part of the summer (Fig. 4.5. B).

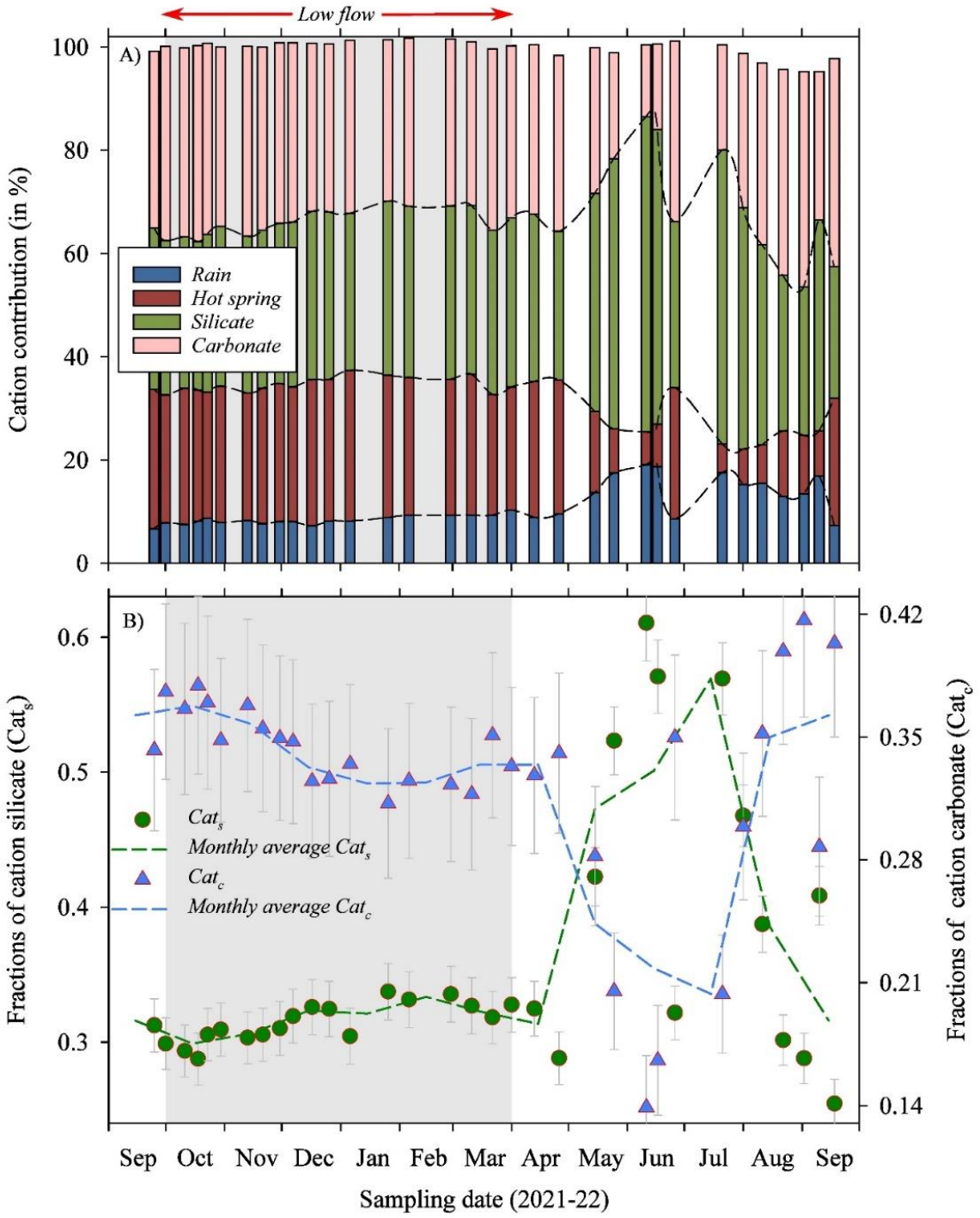

Figure 4.5. *(A) Estimated fractional contribution of cations from four major sources. (B) the cationic supply from silicate (Cat_s) and carbonate (Cat_c) weathering shows significant seasonal change with higher silicate contribution during early part of the summer.*

We hypothesize that the relative rise in silicate weathering during early summer in the Indus may be controlled by temperature changes in this highly-elevated terrain with appreciable glacial coverage (White et al., 1999; Dalai et al., 2002a). The temperature at Leh reaches to sub-zero level and the annual temperature varies from -1.6 to 25.4 ºC with an average of 13 ± 10 ºC (IMD Leh). Earlier studies have documented that a temperature change of similar range (0 ºC to 22 ºC) may account for about 50 times increase in dissolved silica fluxes (154 to 8060 mol/ha/yr) for rivers (White et al., 1999). This increase in silicate dissolution with temperature rise mostly depicts the Arrhenius law relating reaction rate and temperature. The temperature at this location reaches 13 ºC during April which rises to 25 ºC during July (Fig. 4.1. A). This increase in temperature during early summer may strongly affect the silicate dissolution by enhancing reaction rates. As the temperature maxima reaches around July (Fig. 4.1. A), the weathering rates in the subsequent months are majorly controlled by runoff.

4.3.2. Sulfate sources

We have employed an inverse model to compute the sulfate source(s) contributions. Our approach involves both $\delta^{34}S_{SO4}$ and $\delta^{18}O_{SO4}$ values to compute these contributions, unlike earlier studies where only $\delta^{18}O_{SO4}$ values were used to find the sulfide-derived sulfates and pyrite $\delta^{34}S$ values (Relph et al., 2021; Xu et al., 2024). The mass balance equations for $\delta^{34}S_{SO4}$ and $\delta^{18}O_{SO4}$ for sulfates are as follows:

$$\delta^{34}S_{SO4} = f_{rain/halite}(\delta^{34}S_{rain/halite}) + f_{py}\,(\delta^{34}S_{py}) + f_{gy}(\delta^{34}S_{gy}) + f_{hs}(\delta^{34}S_{hs}) \quad (4.3)$$

$$\delta^{18}O_{SO4} = f_{rain/halite}(\delta^{18}O_{rain/halite}) + f_{py}\,(\delta^{18}O_{py}) + f_{gy}(\delta^{18}O_{gy}) + f_{hs}(\delta^{18}O_{hs}) \quad (4.4)$$

$$f_{rain/halite} + f_{py} + f_{gy} + f_{hs} = 1 \quad (4.5)$$

here, the subscripts *rain/halite*, *py*, *gy and hs* reflect the rain/halite, pyrite, gypsum and hot spring respectively. The a-priori data for the end-members are listed in Table 4.2. The $\delta^{18}O_{py}$ has been constrained by adopting the Monte-Carlo approach and reported parameter values of Relph et al., 2021 and Xu et al., 2024. This simulation involves $\delta^{18}O$ values for meteoric water and atmospheric oxygen, related fractionation factors and relative oxygen contribution for oxidation. For this calculation, we have assumed that the $\delta^{18}O_{H2O}$ for the reactive fluid is same as the annual (amount-weighted) average $\delta^{18}O$ value of rain for this region (Lone et al., 2019). The inverse model, using the observed isotopic data and a-priori values, finds the a-posteriori source composition and relative sulfate contribution from major sources (Table 4.2.).

Table 4.2. *A-priori* end-member compositions for major cations and sulfate sources. The *a-posteriori* compositions yielded from the inverse model are also listed for comparison.

	A-priori values				A-posteriori values				*Ref.*
Cationic sources									
	Cl/Na	Ca/Na	Mg/Na	HCO_3/Na	Cl/Na	Ca/Na	Mg/Na	HCO_3/Na	
Rain (Halite)	1.17 ± 0.06	0.02 ± 0.001	0.11 ± 0.01	0.01 ± 0.001	1.29 ± 0.06	0.02 ± 0.001	0.12 ± 0.01	0.005 ± 0.001	*[1]*
Silicate	0.001 ± 0.001	0.7 ± 0.3	0.3 ± 0.15	2 ± 1	0.001 ± 0.001	0.12 ± 0.04	0.4 ± 0.04	1.2 ± 0.2	*[2]*
Carbonate	0.001 ± 0.0001	50 ± 20	20 ± 8	100 ± 40	0.001 ± 0.0001	3.6 ± 0.6	1.6 ± 0.2	13 ± 2	*[3]*
Hot springs	0.5 ± 0.4	0.14 ± 0.27	0.10 ± 0.10	0.8 ± 0.3	0.8 ± 0.1	2 ± 0.5	0.02 ± 0.02	1.2 ± 0.4	*[4]*
Sulfate sources									
	$\delta^{34}S_{SO4}$ (‰)		$\delta^{18}O_{SO4}$(‰)		$\delta^{34}S_{SO4}$ (‰)		$\delta^{18}O_{SO4}$(‰)		
Rain	11.2		11.2		11 ± 0.4		11 ± 0.5		*[5]*
Hot springs	9 ± 5		3 ± 2		7 ± 2		-8 ± 4		*[5,6]*
Pyrite	-6 ± 10		-9 ± 2*		-8 ± 12		-9 ± 2		*[7]*
Gypsum (Mirabilites)	15 ± 2		15 ± 2		10 ± 1		15 ± 2		*[8]*

*[1] Roy-Barman and Jeandel, 2016; [2] Krishnaswami et al., 1999; [3] Millot et al., 2003; [4] Tiwari et al., 2016; [5] This study; [6] Turchyn et al., 2013; [7]: Stebbins et al., 2019, after excluding few data; [8] Xu et al., 2024. * A Monte-Carlo simulation was carried out to estimate the $\delta^{18}O_{SO4}$ of pyrite.*

Estimates from the inverse modeling show that the supply of the sulfate in the Indus water is dominated by sulfides (49 ± 7 %), with appreciable contribution also from gypsum (20 ± 7 %), and hot springs (23 ± 7 %; Table 4.3.).

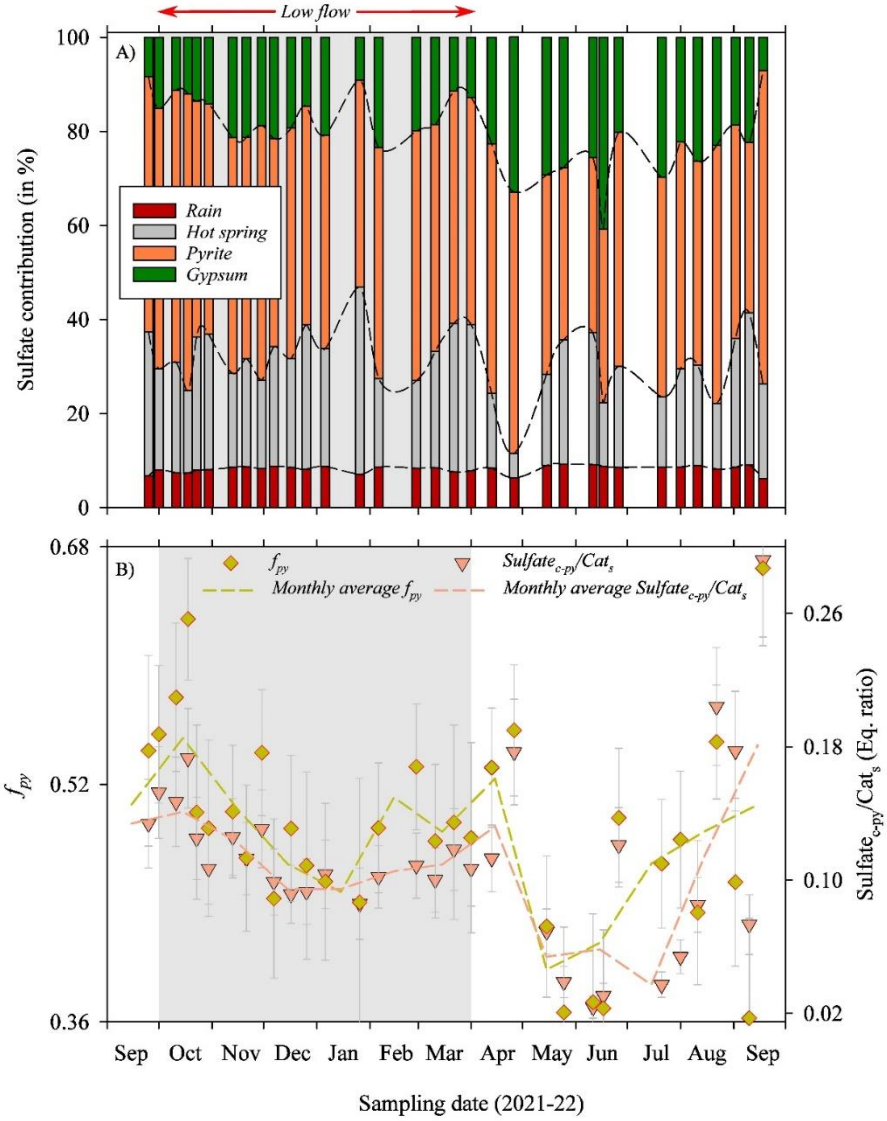

Figure 4.6. *(A) Estimated fractional contribution of sulfates from four major sources. (B) Seasonal trends of (i) fraction of sulfide-derived sulfates (f_{py}) and (ii) ratio between sulfide-derived sulfate associated with carbonates ($Sulfate_{c\text{-}py}$) and silicate-derived cations (Cat_s) show an increase in pyrite oxidation during low flow stages.*

The atmospheric deposition of SO_4 varies from 16 µM to 41 µM with systematically higher values during the high flow stages. The f_{py} for sulfate, however, varies from 0.36 to 0.67 (avg., 0.49 ± 0.07) with relatively higher f_{py} values being observed for low flow stages (Fig. 4.6.). The observed higher pyrite contribution during baseflow is consistent with earlier-reported seasonal trends for the Ganga (62 to 101 %; Kemeny et al., 2021a) and Mackenzie (85 ± 5 %; Calmels et al., 2007).

Table 4.3. *The source apportionment results of various sources for cations and sulfates (rain, silicate (s), carbonate (c), hot springs (hs), pyrite (py) and gypsum (gy)) are provided.*

Sample ID	Date of sampling	Source apportionment results for cations								Source apportionment results for sulfate			
		f_{rain}	f_s	f_c	f_{hs}	Cat_{rain}	Cat_s	Cat_c	Cat_{hs}	f_{rain}	f_{hs}	f_{py}	f_{gy}
IND-22/01	25-09-2021	0.15 ± 0.04	0.48 ± 0.04	0.14 ± 0.02	0.23 ± 0.04	0.07 ± 0.01	0.31 ± 0.02	0.34 ± 0.05	0.27 ± 0.06	0.07 ± 0.07	0.31 ± 0.06	0.54 ± 0.06	0.08 ± 0.06
IND-22/02	01-10-2021	0.18 ± 0.04	0.46 ± 0.04	0.16 ± 0.02	0.21 ± 0.04	0.08 ± 0.01	0.3 ± 0.02	0.38 ± 0.05	0.25 ± 0.05	0.08 ± 0.08	0.22 ± 0.05	0.55 ± 0.05	0.15 ± 0.07
IND-22/03	11-10-2021	0.17 ± 0.04	0.45 ± 0.04	0.15 ± 0.02	0.22 ± 0.05	0.08 ± 0.01	0.29 ± 0.02	0.37 ± 0.05	0.26 ± 0.06	0.07 ± 0.07	0.23 ± 0.05	0.58 ± 0.05	0.11 ± 0.07
IND-22/04	18-10-2021	0.18 ± 0.04	0.44 ± 0.04	0.16 ± 0.02	0.21 ± 0.05	0.08 ± 0.01	0.29 ± 0.02	0.38 ± 0.05	0.25 ± 0.05	0.07 ± 0.07	0.18 ± 0.04	0.63 ± 0.04	0.12 ± 0.06
IND-22/05	23-10-2021	0.19 ± 0.04	0.46 ± 0.04	0.15 ± 0.02	0.2 ± 0.04	0.09 ± 0.01	0.31 ± 0.02	0.37 ± 0.05	0.24 ± 0.05	0.08 ± 0.08	0.28 ± 0.06	0.5 ± 0.06	0.14 ± 0.07
IND-22/06	30-10-2021	0.17 ± 0.04	0.47 ± 0.04	0.14 ± 0.02	0.22 ± 0.04	0.08 ± 0.01	0.31 ± 0.02	0.35 ± 0.05	0.26 ± 0.06	0.08 ± 0.08	0.29 ± 0.06	0.49 ± 0.06	0.14 ± 0.07
IND-22/07	13-11-2021	0.18 ± 0.04	0.46 ± 0.04	0.15 ± 0.02	0.21 ± 0.04	0.08 ± 0.01	0.3 ± 0.02	0.37 ± 0.05	0.25 ± 0.05	0.09 ± 0.08	0.2 ± 0.04	0.5 ± 0.04	0.21 ± 0.08
IND-22/08	21-11-2021	0.17 ± 0.04	0.47 ± 0.04	0.14 ± 0.02	0.22 ± 0.04	0.08 ± 0.01	0.31 ± 0.02	0.35 ± 0.05	0.26 ± 0.06	0.09 ± 0.09	0.23 ± 0.05	0.47 ± 0.05	0.21 ± 0.08
IND-22/09	30-11-2021	0.18 ± 0.04	0.47 ± 0.04	0.14 ± 0.02	0.22 ± 0.04	0.08 ± 0.02	0.31 ± 0.02	0.35 ± 0.05	0.27 ± 0.06	0.08 ± 0.08	0.19 ± 0.04	0.54 ± 0.04	0.19 ± 0.07
IND-22/10	07-12-2021	0.17 ± 0.04	0.48 ± 0.04	0.14 ± 0.02	0.21 ± 0.04	0.08 ± 0.01	0.32 ± 0.02	0.35 ± 0.05	0.26 ± 0.05	0.09 ± 0.09	0.25 ± 0.05	0.44 ± 0.05	0.22 ± 0.08
IND-22/11	17-12-2021	0.16 ± 0.04	0.49 ± 0.04	0.13 ± 0.02	0.23 ± 0.04	0.07 ± 0.01	0.33 ± 0.02	0.32 ± 0.04	0.28 ± 0.06	0.09 ± 0.08	0.23 ± 0.05	0.49 ± 0.05	0.19 ± 0.08
IND-22/12	26-12-2021	0.17 ± 0.04	0.48 ± 0.04	0.13 ± 0.02	0.22 ± 0.04	0.08 ± 0.02	0.32 ± 0.02	0.33 ± 0.04	0.27 ± 0.06	0.08 ± 0.08	0.31 ± 0.06	0.47 ± 0.06	0.15 ± 0.07
IND-22/13	06-01-2022	0.18 ± 0.04	0.45 ± 0.04	0.13 ± 0.02	0.24 ± 0.04	0.08 ± 0.02	0.3 ± 0.02	0.33 ± 0.05	0.29 ± 0.06	0.09 ± 0.09	0.25 ± 0.05	0.45 ± 0.05	0.21 ± 0.08
IND-22/14	26-01-2022	0.18 ± 0.04	0.48 ± 0.04	0.12 ± 0.02	0.21 ± 0.04	0.09 ± 0.02	0.34 ± 0.02	0.31 ± 0.04	0.28 ± 0.06	0.07 ± 0.07	0.4 ± 0.08	0.44 ± 0.08	0.09 ± 0.07
IND-22/15	06-02-2022	0.19 ± 0.04	0.48 ± 0.04	0.12 ± 0.02	0.21 ± 0.04	0.09 ± 0.02	0.33 ± 0.02	0.33 ± 0.04	0.27 ± 0.06	0.09 ± 0.09	0.19 ± 0.04	0.49 ± 0.04	0.23 ± 0.08
IND-22/16	28-02-2022	0.19 ± 0.04	0.48 ± 0.04	0.12 ± 0.02	0.2 ± 0.04	0.09 ± 0.02	0.34 ± 0.02	0.32 ± 0.04	0.26 ± 0.06	0.08 ± 0.08	0.19 ± 0.04	0.53 ± 0.04	0.2 ± 0.07
IND-22/17	11-03-2022	0.19 ± 0.04	0.47 ± 0.04	0.12 ± 0.02	0.21 ± 0.04	0.09 ± 0.02	0.33 ± 0.02	0.32 ± 0.04	0.27 ± 0.06	0.09 ± 0.08	0.25 ± 0.05	0.48 ± 0.05	0.19 ± 0.08
IND-22/18	22-03-2022	0.2 ± 0.04	0.47 ± 0.04	0.14 ± 0.02	0.19 ± 0.04	0.09 ± 0.01	0.32 ± 0.02	0.35 ± 0.05	0.23 ± 0.05	0.08 ± 0.07	0.32 ± 0.06	0.49 ± 0.07	0.11 ± 0.07
IND-22/19	01-04-2022	0.21 ± 0.04	0.47 ± 0.04	0.13 ± 0.02	0.19 ± 0.04	0.1 ± 0.02	0.33 ± 0.02	0.33 ± 0.05	0.24 ± 0.05	0.08 ± 0.08	0.31 ± 0.06	0.48 ± 0.06	0.13 ± 0.07
IND-22/20	13-04-2022	0.19 ± 0.04	0.47 ± 0.04	0.13 ± 0.02	0.21 ± 0.04	0.09 ± 0.02	0.32 ± 0.02	0.33 ± 0.04	0.26 ± 0.06	0.08 ± 0.08	0.16 ± 0.04	0.53 ± 0.04	0.23 ± 0.08
IND-22/21	26-04-2022	0.22 ± 0.04	0.42 ± 0.04	0.14 ± 0.02	0.22 ± 0.05	0.1 ± 0.02	0.29 ± 0.02	0.34 ± 0.05	0.26 ± 0.05	0.06 ± 0.06	0.05 ± 0.05	0.56 ± 0.04	0.33 ± 0.07
IND-22/22	15-05-2022	0.25 ± 0.03	0.54 ± 0.03	0.1 ± 0.01	0.11 ± 0.03	0.14 ± 0.02	0.42 ± 0.02	0.28 ± 0.04	0.16 ± 0.04	0.09 ± 0.09	0.19 ± 0.05	0.42 ± 0.05	0.29 ± 0.08
IND-22/23	25-05-2022	0.28 ± 0.03	0.6 ± 0.03	0.06 ± 0.01	0.05 ± 0.02	0.18 ± 0.02	0.52 ± 0.03	0.21 ± 0.03	0.09 ± 0.03	0.09 ± 0.09	0.26 ± 0.06	0.37 ± 0.06	0.28 ± 0.08
IND-22/24	11-06-2022	0.28 ± 0.03	0.65 ± 0.03	0.04 ± 0.01	0.03 ± 0.02	0.19 ± 0.02	0.61 ± 0.03	0.14 ± 0.03	0.06 ± 0.03	0.09 ± 0.09	0.28 ± 0.06	0.37 ± 0.06	0.26 ± 0.08

IND-22/25	17-06-2022	0.28 ± 0.03	0.63 ± 0.03	0.05 ± 0.01	0.05 ± 0.02	0.19 ± 0.02	0.57 ± 0.03	0.17 ± 0.03	0.08 ± 0.03	0.09 ± 0.09	0.14 ± 0.06	0.37 ± 0.05	0.41 ± 0.09
IND-22/26	26-06-2022	0.18 ± 0.04	0.47 ± 0.04	0.14 ± 0.02	0.2 ± 0.04	0.09 ± 0.02	0.32 ± 0.02	0.35 ± 0.05	0.25 ± 0.05	0.09 ± 0.08	0.22 ± 0.04	0.5 ± 0.05	0.2 ± 0.08
IND-22/28	21-07-2022	0.27 ± 0.03	0.64 ± 0.03	0.06 ± 0.01	0.03 ± 0.02	0.18 ± 0.02	0.57 ± 0.03	0.2 ± 0.03	0.06 ± 0.02	0.09 ± 0.09	0.15 ± 0.04	0.47 ± 0.04	0.3 ± 0.08
IND-22/29	01-08-2022	0.27 ± 0.03	0.59 ± 0.03	0.1 ± 0.01	0.05 ± 0.02	0.15 ± 0.01	0.47 ± 0.02	0.3 ± 0.04	0.07 ± 0.03	0.09 ± 0.09	0.21 ± 0.04	0.48 ± 0.05	0.22 ± 0.08
IND-22/30	11-08-2022	0.31 ± 0.03	0.51 ± 0.03	0.13 ± 0.02	0.06 ± 0.03	0.16 ± 0.02	0.39 ± 0.02	0.35 ± 0.05	0.07 ± 0.03	0.09 ± 0.09	0.21 ± 0.05	0.43 ± 0.05	0.26 ± 0.08
IND-22/31	22-08-2022	0.29 ± 0.04	0.44 ± 0.04	0.16 ± 0.02	0.11 ± 0.04	0.13 ± 0.02	0.3 ± 0.02	0.4 ± 0.05	0.13 ± 0.04	0.08 ± 0.08	0.14 ± 0.04	0.55 ± 0.04	0.23 ± 0.07
IND-22/32	02-09-2022	0.3 ± 0.04	0.43 ± 0.04	0.17 ± 0.02	0.1 ± 0.04	0.13 ± 0.02	0.29 ± 0.02	0.42 ± 0.06	0.11 ± 0.04	0.09 ± 0.08	0.27 ± 0.05	0.45 ± 0.06	0.19 ± 0.08
IND-22/33	10-09-2022	0.32 ± 0.03	0.52 ± 0.03	0.1 ± 0.01	0.06 ± 0.03	0.17 ± 0.02	0.41 ± 0.02	0.29 ± 0.04	0.09 ± 0.03	0.09 ± 0.09	0.32 ± 0.06	0.36 ± 0.07	0.22 ± 0.08
IND-22/34	18-09-2022	0.18 ± 0.04	0.42 ± 0.04	0.18 ± 0.02	0.22 ± 0.05	0.07 ± 0.01	0.25 ± 0.02	0.4 ± 0.05	0.25 ± 0.05	0.06 ± 0.06	0.2 ± 0.05	0.67 ± 0.05	0.07 ± 0.05

This increase in f_{py} during low flow stages in river basins may largely be linked to the availability of oxidants and reactive minerals (Gu et al., 2020a; Shaughnessy et al., 2023). Earlier investigations on weathering profiles from watersheds with variable erosion rates have confirmed that pyrites are completely oxidized in surface layers, and only occur below a deeper (3 -10 m) weathering front (Liao et al., 2022; Fig. 4.7.).

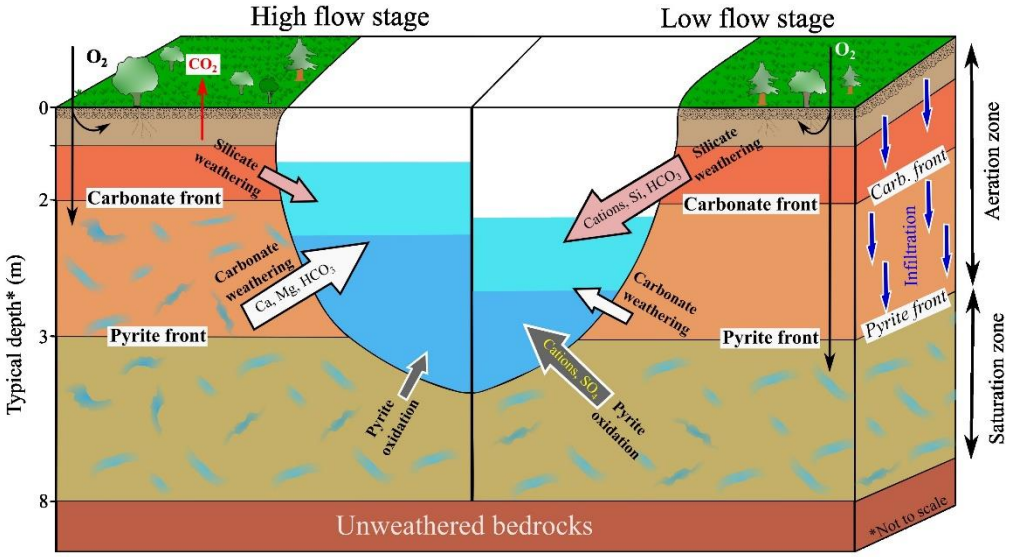

Figure 4.7. *Schematic diagram showing subsurface processes regulating the seasonal changes in pyrite oxidation of the Indus headwater basin. This seasonal change is mainly linked to diffusion of atmospheric oxygen to deeper depths during low water table, enabling oxidation of available pyrites. The arrow marks stand for different weathering pathways, and width of these arrows reflects (not to scale) the weathering intensity. In this generalized picture, we have shown lower silicate weathering during high flow stages, which is valid only in the later part of the summer at Leh (cf. Fig. 4.5.).*

The subsurface pyrite front typically falls below that of the carbonates, and water table during high discharge periods (Gu et al., 2020a). This front mainly reflects the critical depth of atmospheric oxygen ingress, which is controlled by microbial degradation and pyrite oxidation in the aquifer. The oxygen consumption via microbial degradation is largely restricted to top soil horizon, whereas diffusion of atmospheric oxygen to deeper depths is supported by favorable porosity (fracture density) and permeability (self-healing property of clay materials; Gu et al., 2020b). Further, the subsurface oxygen content decreases with the water saturation level and hence, is negligible below the water table. As the water table falls below the pyrite front during baseflow stages, the atmospheric oxygen could penetrate through microfractures into the front and hence, may oxidize the reactive minerals. The density of these microfractures in the aquifer depends on chemical weathering of primary minerals, and/or, structural deformation during tectonic stresses (Gu et al., 2020b). We have shown, in an earlier section,

that mineral dissolution in this basin is largely controlled by temperature than the water level and hence, the generation of microfractures in this region may largely be linked to regional tectonism. The Indus River in its upper reaches (Fig. 2.7.) mainly flows along a shear zone, which may place excessive tectonic stress than the rock strength to develop fractures. In addition to these processes, the fluid flow path may also contribute to the pyrite oxidation rate of a basin. The reactive fluids with deeper flow paths are in constant interaction with pyrite fronts and hence, are characterized by high sulfide-derived sulfates. In case of increased relative fraction of these deeper and "older" waters to rivers during low flow stages may result in higher f_{py} values than that during high flow stages (Kemeny et al., 2021a and b). This effect of fluid path on f_{py}, however, may not be significant for the highly-elevated Indus basin, where the water infiltration is expected to be one-dimensional vertical flow and not interflow type (Liao et al., 2022). We, therefore, hypothesize that the increased f_{py} during baseflow may be linked to the ability of oxygen ingress via tectonic-induced microfractures to the deeper and unsaturated fronts where reactive pyrites are present (Fig. 4.7.). Further, earlier studies have shown that these reactive fronts are narrower in mountainous regions and are wider in river valleys. As our samples belong to a ridge, the narrower depth of the pyrite zone may explain the lower degree of f_{py} seasonality observed at Leh (Fig. 4.6.) than that at other global locations.

4.4. Implications

Our proposed linkage between flow stage variation and oxidation rate has important implications in understanding the climatic sensitivity of riverine acid-alkalinity budget and net CO_2 effect of continental weathering. In tropical regions, baseflow water stages, characterized by high pyrite oxidation, are more reflective of the drier climate of the basin. A drier climate, therefore, may facilitate more H_2SO_4 (than H_2CO_3) acid-mediated weathering, which in turn may increase the amount of CO_2 released to the atmosphere. Further, the H_2SO_4-mediated weathering, owing to its stronger acid strength, is likely to supply more riverine solutes and nutrients to the ocean. These climatological effects on weathering type are more likely to be prominent in supply-limited than weathering-limited regions, where exposure of fresher minerals may not be limited by water levels. Also, any decline in the groundwater table as predicted for recent climatic changes may also promote subsurface pyrite oxidation (Fig. 4.7.), which may increase the acidity of river water. These processes, therefore, must be accounted for understanding past CO_2 excursions, and also, predicting the effect of water table changes.

This page has been intentionally left blank.

Chapter 5

Pyrite oxidation in the Indus headwater basin

This page has been intentionally left blank.

5.1. Introduction

The global Cenozoic cooling event has often been linked to intense silicate weathering over the Himalayan-Tibetan plateau (HTP) river basins. Chemical erosion rates and elemental fluxes from the Himalayan River basins are found to be disproportionally higher than that of other global rivers. Intense silicate weathering over this young orogenic belt has been proposed as a prime trigger for the global Cenozoic cooling (Raymo and Ruddiman, 1992). This proposition has drawn strong support from observed synchronous increasing trends for $^{87}Sr/^{86}Sr$, $^{187}Os/^{188}O$, and $\delta^{7}Li$ (Fig. 5.1.; Misra and Froliech, 2012), indicating steady increase in weathering rates. This linkage, however, generally overlooks the CO_2 release during organic and sulfide oxidation processes, which (unlike silicates) have a positive effect on climate. More recent evidence on stable atmospheric CO_2 trends during last 20 Myr (Wal et, al., 2011), erosion pattern for last 12 Myr (Willenbring and Blanckenburg, 2010) and high CO_2 release/uptake ratio for the Himalayan rivers (Torres et al., 2014) have challenged this tectonic-weathering-climate linkage. In particular, the proposition by Torres et al., (2014) show that the CO_2 release via H_2SO_4-mediated carbonate weathering in the Himalayas may counterbalance the CO_2 uptake rate via silicate weathering, and hence, may have lesser net impact on the CO_2 cycle. The rate and controlling factors for the sulfide oxidation in the HTP regions, however, still remain understudied to assess the net effect of Himalaya weathering on the Cenozoic climate (Turchyn et al., 2013; Relph et al., 2021; Kemeny et al., 2021a; Xu et al., 2024). Available limited studies for the Himalayan River basins have estimated dominant sulfide contribution to the sulfate of the Marsyandi (> 62 %; Kemeny et al., 2021a), Teesta (~ 50 %; Das et al., 2021), and GB (~ 70 %; Galy and France-Lanord, 1999) river system. Quantitative estimation of these rates is not available for the Indus basin from the western Himalaya, although dominant pyrite oxidation for the Indus headwater (Pande et al., 1994; Bhat et al., 2023) and floodplain (Karim and Veizer, 2000) region has been inferred from chemical and isotopic data.

This chapter presents new spatial data on dissolved major ions and $\delta^{34}S_{SO4}$-$\delta^{18}O_{SO4}$ of the upper Indus basin. As mentioned earlier, this sample set includes surface water samples from the Indus mainstream and its major tributaries, and also, potential sulfate sources (rain, glaciers, ground water, hot springs, and anthropogenic supplies) to this basin. These data were inspected to constrain the major sources for cations and sulfates for this basin from the northwestern Himalaya. Further, inverse modeling and Monte-Carlo simulation of these

datasets were used to quantify these source(s) contributions and related CO_2 release/uptake rates. These estimations were further used to assess the net effect of chemical weathering in this part of the Himalaya on the global Cenozoic cooling event. Details on these data distribution, source apportionment modeling and significance of the outcomes are discussed below.

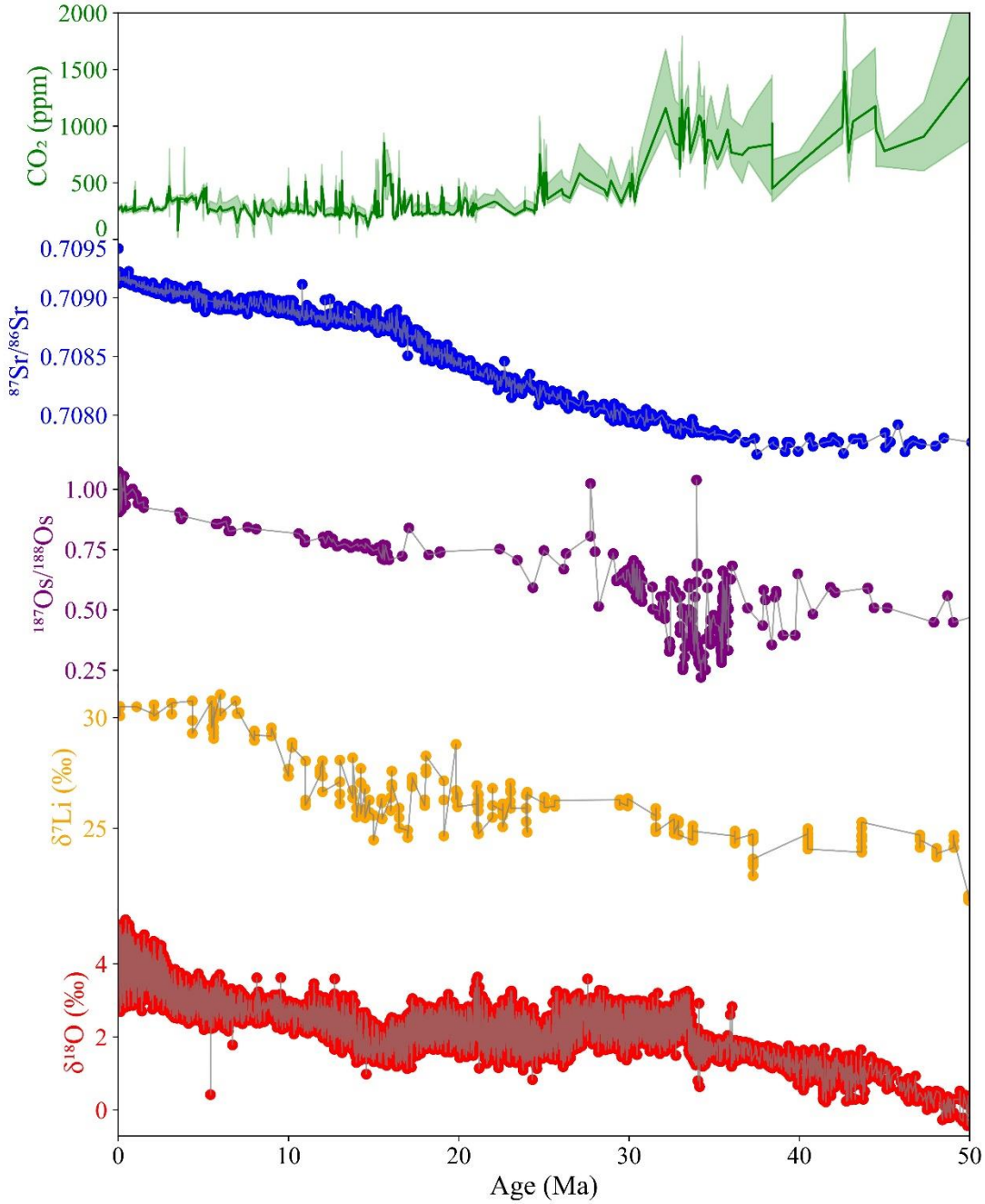

Figure 5.1. *The evolution of Cenozoic (50 Ma) atmospheric CO_2 (Beerling and Royer, 2011). The isotopic excursions for $^{87}Sr/^{86}Sr$ (Veizer et al., 1999), $^{187}Os/^{188}Os$ (excluding one outlier; Peucker-Ehrenbrink and Ravizza, 2012), $\delta^{7}Li$ (Misra and Froelich, 2012) and $\delta^{18}O$ (Zachos et al., 2008) during this time period are also shown for comparison.*

5.2. Results

Data on major ions concentrations, $\delta^{34}S_{SO4}$ and $\delta^{18}O_{SO4}$, and $\delta^{18}O_{H2O}$ from the Indus headwater and its tributaries are provided in Table 5.1. - 5.3. These samples cover about 20-times variation in elevation (~ 200 and 3900 m) and 6-times variation in water temperature (6 °C and 36 °C). The total dissolved solids (TDS) vary between 58 and 502 mg/L, with an average value of 153 ± 73 mg/L. These TDS values, excluding three polluted samples from the lower reaches, exhibit significant correlation ($r = 0.57$; $p < 0.01$; $n = 58$) with temperature, with a slope of 3.5 mg/L per °C. Water chemistry of this basin is typical of that expected for streams with dominant carbonate weathering (Fig. 5.2.). The pH values are mildly-alkaline (7.0 to 9.6), with a water composition of Ca-Mg-HCO_3 type (Fig. 5.2.). The CSI values vary from -1.33 to 1.45 (- 0.02 ± 0.58; $n = 61$), with the positive CSI values being mostly observed for the lower reaches (< 1000 m) samples. The HCO_3 ions, which account for ~ 70 % of the total anions (TZ^-, in Eq. units), vary between 364 and 4260 µM. In particular, lower HCO_3 concentrations are observed for the upstream samples from the Chenab and Beas sub-basins. The HCO_3 concentrations co-vary linearly with Ca+Mg concentrations with a lower Ca+Mg/HCO_3 (in Eq. units) slope (~ 0.73) than unity. The dominant cation, Ca, varies from 247 to 1178 µM, and accounts for 70 % of the total cations (TZ^+, in Eq. units). The Mg (44 - 578 µM) and Na (2 - 2538 µM) concentrations in these samples also contribute 17 % and 10 % of the TZ^+ load, respectively. Upstream samples from selected sub-basins (Suru, Dras, Sind and Chenab) are composed of lower Na concentrations (13 ± 5 µM; $n = 8$) than that observed for all other samples (268 ± 470 µM; $n = 61$). The average silica concentration for all the samples (80 ± 42 µM; $n = 61$) overlaps with that reported for the Indus outflow (100 µM; Karim and Veizer, 2000) and global average for rivers (145 µM; Meybeck, 2003). The Cl and NO_3 concentrations for upper reaches samples (73 ± 89 µM and 22 ± 15 µM, respectively) are significantly lower than those observed for lower reaches (422 ± 655 µM and 78 ± 37 µM, respectively.)

Table 5.1. *The spatial sampling details (locations, pH, temperature and elevations) of the Indus headwater basin are provided.*

River Name	Sample ID	Locations	Latitude	Longitude	Date of collection	pH	Temperature (°C)	Elevation (m)
Indus Mainstream	INDW-21/49	Nior Nis	33.5	78.2	16-08-2021	8.2	13.0	3901
	INDW-21/50	Tirido	33.6	78.1	16-08-2021	8.3	14.7	3483
	INDW-21/51	Upstream Tunah	33.8	77.9	16-08-2021	8.3	14.8	3502
	INDW-21/52	Downstream Karu	34.0	77.7	16-08-2021	8.4	13.9	3309
	INDW-21/53	Spituk	34.1	77.6	17-08-2021	8.5	15.2	3216
	INDW-21/48	Nimoo (Before Zanskar Confluence)	34.2	77.3	13-08-2021	8.2	17.3	3112
	INDW-21/46	Nimoo (After confluence with Zanskar)	34.2	77.3	13-08-2021	8.5	13.5	3115
	INDW-21/45	Uleytokpo	34.3	77.1	13-08-2021	8.2	13.0	3044
	INDW-21/44	Khalsi	34.3	76.9	12-08-2021	8.3	12.6	2947
	INDW-21/43	Skurbuchan	34.4	76.7	12-08-2021	8.3	13.4	2899
	INDW-21/42	3km Upstream Dah	34.6	76.5	12-08-2021	7.9	14.0	2748
	INDW-21/41	Upstream Batalik	34.6	76.4	11-08-2021	8.2	14.4	2619
Tributaries								
Zanskar R.	INDW-21/47	Zanskar (Nimoo)	34.2	77.3	13-08-2021	8.5	12.1	3116
Shyok R.	INDW-21/56	Shoyk (Rangudu)	34.4	77.8	19-08-2021	8.4	12.0	3222
	INDW-21/54	Shoyk (Khalsar)	34.5	77.7	18-08-2021	8.4	13.0	3170
Nubra R.	INDW-21/55	Nubra (Panamik)	34.8	77.5	19-08-2021	8.6	5.9	3184
Suru R.	INDW-21/38	Suru (Kargil)	34.6	76.1	10-08-2021	7.0	11.7	2679
Dras R.	INDW-21/40	Dras [Karkitchoo (After conflu. with Singho)]	34.6	76.1	10-08-2021	7.8	12.5	2725
	INDW-21/39	Dras [Kaksor (Before confluence with Singho)]	34.6	76.0	10-08-2021	7.6	10.6	2726
	INDW-21/37	Dras (Dras)	34.4	75.8	09-08-2021	7.5	7.5	3061
Sind R.	INDW-21/36	Sind (Gund)	34.3	75.1	09-08-2021	8.0	12.0	3428
	INDW-21/35	Sind (Wayul Bridge)	34.3	74.8	09-08-2021	8.1	14.7	1669

Jhelum R.	INDW-21/28	Jhelum (Anantnag)	33.8	75.1	04-08-2021	7.7	19.0	1593
	INDW-21/29	Vaishno [Niana (Before conflu. with Jhelum)]	33.8	75.1	04-08-2021	7.5	21.7	1598
	INDW-21/30	Jhelum [Chechkut (After conflu. with Vaishno)]	33.9	75.0	04-08-2021	7.5	21.4	1593
	INDW-21/34	Jhelum (Sumbal)	34.2	74.7	08-08-2021	7.3	22.2	1582
	INDW-21/33	Jhelum (Sopore)	34.3	74.5	07-08-2021	7.2	22.7	1572
	INDW-21/32	Jhelum (Gantamulla)	34.2	74.2	07-08-2021	7.3	22.4	1548
	INDW-21/31	Jhelum (Dhanisaidan)	34.1	74.1	07-08-2021	8.1	23.2	1309
Chenab R.	INDW-21/58	Chenab (Teling)	32.4	77.2	21-08-2021	8.4	6.4	3071
	INDW-21/57	Chenab (Tandi)	32.5	77.0	21-08-2021	8.7	6.6	2869
	INDW-21/25	Chenab (Doda)	33.1	75.6	03-08-2021	7.7	15.3	848
	INDW-21/26	Chenab (Karol Bridge)	33.2	75.3	03-08-2021	7.6	15.9	689
	INDW-21/27	Chenab (Seri)	33.2	75.2	03-08-2021	8.0	15.8	675
	INDW-21/22	Chenab (Reasi)	33.1	74.8	01-08-2021	9.1	18.0	376
	INDW-21/21	Chenab (Akhnoor)	32.9	74.7	31-07-2021	9.1	18.4	304
Tawi R.	INDW-21/24	Tawi (Chenani)	33.0	75.3	02-08-2021	8.9	23.6	1003
	INDW-21/23	Tawi (Udhampur)	32.9	75.2	01-08-2021	9.1	24.4	613
	INDW-21/20	Tawi (Pingar)	32.8	75.1	30-07-2021	9.1	27.8	436
	INDW-21/19	Tawi (Jammu)	32.7	74.9	30-07-2021	8.8	28.7	318
Degh Nala	INDW-21/18	Degh Nala (Samba)	32.6	75.1	29-07-2021	9.0	31.2	334
Ravi R.	INDW-21/15	Ravi (Ranjit Sagar Dam Lake)	32.4	75.8	28-07-2021	9.1	28.0	506
	INDW-21/16	Ravi (Lakhanpur)	32.4	75.6	29-07-2021	8.2	25.0	337
	INDW-21/17	Ravi River tributary (Forlain)	32.4	75.4	29-07-2021	8.9	30.5	342
Chakki R.	INDW-21/13	Chakki (Pathankot)	32.3	75.7	28-07-2021	8.7	25.2	323
Beas R.	INDW-21/61	Beas (Mandi)	31.7	76.9	21-08-2021	9.6	18.2	759
	INDW-21/60	Beas (Kullu)	32.0	77.1	21-08-2021	9.4	15.1	1230
	INDW-21/59	Beas (Manali)	32.3	77.2	21-08-2021	8.9	12.0	2909

	INDW-21/11	Beas (Downstream Pong Dam)	31.9	75.9	27-07-2021	8.0	24.5	317
	INDW-21/14	Beas (Bela Mastgarh)	32.1	75.6	28-07-2021	8.4	25.5	262
	INDW-21/12	Beas (Kalechpur Kalota)	32.0	75.6	27-07-2021	8.5	23.7	237
	INDW-21/10	Beas (Bhoolpur)	31.7	75.5	27-07-2021	8.4	25.3	231
	INDW-21/04	Beas (Beas)	31.5	75.3	24-07-2021	8.1	25.9	218
	INDW-21/09	Beas [Goindwal Sahib (Before conflu. with Sutlej)]	31.4	75.1	25-07-2021	8.1	29.5	220
Sutlej R.	INDW-21/01	Sutlej (Ropar)	31.0	76.5	22-07-2021	7.9	25.5	270
	INDW-21/03	Sutlej (Begouual)	31.0	76.0	23-07-2021	8.1	31.4	246
	INDW-21/02	Sutlej (Ludhiana)	31.0	75.8	23-07-2021	7.8	30.9	234
	INDW-21/05	Sutlej (Maddepur)	31.0	75.5	24-07-2021	7.2	35.8	225
	INDW-21/06	Sutlej (Thamunwal)	31.0	75.3	24-07-2021	7.6	34.1	220
	INDW-21/08	Sutlej [Mandal (Before conflu. with Beas)]	31.1	75.1	25-07-2021	7.5	35.6	210
	INDW-21/07	Sutlej [Harike (After conflu. with Beas)]	31.1	74.9	25-07-2021	7.8	30.4	202
Rainwater	RW-21/01	Katra	33.0	74.9	01-08-2021	8.2	25.6	821
	RW-21/02	Sri Nagar	34.1	74.8	06-08-2021	7.1	19.2	3607
	Rain-22/01	Leh	34.2	77.6	--	--	--	3524
Glacier water	GLW-21/01	Zozila Pass	34.3	75.4	09-08-2021	7.6	6.3	3423
	GLW-21/02	Zozila Zero Point	34.3	75.5	09-08-2021	6.0	5.7	3498
	GLW-21/03	Chang La pass	34.1	77.9	15-08-2021	9.1	8.2	5060
	GLW-21/04	Khardungla Pass	34.3	77.6	19-08-2021	8.7	0.3	3221
Agriculture water	AGRW-21/01	Roopar	30.8	76.6	22-07-2021	8.8	33.5	295
	AGRW-21/02	Ludhiana	31.0	75.8	23-07-2021	8.1	31.4	239
	AGRW-21/03	Jallowal	31.3	75.4	24-07-2021	7.9	33.7	230
Hot springs	HS-22/01	Chumathang	33.4	78.4	--	--	--	3950
Groundwater	GW21/01	Roopar	30.8	76.6	22-07-2021	7.5	28.0	294
	GW21/02	Begouual	31.0	76.0	23-07-2021	8.1	31.4	245
	GW21/03	Jallowal	31.3	75.4	24-07-2021	7.2	26.5	230

GW21/04	Harike	31.1	74.9	25-07-2021	7.2	26.0	210
GW21/05	Khujala	31.7	75.1	27-07-2021	7.3	26.0	238
GW21/06	Manser	32.7	75.1	30-07-2021	7.5	24.0	679
GW21/07	Karua	33.0	74.9	01-08-2021	9.0	24.5	640
GW21/08	Bali	33.0	75.2	02-08-2021	8.0	23.3	803
GW21/09	Batote	33.1	75.3	03-08-2021	6.9	19.0	1318
GW21/10	Banihal	33.4	75.2	04-08-2021	6.9	16.3	1658
GW21/11	Naina	33.8	75.1	04-08-2021	6.7	21.7	1596
GW21/12	Rampur	34.1	74.2	07-08-2021	7.3	15.4	1461
GW21/13	Kargil	34.6	76.1	10-08-2021	6.9	10.6	2713
GW21/14	Leh	34.2	77.6	17-08-2021	7.6	9.5	3493
GW21/15	Diskit	34.5	77.6	19-08-2021	8.2	9.3	3150
GW21/16	Gondhala	32.5	77.0	21-08-2021	8.7	6.6	2869

Table 5.2. *The major ions, silica and alkalinity concentrations for the water samples (river, rain, glacier, agriculture, hot springs and groundwater) of Indus headwater basin.*

Sample ID	**Na**	**K**	**Ca**	**Mg**	**HCO_3**	**Cl**	**NO_3**	**SO_4**	**F**	**SiO_2**	**TZ^+**	**TZ^-**	**TZ^+/TZ^-**	**NICB**
	(µM)										**(µEq)**			**(%)**
INDW-21/49	482	43	594	229	1414	223	11	239	33	98	2304	2159	1.1	6
INDW-21/50	459	41	583	228	1360	200	11	229	34	97	2121	2062	1.0	3
INDW-21/51	421	43	555	216	1298	183	16	200	33	93	2007	1931	1.0	4
INDW-21/52	417	43	583	222	1366	172	13	203	33	93	2069	1990	1.0	4
INDW-21/53	494	48	661	250	1585	200	13	236	34	104	2364	2305	1.0	3
INDW-21/48	433	45	633	221	1421	172	7	237	29	101	2186	2103	1.0	4
INDW-21/46	113	29	554	181	937	49	11	299	24	46	1612	1619	1.0	0
INDW-21/45	91	29	587	169	959	43	13	322	24	44	1632	1683	1.0	-3
INDW-21/44	89	29	636	191	1100	38	10	352	24	45	1772	1876	0.9	-6
INDW-21/43	103	31	618	184	1087	41	11	323	24	46	1738	1810	1.0	-4

INDW-21/42	89	29	620	174	1100	38	11	346	24	48	1707	1865	0.9	-9
INDW-21/41	97	29	632	187	1114	44	11	342	24	52	1765	1877	0.9	-6
INDW-21/47	25	32	529	197	807	7	10	309	20	31	1509	1463	1.0	3
INDW-21/56	506	82	695	314	1489	352	21	284	24	63	2607	2454	1.1	6
INDW-21/54	571	91	734	367	1664	393	21	312	26	71	2864	2728	1.0	5
INDW-21/55	75	59	392	81	773	12	11	72	27	45	1079	967	1.1	11
INDW-21/38	18	45	667	92	1145	13	20	265	22	38	1580	1730	0.9	-9
INDW-21/40	22	0	417	46	821	0	18	100	0	60	948	1039	0.9	-9
INDW-21/39	8	22	604	136	1237	10	20	163	20	35	1511	1613	0.9	-7
INDW-21/37	2	0	717	136	1400	10	16	186	20	21	1708	1819	0.9	-6
INDW-21/36	12	0	688	264	1203	6	30	407	12	36	1916	2066	0.9	-8
INDW-21/35	16	0	639	195	1216	11	12	287	9	44	1684	1822	0.9	-8
INDW-21/28	76	25	587	88	1330	62	65	40	5	97	1449	1542	0.9	-6
INDW-21/29	115	43	599	119	1337	127	93	48	5	113	1595	1657	1.0	-4
INDW-21/30	87	25	600	92	1303	77	69	40	4	101	1496	1533	1.0	-2
INDW-21/34	127	31	778	170	1762	106	50	105	6	100	2054	2133	1.0	-4
INDW-21/33	83	20	710	124	1589	68	4	78	6	81	1772	1823	1.0	-3
INDW-21/32	81	0	672	118	1548	61	2	78	5	81	1662	1772	0.9	-6
INDW-21/31	81	20	687	114	1528	64	36	105	6	82	1702	1843	0.9	-8
INDW-21/58	12	34	294	107	364	9	13	174	22	31	848	756	1.1	11
INDW-21/57	18	27	340	115	405	20	11	220	22	28	955	898	1.1	6
INDW-21/25	14	52	448	44	683	9	15	213	8	37	1049	1141	0.9	-8
INDW-21/26	26	61	503	47	744	15	26	238	8	43	1188	1269	0.9	-7
INDW-21/27	25	57	489	99	696	11	18	232	10	42	1257	1199	1.0	5
INDW-21/22	22	68	529	56	928	11	21	208	8	49	1259	1383	0.9	-9
INDW-21/21	53	75	544	130	1037	14	28	191	8	46	1476	1470	1.0	0
INDW-21/24	81	29	534	55	1160	30	49	55	7	99	1288	1355	1.0	-5
INDW-21/23	93	41	549	54	1262	36	43	45	7	96	1338	1438	0.9	-7

INDW-21/20	190	43	967	188	2380	73	58	67	19	119	2543	2664	1.0	-5
INDW-21/19	252	59	912	166	2140	106	103	83	19	114	2468	2534	1.0	-3
INDW-21/18	493	75	1178	197	3094	89	60	86	21	153	3317	3435	1.0	-3
INDW-21/15	117	50	604	120	1096	49	49	217	21	13	1616	1649	1.0	-2
INDW-21/16	182	116	844	151	1703	106	112	216	21	137	2289	2373	1.0	-4
INDW-21/17	337	63	941	143	2303	48	53	67	21	135	2570	2560	1.0	0
INDW-21/13	163	66	538	123	1417	49	45	38	21	105	1549	1609	1.0	-4
INDW-21/61	86	45	247	69	453	63	23	90	22	89	762	740	1.0	3
INDW-21/60	80	45	252	55	432	55	16	88	20	78	741	701	1.1	6
INDW-21/59	21	50	299	92	449	13	16	156	0	63	854	791	1.1	8
INDW-21/11	362	75	680	127	1587	293	70	79	21	90	2051	2128	1.0	-4
INDW-21/14	204	70	495	129	1280	90	73	36	21	111	1524	1537	1.0	-1
INDW-21/12	127	61	633	118	1310	54	62	192	19	90	1691	1829	0.9	-8
INDW-21/10	228	66	689	145	1499	147	70	130	21	99	1961	1996	1.0	-2
INDW-21/04	321	70	688	142	1635	257	65	99	21	90	2052	2176	0.9	-6
INDW-21/09	305	75	683	136	1601	244	72	105	21	90	2016	2147	0.9	-6
INDW-21/01	206	52	716	238	1390	112	37	377	21	70	2165	2314	0.9	-7
INDW-21/03	178	61	746	237	1437	82	47	365	22	74	2205	2318	1.0	-5
INDW-21/02	291	77	750	237	1485	156	82	360	22	80	2342	2466	0.9	-5
INDW-21/05	2509	227	996	474	2510	2277	2	425	26	172	5675	5665	1.0	0
INDW-21/06	1296	154	902	338	2065	1044	191	415	24	121	3929	4154	0.9	-6
INDW-21/08	2538	348	1087	578	4260	1797	68	292	29	269	6216	6740	0.9	-8
INDW-21/07	319	72	708	149	1673	252	63	102	22	95	2105	2216	0.9	-5
RW-21/01	13	20	72	4	197	4	9	6	--	--	186	222	0.8	--
RW-21/02	10	7	61	1	112	15	22	13	--	--	141	175	0.8	--
Rain-22/01	0	0	74	63	102	--	--	--	--	0.68	--	--	--	--
GLW-21/01	13	3	689	860	2007	28	31	421	--	52	3115	2908	1.1	--
GLW-21/02	13	21	286	120	344	24	28	201	--	24	845	799	1.1	--

GLW-21/03	0	2	8	4.0	0	19	14	22	--	0	26	77	0.3	--
GLW-21/04	1	2	26	3	0	21	28	0	--	0	62	49	1.3	--
AGRW-21/01	4865	51	370	423	5697	123	38	277	--	165	6501	6411	1.0	--
AGRW-21/02	415	72	687	295	1939	83	12	136	--	139	2450	2305	1.1	--
AGRW-21/03	306	97	748	454	2116	206	18	143	--	179	2806	2626	1.1	--
HS-22/01	13008	448	655	47	7306	2745	25	2473	--	1552	--	--	--	--
GW21/01	5114	66	569	291	6241	109	8	341	70	368	6898	7119	1.0	--
GW21/02	533	200	2258	967	4778	187	80	617	33	283	7182	6313	1.1	--
GW21/03	1108	152	2247	1103	4755	622	285	630	33	500	7961	6957	1.1	--
GW21/04	340	91	1824	486	4641	264	17	0	26	313	5053	4948	1.0	--
GW21/05	1902	202	2053	1291	6439	326	226	317	44	417	8791	7669	1.2	--
GW21/06	4460	84	2598	1000	6664	2122	1565	594	51	374	11740	11590	1.0	--
GW21/07	12342	64	259	168	13087	168	4	59	26	213	13260	13403	1.0	--
GW21/08	535	29	2206	310	3814	103	144	60	26	192	5596	4208	1.3	--
GW21/09	1620	64	1793	592	5907	282	175	61	28	184	6456	6515	1.0	--
GW21/10	1234	75	2634	1172	5178	1170	874	348	0	221	8921	7918	1.1	--
GW21/11	374	0	2227	684	5478	175	0	71	24	304	6195	5820	1.1	--
GW21/12	226	109	1360	230	2621	92	95	365	33	196	3516	3570	1.0	--
GW21/13	490	68	1227	577	2294	229	203	691	21	171	4168	4128	1.0	--
GW21/14	209	61	1012	214	2048	211	158	99	21	283	2722	2636	1.0	--
GW21/15	153	32	1105	200	2294	57	24	92	17	80	2795	2575	1.1	--
GW21/16	112	61	552	153	749	12	5	407	21	164	1582	1599	1.0	--

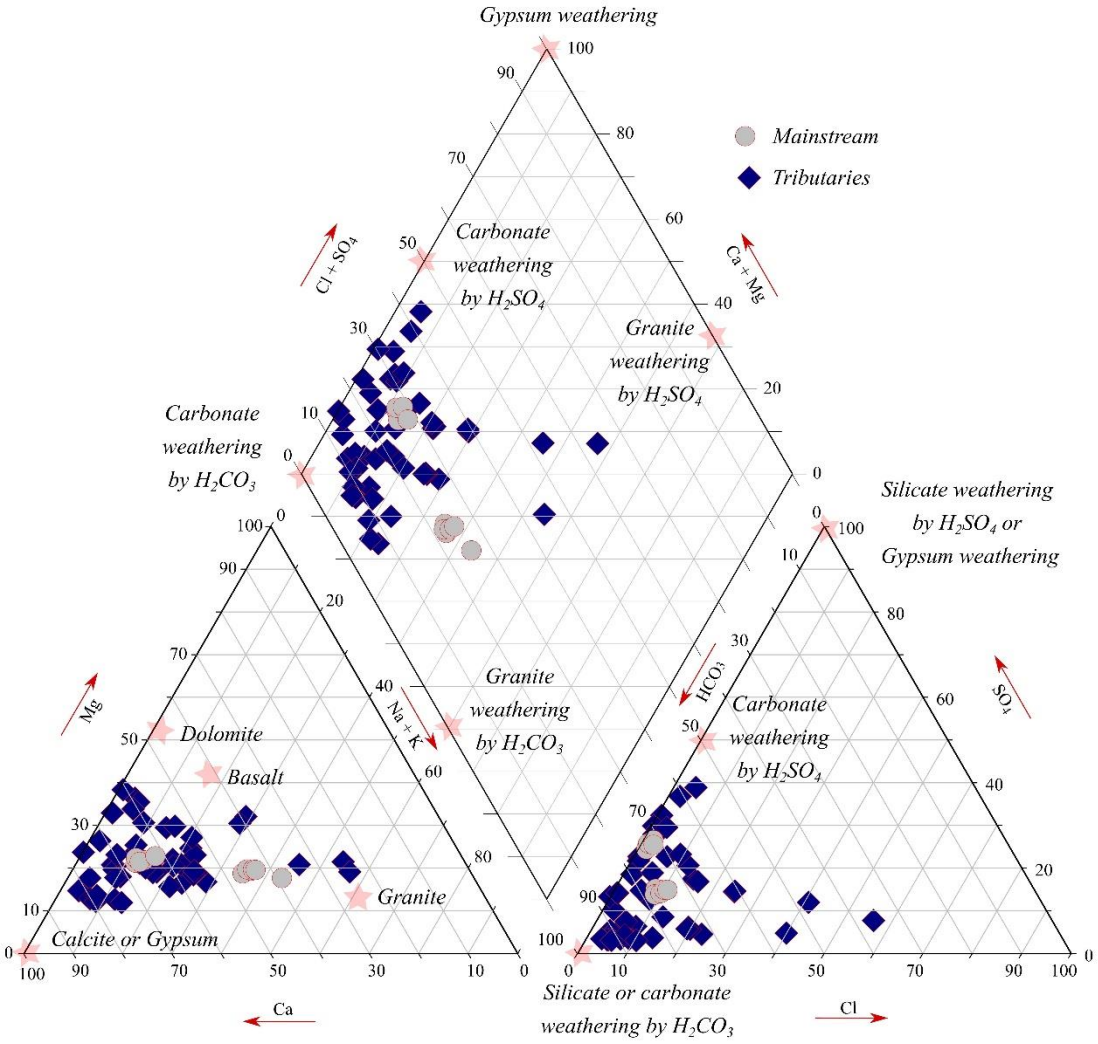

Figure 5.2. *Ternary diagram of the major ions for the upper Indus samples. For reference, typical compositions expected for different weathering pathways (Spence and Telmer, 2005) are also shown.*

The SO_4 concentrations for the Indus headwater basin vary between 36 and 425 µM. Average of these concentrations (195 ± 114 µM; n = 61) is comparable to that reported for the Indus outflow (312 µM; Karim and Veizer, 2000) during high flow stages, and about two times higher than the Ganga (58 µM; Sarin et al., 1989), Brahmaputra (78 µM; Singh et al., 2005) and the global average (pre-industrial) SO_4 for rivers (~ 88 µM; Meybeck, 2003). Figure 5.3. compares the sulfur ($\delta^{34}S_{SO4}$) and oxygen ($\delta^{18}O_{SO4}$) isotopic data for the Indus headwater with those reported for other global rivers (Relph et al., 2021). The $\delta^{34}S_{SO4}$ for our samples fluctuates between - 11.2 ‰ (Dras) and 5.5 ‰ (Sind), with most of the samples (45 out of 50) having systematically lower values than the global average $\delta^{34}S_{SO4}$ for rivers (~ 4.4 ‰, Burke et al., 2018; Fig. 5.3.).

Table 5.3. *The chemical (TDS, TSS, CSI and DSI) and isotopic ($\delta^{34}S_{SO4}$, $\delta^{18}O_{SO4}$, $\delta^{18}O_{H2O}$) datasets for the Indus headwater.*

Sample ID	TDS	TSS	Saturation index		$\delta^{34}S_{SO4}$	$\delta^{18}O_{SO4}$	$\delta^{18}O_{H2O}$
	(mg/L)		Calcite	Dolomite	(‰)		
INDW-21/49	166	37	-0.1	-0.5	-2.8	-4.6	-13.5
INDW-21/50	160	--	0.0	-0.3	-1.5	-4.6	-13.9
INDW-21/51	151	--	-0.1	-0.4	-2.0	-6.1	-13.8
INDW-21/52	156	--	0.1	-0.2	-2.3	-4.4	-13.4
INDW-21/53	180	--	0.3	0.4	-2.5	-5.4	-13.3
INDW-21/48	165	74	0.0	-0.3	-4.6	-4.8	-13.8
INDW-21/46	122	196	0.0	-0.4	-6.1	-4.2	-14.5
INDW-21/45	126	87	-0.3	-1.0	-5.4	-4.2	-14.3
INDW-21/44	139	60	-0.1	-0.5	-6.3	-4.4	-14.4
INDW-21/43	136	90	-0.1	-0.5	-6.3	-4.3	-14.5
INDW-21/42	138	82	-0.4	-1.3	-5.7	-3.4	-14.2
INDW-21/41	140	66	-0.1	-0.7	-6.4	-4.6	-14.3
INDW-21/47	110	--	-0.1	-0.5	-6.2	-3.3	-14.7
INDW-21/56	186	--	0.2	0.2	-0.2	-8.5	-15.6
INDW-21/54	207	218	0.3	0.4	-1.5	-5.7	-15.5
INDW-21/55	80	281	-0.2	-1.1	2.0	-6.5	-16.0
INDW-21/38	131	112	-1.3	-3.4	-3.8	-2.5	-13.4
INDW-21/40	83	--	-0.8	-2.5	-5.4	-5.1	-11.7
INDW-21/39	124	44	-0.7	-2.0	-8.3	-2.7	-11.4
INDW-21/37	138	154	-0.8	-2.2	-11.2	-4.1	-12.8

INDW-21/36	151	--	-0.3	-1.0	5.5	8.7	-9.4
INDW-21/35	136	--	-0.2	-0.9	5.3	9.7	-9.2
INDW-21/28	126	14	-0.5	-1.7	--	--	-7.8
INDW-21/29	135	15	-0.6	-1.8	--	--	-8.0
INDW-21/30	126	21	-0.7	-2.0	--	--	-8.1
INDW-21/34	170	--	-0.6	-1.8	5.1	8.3	-8.2
INDW-21/33	146	--	-0.7	-2.1	--	--	-7.8
INDW-21/32	141	--	-0.7	-2.1	--	--	-7.7
INDW-21/31	146	--	0.1	-0.5	5.0	6.8	-7.8
INDW-21/58	58	77	-0.8	-2.0	-0.2	-3.1	-13.1
INDW-21/57	67	91	-0.4	-1.2	-1.1	-2.9	-12.9
INDW-21/25	87	230	-0.9	-2.8	1.8	-1.9	-12.0
INDW-21/26	97	78	-1.0	-2.9	2.0	-0.7	-11.9
INDW-21/27	94	--	-0.6	-1.8	1.6	-1.7	-11.9
INDW-21/22	107	198	0.6	0.3	1.3	-1.0	-11.4
INDW-21/21	116	900	0.7	0.9	-0.7	-1.6	-11.0
INDW-21/24	112	16	0.6	0.4	--	--	-7.0
INDW-21/23	118	99	0.9	0.8	3.9	8.4	-8.0
INDW-21/20	215	56	1.3	2.0	--	--	-6.9
INDW-21/19	205	155	1.1	1.6	3.1	10.3	-6.7
INDW-21/18	280	62	1.5	2.3	--	--	-6.3
INDW-21/15	125	--	0.8	1.1	4.9	2.3	-7.1
INDW-21/16	190	--	0.4	0.1	2.0	3.2	-7.6
INDW-21/17	212	--	1.2	1.8	--	--	-7.1
INDW-21/13	132	1806	0.5	0.6	--	--	-8.4
INDW-21/61	61	20	0.3	0.2	3.6	1.2	-9.6

INDW-21/60	58	--	0.2	-0.2	2.3	1.5	-7.9
INDW-21/59	64	--	-0.2	-0.8	0.5	0.8	-9.8
INDW-21/11	167	4	0.0	-0.5	3.3	3.6	-6.9
INDW-21/14	127	3773	0.2	-0.1	--	--	-7.0
INDW-21/12	143	125	0.4	0.2	4.0	0.9	-7.7
INDW-21/10	159	109	0.4	0.2	3.7	2.9	-7.2
INDW-21/04	169	69	0.1	-0.3	2.9	4.6	-7.0
INDW-21/09	167	--	0.2	-0.1	4.1	3.7	-7.0
INDW-21/01	173	--	-0.1	-0.6	-7.3	-2.2	-10.7
INDW-21/03	176	--	0.2	0.0	-6.9	-2.0	-10.7
INDW-21/02	187	--	-0.1	-0.6	-7.3	-1.9	-10.2
INDW-21/05	404	--	-0.3	-0.8	-1.5	1.8	-9.6
INDW-21/06	303	48	-0.1	-0.4	-4.2	0.7	-9.8
INDW-21/08	502	--	0.3	0.4	-1.7	2.1	-8.3
INDW-21/07	173	--	0.0	-0.6	1.3	4.9	-6.5
RW-21/01	17	--	-1.5	-4.2	--	--	-12.9
RW-21/02	13	--	-3.1	-7.8	--	--	-2.6
Rain-22/01	11	--	--	--	11.2	11.3	--
GLW-21/01	218	--	-0.6	-1.0	*-3.2*	*0.7*	*-4.6*
GLW-21/02	60	--	-3.3	-6.8	--	*-4.3*	*-5.3*
GLW-21/03	4	--	--	--	--	--	*-12.4*
GLW-21/04	4	--	--	--	--	--	*-11.0*
AGRW-21/01	530	--	1.0	2.3	3.5	16.4	-6.3
AGRW-21/02	190	--	0.3	0.3	-1.7	9.8	-5.3
AGRW-21/03	214	--	0.3	0.4	-14.9	3.1	-5.6
HS-22/01	1219	--	--	--	5.8	2.0	--

GW21/01	591	--	0.0	-0.2	--	13.6	-7.2
GW21/02	514	--	1.1	2.0	2.2	10.3	-7.9
GW21/03	569	--	0.1	0.1	-15.4	3.6	-6.1
GW21/04	409	--	0.1	-0.3	--	--	-7.4
GW21/05	640	--	0.3	0.6	-0.6	9.1	-5.2
GW21/06	894	--	0.6	0.8	7.9	15.9	-4.2
GW21/07	1124	--	1.2	2.3	--	21.8	--
GW21/08	372	--	0.8	0.9	2.0	18.3	-6.2
GW21/09	525	--	-0.3	-0.9	3.9	16.9	-7.9
GW21/10	624	--	-0.2	-0.7	3.4	6.5	-7.0
GW21/11	480	--	-0.4	-1.1	--	14.0	-7.0
GW21/12	286	--	-0.3	-1.4	10.0	12.7	-7.8
GW21/13	315	--	-0.9	-2.1	-6.4	0.3	-14.3
GW21/14	222	--	-0.3	-1.3	5.8	-3.0	-13.3
GW21/15	211	--	0.3	0.0	3.5	-6.7	-13.0
GW21/16	127	--	0.0	-0.5	4.9	7.5	-12.2

Whilst the $\delta^{34}S_{SO4}$ values for the Indus fall intermediate to that reported for its major sources (e.g. pyrite, gypsum, hot springs and pollution), the dataset is more proximal to the pyrite end-member (Fig. 5.3.). The $\delta^{18}O_{H2O}$ values vary between - 16 ‰ and - 6 ‰. These values are comparable to that reported earlier for upper Indus basin (Pande et al., 2000; Sharma et al., 2017), and outflow (~ - 10.5 ‰; Karim et al., 2002). The $\delta^{18}O_{SO4}$ values vary from - 8.5 ‰ to 10.3 ‰, which correspond to an average $\Delta^{18}O_{SO4\text{-}H2O}$ value of 11 ± 3 ‰. This average $\Delta^{18}O_{SO4\text{-}H2O}$ value is depleted with respect to that of the global rivers, and is proximal to the pyrite end-member value (Fig. 5.3.).

The chemical and isotopic data show strong spatial variation for the Indus mainstream in the studied region, despite of minimal altitude (3158 ± 355 m; n = 12) and temperature (14 ± 1 °C; n = 12) variations. The Na (~ 450 µM) and Cl (~ 190 µM) concentrations of the Indus mainstream decrease significantly after its confluence (~ 100 µM and ~ 42 µM, respectively) with the Zanskar tributary. Likewise, the Silica concentrations also decrease by ~ 2 times. This decrease in Na, Cl and SiO_2 concentrations are consistent with the Zanskar water chemistry which is characterized with lower concentrations for these parameters than those of the upstream samples. Each of these concentration changes reflects a supply of 75 - 79 % of the solutes from the Zanskar to the upper Indus mainstream. Average TDS, Ca, Mg and HCO_3 concentrations remain near invariant along the course of the Indus headwater. In contrast, the sulfate concentrations of the Indus (224 ± 18 µM; n = 6) increase by about 1.5 times (331 ± 20 µM; n = 6) after its confluence with the Zanskar. Consistently, the $\delta^{34}S_{SO4}$ values of the Indus decrease from - 2.8 ‰ to - 6.1 ‰ as a result of its confluence with the Zanskar. The $\delta^{18}O_{SO4}$ (-4.6 ± 0.7 ‰; n = 12) and $\delta^{18}O_{H2O}$ (-14.0 ± 0.4 ‰; n = 50) show no major spatial variation. In addition, the $\delta^{34}S_{SO4}$ of the Indus headwater gets enriched by ~ 4.5 ‰ as it flows through the floodplain region, and attains a value of 0.8 ‰ at its outflow (Karim and Veizer, 2000).

5.3. Discussion

5.3.1. Water chemistry and solute sources

Water chemistry of the Indus headwater, like for any river, is controlled by solute supply from dissolution of bedrocks (carbonates, silicates and evaporites), hot springs, and atmospheric and anthropogenic supplies. The silicate rocks present in the basin are mainly from the Higher Himalaya, Trans-Himalaya, and Ladakh and Karakoram batholiths (cf. chapter 2). The ternary plot for the major ions data (Fig. 5.2.) has been used to constrain the major rock-

types and also, acids involved for the weathering reaction. These data from the Indus headwater mainly fall between the carbonate and silicate rocks compositions. Further, most of the dataset cluster around the zones expected for H_2CO_3 and H_2SO_4 acid-mediated carbonate weathering, and also, H_2CO_3-mediated silicate weathering (Fig. 5.2.).

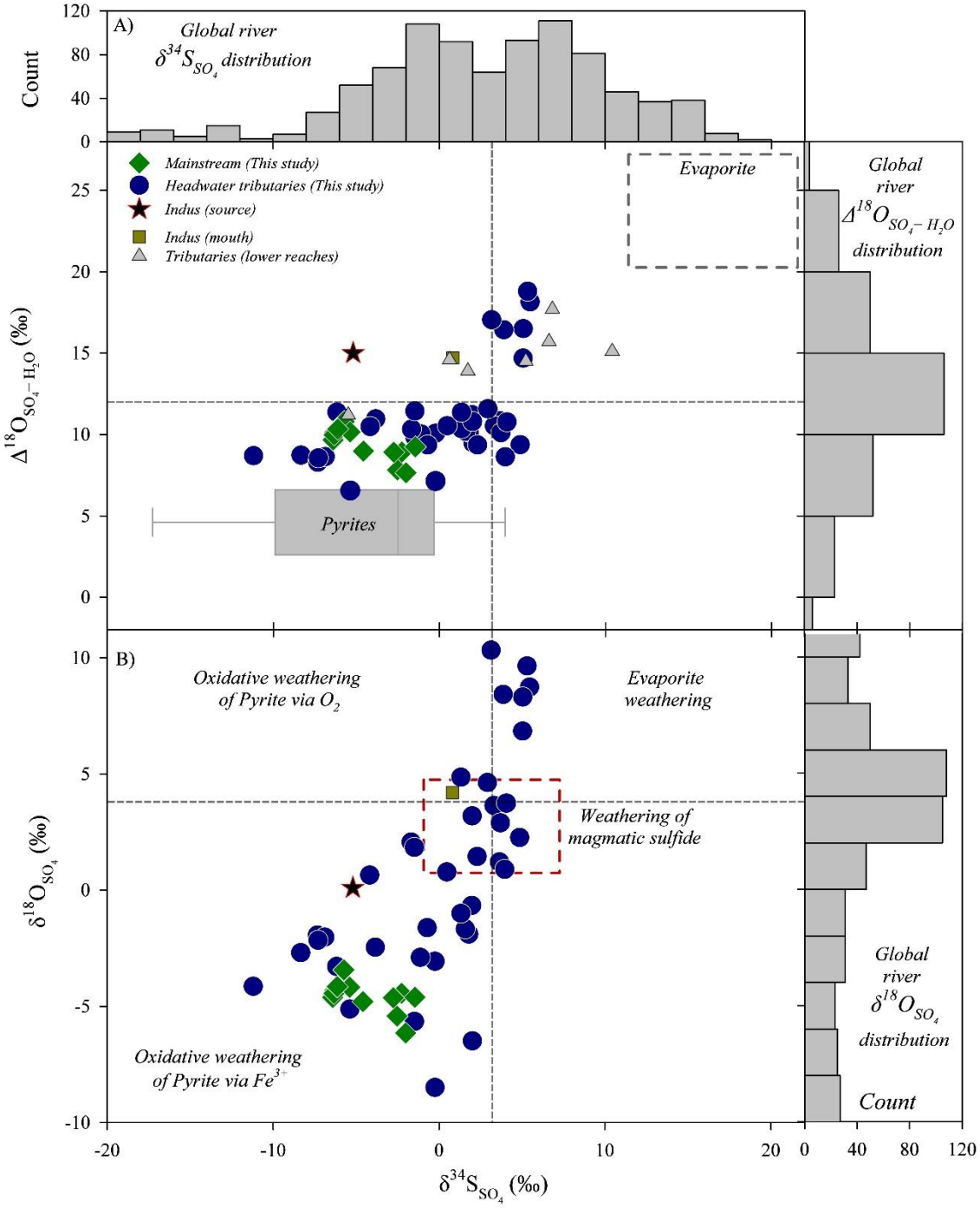

Figure 5.3. *Co-variation plot for (A) $\Delta^{18}O_{SO4\text{-}H2O}$, and (B) $\delta^{18}O_{SO4}$ with $\delta^{34}S_{SO4}$ for the upper Indus samples. For reference, the typical end-member values (e.g., pyrite: Stebbins et al., 2019 and evaporites: Relph et al., 2021) and frequency distribution of reported isotopic data for global rivers (Relph et al., 2021) are also shown.*

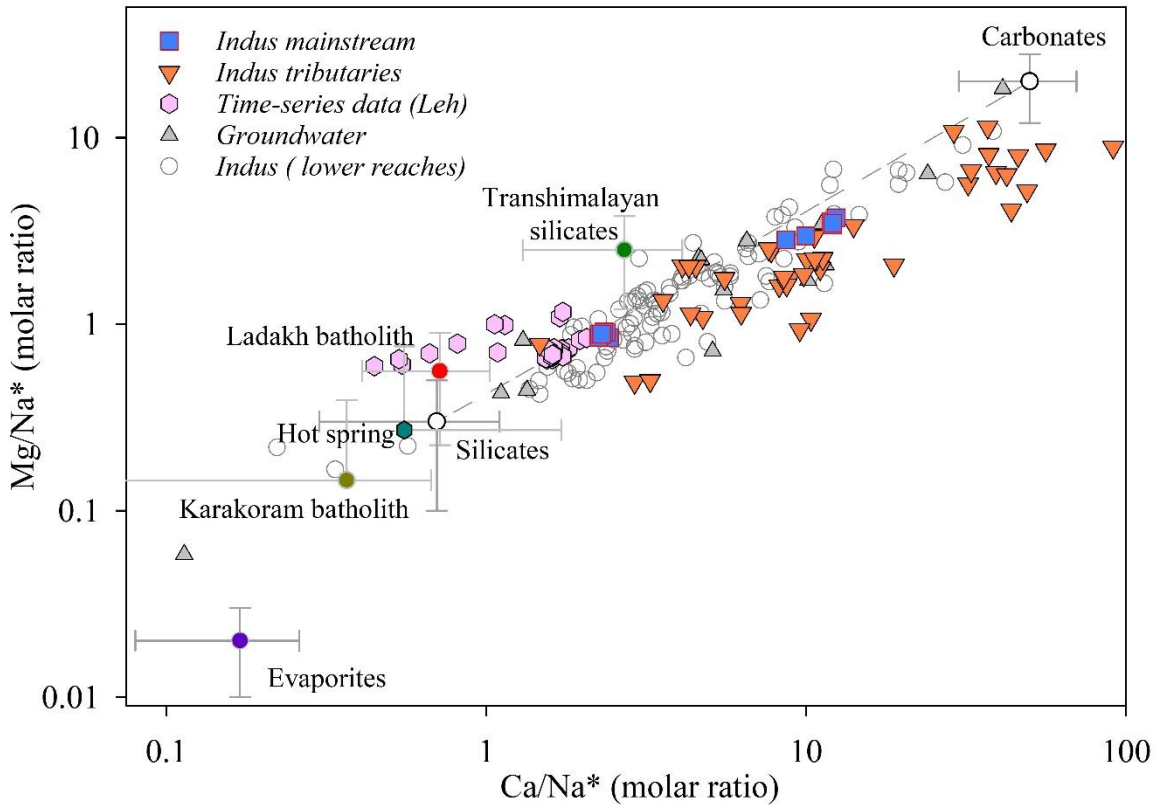

Figure 5.4. *Mixing plot between Ca/Na* and Mg/Na* for the upper Indus samples. The time-series data for Leh is also shown for comparison. The average compositions for selected major sources are also shown for reference. (Data source: Krishnaswami et al., 1999; Karim and Veizer, 2000; Millot et al., 2003; Singh et al., 2005; Reichardt et al., 2010; Heri et al., 2015; Tiwari et al., 2016).*

We have also inspected the mixing plot between Ca/Na* and Mg/Na* ratios to assess the solute source contribution (Fig. 5.4.). The highest Ca/Na* ratio, however, is observed for a sample from the glacier-dominated Suru (~ 138) River, indicating dominancy of carbonate dissolution in the basin. Similarly, most of the samples from the high-elevated terrains fall closer to the silicate end-member in the Ca/Na*- Mg/Na* plot (Fig. 5.4.). In this plot, four samples with negative Na* values have not been included. Two of these samples are from the Dras region with near-zero Na concentrations (Table 5.2.), pointing to dominancy of carbonate dissolution in this glaciated sub-basin; whereas, the other two samples from the lower reaches (Vaishno and Chenab) possibly hint at influence of anthropogenic supplies. Interestingly, several samples from the lower reaches (particularly from the Chenab and Jhelum) are characterized with high Ca/Na* and Mg/Na* ratios and fall closer to the carbonate and anthropogenic compositions (Fig. 5.4.). As carbonates are often devoid of Na, these high ratios possibly point to high anthropogenic supplies to these basins with significant agricultural

activities. This plot, therefore, indicates multiple solute sources (silicate, carbonate and anthropogenic) to the upper Indus, which must be involved in the source apportionment calculations.

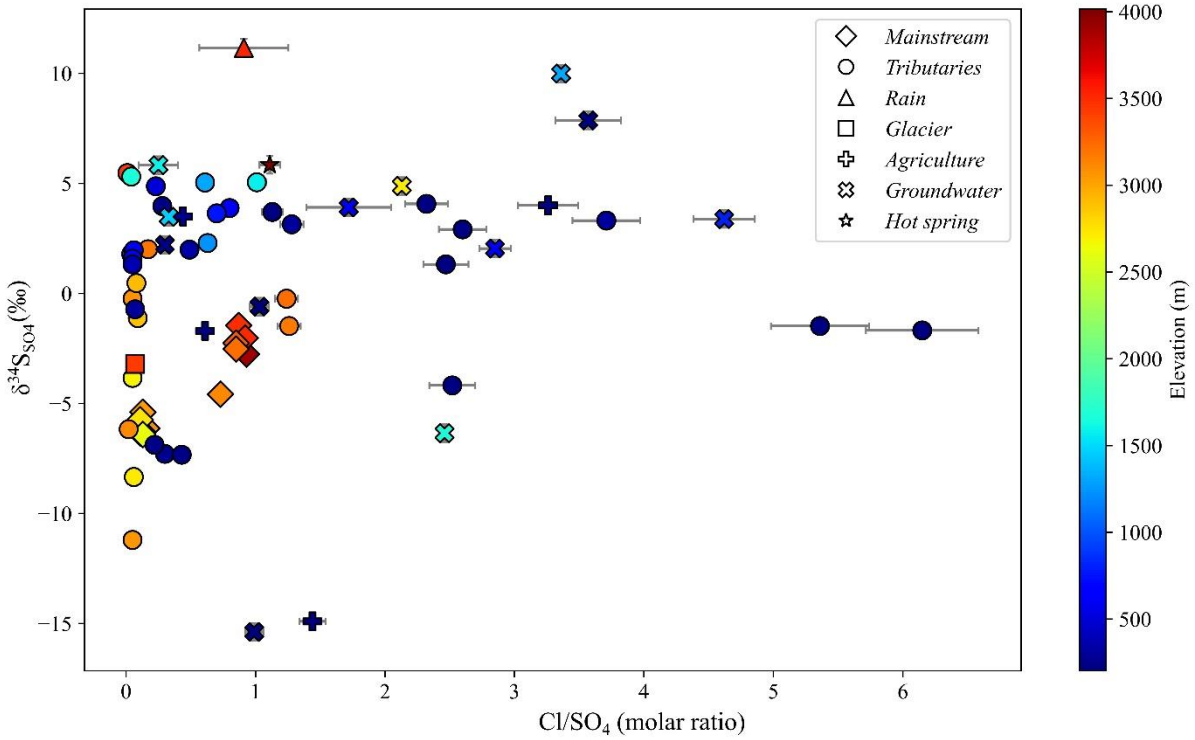

Figure 5.5. *Co-variation between Cl/SO$_4$ and $\delta^{34}S_{SO4}$ for Indus samples and their sources (rain, glacier, agriculture, groundwater and hot springs) are shown. The colorbar represents the elevation of the corresponding sampling locations. The samples from the higher altitude regions, showing lighter sulfur isotopic signatures point to relatively higher sulfide oxidation rates in these regions.*

The co-variation plot between dissolved Cl/SO$_4$ and $\delta^{34}S_{SO4}$ values of the upper Indus also points to multiple sulfate sources to the basin (Fig. 5.5.). Like for cations, samples from lower reaches, particularly those from the Chenab and Beas, are characterized by high Cl/SO$_4$ ratio, attributable to sewage supply from agricultural and other man-made activities. The $\delta^{34}S_{SO4}$ for these samples are also found overlapping with that of agricultural wastes (Fig. 5.5.). Excluding these, the elemental and isotopic values for the upper reaches samples mostly fall between the end-member compositions expected for major minerals (gypsum and pyrite) and also, glaciers and hot springs. In particular, the average $\delta^{34}S_{SO4}$ value for the samples from high-elevation (>2500 m; n = 24) is found to be ~ - 3 ‰, which is closer to that of the pyrites (~ - 12 ‰; Burke et al., 2018) than the gypsum (~ 17 ‰). Further, selected samples from sub-basins with occurrences of hot springs also show overlapping $\delta^{34}S_{SO4}$ and Cl/SO$_4$ values with that expected for this source (Fig. 5.5.).

5.3.2. Estimation of weathering rates

5.3.2.1. Cationic sources

We have used an inversion approach involving elemental ratios to quantify the contributions of cations from major sources. The algorithm used for this modeling is same as that of Tripathy and Das (2014), which has been successfully used for apportioning sources of river water (Tripathy and Singh, 2010; Samanta et al., 2021), coastal (Danish et al., 2021) and open (Goswami et al., 2014) seawater, and oceanic sediments (Tripathy et al., 2014). Briefly, this model uses a Quasi-Newton non-linear optimization algorithm, which iterates from *a-priori* defined end-member compositions to find a best-fit solution for the following set of equations. These mass balance equations relate observed data with model parameters for the water samples (Table 5.1.-5.5.) are as follows.

$$\left(\frac{X}{Na}\right)_{riv} = \sum_{i=1}^{i=5}\left(\frac{X}{Na}\right)_i \quad (5.1)$$

$$1 = \sum_{i=1}^{i=5} f_i \quad (5.2)$$

here, the subscripts, *riv* and *i*, stand for the sample and end-member compositions. The *i* value varies from 1 to 5, reflecting five major sources (rain, silicate, carbonate, hot springs and pollution) for the Indus headwater basin. The $(X/Na)_i$ stands for the Na-normalized ratio for element, X (= Cl, Ca, Mg and alkalinity), for the source, *i*. We have assumed that all the rain-corrected K is derived from silicate sources. The f_i value reflects the relative contribution of Na for source, *i*. The *a-priori* source data and outcomes of these model are provided in the Table 5.4.–5.7. The average compositions for the Himalayan silicates (Krishnaswami et al., 1999), hot springs from the Indus headwater basin (Tiwari et al., 2016), and conventional carbonates are taken from literature (Millot et al., 2003). We have used average seawater composition as end-member compositions for rain and halite sources (Roy-Barman and Jeandel, 2016). Selected samples from the lower reaches, mainly from the Sutlej, Beas, Ravi, Jhelum, and Tawi sub-basins, are also influenced by agricultural and other anthropogenic sources. We have analysed three agricultural samples from the Sutlej sub-basin, and average compositions of these samples have been used as pollution end-member.

Estimated cation supply from rain (4 ± 5 %), silicate (17 ± 11 %), carbonate (66 ± 17 %), hot springs (6 ± 5 %) and pollution (6 ± 7 %) sources for the Indus samples are shown in Fig. 5.6.

Table 5.4. *A-priori end-member compositions for major cations sources for sample sets with no pollution end-member from the upper reaches. The a-posteriori compositions yielded from the inverse model are also listed for comparison.*

	Apriori data				**Aposteriori data**				*Ref.*
Cationic sources									
	Cl/Na	**Ca/Na**	**Mg/Na**	**HCO_3/Na**	**Cl/Na**	**Ca/Na**	**Mg/Na**	**HCO_3/Na**	
Rain (halite)	1.17 ± 0.06	0.02 ± 0.001	0.11 ± 0.01	0.01 ± 0.001	1.40 ± 0.06	0.02 ± 0.001	0.11 ± 0.01	0.01 ± 0.001	*[1]*
Silicate	0.001 ± 0.001	0.7 ± 0.3	0.3 ± 0.15	2 ± 1	0.001 ± 0.001	0.19 ± 0.08	0.07 ± 0.03	1.4 ± 0.2	*[2]*
Carbonate	0.001 ± 0.0001	50 ± 20	20 ± 8	100 ± 40	0.001 ± 0.0001	202.0 ± 14.4	21.3 ± 2.0	335.8 ± 24.3	*[3]*
Hotspring	0.5 ± 0.4	0.14 ± 0.27	0.10 ± 0.10	0.8 ± 0.3	1.68 ± 0.18	0.12 ± 0.23	14.5 ± 1.8	0.7 ± 0.3	*[4]*

[1] Roy-Barman and Jeandel, 2016; [2] Krishnaswami et al., 1999; [3] Millot et al., 2003; [4] Tiwari et al., 2016

Table 5.5. *A-priori end-member compositions for major cations sources for sample sets with pollution end-member from the lower reaches. The a-posteriori compositions yielded from the inverse model are also listed for comparison.*

	Apriori data				**Aposteriori data**				*Ref.*
Cationic sources									
	Cl/Na	**Ca/Na**	**Mg/Na**	**HCO_3/Na**	**Cl/Na**	**Ca/Na**	**Mg/Na**	**HCO_3/Na**	
Rain (halite)	1.17 ± 0.06	0.02 ± 0.001	0.11 ± 0.01	0.01 ± 0.001	1.14 ± 0.06	0.02 ± 0.001	0.11 ± 0.01	0.005 ± 0.001	*[1]*
Silicate	0.001 ± 0.001	0.7 ± 0.3	0.3 ± 0.15	2 ± 1	0.001 ± 0.001	0.2 ± 0.1	0.06 ± 0.03	1.0 ± 0.2	*[2]*
Carbonate	0.001 ± 0.0001	50 ± 20	20 ± 8	100 ± 40	0.001 ± 0.0001	26.4 ± 2.5	2.1 ± 0.4	57.7 ± 5.3	*[3]*
Hotspring	0.5 ± 0.4	0.14 ± 0.27	0.10 ± 0.10	0.8 ± 0.3	3.5 ± 0.5	0.05 ± 0.09	0.05 ± 0.05	0.7 ± 0.2	*[4]*
Pollution	0.3 ± 0.3	1.4 ± 1.2	0.8 ± 0.7	4.3 ± 2.9	0.12 ± 0.11	1.0 ± 0.6	2.7 ± 0.4	1.4 ± 0.9	*This study*

[1] Roy-Barman and Jeandel, 2016; [2] Krishnaswami et al., 1999; [3] Millot et al., 2003; [4] Tiwari et al., 2016

The contribution for the silicate derived cations (Cat_s) for the Indus headwater basin varies from 0.1 % to 53 % with highest contribution is observed for the Sutlej sub-basin whereas, the lowest is observed for Dras River basin. The carbonate-derived cations for these two streams are estimated to be 97 % (Dras) and 17 % (Sutlej). Samples from the lower reaches (Sutlej, Beas, Ravi, Tawi and Jhelum) are found to have significant (0 to 26 %) cationic contribution from anthropogenic sources. These basins are actively influenced by the extensive agricultural practices in these regions. Further, appreciable supply of hot springs contribution is observed for selected sub-basins (Indus, Shyok, Chenab and Sutlej River). Highest contribution from this source is observed for the Shyok sub-basin (~ 15 %). We have used the estimated data for the Indus mainstream at Batalik (Fig. 2.4.) to compute the representative CO_2 consumption rate for the upper Indus basin. At this location, the silicate-derived cation (Cat_s) is 205 ± 12 µEq, which is about five times lower than that derived by carbonate (1290 ± 132 µEq) weathering. This Cat_s value corresponds to a CO_2 consumption rate of $2 \pm 0.1 \times 10^5$ mol/km^2/yr. This rate is a few times lower than that reported for the headwater of the Ganga (3.8×10^5 mol/km^2/yr; Krishnaswami et al., 1999), and Brahmaputra at eastern syntaxis (19×10^5 mol/km^2/yr; Singh et al., 2005), and about two times higher than that observed for global average for rivers (0.9×10^5 mol/km^2/yr; Gaillardet et al., 1999). The Indus River originates from a high elevation (~ 5486 m), and its basin relief for the mainstream in the studied region changes by ~ 1300 m for a traverse of ~ 400 km length. This relief change, however, seem to have minimal effect on chemical weathering in this region with colder climate, as evident from insignificant correlation between elevation and TDS of samples. We, therefore, have assessed the role of temperature in regulating the silicate weathering in this region. For this, co-variation between 1/T (inverse of water temperature) and logarithm of silica concentrations has been evaluated. A strong anti-correlation between these two parameters has been observed (Fig. 5.6. B), which is consistent with the Arrhenius kinetic equation (White et al., 1999; Dalai et al., 2002a). Samples with lower temperature are found to have lower silica concentrations, indicating strong control of temperature on mineral dissolution in this basin.

5.3.2.2. Sulfate sources

The $\delta^{18}O_{SO4}$ of water samples is mainly regulated by the $\delta^{18}O_{SO4}$ values of major minerals (pyrites and gypsum), and other sulfate sources (rain, hot springs, and pollution), and their relative contributions. The $\delta^{18}O_{SO4}$ serve as a better proxy (over sulfur isotopes) for source apportionment as this value for the major sulfur-bearing minerals exhibits limited variations.

Table 5.6. *The source apportionment results of various sources for cations and sulfates (rain, silicate (s), carbonate (c), hot springs (hs), pollution (poll), pyrite (py) and gypsum (gy)) are provided.*

Sample ID	Source apportionment results for cations					Source apportionment results for sulfate				
	Cat_{rain}	Cat_{s}	Cat_{c}	Cat_{hs}	Cat_{poll}	f_{rain}	f_{hs}	f_{poll}	f_{py}	f_{gy}
INDW-21/49	0.12 ± 0.01	0.33 ± 0.02	0.46 ± 0.05	0.11 ± 0.02	0 ± 0	0.04 ± 0	0.01 ± 0	0 ± 0	0.79 ± 0.06	0.16 ± 0.01
INDW-21/50	0.11 ± 0.01	0.34 ± 0.02	0.46 ± 0.05	0.12 ± 0.02	0 ± 0	0.03 ± 0	0.01 ± 0	0 ± 0	0.78 ± 0.06	0.17 ± 0.01
INDW-21/51	0.11 ± 0.01	0.33 ± 0.02	0.47 ± 0.05	0.12 ± 0.02	0 ± 0	0.04 ± 0	0.01 ± 0	0 ± 0	0.84 ± 0.06	0.11 ± 0.01
INDW-21/52	0.1 ± 0.01	0.33 ± 0.02	0.48 ± 0.05	0.12 ± 0.02	0 ± 0	0.03 ± 0	0.01 ± 0	0 ± 0	0.79 ± 0.06	0.17 ± 0.01
INDW-21/53	0.1 ± 0.01	0.34 ± 0.02	0.48 ± 0.05	0.11 ± 0.02	0 ± 0	0.03 ± 0	0.01 ± 0	0 ± 0	0.83 ± 0.06	0.12 ± 0.01
INDW-21/48	0.09 ± 0.01	0.33 ± 0.02	0.49 ± 0.05	0.11 ± 0.02	0 ± 0	0.03 ± 0	0.01 ± 0	0 ± 0	0.79 ± 0.06	0.17 ± 0.01
INDW-21/46	0.03 ± 0	0.14 ± 0.01	0.66 ± 0.07	0.15 ± 0.03	0 ± 0	0.01 ± 0	0.01 ± 0	0 ± 0	0.75 ± 0.06	0.24 ± 0.02
INDW-21/45	0.03 ± 0	0.12 ± 0.01	0.7 ± 0.07	0.13 ± 0.02	0 ± 0	0 ± 0	0.01 ± 0	0 ± 0	0.75 ± 0.06	0.23 ± 0.02
INDW-21/44	0.02 ± 0	0.11 ± 0.01	0.73 ± 0.07	0.14 ± 0.03	0 ± 0	0 ± 0	0.01 ± 0	0 ± 0	0.76 ± 0.06	0.23 ± 0.02
INDW-21/43	0.02 ± 0	0.13 ± 0.01	0.72 ± 0.07	0.13 ± 0.02	0 ± 0	0 ± 0	0.01 ± 0	0 ± 0	0.76 ± 0.06	0.23 ± 0.02
INDW-21/42	0.02 ± 0	0.11 ± 0.01	0.75 ± 0.08	0.12 ± 0.02	0 ± 0	0 ± 0	0.01 ± 0	0 ± 0	0.73 ± 0.06	0.26 ± 0.02
INDW-21/41	0.03 ± 0	0.12 ± 0.01	0.73 ± 0.07	0.13 ± 0.02	0 ± 0	0 ± 0	0.01 ± 0	0 ± 0	0.77 ± 0.06	0.21 ± 0.02
INDW-21/47	0 ± 0	0.07 ± 0	0.75 ± 0.08	0.08 ± 0.01	0 ± 0	0 ± 0	0 ± 0	0 ± 0	0.71 ± 0.06	0.28 ± 0.02
INDW-21/56	0.16 ± 0.01	0.26 ± 0.02	0.46 ± 0.05	0.14 ± 0.03	0 ± 0	0.05 ± 0	0.02 ± 0	0 ± 0	0.88 ± 0.06	0.06 ± 0
INDW-21/54	0.16 ± 0.01	0.27 ± 0.02	0.45 ± 0.05	0.16 ± 0.03	0 ± 0	0.05 ± 0	0.02 ± 0	0 ± 0	0.77 ± 0.06	0.16 ± 0.01
INDW-21/55	0.01 ± 0	0.23 ± 0.01	0.73 ± 0.07	0.06 ± 0.01	0 ± 0	0 ± 0	0.01 ± 0	0 ± 0	0.8 ± 0.06	0.19 ± 0.01
INDW-21/38	0.01 ± 0	0.06 ± 0	0.89 ± 0.09	0.03 ± 0.01	0 ± 0	0 ± 0	0 ± 0	0 ± 0	0.71 ± 0.06	0.29 ± 0.02
INDW-21/40	0 ± 0	0.05 ± 0	0.97 ± 0.1	0.01 ± 0	0 ± 0	0 ± 0	0 ± 0	0 ± 0	0.88 ± 0.07	0.11 ± 0.01
INDW-21/39	0 ± 0	0.03 ± 0	0.89 ± 0.09	0.08 ± 0.01	0 ± 0	0 ± 0	0.01 ± 0	0 ± 0	0.78 ± 0.06	0.21 ± 0.02
INDW-21/37	0 ± 0	0 ± 0	0.43 ± 0.04	0 ± 0	0 ± 0	0 ± 0	0 ± 0	0 ± 0	0.8 ± 0.06	0.2 ± 0.02
INDW-21/36	0 ± 0	0.01 ± 0	0.86 ± 0.09	0.05 ± 0.01	0 ± 0	0 ± 0	0 ± 0	0 ± 0	0.28 ± 0.08	0.72 ± 0.21
INDW-21/35	0 ± 0	0.01 ± 0	0.91 ± 0.09	0.1 ± 0.02	0 ± 0	0 ± 0	0.01 ± 0	0 ± 0	0.23 ± 0.08	0.76 ± 0.28
INDW-21/28	0.02 ± 0.01	0.06 ± 0.01	0.83 ± 0.11	0.02 ± 0.02	0.09 ± 0.02	--	--	--	--	--

INDW-21/29	0.02 ± 0.01	0.08 ± 0.01	0.73 ± 0.09	0.04 ± 0.03	0.13 ± 0.03	--	--	--	--	--
INDW-21/30	0.02 ± 0.01	0.06 ± 0.01	0.79 ± 0.1	0.02 ± 0.02	0.09 ± 0.02	--	--	--	--	--
INDW-21/34	0.02 ± 0.01	0.05 ± 0.01	0.76 ± 0.1	0.02 ± 0.03	0.15 ± 0.03	0.01 ± 0	0.07 ± 0.01	0.1 ± 0.02	0.26 ± 0.07	0.57 ± 0.15
INDW-21/33	0.05 ± 0	0.07 ± 0.01	0.92 ± 0.09	0.05 ± 0.01	0 ± 0	--	--	--	--	--
INDW-21/32	0.05 ± 0	0.05 ± 0.01	0.94 ± 0.1	0.05 ± 0.01	0 ± 0	--	--	--	--	--
INDW-21/31	0.01 ± 0.01	0.04 ± 0.01	0.82 ± 0.1	0.02 ± 0.02	0.1 ± 0.02	0.01 ± 0	0.04 ± 0.01	0.05 ± 0.01	0.37 ± 0.07	0.54 ± 0.1
INDW-21/58	0 ± 0	0.09 ± 0	0.61 ± 0.06	0.16 ± 0.03	0 ± 0	0 ± 0	0.01 ± 0	0 ± 0	0.74 ± 0.06	0.25 ± 0.02
INDW-21/57	0.01 ± 0	0.07 ± 0	0.61 ± 0.06	0.19 ± 0.03	0 ± 0	0 ± 0	0.01 ± 0	0 ± 0	0.74 ± 0.06	0.25 ± 0.02
INDW-21/25	0.01 ± 0	0.11 ± 0	0.79 ± 0.08	0.01 ± 0.01	0 ± 0	0 ± 0	0 ± 0	0 ± 0	0.73 ± 0.06	0.27 ± 0.02
INDW-21/26	0.02 ± 0	0.12 ± 0.01	0.74 ± 0.08	0.01 ± 0.01	0 ± 0	0 ± 0	0 ± 0	0 ± 0	0.68 ± 0.06	0.32 ± 0.03
INDW-21/27	0.01 ± 0	0.11 ± 0	0.73 ± 0.07	0.08 ± 0.02	0 ± 0	0 ± 0	0 ± 0	0 ± 0	0.72 ± 0.06	0.27 ± 0.02
INDW-21/22	0.01 ± 0	0.12 ± 0.01	0.82 ± 0.08	0.01 ± 0.01	0 ± 0	0 ± 0	0 ± 0	0 ± 0	0.71 ± 0.06	0.29 ± 0.03
INDW-21/21	0.01 ± 0	0.16 ± 0.01	0.79 ± 0.08	0.09 ± 0.02	0 ± 0	0 ± 0	0.01 ± 0	0 ± 0	0.74 ± 0.06	0.25 ± 0.02
INDW-21/24	0.02 ± 0.01	0.12 ± 0.01	0.8 ± 0.1	0.01 ± 0.01	0.04 ± 0.03	--	--	--	--	--
INDW-21/23	0.02 ± 0.01	0.14 ± 0.01	0.79 ± 0.1	0.01 ± 0.01	0.03 ± 0.03	0.02 ± 0.01	0.04 ± 0.01	0.03 ± 0.01	0.28 ± 0.08	0.63 ± 0.17
INDW-21/20	0.02 ± 0.01	0.1 ± 0.01	0.77 ± 0.1	0.01 ± 0.03	0.13 ± 0.03	--	--	--	--	--
INDW-21/19	0.03 ± 0.01	0.16 ± 0.01	0.7 ± 0.09	0.01 ± 0.02	0.11 ± 0.03	0.03 ± 0.01	0.07 ± 0.02	0.11 ± 0.02	0.15 ± 0.08	0.64 ± 0.34
INDW-21/18	0.02 ± 0.01	0.28 ± 0.02	0.65 ± 0.08	0.01 ± 0.02	0.08 ± 0.04	--	--	--	--	--
INDW-21/15	0.02 ± 0.01	0.12 ± 0.01	0.63 ± 0.08	0.01 ± 0.03	0.15 ± 0.03	0 ± 0	0.01 ± 0	0.04 ± 0.01	0.66 ± 0.07	0.29 ± 0.03
INDW-21/16	0.03 ± 0.01	0.16 ± 0.01	0.65 ± 0.08	0.02 ± 0.02	0.11 ± 0.03	0.01 ± 0	0.03 ± 0.01	0.04 ± 0.01	0.58 ± 0.06	0.34 ± 0.04
INDW-21/17	0.02 ± 0.01	0.26 ± 0.02	0.67 ± 0.09	0 ± 0.02	0.07 ± 0.03	--	--	--	--	--
INDW-21/13	0.02 ± 0.01	0.2 ± 0.01	0.67 ± 0.09	0.01 ± 0.03	0.14 ± 0.03	--	--	--	--	--
INDW-21/61	0.1 ± 0.01	0.22 ± 0.01	0.6 ± 0.06	0.09 ± 0.02	0 ± 0	0.03 ± 0	0.01 ± 0	0 ± 0	0.64 ± 0.06	0.32 ± 0.03
INDW-21/60	0.09 ± 0.01	0.22 ± 0.01	0.61 ± 0.06	0.06 ± 0.01	0 ± 0	0.02 ± 0	0.01 ± 0	0 ± 0	0.69 ± 0.07	0.28 ± 0.03
INDW-21/59	0.01 ± 0	0.14 ± 0.01	0.67 ± 0.07	0.14 ± 0.03	0 ± 0	0 ± 0	0.01 ± 0	0 ± 0	0.67 ± 0.06	0.33 ± 0.03
INDW-21/11	0.06 ± 0.03	0.25 ± 0.02	0.55 ± 0.07	0.05 ± 0.02	0.09 ± 0.04	0.05 ± 0.02	0.23 ± 0.05	0.08 ± 0.02	0.42 ± 0.05	0.21 ± 0.02
INDW-21/14	0.04 ± 0.02	0.24 ± 0.02	0.59 ± 0.08	0.02 ± 0.03	0.16 ± 0.04	--	--	--	--	--
INDW-21/12	0.02 ± 0.01	0.14 ± 0.01	0.68 ± 0.09	0.01 ± 0.03	0.12 ± 0.03	0.01 ± 0	0.01 ± 0	0.04 ± 0.01	0.71 ± 0.07	0.23 ± 0.02

INDW-21/10	0.04 ± 0.02	0.18 ± 0.02	0.62 ± 0.08	0.03 ± 0.03	0.13 ± 0.03	0.02 ± 0.01	0.07 ± 0.02	0.07 ± 0.01	0.57 ± 0.06	0.27 ± 0.03
INDW-21/04	0.05 ± 0.02	0.22 ± 0.02	0.58 ± 0.07	0.05 ± 0.03	0.11 ± 0.04	0.03 ± 0.02	0.16 ± 0.04	0.08 ± 0.01	0.41 ± 0.05	0.31 ± 0.04
INDW-21/09	0.05 ± 0.02	0.22 ± 0.02	0.59 ± 0.08	0.05 ± 0.03	0.11 ± 0.03	0.03 ± 0.01	0.15 ± 0.03	0.07 ± 0.01	0.48 ± 0.05	0.27 ± 0.03
INDW-21/01	0.03 ± 0.01	0.11 ± 0.01	0.55 ± 0.07	0.02 ± 0.05	0.26 ± 0.05	0 ± 0	0.02 ± 0	0.05 ± 0.01	0.76 ± 0.06	0.17 ± 0.01
INDW-21/03	0.02 ± 0.01	0.1 ± 0.01	0.57 ± 0.07	0.01 ± 0.05	0.25 ± 0.05	0 ± 0	0.01 ± 0	0.05 ± 0.01	0.76 ± 0.06	0.18 ± 0.01
INDW-21/02	0.04 ± 0.02	0.18 ± 0.02	0.51 ± 0.07	0.02 ± 0.05	0.23 ± 0.05	0.01 ± 0	0.02 ± 0.01	0.05 ± 0.01	0.76 ± 0.06	0.16 ± 0.01
INDW-21/05	0.28 ± 0.06	0.37 ± 0.05	0.17 ± 0.03	0.08 ± 0.03	0.11 ± 0.08	0.14 ± 0.04	0.23 ± 0.07	0.07 ± 0.01	0.44 ± 0.04	0.12 ± 0.01
INDW-21/06	0.15 ± 0.05	0.36 ± 0.04	0.26 ± 0.04	0.07 ± 0.04	0.14 ± 0.06	0.05 ± 0.02	0.13 ± 0.04	0.06 ± 0.01	0.58 ± 0.05	0.19 ± 0.02
INDW-21/08	0.09 ± 0.04	0.53 ± 0.04	0.18 ± 0.04	0.09 ± 0.04	0.14 ± 0.07	0.08 ± 0.04	0.4 ± 0.09	0.14 ± 0.03	0.32 ± 0.03	0.06 ± 0.01
INDW-21/07	0.05 ± 0.02	0.22 ± 0.02	0.58 ± 0.08	0.05 ± 0.03	0.12 ± 0.03	0.03 ± 0.02	0.15 ± 0.03	0.09 ± 0.01	0.42 ± 0.05	0.31 ± 0.04

Table 5.7. *The estimated results derived from the Monte-Carlo simulation and the calculated weathering fractions are provided.*

Sample ID	***Estimated results from Monte-Carlo simulation***		***Carbonate weathering fraction (R)***	***Sulfuric acid weathering fraction (Z)***
	Estimated f_{py} from OWP_{Slope}	***$\delta^{18}O_{SO4\text{-}py}$ (‰)***	***$\delta^{34}S_{py}$ (‰)***		
INDW-21/49	0.91 ± 0.15	-9.47 ± 1.6	-7.35 ± 1.83	0.72 ± 0.04	0.22 ± 0.01
INDW-21/50	0.89 ± 0.15	-9.75 ± 1.62	-5.98 ± 1.78	0.71 ± 0.04	0.21 ± 0.01
INDW-21/51	0.97 ± 0.13	-9.69 ± 1.61	-5 ± 1.59	0.72 ± 0.04	0.21 ± 0.01
INDW-21/52	0.9 ± 0.16	-9.3 ± 1.59	-6.84 ± 1.82	0.73 ± 0.04	0.19 ± 0.01
INDW-21/53	0.95 ± 0.15	-9.2 ± 1.6	-5.92 ± 1.7	0.72 ± 0.04	0.2 ± 0.01
INDW-21/48	0.9 ± 0.15	-9.69 ± 1.61	-9.76 ± 2.04	0.74 ± 0.04	0.21 ± 0.01
INDW-21/46	0.83 ± 0.17	-10.32 ± 1.64	-13.35 ± 2.39	0.91 ± 0.05	0.35 ± 0.02
INDW-21/45	0.83 ± 0.17	-10.18 ± 1.63	-12.17 ± 2.34	0.93 ± 0.05	0.37 ± 0.02
INDW-21/44	0.84 ± 0.16	-10.28 ± 1.64	-13.14 ± 2.36	0.94 ± 0.05	0.36 ± 0.02
INDW-21/43	0.84 ± 0.17	-10.3 ± 1.64	-13.24 ± 2.38	0.92 ± 0.05	0.34 ± 0.02
INDW-21/42	0.8 ± 0.2	-10.09 ± 1.63	-13.67 ± 2.52	0.94 ± 0.05	0.35 ± 0.02
INDW-21/41	0.86 ± 0.16	-10.14 ± 1.64	-12.8 ± 2.33	0.93 ± 0.05	0.36 ± 0.02

INDW-21/47	0.78 ± 0.2	-10.5 ± 1.65	-15.02 ± 2.66	0.98 ± 0.05	0.37 ± 0.02
INDW-21/56	1.02 ± 0.11	-11.36 ± 1.68	-2.1 ± 1.29	0.79 ± 0.04	0.27 ± 0.01
INDW-21/54	0.9 ± 0.12	-11.25 ± 1.68	-6.14 ± 1.72	0.78 ± 0.04	0.24 ± 0.01
INDW-21/55	0.89 ± 0.12	-11.7 ± 1.7	-1.29 ± 1.41	0.9 ± 0.05	0.12 ± 0.01
INDW-21/38	0.78 ± 0.27	-9.36 ± 1.6	-11.73 ± 2.48	0.99 ± 0.05	0.26 ± 0.01
INDW-21/40	0.97 ± 0.17	-7.75 ± 1.54	-8.18 ± 1.88	0.97 ± 0.05	0.18 ± 0.01
INDW-21/39	0.86 ± 0.27	-7.52 ± 1.53	-15.17 ± 2.64	1 ± 0.05	0.19 ± 0.01
INDW-21/37	0.88 ± 0.19	-8.81 ± 1.57	-17.84 ± 2.67	1 ± 0.04	0.4 ± 0.02
INDW-21/36	0.31 ± 0.04	-5.68 ± 1.46	--	1 ± 0.05	0.14 ± 0.02
INDW-21/35	0.26 ± 0.03	-5.44 ± 1.45	--	0.99 ± 0.05	0.09 ± 0.02
INDW-21/28	--	--	--	0.98 ± 0.07	--
INDW-21/29	--	--	--	0.97 ± 0.07	--
INDW-21/30	--	--	--	0.98 ± 0.07	--
INDW-21/34	0.34 ± 0.05	-4.57 ± 1.42	-19.48 ± 22.17	0.98 ± 0.07	0.03 ± 0
INDW-21/33	--	--	--	0.97 ± 0.05	--
INDW-21/32	--	--	--	0.97 ± 0.05	--
INDW-21/31	0.45 ± 0.08	-4.24 ± 1.4	-10.06 ± 6.49	0.99 ± 0.07	0.05 ± 0.01
INDW-21/58	0.82 ± 0.23	-9.09 ± 1.59	-5.61 ± 1.89	0.99 ± 0.05	0.47 ± 0.03
INDW-21/57	0.82 ± 0.24	-8.9 ± 1.58	-6.83 ± 2.03	0.99 ± 0.05	0.53 ± 0.03
INDW-21/25	0.8 ± 0.35	-8.07 ± 1.54	-3.32 ± 1.91	0.99 ± 0.05	0.35 ± 0.02
INDW-21/26	0.74 ± 0.9	-7.92 ± 1.55	-4.44 ± 2.16	0.98 ± 0.05	0.33 ± 0.02
INDW-21/27	0.79 ± 0.39	-7.92 ± 1.55	-3.75 ± 1.93	0.98 ± 0.05	0.33 ± 0.02
INDW-21/22	0.77 ± 0.64	-7.47 ± 1.52	-4.54 ± 2.07	0.98 ± 0.05	0.26 ± 0.02
INDW-21/21	0.82 ± 0.42	-7.11 ± 1.52	-6.22 ± 2.05	0.95 ± 0.05	0.22 ± 0.01
INDW-21/24	--	--	--	0.95 ± 0.06	--
INDW-21/23	0.34 ± 0.05	-4.41 ± 1.41	-25.39 ± 22.5	0.94 ± 0.06	0.02 ± 0
INDW-21/20	--	--	--	0.94 ± 0.06	--
INDW-21/19	0.22 ± 0.03	-3.23 ± 1.37	--	0.9 ± 0.06	0.02 ± 0.01

INDW-21/18	--	--	--	0.81 ± 0.06	--
INDW-21/15	0.76 ± 0.35	-3.58 ± 1.38	0.56 ± 1.9	0.94 ± 0.06	0.13 ± 0.01
INDW-21/16	0.69 ± 0.22	-4.02 ± 1.4	-6.21 ± 2.86	0.94 ± 0.06	0.12 ± 0.01
INDW-21/17	--	--	--	0.83 ± 0.06	--
INDW-21/13	--	--	--	0.89 ± 0.06	--
INDW-21/61	0.73 ± 0.67	-5.88 ± 1.47	-2.63 ± 2.19	0.89 ± 0.05	0.19 ± 0.01
INDW-21/60	0.77 ± 0.55	-4.31 ± 1.41	-3.54 ± 2.15	0.89 ± 0.05	0.21 ± 0.01
INDW-21/59	0.73 ± 0.84	-6 ± 1.47	-7.01 ± 2.49	0.97 ± 0.05	0.33 ± 0.02
INDW-21/11	0.72 ± 0.25	-3.38 ± 1.38	-6.21 ± 2.78	0.82 ± 0.06	0.02 ± 0
INDW-21/14	--	--	--	0.86 ± 0.06	--
INDW-21/12	0.82 ± 1.5	-4.15 ± 1.41	0.23 ± 1.73	0.94 ± 0.06	0.23 ± 0.02
INDW-21/10	0.74 ± 0.3	-3.66 ± 1.38	-2.12 ± 2.24	0.89 ± 0.06	0.08 ± 0.01
INDW-21/04	0.63 ± 0.15	-3.43 ± 1.38	-9.02 ± 3.82	0.85 ± 0.06	0.04 ± 0
INDW-21/09	0.7 ± 0.21	-3.51 ± 1.38	-3.57 ± 2.59	0.86 ± 0.06	0.08 ± 0.01
INDW-21/01	0.89 ± 0.26	-6.88 ± 1.5	-13.21 ± 2.39	0.93 ± 0.07	0.35 ± 0.02
INDW-21/03	0.89 ± 0.28	-6.83 ± 1.51	-12.94 ± 2.46	0.94 ± 0.07	0.46 ± 0.03
INDW-21/02	0.9 ± 0.28	-6.44 ± 1.48	-13.18 ± 2.43	0.87 ± 0.06	0.41 ± 0.03
INDW-21/05	0.85 ± 0.54	-5.86 ± 1.47	-14.4 ± 2.72	0.46 ± 0.05	0.24 ± 0.02
INDW-21/06	0.82 ± 0.69	-6.07 ± 1.47	-14.84 ± 2.78	0.58 ± 0.05	0.29 ± 0.02
INDW-21/08	0.92 ± 0.52	-4.62 ± 1.42	-17.58 ± 2.91	0.39 ± 0.05	0.12 ± 0.01
INDW-21/07	0.63 ± 0.15	-3.03 ± 1.37	-12.66 ± 4.24	0.86 ± 0.06	0.06 ± 0

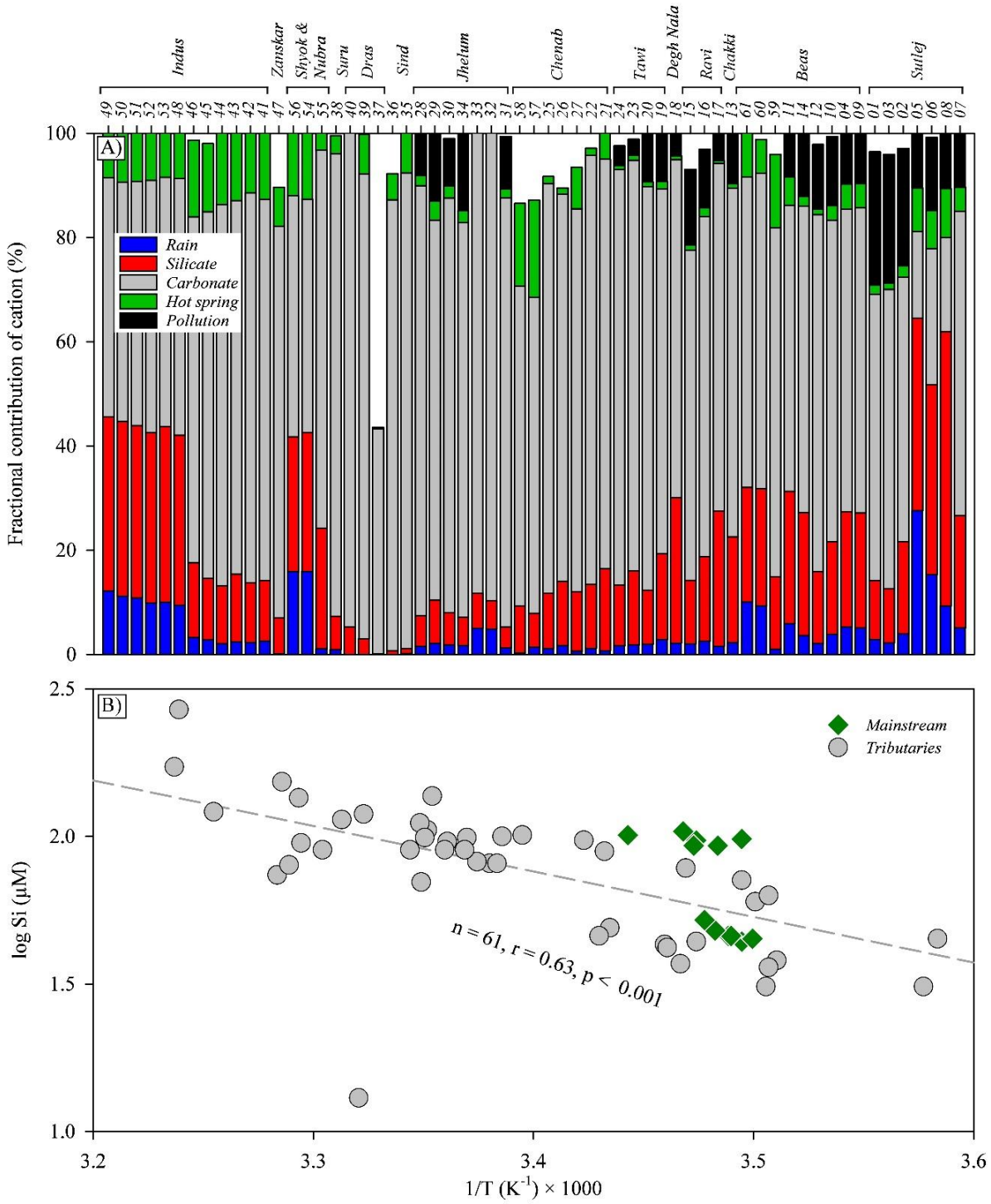

Figure 5.6. *Estimates of solute contribution for (A) cations and B) correlation between log Si with water temperature for the upper Indus samples.*

The $\delta^{18}O_{SO4}$ values for gypsum minerals for Phanerozoic Eon vary from 10 ‰ to 30 ‰, with an average value of ~ 15 ‰ (Relph et al., 2021; Turchyn and Schrag, 2004; Claypool et al., 1980). The $\delta^{18}O_{SO4}$ of pyrites depends on the oxygen sources for oxidation (meteoric water and atmospheric oxygen) in a given basin, their isotopic compositions, and related fractionation factors (cf. Eq. 5.5). Although theoretical observations hint at dominant involvement of

atmospheric O_2 (~ 87.5 %) in sulfide oxidation reactions (Balci et al., 2007), lab-controlled experiments (Balci et al., 2007) and studies from river basins (Relph et al., 2021; Gu et al., 2020a) document that these processes are mainly mediated through meteoric water, with minimal (< 17 %) atmospheric oxygen contribution. Prior to f_{py} estimation, the $\delta^{18}O$ values used in this simulation approach have to be corrected for all other sources (rain, pollution and hot springs) using the following equation:

$$\delta^{18}O_{SO_4}{}^{*} = \frac{\delta^{18}O_{SO_4\,riv} - (\delta^{18}O_{SO_4\,x} \times f_i)}{(1-f_i)} \quad (5.3)$$

where subscripts *riv and i* denotes the river and end-members (rain, hot springs and pollution) respectively. This correction requires data on relative sulfate contribution from the sources, and hence, information on average SO_4/Na and amount of Na supplied from different sources. The average SO_4/Na ratio used for the oceanic (0.06; Roy-Barman and Jeandel, 2016), hot springs (0.3; Tiwari et al., 2016), and anthropogenic (0.28; this study) sources have been compiled from the literature. The estimated sodium contributions for each source using the inverse modeling (Tripathy and Singh, 2010) are used for this simulation.

In an interesting observation, the corrected $\delta^{18}O_{SO4}$ and $\delta^{18}O_{H2O}$ exhibit linear co-variation, with the slope of their regression lines being dependent on the f_{py} values. Further, the regression lines for different combination of f_{py} value intersect at a common point, where the $\delta^{18}O_{SO4}$ value is same as that of the gypsum mineral. This intersection point reflects a unique condition where $\delta^{18}O_{SO4} = \delta^{18}O_{Pyrite} = \delta^{18}O_{Gypsum}$. This situation arises when $\delta^{18}O_{H2O}$ corresponds to 12.8 ‰, considering an average $\delta^{18}O_{Gypsum}$ value of 14 ‰. These observations, therefore, ascertain that the slope of the $\delta^{18}O_{SO4}$- $\delta^{18}O_{H2O}$ line, computed as below, co-vary linearly with the f_{py} value. This slope (OWP_{slope}) can be computed using following equation, which reflects higher degree of sulfide oxidation for a sample with lower slope.

$$OWP_{slope} = \left(\frac{\delta^{18}O_{SO4} - \delta^{18}O_{Gypsum}}{\delta^{18}O_{H2O} - 12.8}\right) \quad (5.4)$$

This regression equation can be used efficiently to compute the f_{py} values with given $\delta^{18}O$ composition for water and their sulfate fraction. As a sensitivity test, we computed f_{py} values for previously-estimated $\delta^{18}O_{SO4}$ and $\delta^{18}O_{H2O}$ data (Relph et al., 2021; Xu et al., 2024) using Monte-Carlo simulation (Fig. 5.7. B). The estimated f_{py} values for these samples using OWP_{slope} approach match well with that obtained from the Monte-Carlo simulation, confirming reliability of our approach (with no iterative algorithm) to estimate the f_{py} values accurately.

Further, this additional approach, together with Monte-Carlo simulation, may validate the reliability of using measured $\delta^{18}O_{H2O}$ as reactive fluid composition for a given basin.

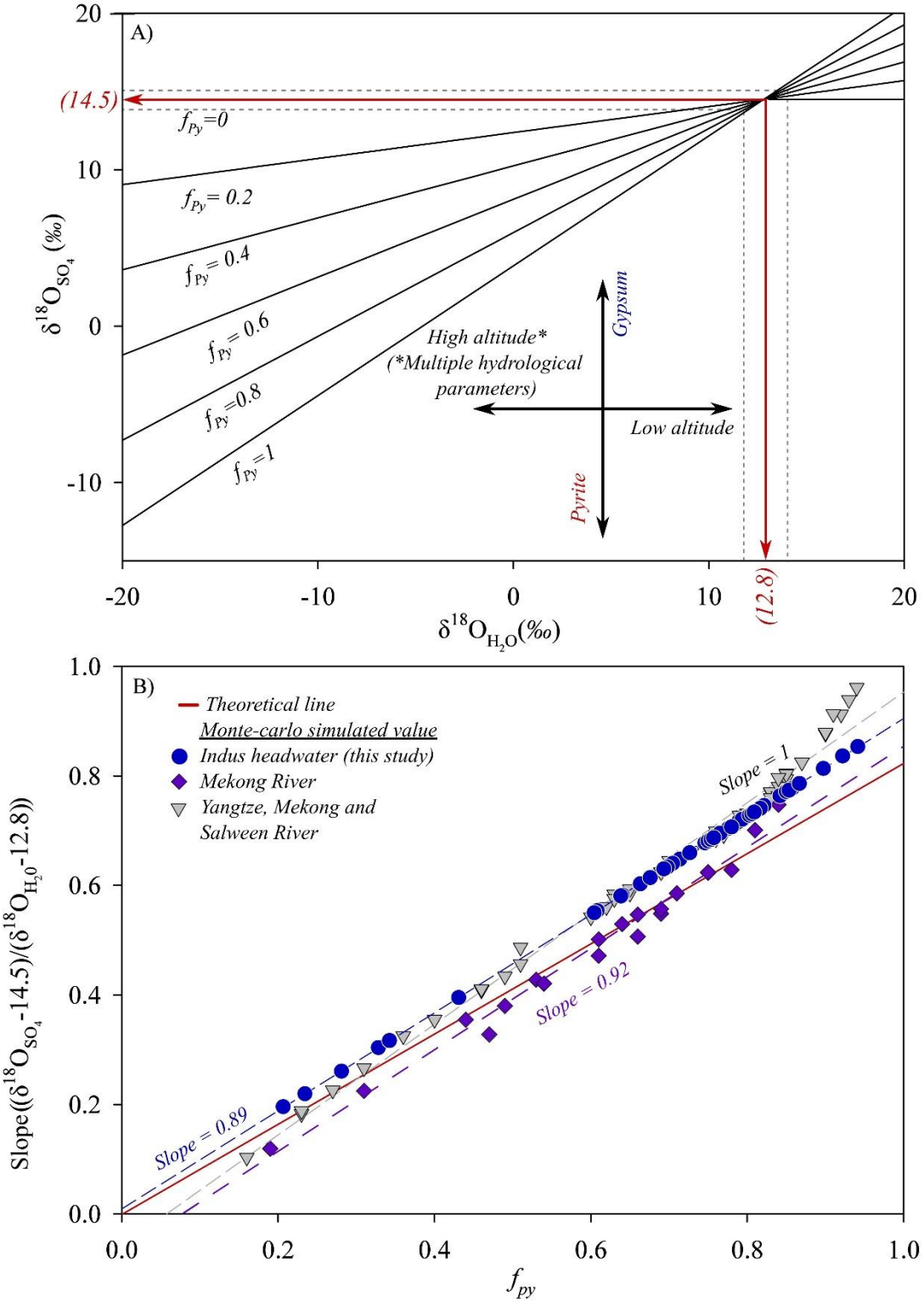

Figure 5.7. *(A) $\delta^{18}O_{H2O}$ and $\delta^{18}O_{SO4}$ of Indus samples co-vary linearly, with its slope being a function of f_{py}. (B) the linear dependency of f_{py} with the slope of the $\delta^{18}O_{SO4}$ - $\delta^{18}O_{H2O}$ line. The estimated f_{py} values for this study and literature data (Relph et al., 2021 and Xu et al., 2024) match well with the theoretical line.*

For ready comparison with available literature data for global rivers, we have adopted the Monte-Carlo approach of Relph et al., (2021) to compute the sulfate contributions from major sources to the Indus headwater. This simulation computes the sulfate contribution from sulfide minerals and gypsum dissolution using $\delta^{18}O_{SO4}$ values for major minerals, oxygen sources, and related fractionation factors:

$$\delta^{18}O_{SO4\,py} = f_{O_2}\,(\delta^{18}O_{O_2} + \varepsilon_{SO_4-O_2}) + f_{H_2O}(\delta^{18}O_{H_2O} + \varepsilon_{SO_4-H_2O}) \quad (5.5)$$

$$f_{O_2} + f_{H_2O} = 1 \quad (5.6)$$

here, f_{O2} and f_{H2O} is the atmospheric and meteoric water fractions of oxygen that incorporates into the sulfate during the oxidation of sulfides, respectively. The $\delta^{18}O_{H2O}$ is the isotopic values for the local water samples whereas $\delta^{18}O_{O2}$ is the typical atmospheric value. The ε_{SO4-O2} and $\varepsilon_{SO4-H2O}$ are the fractionation factors between oxygen - sulfate and water - sulfate respectively. Further, the $\delta^{18}O_{SO4}$ of pyritic sulfate is largely controlled by $\delta^{18}O_{H2O}$ of reactive water, as $\delta^{18}O$ of atmospheric O_2 (~ 23 ‰; Xu et al., 2024) and its oxygen contribution (< 0.17) are well constrained. We have computed the expected $\delta^{18}O_{SO4}$ value by varying $\delta^{18}O_{H2O}$ value of water and f_{py} value (Fig. 5.6.). Results from the Monte-Carlo approach was further used to calculate the $\delta^{34}S$ value for pyrites using the following equation:

$$\delta^{34}S_{SO_4\,py} = \frac{\delta^{34}S^{*}SO_4 - (1-f_{py})\,(\delta^{34}S_{SO_4\,gy})}{f_{py}} \quad (5.7)$$

here, subscripts, *py and gy* stand for pyrite and gypsum respectively.

The f_{py} for the Indus mainstream varies between 0.73 and 0.84 with an average f_{py} of 0.78. These values match well with that computed using OWP_{slope} approach for the Indus mainstream (0.80 to 0.97). The estimated f_{py} values from the Monte-Carlo simulation vary from 0.15 to 0.88 with the highest f_{py} *is* observed for the Dras sub-basin while the lowest is for Tawi River. Further, this simulation approach (cf. Eq. 5.7) enables us to compute the $\delta^{34}S_{py}$ values, which range between - 25 ‰ and 1 ‰ (avg., - 9 ± 6 ‰; n = 47 (Table 5.7.; excluding 3 outliers)). As suspended sediments often do not comprise of pyrite minerals with fast dissolution kinetics, these data provide a good handle on the source composition. Average $\delta^{34}S_{py}$ value for the Indus headwater basin is found overlapping with that reported from the Tethyan sedimentary sequences (Xu et al., 2024).

The sulfates are dominantly supplied from major sulfate bearing sources such as pyrite (64 ± 19 %) and gypsum (27 ± 16 %) with minor contributions from hot springs (~ 4 %), rain (~ 2 %) and anthropogenic input (~ 2 %; Fig. 5.8.). The hot springs contribution varies between 0.02 % and 40 % with the highest contribution being observed for the Sutlej sub-basin. The sulfate contribution via anthropogenic supply is mostly higher for the tributaries from lower reaches (Sutlej, Beas, Ravi, Tawi and Jhelum). As mentioned in the earlier section the anthropogenic sources are mostly from agricultural land which can provide substantial sulfate to the stream.

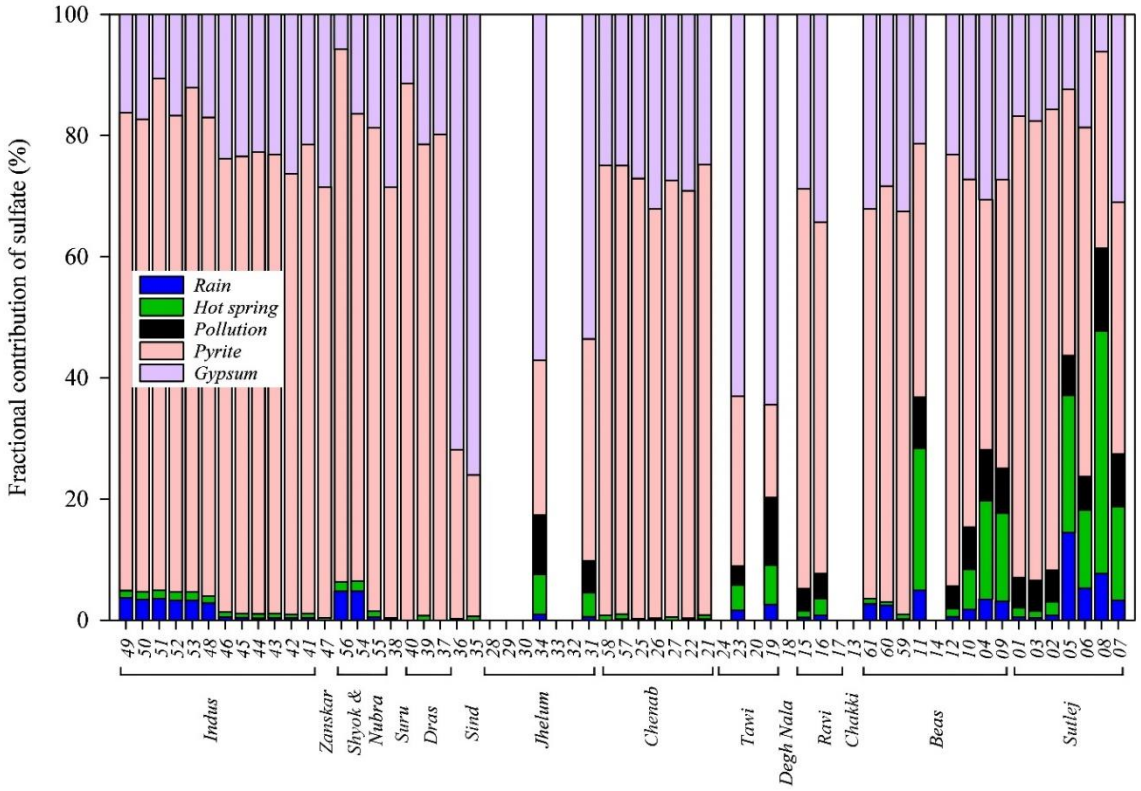

Figure 5.8. *Estimates of solute contribution for sulfates for the Indus headwater.*

At Batalik (exit point of Indus mainstream in this study), the relative sulfate contribution for the rain (0.38 ± 0.05 %), hot springs (0.7 ± 0.1 %), pyrite (77 ± 6 %) and gypsum (21 ± 2 %), has been estimated. The sulfide-derived sulfate at this location is ~ 530 µEq. The sulfate derived from sulfuric acid-mediated carbonate weathering for Indus at Batalik is 387 ± 40 µEq which corresponds to a CO_2 release of $3.7 \pm 0.4 \times 10^5$ mol/km^2/yr. This rate is significantly higher than the estimated CO_2 uptake rate via silicate weathering ($2.0 \pm 0.1 \times 10^5$ mol/km^2/yr) at this location. High sulfide oxidation in the upper Indus basin is mostly linked to conducive lithology and glacial coverage, which has been discussed in detail in the following section.

5.4. Pyrite oxidation in the Indus headwater and its significance

The H_2CO_3-mediated silicate weathering and sulfide oxidation coupled carbonate weathering influence the alkalinity and DIC of the ocean-atmosphere system. The silicate weathering generates alkalinity (ALK), which subsequently get consumed during oceanic $CaCO_3$ deposition. While the conversion from $CaSiO_3$ to $CaCO_3$ consumes DIC, the sulfide oxidation consumes alkalinity. Kemeny et al., (2021a) have assessed the effect of parameters, R (ratio of carbonate to total weathering) and Z (fraction of H_2SO_4-mediated weathering) on ALK/DIC of a weathering system. Figure 5.9. depicts the R and Z correlation and compares CO_2 release/uptake rates between the headwater (this study), and entire (estimated using data from Karim and Veizer (2000)) basin of the Indus. This comparison does not include the organic oxidation pathway and hence, the present release rate must be considered a lower limit only. Further, this discussion, focusing on the continental weathering pathways, does not include the CO_2 consumption via organic burial in oceanic settings. The rate comparison indicates the weathering process in the headwater basin serves as a net CO_2 source, whereas the lower reaches of the Indus serve as net CO_2 sink. Considering the CO_2 release via sulfide oxidation (4.5 ± 0.5 tC/km^2/yr) and consumption via silicate weathering (2.4 ± 0.1 tC/km^2/yr), the net effect of the chemical weathering in the headwater basin (at Batalik) on CO_2 is 2.1 ± 0.5 tC/km^2/yr which acts as a source of CO_2. In comparison, the net CO_2 effect for the Indus outflow is found to be $- 0.8 \pm 0.2$ tC/km^2/yr. The observed net CO_2 release from mountainous regions of the Indus basin is consistent with that reported in a few earlier studies (Peel: 2.80 tC/km^2/yr and Liard: 1.70 tC/km^2/yr) and higher than Mackenzie (0.75 tC/km^2/yr), Peace (0.44 tC/km^2/yr), Slave (0.26 tC/km^2/yr), Athabasca (0.29 tC/km^2/yr) and Ganges and Brahmaputra (0.66 tC/km^2/yr) River system (Galy and France-Lanord, 1999; Calmels et al., 2007; Hilton and West, 2020). This release from weathering-limited regimes has been linked to continuous exposure of fresher minerals, and also, presence of disseminated pyrites in the glaciated terrains. In contrast, this oxidative weathering is less intense in transport-limited (or, lower reaches) regime of the basin, where intense weathering of silicate minerals may be encountered due to high water-rock interaction time. Our earlier discussion (cf. section 5.3.2.1.) has established strong control of temperature in regulating the silicate weathering rate in the upper Indus basin.

The average temperature for the upper Indus basin (this study) is very low compared to that observed for the lower reaches (Karim and Veizer, 2000). This temperature gradient may

explain the estimated lower CO_2 uptake rate for the upper Indus.

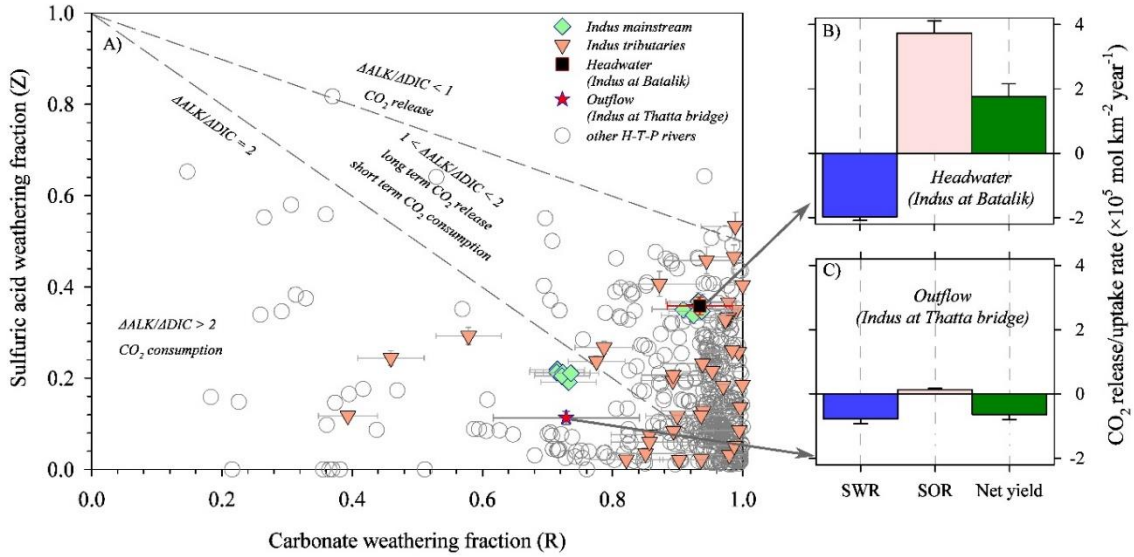

Figure 5.9. *The figure depicts A) the sulfuric acid weathering fraction (Z) against the carbonate weathering fraction (R). Most of our samples fall in the zone of long-term CO_2 release and short-term CO_2 consumption. The Indus mainstream data are shown in diamond whereas the tributaries are in triangle symbol. Trends for CO_2 release/consumption are from literature (Kemeny et al., 2021a; Xu et al., 2024). The Indus headwater at Batalik (marked as black square) clusters in the CO_2 release zone whereas the Indus outflow at Thatta bridge is presented as red star mark, falls in the consumption zone. For comparison, we have also shown the estimated R-Z values for other HTP Rivers (Ma et al., 2023; Xu et al., 2024) in open grey circles. The CO_2 release/uptake rates for the B) Indus headwater (this study) and C) outflows (Karim and Veizer, 2000). The chemical weathering in the headwater basin serves as a net source of CO_2.*

However, the glaciated terrains and a conducive lithology with exposures of pyritic sedimentary rocks support intense pyrite oxidation in the upper reaches. As a combined effect of temperature (on silicate weathering) and lithology (on sulfide oxidation), the chemical weathering in the upper Indus basin serves a net CO_2 source. Our new observation on net release of CO_2 from the northwestern Himalaya is not consistent with earlier suggested role of Himalaya weathering on the Cenozoic cooling (Raymo et al., 1988). This tectonic-weathering-climate hypothesis assumes intense silicate weathering in these young orogenic belts which may trigger a global cooling event (Raymo and Ruddiman, 1992). Our results from the upper Indus, although restricted to northwestern part of the Himalaya, do not support this proposition and warrants the need to include the CO_2 release (sulfide and organic oxidation) pathways in understanding the past climate and seawater chemistry changes.

Chapter 6

Conclusion and future perspectives

This page has been intentionally left blank.

This thesis work presents comprehensive investigation of chemical and isotopic compositions, both at spatial and temporal scales, for selected Indian River basins. These datasets and their mass balance modeling have enabled to establish the rates and factors regulating the pyrite oxidation in weathering- and transport-limited river basins. Towards this, we have used time-series sampling (at weekly interval for a duration of one-year) of surface water samples from the Mahanadi River and the Indus headwater regions. Here, the samples from the Mahanadi represent a transport-limited large river basin from the core-monsoon zone, whereas the Indus headwater represents a weathering-limited glaciated terrain from the northwestern Himalaya. Additionally, a detailed spatial sampling in the upper Indus basin (in India) was also carried out to assess the net effect of chemical weathering in this part of the Himalaya on CO_2 cycle. Some of the key outcomes from this thesis work are summarized below.

6.1. Net effect of weathering in a large tropical river basin on carbon cycle

Time-series analyses of water chemistry (major ions, silica and rhenium concentrations) and $\delta^{34}S_{SO4}$ values of one of the distributaries of the Mahanadi River (India) have been investigated to constrain the net feedback of tropical weathering on atmospheric CO_2 cycle. Variations in these elemental and isotopic compositions show relatively higher (18 ± 9 %) groundwater influx to the river during low (than high) flow stages, with no major seasonal change in relative solute supply from silicate weathering. Our calculations show that the CO_2 release/uptake rates in this basin is dominated by silicate weathering (-2.4 ± 1.6 tC/km^2/yr) and organic oxidation (0.50 ± 0.57 tC/km^2/yr), with minimal impact through carbon burial (-0.27 ± 0.12 tC/km^2/yr) and sulfide oxidation (0.1 ± 0.1 tC/km^2/yr). The amount of CO_2 consumed by silicate dissolution is partly (~ 20 %) counterbalanced by CO_2 release via organic oxidation. Our detailed investigation of four continental weathering pathways confirms that considering only the negative feedback of silicate weathering on carbon budget may overestimate its role in regulating global cooling events and related chemical cycles, and therefore, warrants the need to consider all these reactions for a precise geochemical budget. The basin lithology and tropical climate seem to control high silicate erosion, whereas limited physical erosion in this supply-limited regime limits the sulfide oxidation in the basin.

6.2. Pyrite oxidation in the upper Indus basin and its seasonal changes

Time-series data for water chemistry and $\delta^{34}S_{SO4}$-$\delta^{18}O_{SO4}$ of the (upper) Indus mainstream at Leh, India have been investigated at weekly intervals for one-year duration (2021-22). This data distribution and their inverse modeling were used to quantify the seasonal changes in cationic and sulfate source(s) contributions, and related controlling factors. Concentrations of most of these elements show lower concentrations during high (than low) flow stages, which cannot be attributed to water dilution alone. The near-zero silica concentrations for some of the summer samples, and lower Si/Na* ratios for all the samples (compared to that for other Himalayan Rivers) indicate the impact of biological uptake and contribution from Na_2SO_4-type evaporites (mirabilites). Inverse modeling of the elemental ratios estimates that the solutes are largely supplied by silicate (35 ± 9 %) and carbonate (32 ± 6 %) weathering. Unlike earlier studies, the estimated Cat_s values were found higher during early part of the high flow stage, attributable to impact of temperature on silicate dissolution at this site. The $\delta^{34}S_{SO4}$ (-2.6 ‰ to 2.9 ‰) and $\delta^{18}O_{SO4}$ (-5.9 ‰ to 2.6 ‰) values exhibit significant seasonal variation with depleted values for the baseflow samples. Source apportionment calculations indicate that the f_{py} values for the high flow stages are lower than that for baseflow stages. This f_{py} increase during low flow stages is largely linked to the diffusion of atmospheric oxygen via tectonic-induced microfractures to deep reactive pyrite fronts during the fall of the water table. Whilst the oxidation rate is linked to subsurface oxygen availability, the degree of f_{py} change at Leh is lower than that for other global basins, which may be linked to narrow depth of reactive front at this ridge than that for river valley. Our suggested coupling between flow stages and pyrite oxidation will have significance in understanding past CO_2 changes and riverine acidity in response to climatic changes.

6.3. Pyrite oxidation in the upper Indus basin and its spatial distribution

Spatial distribution of water chemistry and $\delta^{34}S_{SO4}$- $\delta^{18}O_{SO4}$ from the Indus mainstream and its tributaries were investigated to establish the rate and controls for pyrite oxidation in the northwestern Himalaya. The observed chemical and isotopic compositions for the (upper) Indus mainstream confirm dominant solute supply from the Zanskar tributary. Average sulfate concentrations for these samples (~ 200 µM) was about two times higher than that reported for global rivers (88 µM). Ternary plot for the major ions and $\delta^{34}S_{SO4}$ variability (-11 ‰ to 5 ‰) points to intense sulfide oxidation in the basin. The $\Delta^{18}O_{SO4\text{-}H2O}$ for these samples (7 ‰ to 19 ‰; mean: 11 ± 3 ‰) are systematically depleted than that reported for the lower Indus basin

(~ 15 ‰) and overlap with that of global rivers (12 ± 7 ‰), and also, fall intermediate to that expected for sedimentary sulfide (~ 3 to 6 ‰) and gypsum (~ 19 to 27 ‰). The slope of the $\delta^{18}O_{H2O}$-$\delta^{18}O_{SO4}$ linear trend reflects the f_{py} value for a basin. Further, source apportionment modeling estimates the sulfide-derived sulfate (0.6 ± 0.2), and silicate-derived cations (0.2 ± 0.1). These estimates establish intense sulfide oxidation in the basin, facilitated by conducive lithology and glacial coverage. Comparison of silicate weathering (2×10^5 mol/km^2/yr) and sulfide oxidation (4×10^5 mol/km^2/yr) rates confirms net release of CO_2 from these mountainous regions. This observation, therefore, rules out the importance of chemical weathering in the northwestern Himalaya in triggering the global Cenozoic cooling event.

6.4. Future scope of work

Outcomes of this study have provided better insights on the release of CO_2 from the northwestern Himalayan regions via pyrite oxidation, which counterbalances the CO_2 consumed by silicate weathering. This observation confirms a net release of CO_2 from the mountainous and glaciated regions, and hence, challenges the previously-suggested linkage between Himalaya weathering and Cenozoic cooling. This study, however, is restricted to a specific region of the Himalaya with conducive lithologies for sulfide oxidation, and may not be extended to the entire HTP region. Future studies, therefore, must focus in establishing the spatial and seasonal distribution of this oxidative weathering processes for central and eastern Himalaya and also, Tibetan River basins. This comprehensive dataset, together with the silicate weathering rates, can be used to estimate the net effect of Himalaya weathering on the carbon cycle. A net negative effect of these processes on CO_2 budget for the entire HTP River basins is required to establish the tectonic-weathering-climate hypothesis. In addition to sulfide oxidation, oxidation of petrogenic carbon may also supply CO_2 to the atmosphere. A thorough assessment of the net CO_2 budget during Himalaya weathering must also include this CO_2 supply pathway.

Another important aspect of pyrite oxidation in the Himalayan basins is to assess the effect of sulfate supply on the seawater $\delta^{34}S_{SO4}$ evolution during the Cenozoic period. Earlier studies have established the significance of Himalaya weathering in regulating the seawater $^{87}Sr/^{86}Sr$, $^{187}Os/^{188}Os$ and δ^7Li trends. A similar effort to evaluate the role of oxidative weathering in this young orogenic belt on the Cenozoic $\delta^{34}S_{SO4}$ trend can be useful in constraining its global impact. For this, a mass balance calculation involving elemental and

isotopic values for HTP and non-HTP Rivers, along with other sources and sinks, during different time-bins will be useful.

This thesis work establishes the effect of subsurface diffusion of atmospheric oxygen and availability of microfractures in aquifers in regulating the intensity of pyrite oxidation in a given basin. Further, the direction of groundwater flow (vertical versus interflow type) and its composition also contribute to these oxidation processes. Considering global significance of this trace lithology, future studies must focus on gaining details on these subsurface weathering processes. A comprehensive study must be attempted to track the availability and dissolution of pyrites in basins by investigating (i) fracture density data for aquifers, (ii) borehole and geophysical data for lithological imaging, (iii) $\delta^{34}S_{SO4}$ data for groundwater from different depths/seasons, and (iv) concentration of aqueous and gaseous oxygen. These subsurface data should be used to provide a 3-D subsurface map to trace the sulfate formation and its dispersion in river basins. Further, the process of pyrite oxidation varies significantly depending on basin lithology and glacial extent. Focused studies from basins with significant variation in these two parameters may provide clues on sensitivity of pyrite oxidation for these two variables. At present, it is assumed that the oxygen for these oxidation reactions mainly comes from atmosphere than the meteoric water- an assumption which must also be confirmed in future studies.

The observed water chemistry of the Indus headwater hints at appreciable influence of biological uptake and sulfate-rich evaporites. These solute sources and their influence on river chemistry have not been explored in earlier studies. The near-zero silica concentrations for some of the streams during summer season is very intriguing. The exact causes for this observation may be explored in future studies using silicon isotopes of these samples. These data will be useful in quantifying the influence of silicate weathering, hot springs, biological uptake and ion-exchange process. Further, studies on formation and solute contribution from sulfate-rich evaporites will be crucial in better understanding the riverine sulfate inventory for arid regions, and also, to quantify the pyrite oxidation rates for these basins more accurately.

References

This page has been intentionally left blank.

Acharya, S.S., Hishamunda, V. and Chakrabarti, R., 2022. Natural Sources and Anthropogenic Influences on the River Water and Groundwater Chemistry of the Lower Mahanadi Basin: Insights From Radiogenic Sr Isotopes and Major Ion Chemistry. *Frontiers in Water*, 4, pp.846438.

Ahmad, T., Khanna, P.P., Chakrapani, G.J. and Balakrishnan, S., 1998. Geochemical characteristics of water and sediment of the Indus river, Trans-Himalaya, India: constraints on weathering and erosion. *Journal of Asian Earth Sciences*, 16(2-3), pp.333-346.

Ali, K.F. and De Boer, D.H., 2010. Spatially distributed erosion and sediment yield modeling in the upper Indus River basin. *Water Resources Research*, pp.46(8).

Balci, N., Shanks III, W.C., Mayer, B. and Mandernack, K.W., 2007. Oxygen and sulfur isotope systematics of sulfate produced by bacterial and abiotic oxidation of pyrite. *Geochimica et Cosmochimica Acta*, 71(15), pp.3796-3811.

Banerjee, D.M., Deb, M. and Strauss, H., 1992. Organic carbon isotopic composition of Proterozoic sedimentary rocks from India: preliminary results. *Early Organic Evolution: Implications for Mineral and Energy Resources*, pp.232-240.

Bao, H., 2006. Purifying barite for oxygen isotope measurement by dissolution and reprecipitation in a chelating solution. *Analytical chemistry*, 78(1), pp.304-309.

Bastia, F. and Equeenuddin, S.M., 2016. Spatio-temporal variation of water flow and sediment discharge in the Mahanadi River, India. *Global and Planetary Change*, 144, pp.51-66.

Bastia, F. and Equeenuddin, S.M., 2019. Chemical weathering and associated CO_2 consumption in the Mahanadi river basin, India. *Journal of Asian Earth Sciences*, 174, pp.218-231.

Bastia, F., Equeenuddin, S.M., Roy, P.D. and Hernández-Mendiola, E., 2020. Geochemical signatures of surface sediments from the Mahanadi river basin (India): Chemical weathering, provenance, and tectonic settings. *Geological Journal*, 55(7), pp.5294-5307.

Benn, D.I. and Owen, L.A., 1998. The role of the Indian summer monsoon and the mid-latitude westerlies in Himalayan glaciation: review and speculative discussion. *Journal of the Geological Society*, 155(2), pp.353-363.

Beerling, D.J. and Royer, D.L., 2011. Convergent Cenozoic CO_2 history. *Nature Geoscience*, 4(7), pp.418-420.

Berner, R.A., Lasaga, A.C. and Garrels, R.M., 1983. Carbonate-silicate geochemical cycle and its effect on atmospheric carbon dioxide over the past 100 million years. *American Journal of Science, (United States)*, pp.283(7).

Berner E. K. and Berner R. A., 1996. Global Environment: Water, Air and Geochemical Cycles. Prentice Hall, New Jersey, pp. 376.

Bhat, M.A., Xu, S., Fan, D., Dar, T. and Li, S.L., 2023. Chemical weathering processes impacted by pyrite oxidation in the upper Indus River basin, Western Himalaya. *Journal of Asian Earth Sciences*, 245, pp.105573.

Bickle, M.J., Chapman, H.J., Bunbury, J., Harris, N.B., Fairchild, I.J., Ahmad, T. and Pomiès, C., 2005. Relative contributions of silicate and carbonate rocks to riverine Sr fluxes in the headwaters of the Ganges. *Geochimica et Cosmochimica Acta*, 69(9), pp.2221-2240.

Bickle, M.J., Chapman, H.J., Tipper, E., Galy, A., Christina, L. and Ahmad, T., 2018. Chemical weathering outputs from the flood plain of the Ganga. *Geochimica et Cosmochimica Acta*, 225, pp.146-175.

Bickle, M.J., Harris, N.B.W., Bunbury, J.M., Chapman, H.J., Fairchild, I.J. and Ahmad, T., 2001. Controls on the $^{87}Sr/^{86}Sr$ ratio of carbonates in the Garhwal Himalaya, headwaters of the Ganges. *The Journal of Geology*, 109(6), pp.737-753.

Bluth, G.J. and Kump, L.R., 1994. Lithologic and climatologic controls of river chemistry. *Geochimica et Cosmochimica Acta*, 58(10), pp.2341-2359.

Burke, A., Present, T.M., Paris, G., Rae, E.C., Sandilands, B.H., Gaillardet, J., Peucker-Ehrenbrink, B., Fischer, W.W., McClelland, J.W., Spencer, R.G. and Voss, B.M., 2018. Sulfur isotopes in rivers: Insights into global weathering budgets, pyrite oxidation, and the modern sulfur cycle. *Earth and Planetary Science Letters*, 496, pp.168-177.

Calmels, D., Gaillardet, J., Brenot, A. and France-Lanord, C., 2007. Sustained sulfide oxidation by physical erosion processes in the Mackenzie River basin: Climatic perspectives. *Geology*, 35(11), pp.1003-1006.

Canfield, D.E., 1994. Factors influencing organic carbon preservation in marine sediments. *Chemical Geology*, 114(3-4), pp.315-329.

Chakrapani, G.J. and Subramanian, V., 1990. Factors controlling sediment discharge in the Mahanadi River Basin, India. *Journal of Hydrology*, 117(1-4), pp.169-185.

Chakrapani, G.J. and Subramanian, V., 1993. Rates of erosion and sedimentation in the Mahanadi River basin, India. Journal of hydrology, 149(1-4), pp.39-48.

Chakrapani, G.J. and Veizer, J., 2006. Source of dissolved sulphate in the Alakananda–Bhagirathi rivers in the Himalayas. *Current Science*, 90(4), pp.500-503.

Chamberlin, T.C., 1899. An attempt to frame a working hypothesis of the cause of glacial periods on an atmospheric basis. *The Journal of Geology*, 7(6), pp.545-584.

Chapman, H., Bickle, M., Thaw, S.H. and Thiam, H.N., 2015. Chemical fluxes from time series sampling of the Irrawaddy and Salween Rivers, Myanmar. *Chemical Geology*, 401, pp.15-27.

Chevalier, M.L., Ryerson, F.J., Tapponnier, P., Finkel, R.C., Van Der Woerd, J., Haibing, L. and Qing, L., 2005. Slip-rate measurements on the Karakorum fault may imply secular variations in fault motion. *Science*, 307(5708), pp.411-414.

Chmielewski, A., Wierzchnicki, R., Derda, M. and Mikołajczuk, A., 2002. Sulfur isotope composition of selected Polish coals. *Nukleonika*, 47(suppl.1), pp.67-68, https://www.infona.pl//resource/bwmeta1.element.baztech-article-BUJ6-0006-0070.

Claypool, G.E., Holser, W.T., Kaplan, I.R., Sakai, H. and Zak, I., 1980. The age curves of sulfur and oxygen isotopes in marine sulfate and their mutual interpretation. *Chemical Geology*, 28, pp.199-260.

Colodner, D., Sachs, J., Ravizza, G., Turekian, K., Edmond, J. and Boyle, E., 1993. The geochemical cycle of rhenium: a reconnaissance. *Earth and Planetary Science Letters*, 117(1-2), pp.205-221.

Dalai, T.K., Krishnaswami, S. and Sarin, M.M., 2002a. Major ion chemistry in the headwaters of the Yamuna River system:: Chemical weathering, its temperature dependence and CO_2 consumption in the Himalaya. *Geochimica et Cosmochimica Acta*, 66(19), pp.3397-3416.

Dalai, T.K., Singh, S.K., Trivedi, J.R. and Krishnaswami, S., 2002b. Dissolved rhenium in the Yamuna River System and the Ganga in the Himalaya: Role of black shale weathering on the budgets of Re, Os, and U in rivers and CO_2 in the atmosphere. *Geochimica et Cosmochimica Acta*, 66(1), pp.29-43.

Danish, M., Tripathy, G.R. and Rahaman, W., 2020. Submarine groundwater discharge to a tropical coastal lagoon (Chilika lagoon, India): An estimation using Sr isotopes. *Marine Chemistry*, 224, pp.103816.

Danish, M., Tripathy, G.R., Mitra, S., Rout, R.K. and Raskar, S., 2021. Non-conservative removal of dissolved rhenium from a coastal lagoon: Clay adsorption versus biological uptake. *Chemical Geology*, 580, pp.120378.

Das, A., Chung, C.H. and You, C.F., 2012. Disproportionately high rates of sulfide oxidation from mountainous river basins of Taiwan orogeny: Sulfur isotope evidence. *Geophysical Research Letters*, pp.39(12).

Das, A., Krishnaswami, S., Sarin, M.M. and Pande, K., 2005. Chemical weathering in the Krishna Basin and Western Ghats of the Deccan Traps, India: Rates of basalt weathering and their controls. *Geochimica et Cosmochimica Acta*, 69(8), pp.2067-2084.

Das, A., Pawar, N.J. and Veizer, J., 2011. Sources of sulfur in Deccan Trap rivers: A reconnaissance isotope study. *Applied Geochemistry*, 26(3), pp.301-307.

Das, S., Tripathy, G.R., Rai, S.K., Danish, M., Thakur, D., Dutt, S. and Sarangi, S., 2021. The role of sulfuric acid in continental weathering: Insights from dissolved major ions and inorganic carbon isotopes of the Teesta River, lower Brahmaputra system. *Geochemistry, Geophysics, Geosystems*, 22(4), pp.e2020GC009324.

Derry, L.A. and France-Lanord, C., 1997. Himalayan weathering and erosion fluxes: climate and tectonic controls. *In Tectonic uplift and climate change* (pp. 289-312). Boston, MA: Springer US.

Dessert, C., Dupré, B., François, L.M., Schott, J., Gaillardet, J., Chakrapani, G. and Bajpai, S., 2001. Erosion of Deccan Traps determined by river geochemistry: impact on the global climate and the 87Sr/86Sr ratio of seawater. *Earth and Planetary Science Letters*, 188(3-4), pp.459-474.

Dora, M.L., Upadhyay, D., Randive, K.R., Shareef, M., Baswani, S.R. and Ranjan, S., 2020. Trace element geochemistry of magnetite and pyrite and sulfur isotope geochemistry of pyrite and barite from the Thanewasna Cu-(Au) deposit, western Bastar Craton, central India: Implication for ore genesis. *Ore Geology Reviews*, 117, pp.103262.

Drever, J. (1997), The Geochemistry of Natural Waters, Prentice-Hall, ISBN 0132727900, 9780133514032.

Druschel, G. and Borda, M., 2006. Comment on “Pyrite dissolution in acidic media” by M. Descostes, P. Vitorge, and C. Beaucaire. *Geochimica et Cosmochimica Acta*, 70(20), pp.5246-5250.

Dunlap, W.J., Weinberg, R.F. and Searle, M.P., 1998. Karakoram fault zone rocks cool in two phases. *Journal of the Geological Society*, 155(6), pp.903-912.

Dutta, A., Mishra, P., Absar, A., Malviya, V.P., Singh, P.K., Srivastava, A., Ray, B., Kumar, A. and Nitnaware, N.V., 2023. Tracing hydrothermal mineral thenardite in geysers/hot springs of North-western Himalayan belt, Ladakh Geothermal Province, India by

hydrogeochemistry, fluid-mineral equilibria and isotopic studies. *Geochemistry*, 83(2), pp.125973.

Edmond, J.M. and Huh, Y., 1997. Chemical weathering yields from basement and orogenic terrains in hot and cold climates. *In Tectonic uplift and climate change* (pp. 329-351). Boston, MA: Springer US.

Emerson, S. and Hedges, J.I., 1988. Processes controlling the organic carbon content of open ocean sediments. *Paleo-oceanography*, 3(5), pp.621-634.

Evans, M.J., Derry, L.A. and France-Lanord, C., 2004. Geothermal fluxes of alkalinity in the Narayani river system of central Nepal. *Geochemistry, Geophysics, Geosystems*, pp.5(8).

Farhan, M., Arif, M., Ye, Y., Li, C.F., Chen, X., Wu, T., Ullah, Z., Turab, S.A., Zafar, T., Hussain, Z. and Sadiq, I., 2023. Metamorphism of Ladakh Island Arc terrain in the Himalayan region: implications from sulfide geochemistry and petrography. *Arabian Journal of Geosciences*, 16(10), pp.565.

Fontorbe, G., Christina, L., Chapman, H.J. and Bickle, M.J., 2013. The silicon isotopic composition of the Ganges and its tributaries. *Earth and Planetary Science Letters*, 381, pp.21-30.

France-Lanord, C. and Derry, L.A., 1997. Organic carbon burial forcing of the carbon cycle from Himalayan erosion. *Nature*, 390(6655), pp.65-67.

Gaillardet, J. and Galy, A., 2008. Himalaya-Carbon Sink or Source?. *Science*, 320(5884), pp.1727-1728.

Gaillardet, J., Dupré, B., Louvat, P. and Allegre, C.J., 1999. Global silicate weathering and CO_2 consumption rates deduced from the chemistry of large rivers. *Chemical Geology*, 159(1-4), pp.3-30.

Galy, A. and France-Lanord, C., 1999. Weathering processes in the Ganges–Brahmaputra basin and the riverine alkalinity budget. *Chemical Geology*, 159(1-4), pp.31-60.

Galy, V., Peucker-Ehrenbrink, B. and Eglinton, T., 2015. Global carbon export from the terrestrial biosphere controlled by erosion. *Nature*, 521(7551), pp.204-207.

Garzanti, E., Vezzoli, G., Andò, S., Paparella, P. and Clift, P.D., 2005. Petrology of Indus River sands: a key to interpret erosion history of the Western Himalayan Syntaxis. *Earth and Planetary Science Letters*, 229(3-4), pp.287-302.

Godsey, S.E., Kirchner, J.W. and Clow, D.W., 2009. Concentration–discharge relationships reflect chemostatic characteristics of US catchments. *Hydrological Processes: An International Journal*, 23(13), pp.1844-1864.

Goswami, V., Singh, S.K. and Bhushan, R., 2014. Impact of water mass mixing and dust deposition on Nd concentration and ε_{Nd} of the Arabian Sea water column. *Geochimica et Cosmochimica Acta*, 145, pp.30-49.

Govil, H., Mishra, G., Gill, N., Taloor, A. and Diwan, P., 2021. Mapping hydrothermally altered minerals and gossans using hyperspectral data in Eastern Kumaon Himalaya, India. *Applied Computing and Geosciences*, 9, pp.100054.

Gu, X., Heaney, P.J., Reis, F.D.A. and Brantley, S.L., 2020a. Deep abiotic weathering of pyrite. *Science*, 370(6515), pp.eabb8092.

Gu, X., Rempe, D.M., Dietrich, W.E., West, A.J., Lin, T.C., Jin, L. and Brantley, S.L., 2020b. Chemical reactions, porosity, and microfracturing in shale during weathering: The effect of erosion rate. *Geochimica et Cosmochimica Acta*, 269, pp.63-100.

Gupta, C., Kulkarni, A.V. and Taloor, A.K., 2021. Streamflow modeling and contribution of snow and glacier melt runoff in glacierized Upper Indus Basin. *Environmental Monitoring and Assessment*, 193(11), pp.761.

Gupta, G.V.M., Sarma, V.V.S.S., Robin, R.S., Raman, A.V., Jai Kumar, M., Rakesh, M. and Subramanian, B.R., 2008. Influence of net ecosystem metabolism in transferring riverine organic carbon to atmospheric CO_2 in a tropical coastal lagoon (Chilka Lake, India). *Biogeochemistry*, 87, pp.265-285.

Gupta, M. L., 1975, August. Geochemistry of thermal waters from various geothermal provinces of India. *In Proceedings of the Grenoble Symposium*.

Gurumurthy, G.P., Balakrishna, K., Riotte, J., Braun, J.J., Audry, S., Shankar, H.U. and Manjunatha, B.R., 2012. Controls on intense silicate weathering in a tropical river, southwestern India. *Chemical Geology*, 300, pp.61-69.

Hemingway, J.D., Olson, H., Turchyn, A.V., Tipper, E.T., Bickle, M.J. and Johnston, D.T., 2020. Triple oxygen isotope insight into terrestrial pyrite oxidation. *Proceedings of the National Academy of Sciences*, 117(14), pp.7650-7657.

Heri, A.R., Aitchison, J.C., King, J.A. and Villa, I.M., 2015. Geochronology and isotope geochemistry of Eocene dykes intruding the Ladakh Batholith. *Lithos*, 212, pp.111-121.

Hilley, G.E. and Porder, S., 2008. A framework for predicting global silicate weathering and CO_2 drawdown rates over geologic time-scales. *Proceedings of the National Academy of Sciences*, 105(44), pp.16855-16859.

Hilton, R.G. and West, A.J., 2020. Mountains, erosion and the carbon cycle. Nature Reviews Earth & Environment, 1(6), pp.284-299.

Hilton, R.G., Gaillardet, J., Calmels, D. and Birck, J.L., 2014. Geological respiration of a mountain belt revealed by the trace element rhenium. *Earth and Planetary Science Letters*, 403, pp.27-36.

Hilton, R.G., Galy, A. and Hovius, N., 2008. Riverine particulate organic carbon from an active mountain belt: Importance of landslides. *Global Biogeochemical Cycles*, pp.22(1).

Hilton, R.G., Galy, V., Gaillardet, J., Dellinger, M., Bryant, C., O'Regan, M., Gröcke, D.R., Coxall, H., Bouchez, J. and Calmels, D., 2015. Erosion of organic carbon in the Arctic as a geological carbon dioxide sink. *Nature*, 524(7563), pp.84-87.

Hilton, R.G., Turowski, J.M., Winnick, M., Dellinger, M., Schleppi, P., Williams, K.H., Lawrence, C.R., Maher, K., West, M. and Hayton, A., 2021. Concentration-discharge relationships of dissolved rhenium in Alpine catchments reveal its use as a tracer of oxidative weathering. *Water Resources Research*, 57(11), pp.e2021WR029844.

Holland, H.D., 2005. Sea level, sediments and the composition of seawater. *American Journal of Science*, 305(3), pp.220-239.

Horan, K., Hilton, R.G., Dellinger, M., Tipper, E., Galy, V., Calmels, D., Selby, D., Gaillardet, J., Ottley, C.J., Parsons, D.R. and Burton, K.W., 2019. Carbon dioxide emissions by rock organic carbon oxidation and the net geochemical carbon budget of the Mackenzie River Basin. *American Journal of Science*, pp.319(6).

Horan, K., Hilton, R.G., Selby, D., Ottley, C.J., Gröcke, D.R., Hicks, M. and Burton, K.W., 2017. Mountain glaciation drives rapid oxidation of rock-bound organic carbon. *Science Advances*, 3(10), pp.e1701107.

Hren, M.T., Chamberlain, C.P., Hilley, G.E., Blisniuk, P.M. and Bookhagen, B., 2007. Major ion chemistry of the Yarlung Tsangpo–Brahmaputra river: chemical weathering, erosion, and CO_2 consumption in the southern Tibetan plateau and eastern syntaxis of the Himalaya. *Geochimica et Cosmochimica Acta*, 71(12), pp.2907-2935.

Ibarra, D.E., Caves, J.K., Moon, S., Thomas, D.L., Hartmann, J., Chamberlain, C.P. and Maher, K., 2016. Differential weathering of basaltic and granitic catchments from concentration–discharge relationships. *Geochimica et Cosmochimica Acta*, 190, pp.265-293.

Immerzeel, W.W., Van Beek, L.P. and Bierkens, M.F., 2010. Climate change will affect the Asian water towers. *Science*, 328(5984), pp.1382-1385.

Isson, T.T. and Planavsky, N.J., 2018. Reverse weathering as a long-term stabilizer of marine pH and planetary climate. *Nature*, 560(7719), pp.471-475.

Jacks, G., Sharma, V.P., Torssander, P. and Åberg, G., 1994. Origin of sulphur in soil and water in a Precambrian terrain, S. India. *Geochemical Journal*, 28(4), pp.351-358.

Jacobson, A.D. and Blum, J.D., 2000. Ca/Sr and $^{87}Sr/^{86}Sr$ geochemistry of disseminated calcite in Himalayan silicate rocks from Nanga Parbat: Influence on river-water chemistry. *Geology*, 28(5), pp.463-466.

Jacobson, A.D., Andrews, M.G., Lehn, G.O. and Holmden, C., 2015. Silicate versus carbonate weathering in Iceland: New insights from Ca isotopes. *Earth and Planetary Science Letters*, 416, pp.132-142.

Jaffe, L.A., Peucker-Ehrenbrink, B. and Petsch, S.T., 2002. Mobility of rhenium, platinum group elements and organic carbon during black shale weathering. *Earth and Planetary Science Letters*, 198(3-4), pp.339-353.

Jain, S.K., Agarwal, P.K. and Singh, V.P., 2007. Hydrology and water resources of India (Vol. 57). Springer Science & Business Media, Volume 57 of *Water Science and Technology Library*, ISBN: 1402051808, 9781402051807.

Jha, P.K., Tiwari, J., Singh, U.K., Kumar, M. and Subramanian, V., 2009. Chemical weathering and associated CO_2 consumption in the Godavari River basin, India. *Chemical Geology*, 264(1-4), pp.364-374.

Jochum, K.P., Weis, U., Schwager, B., Stoll, B., Wilson, S.A., Haug, G.H., Andreae, M.O. and Enzweiler, J., 2016. Reference values following ISO guidelines for frequently requested rock reference materials. *Geostandards and Geoanalytical Research*, 40(3), pp.333-350.

Jonell, T.N., Carter, A., Böning, P., Pahnke, K. and Clift, P.D., 2017. Climatic and glacial impact on erosion patterns and sediment provenance in the Himalayan rain shadow, Zanskar River, NW India. *Bulletin*, 129(7-8), pp.820-836.

Juyal, N., 2014. Ladakh: the high-altitude Indian cold desert. *Landscapes and landforms of India*, pp.115-124.

Kampschulte, A. and Strauss, H., 2004. The sulfur isotopic evolution of Phanerozoic seawater based on the analysis of structurally substituted sulfate in carbonates. *Chemical Geology*, 204(3-4), pp.255-286.

Karim, A. and Veizer, J., 2000. Weathering processes in the Indus River Basin: implications from riverine carbon, sulfur, oxygen, and strontium isotopes. *Chemical Geology*, 170(1-4), pp.153-177.

Kemeny, P.C., Lopez, G.I., Dalleska, N.F., Torres, M., Burke, A., Bhatt, M.P., West, A.J., Hartmann, J. and Adkins, J.F., 2021a. Sulfate sulfur isotopes and major ion chemistry

reveal that pyrite oxidation counteracts CO_2 drawdown from silicate weathering in the Langtang-Trisuli-Narayani River system, Nepal Himalaya. *Geochimica et Cosmochimica Acta*, 294, pp.43-69.

Kemeny, P.C., Torres, M.A., Lamb, M.P., Webb, S.M., Dalleska, N., Cole, T., Hou, Y., Marske, J., Adkins, J.F. and Fischer, W.W., 2021b. Organic sulfur fluxes and geomorphic control of sulfur isotope ratios in rivers. *Earth and Planetary Science Letters*, 562, pp.116838.

Killingsworth, B.A., Bao, H. and Kohl, I.E., 2018. Assessing pyrite-derived sulfate in the Mississippi River with four years of sulfur and triple-oxygen isotope data. *Environmental Science & Technology*, 52(11), pp.6126-6136.

Kornexl, B.E., Gehre, M., Höfling, R. and Werner, R.A., 1999. On-line $\delta^{18}O$ measurement of organic and inorganic substances. *Rapid Communications in Mass Spectrometry*, 13(16), pp.1685-1693.

Krishnaswami, S., Singh, S. K., & Dalai, T., 1999. Silicate weathering in the Himalaya: Role in contributing to major ions and radiogenic Sr to the Bay of Bengal. Ocean science, trends and future directions, pp. 23–51, New Delhi: *Indian Natl. Sci. Acad. and Akad. Int.*, CRID: 1574231874633431936, NII Article ID: 10014672612.

Krishnaswami, S., Trivedi, J.R., Sarin, M.M., Ramesh, R. and Sharma, K.K., 1992. Strontium isotopes and rubidium in the Ganga-Brahmaputra River system: Weathering in the Himalaya, fluxes to the Bay of Bengal and contributions to the evolution of oceanic $^{87}Sr/^{86}Sr$. *Earth and Planetary Science Letters*, 109(1-2), pp.243-253.

Krishnaswami, S., & Tripathy, G. R., 2012. Chemical and physical erosion of river basins of India: Links to climate and tectonics. Proceedings of the Indian National Science Academy, 78, pp.299–311.

Larsen, I.J., Montgomery, D.R. and Greenberg, H.M., 2014. The contribution of mountains to global denudation. *Geology*, 42(6), pp.527-530.

Laskar, A.H., Yadava, M.G. and Ramesh, R., 2016. Stable and radioactive carbon in forest soils of Chhattisgarh, Central India: Implications for tropical soil carbon dynamics and stable carbon isotope evolution. *Journal of Asian Earth Sciences*, 123, pp.47-57.

Lerman, A., Wu, L. and Mackenzie, F.T., 2007. CO_2 and H_2SO_4 consumption in weathering and material transport to the ocean, and their role in the global carbon balance. *Marine Chemistry*, 106(1-2), pp.326-350.

Li, G. and Elderfield, H., 2013. Evolution of carbon cycle over the past 100 million years. *Geochimica et Cosmochimica Acta*, 103, pp.11-25.

Li, S.L., Calmels, D., Han, G., Gaillardet, J. and Liu, C.Q., 2008. Sulfuric acid as an agent of carbonate weathering constrained by $\delta^{13}C_{DIC}$: examples from Southwest China. *Earth and Planetary Science Letters*, 270(3-4), pp.189-199.

Liao, R., Gu, X. and Brantley, S.L., 2022. Weathering of chlorite from grain to watershed: The role and distribution of oxidation reactions in the subsurface. *Geochimica et Cosmochimica Acta*, 333, pp.284-307.

Lin, Z., Sun, X., Chen, K., Strauss, H., Klemd, R., Smrzka, D., Chen, T., Lu, Y. and Peckmann, J., 2022. Effects of sulfate reduction processes on the trace element geochemistry of sedimentary pyrite in modern seep environments. *Geochimica et Cosmochimica Acta*, 333, pp.75-94.

Lone, S.A., Jeelani, G., Deshpande, R.D. and Mukherjee, A., 2019. Stable isotope ($\delta^{18}O$ and δD) dynamics of precipitation in a high altitude Himalayan cold desert and its surroundings in Indus River basin, Ladakh. *Atmospheric Research*, 221, pp.46-57.

Ma, T., Xu, S., Zhong, J., Li, S.L., Chen, S., Wang, W. and Liu, C.Q., 2023. Sulfuric acid weathering counteracts CO_2 drawdown from silicate weathering in mountainous catchments from southwest China. *Journal of Hydrology*, 618, pp.129167.

Mackenzie, F.T. and Kump, L.R., 1995. Reverse weathering, clay mineral formation, and oceanic element cycles. *Science*, 270(5236), pp.586-586.

Maher, K., 2011. The role of fluid residence time and topographic scales in determining chemical fluxes from landscapes. *Earth and Planetary Science Letters*, 312(1-2), pp.48-58.

Mandal, S.K., Lupker, M., Burg, J.P., Valla, P.G., Haghipour, N. and Christl, M., 2015. Spatial variability of 10Be-derived erosion rates across the southern Peninsular Indian escarpment: A key to landscape evolution across passive margins. Earth and Planetary Science Letters, 425, pp.154-167.

Meybeck, M., 2003. Global occurrence of major elements in rivers. *Treatise on Geochemistry*, 5, pp. 605. 10.1016/B0-08-043751-6/05164-1.

Middlemiss, C.S., 1910. Revision of the Silurian-Trias Sequence in Kashmir: Records of the *Geological Survey of India*, v. 40.

Milliman, J.D. and Syvitski, J.P., 1992. Geomorphic/tectonic control of sediment discharge to the ocean: the importance of small mountainous rivers. *The Journal of Geology*, 100(5), pp.525-544.

Millot, R., Gaillardet, J., Dupré, B. and Allègre, C.J., 2003. Northern latitude chemical weathering rates: clues from the Mackenzie River Basin, Canada. *Geochimica et Cosmochimica Acta*, 67(7), pp. 1305-1329.

Mishra, V., Chakravarty, S., Finkelman, R.B. and Varma, A.K., 2019. Geochemistry of rare earth elements in lower Gondwana coals of the Talchir Coal Basin, India. *Journal of Geochemical Exploration*, 204, pp.43-56.

Misra, S. and Froelich, P.N., 2012. Lithium isotope history of Cenozoic seawater: changes in silicate weathering and reverse weathering. *Science*, 335(6070), pp.818-823.

Moon, S., Huh, Y., Qin, J. and van Pho, N., 2007. Chemical weathering in the Hong (Red) River basin: rates of silicate weathering and their controlling factors. *Geochimica et Cosmochimica Acta*, 71(6), pp.1411-1430.

Mukherjee, A. and Fryar, A.E., 2008. Deeper groundwater chemistry and geochemical modeling of the arsenic affected western Bengal basin, West Bengal, India. *Applied Geochemistry*, 23(4), pp.863-894.

Mukherjee, R., Muduli, P.R., Barik, S.K. and Kumar, S., 2019. Sources and transformations of organic matter in sediments of Asia's largest brackish water lagoon (Chilika, India) and nearby mangrove ecosystem. *Environmental Earth Sciences*, 78, pp.1-15.

Mukhopadhyay, B. and Khan, A., 2015. A reevaluation of the snowmelt and glacial melt in river flows within Upper Indus Basin and its significance in a changing climate. *Journal of Hydrology*, 527, pp.119-132.

Narayana, B.L., Rao, P.R., Reddy, G.L.N. and Rao, V.D., 1999. Geochemistry and origin of megacrystic granitoid rocks from Eastern Ghats Granulite Belt. *Gondwana Research*, 2(1), pp.105-115.

Négrel, P., Allègre, C.J., Dupré, B. and Lewin, E., 1993. Erosion sources determined by inversion of major and trace element ratios and strontium isotopic ratios in river water: the Congo Basin case. *Earth and Planetary Science Letters*, 120(1-2), pp.59-76.

Ódri, Á., Becker, M., Broadhurst, J., Harrison, S.T. and Edraki, M., 2020. Stable isotope imprints during pyrite leaching: implications for acid rock drainage characterization. *Minerals*, 10(11), pp.982.

Oliver, L., Harris, N., Bickle, M., Chapman, H., Dise, N. and Horstwood, M., 2003. Silicate weathering rates decoupled from the 87Sr/86Sr ratio of the dissolved load during Himalayan erosion. *Chemical Geology*, 201(1-2), pp.119-139.

Otero, N., Soler, A. and Canals, À., 2008. Controls of $\delta^{34}S$ and $\delta^{18}O$ in dissolved sulphate: learning from a detailed survey in the Llobregat River (Spain). *Applied Geochemistry*, 23(5), pp.1166-1185.

Owen, L.A., 2011. Quaternary glaciation of northern India. In Developments in Quaternary *Sciences* (Vol. 15, pp. 929-942). Elsevier.

Pandalai, H.S., Changkakoti, A., Krouse, H.R. and Gunalan, N., 1991. The relationship between carbon, sulfur, and pyritic iron in the Amjhore Deposit, Bihar, India. *Economic Geology*, 86(4), pp.862-869.

Pande, K., Padia, J.T., Ramesh, R. and Sharma, K.K., 2000. Stable isotope systematics of surface water bodies in the Himalayan and Trans-Himalayan (Kashmir) region. *Journal of Earth System Science*, 109, pp.109-115.

Pande, K., Sarin, M.M., Trivedi, J.R., Krishnaswami, S. and Sharma, K.K., 1994. The Indus River system (India-Pakistan): Major-ion chemistry, uranium and strontium isotopes. *Chemical Geology*, 116(3-4), pp.245-259.

Parsons, A.J., Hosseini, K., Palin, R.M. and Sigloch, K., 2020. Geological, geophysical and plate kinematic constraints for models of the India-Asia collision and the post-Triassic central Tethys oceans. *Earth-Science Reviews*, 208, pp.103084.

Pattanaik, J.K., Balakrishnan, S., Bhutani, R. and Singh, P., 2013. Estimation of weathering rates and CO_2 drawdown based on solute load: Significance of granulites and gneisses dominated weathering in the Kaveri River basin, Southern India. *Geochimica et Cosmochimica Acta*, 121, pp.611-636.

Paul, D.K., Barman, T.R., McNaughton, N.J., Fletcher, I.R., Potts, P.J., Ramakrishnan, M. and Augustine, P.F., 1990. Archean-Proterozoic evolution of Indian charnockites: isotopic and geochemical evidence from granulites of the Eastern Ghats Belt. *The Journal of Geology*, 98(2), pp.253-263.

Penman, D.E., Rugenstein, J.K.C., Ibarra, D.E. and Winnick, M.J., 2020. Silicate weathering as a feedback and forcing in Earth's climate and carbon cycle. *Earth-Science Reviews*, 209, pp.103298.

Peucker-Ehrenbrink, B. and Hannigan, R.E., 2000. Effects of black shale weathering on the mobility of rhenium and platinum group elements. *Geology*, 28(5), pp.475-478.

Peucker-Ehrenbrink, B., and Ravizza, G.E., 2012, Osmium isotope stratigraphy - chapter 8. In Gradstein, F.M., Ogg, J.G., Schmitz, M.D., and Ogg, G.M. (eds), *The Geologic Time Scale 2012*. Elsevier, Oxford, Vol. 1: pp.145-166

Qazi, N.Q., Jain, S.K., Thayyen, R.J., Patil, P.R. and Singh, M.K., 2020. Hydrology of the Himalayas. *Himalayan Weather and Climate and their Impact on the Environment*, pp.419-450.

Quade, J., English, N. and DeCelles, P.G., 2003. Silicate versus carbonate weathering in the Himalaya: a comparison of the Arun and Seti River watersheds. *Chemical Geology*, 202(3-4), pp.275-296.

Rahaman, W., Singh, S.K. and Shukla, A.D., 2012. Rhenium in Indian rivers: Sources, fluxes, and contribution to oceanic budget. *Geochemistry. Geophysics. Geosystems.*, pp.13(8).

Rai, K.L. and Changkakoti, A., 1996. Ore Genetic Implications of the Stable Isotope Geochemistry of Sulphur and Lead in Sargipali Deposit, Orissa, India. *Magmatism in Relation to Diverse Tectonic Settings*, pp.123, ISBN: 9054102756, 9789054102755, CRC Press, 1996.

Rai, S.K., Singh, S.K. and Krishnaswami, S., 2010. Chemical weathering in the plain and peninsular sub-basins of the Ganga: impact on major ion chemistry and elemental fluxes. *Geochimica et Cosmochimica Acta*, 74(8), pp.2340-2355.

Rao, M.S. and Rao, V.D., 1988. Chemical constraints on the origin of the charnockites in the Eastern Ghat Mobile belt, India. *Chemical Geology*, 69(1-2), pp.37-48.

Rather, M.I., Rashid, I., Shahi, N., Murtaza, K.O., Hassan, K., Yousuf, A.R., Romshoo, S.A. and Shah, I.Y., 2016. Massive land system changes impact water quality of the Jhelum River in Kashmir Himalaya. *Environmental Monitoring and Assessment*, 188, pp.1-20.

Ravizza, G.E. and Zachos, J.C., 2003. Records of Cenozoic ocean chemistry. *Treatise on Geochemistry*, 6, pp.625.

Ray, E. and Paul, D., 2021. Major and trace element characteristics of the average Indian post-archean shale: Implications for provenance, weathering, and depositional environment. *ACS Earth and Space Chemistry*, 5(5), pp.1114-1129.

Raymo, M.E. and Ruddiman, W.F., 1992. Tectonic forcing of late Cenozoic climate. *Nature*, 359(6391), pp.117-122.

Raymo, M.E., Ruddiman, W.F. and Froelich, P.N., 1988. Influence of late Cenozoic mountain building on ocean geochemical cycles. *Geology*, 16(7), pp.649-653.

Reichardt, H., Weinberg, R.F., Andersson, U.B. and Fanning, C.M., 2010. Hybridization of granitic magmas in the source: the origin of the Karakoram Batholith, Ladakh, NW India. Lithos, 116(3-4), pp.249-272.

Relph, K.E., Stevenson, E.I., Turchyn, A.V., Antler, G., Bickle, M.J., Baronas, J.J., Darby, S.E., Parsons, D.R. and Tipper, E.T., 2021. Partitioning riverine sulfate sources using

oxygen and sulfur isotopes: Implications for carbon budgets of large rivers. *Earth and Planetary Science Letters*, 567, pp.116957.

Rout, R.K. and Tripathy, G.R., 2024. Net effect of chemical erosion in a tropical basin on carbon cycle: Constraints from elemental and sulfur isotopic composition of the Mahanadi River water. *Chemical Geology*, 644, pp.121859.

Roy-Barman, M. and Jeandel, C., 2016. Marine geochemistry: ocean circulation, carbon cycle and climate change. *Oxford University Press*. ISBN 978-0-19-878749-5 (hbk.).

Roylands, T., Hilton, R.G., Garnett, M.H., Soulet, G., Newton, J.A., Peterkin, J.L. and Hancock, P., 2022. Capturing the short-term variability of carbon dioxide emissions from sedimentary rock weathering in a remote mountainous catchment, New Zealand. *Chemical Geology*, 608, pp.121024.

Rudnick, R.L., Gao, S., Holland, H.D. and Turekian, K.K., 2003. Composition of the continental crust. The Crust, 3, pp.1-64.

Saha, A.K., 1994. Crustal evolution of Singhbhum-north Orissa, eastern India. *Mem. Geol. Soc. India*, 27, pp.341, CRID: 1572824500303973504, NII Article ID: 10019557189.

Samanta, A., Tripathy, G.R. and Das, R., 2019. Temporal variations in water chemistry of the (lower) Brahmaputra River: Implications to seasonality in mineral weathering. *Geochemistry, Geophysics, Geosystems*, 20(6), pp.2769-2785.

Samanta, A., Tripathy, G.R., Nath, B.N., Bhushan, R., Panchang, R., Bharti, N. and Shrivastava, A., 2022. Holocene variability in chemical weathering and ocean redox state: A reconstruction using sediment geochemistry of the Arabian Sea. *Journal of Asian Earth Sciences*, 224, pp.105029.

Samanta, A., Tripathy, G.R., Pradeep, A.T. and Mandal, A., 2021. Major ion chemistry of two cratonic rivers in the tropics: Weathering rates and their controlling factors. *Hydrological Processes*, 35(2), pp.e14035.

Sarin, M.M., Krishnaswami, S., Dilli, K., Somayajulu, B.L.K. and Moore, W.S., 1989. Major ion chemistry of the Ganga-Brahmaputra River system: weathering processes and fluxes to the Bay of Bengal. *Geochimica et cosmochimica acta*, 53(5), pp.997-1009.

Sarin, M.M., Krishnaswami, S., Trivedi, J.R. and Sharma, K.K., 1992. Major ion chemistry of the Ganga source waters: weathering in the high altitude Himalaya. *Proceedings of the Indian Academy of Sciences-Earth and Planetary Sciences*, 101, pp.89-98.

Sarkar, A., Chakraborty, P.P., Mishra, B., Bera, M.K., Sanyal, P. and Paul, S., 2010. Mesoproterozoic sulphidic ocean, delayed oxygenation and evolution of early life:

sulphur isotope clues from Indian Proterozoic basins. *Geological Magazine*, 147(2), pp.206-218.

Sharma, R., Chauhan, D.S. and Rao, D.R., 2010. Polymetallic sulphide mineralization in Chiplakot crystallines, northeast Kumaun Himalaya. *Current Science*, 98(5), pp.698-702.

Sharma, A., Kumar, K., Laskar, A., Singh, S.K. and Mehta, P., 2017. Oxygen, deuterium, and strontium isotope characteristics of the Indus River water system. *Geomorphology*, 284, pp.5-16.

Shaughnessy, A.R., Forgeng, M.J., Wen, T., Gu, X., Hemingway, J.D. and Brantley, S.L., 2023. Linking stream chemistry to subsurface redox architecture. *Water Resources Research*, 59(5), pp.e2022WR033445.

Sheen, A.I., Kendall, B., Reinhard, C.T., Creaser, R.A., Lyons, T.W., Bekker, A., Poulton, S.W. and Anbar, A.D., 2018. A model for the oceanic mass balance of rhenium and implications for the extent of Proterozoic ocean anoxia. *Geochimica et Cosmochimica Acta*, 227, pp.75-95.

Shrestha, A.B., Agrawal, N.K., Alfthan, B., Bajracharya, S.R., Maréchal, J. and Oort, B.V., 2015. The Himalayan Climate and Water Atlas: impact of climate change on water resources in five of Asia's major river basins.

Singh, K., Dhiman, S. and Kishor, B., 2023, February. Spatio-Temporal Variations in Physico-Chemical Parameters of River Tawi. In IOP Conference Series: *Earth and Environmental Science* (Vol. 1110, No. 1, p. 012050). IOP Publishing.

Singh, P., Jain, S.K. and Kumar, N., 1997. Estimation of snow and glacier-melt contribution to the Chenab River, Western Himalaya. *Mountain Research and Development*, pp.49-56.

Singh, S.K., Sarin, M.M. and France-Lanord, C., 2005. Chemical erosion in the eastern Himalaya: major ion composition of the Brahmaputra and δ13C of dissolved inorganic carbon. *Geochimica et Cosmochimica Acta*, 69(14), pp.3573-3588.

Singh, S.P., Singh, S.K. and Bhushan, R., 2011. Behavior of dissolved redox sensitive elements (U, Mo and Re) in the water column of the Bay of Bengal. *Marine Chemistry*, 126(1-4), pp.76-88.

Sinha, D.K., Raju, K.A., Bhaskar, D.V. and Asha, K., 2001. Sulphur Isotopic Characteristics of pyrite and galena from the Singhora Group, Chhattisgarh supergroup, India: Genetic implications. *Geological Society of India*, 57(2), pp.171-177.

Soulet, G., Hilton, R.G., Garnett, M.H., Dellinger, M., Croissant, T., Ogrič, M. and Klotz, S., 2018. In situ measurement of flux and isotopic composition of CO_2 released during oxidative weathering of sedimentary rocks. *Biogeosciences*, 15(13), pp.4087-4102.

Spence, J. and Telmer, K., 2005. The role of sulfur in chemical weathering and atmospheric CO2 fluxes: evidence from major ions, $\delta^{13}C_{DIC}$, and $\delta^{34}S_{SO4}$ in rivers of the Canadian Cordillera. Geochimica et Cosmochimica Acta, 69(23), pp.5441-5458.

Stallard, R.F. and Edmond, J.M., 1983. Geochemistry of the Amazon: 2. The influence of geology and weathering environment on the dissolved load. *Journal of Geophysical Research: Oceans*, 88(C14), pp.9671-9688.

Stebbins, A., Williams, J., Brookfield, M., Nye Jr, S.W. and Hannigan, R., 2019. Frequent euxinia in southern Neo-Tethys Ocean prior to the end-Permian biocrisis: Evidence from the Spiti region, India. *Palaeogeography, Palaeoclimatology, Palaeoecology*, 516, pp.1-10.

Stüben, D., Berner, Z., Chandrasekharam, D. and Karmakar, J., 2003. Arsenic enrichment in groundwater of West Bengal, India: geochemical evidence for mobilization of As under reducing conditions. *Applied Geochemistry*, 18(9), pp.1417-1434.

Tipper, E.T., Bickle, M.J., Galy, A., West, A.J., Pomiès, C. and Chapman, H.J., 2006. The short term climatic sensitivity of carbonate and silicate weathering fluxes: insight from seasonal variations in river chemistry. *Geochimica et Cosmochimica Acta*, 70(11), pp.2737-2754.

Tipper, E.T., Stevenson, E.I., Alcock, V., Knight, A.C., Baronas, J.J., Hilton, R.G., Bickle, M.J., Larkin, C.S., Feng, L., Relph, K.E. and Hughes, G., 2021. Global silicate weathering flux overestimated because of sediment–water cation exchange. *Proceedings of the National Academy of Sciences*, 118(1), pp.e2016430118.

Tiwari, A.K., Singh, A.K., Phartiyal, B. and Sharma, A., 2021. Hydrogeochemical characteristics of the Indus river water system. *Chemistry and Ecology*, 37(9-10), pp.780-808.

Tiwari, S., Chate, D.M., Bisht, D.S., Srivastava, M.K. and Padmanabhamurty, B., 2012. Rainwater chemistry in the North Western Himalayan Region, India. *Atmospheric Research*, 104, pp.128-138.

Tiwari, S.K., Rai, S.K., Bartarya, S.K., Gupta, A.K. and Negi, M., 2016. Stable isotopes ($\delta^{13}C_{DIC}$, δD, $\delta^{18}O$) and geochemical characteristics of geothermal springs of Ladakh and Himachal (India): Evidence for CO_2 discharge in northwest Himalaya. *Geothermics*, 64, pp.314-330.

Torres, M.A., West, A.J. and Li, G., 2014. Sulphide oxidation and carbonate dissolution as a source of CO_2 over geological timescales. *Nature*, 507(7492), pp.346-349.

Tostevin, R., Turchyn, A.V., Farquhar, J., Johnston, D.T., Eldridge, D.L., Bishop, J.K. and McIlvin, M., 2014. Multiple sulfur isotope constraints on the modern sulfur cycle. *Earth and Planetary Science Letters*, 396, pp.14-21.

Tréguer, P.J. and De La Rocha, C.L., 2013. The world ocean silica cycle. *Annual Review of Marine Science*, 5(1), pp.477-501.

Tripathy, G.R. and Das, A., 2014. Modeling geochemical datasets for source apportionment: Comparison of least square regression and inversion approaches. *Journal of Geochemical Exploration*, 144, pp.144-153.

Tripathy, G.R. and Singh, S.K., 2010. Chemical erosion rates of river basins of the Ganga system in the Himalaya: Reanalysis based on inversion of dissolved major ions, Sr, and $^{87}Sr/^{86}Sr$. *Geochemistry, Geophysics, Geosystems*, pp.11(3).

Tripathy, G.R., Goswami, V., Singh, S.K. and Chakrapani, G.J., 2010. Temporal variations in Sr and $^{87}Sr/^{86}Sr$ of the Ganga headwaters: estimates of dissolved Sr flux to the mainstream. *Hydrological Processes: An International Journal*, 24(9), pp.1159-1171.

Tripathy, G.R., Singh, S.K. and Ramaswamy, V., 2014. Major and trace element geochemistry of Bay of Bengal sediments: Implications to provenances and their controlling factors. *Palaeogeography, Palaeoclimatology, Palaeoecology*, 397, pp.20-30.

Tripathy, G.R. and Singh, S.K., 2015. Re–Os depositional age for black shales from the Kaimur Group, Upper Vindhyan, India. *Chemical Geology*, 413, pp.63-72.

Tripathy, G.R., Mishra, S., Danish, M. and Ram, K., 2019. Elevated Barium concentrations in rain water from east-coast of India: role of regional lithology. *Journal of Atmospheric Chemistry*, 76, pp.59-72.

Turchyn, A.V. and Schrag, D.P., 2004. Oxygen isotope constraints on the sulfur cycle over the past 10 million years. *Science*, 303(5666), pp.2004-2007.

Turchyn, A.V., Tipper, E.T., Galy, A., Lo, J.K. and Bickle, M.J., 2013. Isotope evidence for secondary sulfide precipitation along the Marsyandi River, Nepal, Himalayas. *Earth and Planetary Science Letters*, 374, pp.36-46.

Van de Wal, R.S.W., De Boer, B., Lourens, L.J., Köhler, P. and Bintanja, R., 2011. Reconstruction of a continuous high-resolution CO_2 record over the past 20 million years. *Climate of the Past*, 7(4), pp.1459-1469.

Veizer, J., Ala, D., Azmy, K., Bruckschen, P., Buhl, D., Bruhn, F., Carden, G.A., Diener, A., Ebneth, S., Godderis, Y. and Jasper, T., 1999. $^{87}Sr/^{86}Sr$, $\delta^{13}C$ and $\delta^{18}O$ evolution of Phanerozoic seawater. *Chemical Geology*, 161(1-3), pp.59-88.

Venugopal, A., Tripathy, G.R., Goswami, V., Ghosh, S.K. and Singh, D., 2023. Oceanic Redox State During the Early Cambrian: Insights From Mo-S Isotopes and Geochemistry of Himalayan Shales. *Geochemistry, Geophysics, Geosystems*, 24(12), pp.e2023GC011182.

Verma, M., Kanhaiya, S., Singh, B.P. and Singh, S., 2022. Signatures of provenance, tectonics and chemical weathering in the Tawi River sediments of the western Himalayan Foreland, India. *Journal of Sedimentary Environments*, 7(3), pp.425-441.

Walker, J.C., Hays, P.B. and Kasting, J.F., 1981. A negative feedback mechanism for the long-term stabilization of Earth's surface temperature. *Journal of Geophysical Research: Oceans*, 86(C10), pp.9776-9782.

Wani, A.A., Bali, B.S., Bhat, G.R. and Hussain, N., 2020. Impact of tectonics on drainage network evolution of Suru basin, Kargil N/w Himalaya, Jammu and Kashmir, India. *Environmental Earth Sciences*, 79, pp.1-13.

West, A.J., Galy, A. and Bickle, M., 2005. Tectonic and climatic controls on silicate weathering. *Earth and Planetary Science Letters*, 235(1-2), pp.211-228.

White, A.F., Blum, A.E., Bullen, T.D., Vivit, D.V., Schulz, M. and Fitzpatrick, J., 1999. The effect of temperature on experimental and natural chemical weathering rates of granitoid rocks. *Geochimica et Cosmochimica Acta*, 63(19-20), pp.3277-3291.

Willenbring, J.K. and Von Blanckenburg, F., 2010. Long-term stability of global erosion rates and weathering during late-Cenozoic cooling. *Nature*, 465(7295), pp.211-214.

Winnick, M.J., Carroll, R.W., Williams, K.H., Maxwell, R.M., Dong, W. and Maher, K., 2017. Snowmelt controls on concentration-discharge relationships and the balance of oxidative and acid-base weathering fluxes in an alpine catchment, E ast R iver, C olorado. *Water Resources Research*, 53(3), pp.2507-2523.

Xu, S., Bufe, A., Li, S.L., Erlanger, E.D., Ran, L., Zhong, J., Yang, C.J., Zhang, L., Ma, T. and Sachse, D., 2024. Erosional modulation of the balance between alkalinity and acid generation from rock weathering. *Geochimica et Cosmochimica Acta*, 368, pp.126-146.

Zachos, J.C., Dickens, G.R. and Zeebe, R.E., 2008. An early Cenozoic perspective on greenhouse warming and carbon-cycle dynamics. *Nature*, 451(7176), pp.279-283.

Zondervan, J.R., Hilton, R.G., Dellinger, M., Clubb, F.J., Roylands, T. and Ogrič, M., 2023. Rock organic carbon oxidation CO_2 release offsets silicate weathering sink. *Nature,* 623(7986), pp.329-333.

This page has been intentionally left blank.

List of Publications

Peer reviewed

1. **Rout, R.K.** and Tripathy, G.R., 2024. Net effect of chemical erosion in a tropical basin on carbon cycle: Constraints from elemental and sulfur isotopic composition of the Mahanadi River water. *Chemical Geology*, 644, p.121859.
2. Das, S., Singh, S.K., Rai, S.K., Singhal, S., Rahaman, W., **Rout, R.K.** and Ali, S., 2024. Tectonics and climate controlled sedimentary provenance in the Teesta basin since mid-Holocene. *Geochemistry*, p.126224.
3. Ahmad, N., Singh, S.P., Sahu, S., Bhattacharyya, R., Maurya, A.S., Kumar, N., **Rout, R.K.** and Tripathy, G.R., 2024. Isotopic evidence of autochthonous organic matter acting as a major sink of anthropogenic heavy metals in modern lacustrine sediments. *Environmental Pollution*, 349, p.123964.
4. Danish, M., Tripathy, G.R., Mitra, S., **Rout, R.K.** and Raskar, S., 2021. Non-conservative removal of dissolved rhenium from a coastal lagoon: Clay adsorption versus biological uptake. *Chemical Geology*, 580, p.120378.
5. **Rout, R.K.**, Tripathy, G.R., Ahmad, M. Z., Ganie, S. H. Diffusion of subsurface oxygen intensifies the pyrite oxidation during baseflow stages of the Indus headwater (*in preparation*).

Conference Abstracts:

I. **Rout, R.K.** and Tripathy, G.R., 2021. Impact of extreme rainfall events on chemical weathering in a tropical river basin (Mahanadi River, India). National Conference on '*Frontiers in Geoscience Research Conference*', Physical Research Laboratory, Ahmedabad, India, 27th- 28th September 2021.

II. **Rout, R.K.** and Tripathy, G.R., 2023. Dissolved sulfur isotopic composition of the Mahanadi River, India: Seasonality and sulfate sources. *International Conference on 'Geology: Emerging Methods and Applications*', Christ College, Kerala, India, 25th-27th January 2023.

III. **Rout, R.K.** and Tripathy, G.R., 2023. Sulfide oxidation in the Brahmaputra River basin: A sulfur isotopic study. National Conference on '*Frontiers in Geoscience Research Conference*', Physical Research Laboratory, Ahmedabad, India, 1st-3rd February 2023.

IV. **Rout, R.K.** and Tripathy, G.R., Das, S., and Rai, S.K., 2023. Intense sulfide oxidation in the western Himalaya compared to Indus floodplain: Constraints from sulfur isotopic study. *Goldschmidt, 2023*.

V. **Rout, R.K.** and Tripathy, G.R., Das, S., and Rai, S.K., 2023. Pyrite oxidation and related CO_2 release from the Himalayas: A dissolved sulfur isotopic study, *AGU Fall meeting, 2023*.

VI. **Rout, R.K.** and Tripathy, G.R., Das, S., and Rai, S.K., 2024. Net CO_2 release during chemical weathering in the northwestern Himalaya: A dominant role of pyrite oxidation. *EGU, 2024*.